WIDE-ANGLE MULTISTATIC
SYNTHETIC APERTURE RADAR:
FOCUSED IMAGE FORMATION AND
ALIASING ARTIFACT MITIGATION

DISSERTATION

Jonathan E. Luminati, Captain, USAF

AFIT/DS/ENG/05-04

DEPARTMENT OF THE AIR FORCE
AIR UNIVERSITY

AIR FORCE INSTITUTE OF TECHNOLOGY

Wright-Patterson Air Force Base, Ohio

AFIT/DS/ENG/05-04

Wide-Angle Multistatic Synthetic Aperture Radar: Focused Image Formation and Aliasing Artifact Mitigation

DISSERTATION

Presented to the Faculty

Department of Electrical and Computer Engineering

Graduate School of Engineering and Management

Air Force Institute of Technology

Air University

Air Education and Training Command

In Partial Fulfillment of the Requirements for the

Degree of Doctor of Philosophy

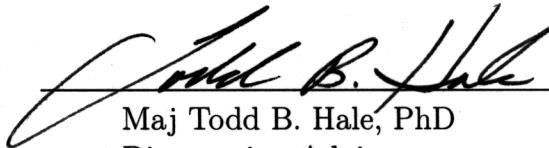Jonathan E. Luminati, B.S.E.E., M.Eng.E.E.

Captain, USAF

July 2005

WIDE-ANGLE MULTISTATIC SYNTHETIC APERTURE RADAR: FOCUSED IMAGE FORMATION AND ALIASING ARTIFACT MITIGATION

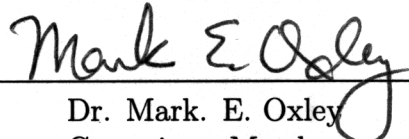Jonathan E. Luminati, B.S.E.E., M.Eng.E.E.

Captain, USAF

Approved:

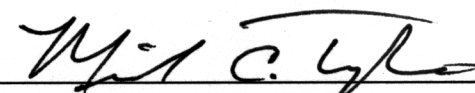_____   _____
Maj Todd B. Hale, PhD   13 JUL 05
Dissertation Advisor   Date

_____   _____
Dr. Michael J. Havrilla   13 Jul 2005
Committee Member   Date

_____   _____
Dr. Mark. E. Oxley   14 July 2005
Committee Member   Date

_____   _____
Dr. Michael A. Temple   14 Jul 05
Committee Member   Date

_____   _____
Dr. Milton E. Franke   15 July 2005
Dean's Representative   Date

Accepted:

_____   _____
Robert A. Calico, Jr.   21 July 05
Dean, Graduate School of Engineering and Management   Date

AFIT/DS/ENG/05-04

Abstract

Traditional Synthetic Aperture Radar (SAR) platforms use narrow radar beams, forcing the user to choose between two image types: larger, low resolution images or smaller, high resolution images. SAR platforms also usually operate in a monostatic configuration, transmitting and receiving radar echoes from the same antenna.

Switching to a wide-angle multistatic approach dramatically improves SAR performance. The wide beam enables simultaneous high resolution image production over large ground swaths. The multistatic configuration provides additional data diversity and promotes platform survivability. Combining these two attributes results in an approach termed Wide-Angle Multistatic Synthetic Aperture Radar (WAM-SAR).

Unfortunately, WAM-SAR suffers from two significant implementation problems. First, wavefront curvature effects, non-linear flight paths, and warped ground planes lead to image defocusing with traditional SAR processing methods. A new 3-D monostatic/bistatic image formation routine solves the defocusing problem, correcting for all relevant wide-angle effects. This routine consists of a variable bistatic tomographic imaging algorithm with near-field and warped ground plane corrections. Inverse Synthetic Aperture Radar (ISAR) imagery produced using Radar Cross Section (RCS) chamber data validates this approach.

The second implementation problem stems from the large Doppler spread in the wide-angle scene, leading to severe aliasing problems. This research effort develops a new anti-aliasing technique using randomized Stepped-Frequency (SF) waveforms. The SAR imaging process coherently combines the individual waveform ambiguity functions, resulting in a $|\mathrm{sinc}|^2$ structure which places Doppler nulls at aliasing artifact locations. This approach does not increase the image formation algorithm's computational complexity. Both simulation and laboratory results demonstrate effective aliasing artifact mitigation, eliminating more than 99% of the aliased energy.

Acknowledgements

Table of Contents

List of Figures

xi

List of Tables

List of Symbols

Symbol   Page

xxiii

List of Abbreviations

WIDE-ANGLE MULTISTATIC
SYNTHETIC APERTURE RADAR:
FOCUSED IMAGE FORMATION AND
ALIASING ARTIFACT MITIGATION

I. Introduction

Synthetic Aperture Radar (SAR) was first developed in the 1950's to provide multi-dimensional radar imagery of fixed ground patches using a moving radar platform (Sec. 3.1) [8, 74, 114, 133, 134]. While SAR images are typically lower in resolution then optical images, the ability to collect SAR data during the day or night as well as in all weather conditions has helped make SAR a critical player on the modern battlefield as well as for remote sensing applications [36].

SAR systems transmit a series of radar pulses into the surrounding environment. The echoes from each pulse are processed into individual One-Dimensional (1-D) range profiles, denoting the scene's response to the illuminating wave as a function of range. Collectively, all pulse echoes span a time period known as the Coherent Processing Interval (CPI) [116]. As the SAR platform moves, the changing platform location changes the range profile. Using appropriate processing methods, the 1-D range profiles can be combined to form multi-dimensional imagery. The distance covered by the SAR platform during the CPI determines the *synthetic* antenna length and the final image resolution [121].

1.1 Current SAR Limitations

Over time, SAR image quality has increased dramatically. Improved radar hardware, digital processing, and new algorithms combine to yield substantially higher resolution imagery than earlier systems. Modern SAR systems usually operate in one of two data collection modes: stripmap (Sec. 3.4) or spotlight (Sec. 3.5) [65,

1

100, 117]. In stripmap mode, the radar images vast ground patches at moderate-to-low resolution. In spotlight mode, the radar produces high resolution imagery of small ground patches. While some SAR platforms operate in either mode, they cannot work in both simultaneously, forcing the user to choose: large, low resolution images or small, high resolution images. Neither option is ideal in today's increasingly unpredictable battlefield environments.

1.1.1 Narrow Transmit Beams. One feature common to most stripmap and spotlight SAR modes is a narrow transmit/receive beam, typically only a couple degrees wide. While the use of narrow beams greatly simplifies data collection and processing, it also precludes high resolution image formation over large ground patches. Conversely, widening the beam makes feasible a whole host of performance improvements over-and-above the promise of large, high resolution images. These benefits include high resolution imaging with narrowband waveforms (Sec. 2.2.4) [116, 143], simultaneous SAR and Moving Target Indication (MTI) missions (Sec. 2.2.5) [44, 45, 66, 94, 143], and high resolution coherent and non-coherent change detection (Sec. 2.2.6) [110, 127, 143].

1.1.2 Monostatic Data Collection. Traditional SAR platforms usually operate in a monostatic mode, with a single radar platform acting as both transmitter and receiver. While monostatic radar systems are relatively simple, they suffer from a number of potential pitfalls. First, by broadcasting their presence with high powered transmit waveforms, they are inherently vulnerable to both physical and Electronic Warfare (EW) attacks [121]. Second, the proliferation of stealth technology designed to minimize monostatic radar scattering means some militarily significant targets cannot be reliably imaged using monostatic radars [73]. Third, SAR images often suffer from shadowing effects, where large foreground scattering objects hide returns from small background objects. Shadowing effects are particularly severe in urban and forested environments [18].

In recent years, there has been increasing interest in bistatic radar, where signals transmitted by one platform are received by another, geographically separated, platform [116]. Bistatic collection geometries mitigate monostatic data collection paradigm limitations including both platform survivability and shadowed target concerns. A natural extension to bistatic radar is multistatic radar where several platforms receive echoes from multiple platforms' transmit waveforms. This procedure dramatically increases data diversity over a given ground patch. Since each collection geometry provides a unique set of shadows, fusion of multistatic SAR imagery would dramatically reduce shadowing impacts as well as improve overall system redundancy.

1.2   WAM-SAR Research

Motivated by the traditional SAR limitations outlined in the preceding section, this research effort focuses on a concept termed Wide-Angle Multistatic Synthetic Aperture Radar (WAM-SAR). By combining both wide-angle and multistatic attributes, WAM-SAR provides high resolution persistent surveillance of large ground swaths while minimizing concerns about EW and target shadowing.

With so many perceived benefits, one wonders why the WAM-SAR concept has not already been implemented. Although implementation challenges exist in a number of different areas, two fundamental problems preclude high quality WAM-SAR imaging. Solving these two problems forms the basis for this research effort. By demonstrating solutions to these issues, this document motivates the transition of WAM-SAR from research towards eventual implementation.

1.2.1   Focused Image Formation.   The first WAM-SAR implementation problem addressed is focused image formation (Sec. 2.4). Traditional narrow-angle SAR systems make many idealistic assumptions including perfectly linear platform flight paths, planar ground patches, and plane wave illumination [65]. None of these assumptions are valid in the wide-angle case, leading to defocused SAR imagery. While a number of different algorithms have appeared to correct these issues individually,

none of them is capable of handling the general 3-D wide-angle multistatic scenario implied by WAM-SAR. Together with supporting material from Chapters III and IV, Chapter V develops a new processing method, based on tomographic principles, capable of solving all these problems. Inverse Synthetic Aperture Radar (ISAR) data (Chapter IV) from the Air Force Institute of Technology's (AFIT's) Radar Cross Section (RCS) chamber is used to validate this new imaging method in Chapter V.

1.2.2   Aliasing Artifact Mitigation.   Producing focused wide-angle imagery is only part of the problem. By widening the radar's beam, the ground echo's Doppler spread also increases substantially. As a result, the required sampling frequency along the synthetic aperture becomes much higher. This requirement manifests itself as a need for a higher radar Pulse Repetition Frequency (PRF). However, in the wide-angle case, the required PRF is impractical (Sec. 2.5.1) [27, 36, 121]. Failing to meet the PRF requirement results in undersampled data and causes Doppler aliasing in the resulting imagery. Aliasing artifact mitigation is the second WAM-SAR implementation problem and the focus of Chapters VI-IX.

Previous SAR aliasing artifact mitigation efforts primarily focus on spatial filtering methods using active phased array antennas (Sec. 2.5.2.1) [27, 56, 141–143]. By independently digitizing and recording the radar echoes from each antenna element, digital spatial filters can be built, removing the aliasing artifacts. Unfortunately, even simple phased arrays are very expensive to build and operate. The data storage and communication bandwidth requirements for such an approach are also prohibitive.

Another class of anti-aliasing techniques revolves around waveform diversity methods [27]. Despite the recent advent of diverse waveform generation hardware, most SAR systems use Linear Frequency Modulation (LFM) waveforms. While there has been increased interest in waveform diversity within the general radar community, waveform diverse SAR applications are quite limited (Sec. 2.5.2.2).

The anti-aliasing technique introduced in Chapter VI uses randomized Continuous Wave (CW) Stepped-Frequency (SF) waveforms to place Doppler filter nulls on

top of aliasing artifacts, removing them from the imagery. As opposed to the phased array approach, the SF waveform method only requires a two channel radar, reducing antenna complexity, digitization hardware, communication system bandwidth, and image processing routine complexity. Additionally, by using a CW frequency-hopped radar signal, the transmission platform is much less vulnerable to attack, even when operating in a monostatic mode.

1.2.3 Research Contribution Summary. Figure 1.1 provides a graphical overview of the major research results. The user desires a wide-angle data collection enabling simultaneous high resolution image formation over large ground swaths. Using conventional SAR processing methods, the wide-angle data is essentially useless. The two images under the "conventional processing" heading illustrate this fact. The top image shows a high resolution point scatterer image obtained from RCS chamber data (upper left-hand scatterer in Fig. 5.16(a)). Total image area is 20 cm^2. The point scatterer is defocused and translated due to the wide-angle data collection. Application of near-field corrections using the tomographic WAM-SAR processing method results in the right-hand image (upper left-hand scatterer in Fig. 5.16(b)). In this case, the scatterer is both well focused and correctly located.

The lower images in Fig. 1.1 have an area of 1 km^2. The left-hand "conventional" image shows a well focused scatterer at the scene center surrounded by eight large aliasing artifacts (Fig. 7.26). Using WAM-SAR's randomized SF waveform approach, these artifacts are mitigated in the lower right-hand image (Fig. 7.26). Taken together, the images in Fig. 1.1 illustrate WAM-SAR's ability to produce focused alias-free high resolution imagery over large ground swaths, encapsulating the contributions of this research effort.

1.3 Notation and Terminology

In this document, most notation and terminology is defined as needed. None-the-less, these initial notes should help avoid confusion:

Wide-angle data collection

Conventional
processing

WAM-SAR
processing

Focused imagery via
near-field tomography

Chapters III-V

Anti-aliasing via
waveform diversity

Chapters VI-IX
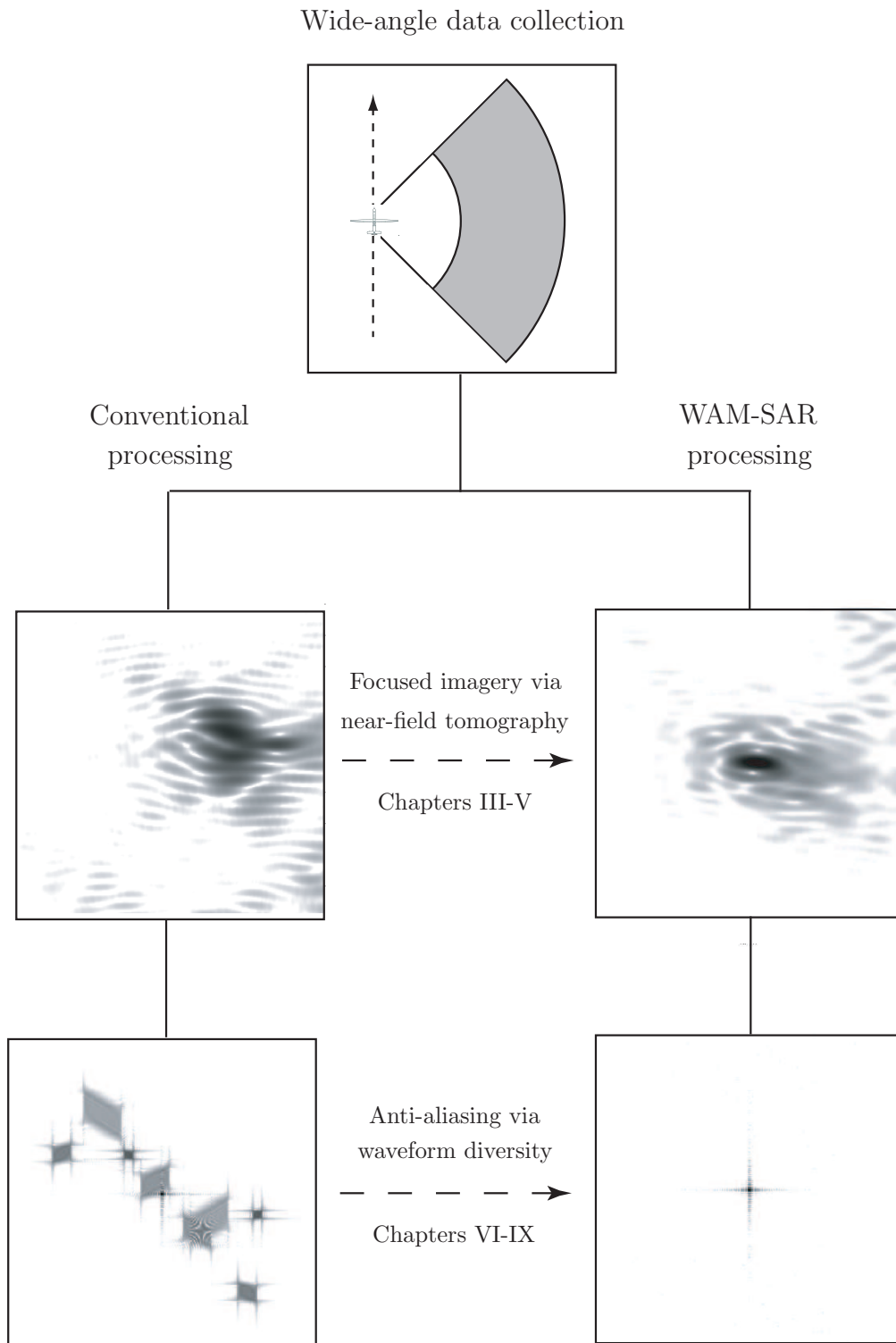
Figure 1.1:   WAM-SAR improvements over conventional processing for wide-angle data. Conventional processing of wide-angle results in defocusing (upper left-hand image) and aliasing (lower left hand image). WAM-SAR processing solves both the focusing (upper right-hand image) and aliasing (lower right-hand image) problems.

- The Latin abbreviation i.e. (for *id est*) means "in other words."

- The Latin abbreviation e.g. (for *exempli gratia*) means "for example."

- All vectors are column vectors and denoted with an overbar (e.g., $\bar{u}_{\mathrm{TX}}$, see (5.1)).

- In the text, vectors are written with a superscripted $^{\mathrm{T}}$ indicating a matrix transpose (e.g., $\bar{u}_{\mathrm{TX}} = [u_x, u_y, u_z]^{\mathrm{T}}$).

- Matrices are denoted with a bolded capital letter (e.g., $\mathbf{Z}_c$, see (6.46)).

- The symbol $*$ denotes convolution.

- The superscripted symbol * denotes conjugation.

- The symbol $!$ denotes factorial.

- The symbol $\times$ denotes cross product.

- The symbol $\cdot$ denotes dot product.

- The symbol $\triangleq$ denotes definition.

- The letter j is defined as $\sqrt{-1}$.

- Vertical bars $|\cdot|$ denote modulus of a complex number or magnitude of a real number (e.g., $|a + jb| = \sqrt{a^2 + b^2}$). When surrounding a vector, these bars indicate a Euclidean norm.

- The function $\delta(\cdot)$ denotes the Dirac Delta function, a generalized function

- When paired with a scalar, δ denotes resolution or spacing (e.g., δx denotes resolution in the x-direction, see (3.20)).

- When paired with a scalar, Δ denotes extent (e.g., Δk_x denotes extent of available spatial frequency data in the k_x-direction, see (3.20)).

- Fourier function pairs use lowercase letters in the time (spatial) domain and capital letters in the frequency (spatial frequency) domain (e.g., $f(x)$ and $F(k_x)$).

- Punctuation marks are included at the end of equations as dictated by the contextual grammatical requirements. The periods or commas appearing at the end of these equations have no mathematical significance.

In addition to defining mathematical symbols, there are a few terms warranting mention. The terms "scene," "scatterer," and "target" all refer to objects being imaged by the SAR sensor, although they each have nuances of meaning. The word "scene" denotes a traditional SAR image containing terrain, vegetation, vehicles, etc. The term "target" refers to an isolated object or set of objects, often contained within an RCS chamber. The word "scatterer" indicates a specific point reflecting incoming radar waves (Sec. 3.7). Both scenes and targets are typically composed of numerous scatterers.

The terms "range" and "cross range" also merit introduction. Although there are different kinds of "range" (Fig. 3.2), the term essentially denotes distance between the radar and a scatterer[1]. The term "cross range" is defined orthogonal to the range direction, parallel to the SAR platform flight path. In narrow-angle SAR, traditional pulse compression techniques provide range resolution while SAR processing provides cross range resolution (Sec. 3.9). In the wide-angle case, these effects are coupled (Sec. 5.3). Chapters II and III use the typical narrow-angle SAR convention, defining range in the x-direction and cross range in the y-direction. Range resolution is therefore denoted δx while cross range resolution is denoted δy. From Chapter V forward, the 3-D wide-angle case necessitates taking a more general approach, allowing arbitrary rotation of the 3-D range r, horizontal cross range h, vertical cross range v coordinate system relative to the (x, y, z) image domain containing the scene.

1.4 Document Overview

The remainder of this document is divided into nine chapters. Chapter II begins by providing a more detailed introduction to the WAM-SAR concept, illustrating the substantial benefits and challenges inherent in this approach. It outlines the status of current research efforts in the two problem areas: focused image formation and aliasing artifact mitigation. Discovering and demonstrating solutions to these two problems form the basis for subsequent chapters.

---

[1]This conceptual definition becomes more complex in the bistatic case (Sec. 5.1.2).

Chapter III provides a detailed overview of Two-Dimensional (2-D) SAR data collection and processing. It begins by reviewing key events in SAR history and discussing the role of SAR systems in both military and non-military applications. After introducing the two primary SAR operating modes (stripmap and spotlight), the chapter illustrates how individual radar waveform echoes can be used to represent a scene's spatial frequency content. This spatial frequency content is then transformed into 2-D imagery using traditional Fourier Transform (FT) processing methods. Narrow-angle approximations, sampling requirements, and resulting image resolution are also introduced. Portions of Chapter III were published in [90].

RCS chamber data is particularly useful to the research effort, providing a rapid and inexpensive method for collecting real radar scattering data in a laboratory environment. Chapter IV provides an introduction to RCS chamber design, data collection, and calibration. It begins by identifying different chamber types, focusing on the indoor far-field range, the type operated by AFIT. Data from AFIT's chamber is used in Chapters V and IX, validating the various research efforts. After discussing specific limitations of AFIT's chamber, Chapter IV reviews relevant data collection and calibration procedures. The method entails collecting four data files for each scattering target. Combining these files through a procedure known as "vector background subtraction" results in data approximating the target's free-space scattering signature. In addition to research efforts discussed in this document, the calibration code processed RCS data in [43, 76].

Chapter V solves the focused image formation problem, deriving and demonstrating a Three-Dimensional (3-D) near-field monostatic/bistatic data processing method capable of producing focusing imagery over warped surfaces using arbitrary data collection geometries. The first few sections of Chapter V extend Chapter III's 2-D far-field monostatic spatial frequency plane paradigm to the 3-D far-field bistatic case. Wide-angle resolution metrics are also derived. These results are validated using ISAR data from AFIT's RCS chamber and correct errors from a recent publication [108]. The chapter then extends the image formation approach to accommodate

9

radiative near-field scattering data. Although moving to the near-field breaks the spatial frequency domain paradigm, the resulting image domain approach easily accommodates the near-field situation, correcting not only for wavefront curvature, but also for amplitude distortions caused by non-uniform antenna patterns and range attenuation. The near-field imaging method is tested in a variety of 2-D and 3-D situations. Most significantly, it corrects for warped ground plane effects in a 3-D near-field bistatic scenario. This situation mirrors the WAM-SAR data focusing problem.

Having solved the focused image formation problem, the research effort shifts to address aliasing artifact mitigation. Chapter VI introduces a new waveform diversity-based anti-aliasing technique for 2-D monostatic SAR. First, it re-introduces the anti-aliasing problem from a grating lobe perspective. It then attacks the problem from an information theory paradigm, demonstrating *what* information is required for aliasing mitigation without specifying *how* to obtain that information. With the new information requirements, traditional LFM SAR waveforms are set aside in favor of randomized SF waveforms. SF waveforms provide the required information, allowing construction of Doppler filter nulls at aliasing artifact locations. The chapter concludes by developing a procedure generating orthogonal randomized SF waveform sets and minimizing cross-correlation effects while improving Doppler filter performance. The anti-aliasing concept was first published in [87,88] and has been expanded in [89].

Chapter VII uses an idealized point scatterer simulator for testing the anti-aliasing technique developed in Chapter VI. The chapter's first half focuses on simulator development, illustrating the time and frequency domain behavior of digitized LFM and SF waveforms. After combining the waveform simulation code with a 2-D monostatic data collection geometry, the chapter moves on to test technique performance using a set of realistic SAR platform parameters. Results are presented using both qualitative SAR images and a quantitative energy metric, demonstrating technique effectiveness. This chapter's results were published in [87–89] and independently verified in [92].

While Chapter VII provides impressive 2-D monostatic results, WAM-SAR requires aliasing artifact mitigation in a more general 3-D monostatic/bistatic geometry. Unfortunately, implementation in these situations violates one of the technique's assumptions. None-the-less, Chapter VIII demonstrates effective aliasing artifact mitigation in non-ideal 3-D scenarios. The chapter begins by deriving an expression for Doppler shift in 3-D bistatic geometries. This expression is used to calculate qualitative and quantitative measures of technique effectiveness in different scenarios. These scenarios include a high altitude 3-D monostatic platform, a stand-off transmitter with a passive bistatic close-range receiver, and a multistatic circular-orbit data collection. In each case, the technique performs well, eliminating more than 99% of aliasing artifact energy.

Chapters VII and VIII demonstrate anti-aliasing performance using simulated point scatterer data. However, real targets have substantially more complex returns. Chapter IX validates SF waveform Doppler filtering performance on complex targets using both a high-fidelity simulator (i.e., Xpatch [112]) and real RCS chamber data. However, both the high-fidelity simulation data and RCS chamber data are calculated/measured in the spatial frequency domain, and are therefore essentially waveform independent. As a result, a new technique was needed to convert *post*-matched filter spatial frequency plane data into *pre*-matched filter SF waveform echoes. Developed during this research effort and published in [84], this technique eliminates the need for an expensive arbitrary waveform generator for validating SF waveform Doppler filtering performance. Using the converted complex target spatial frequency data, anti-aliasing performance is demonstrated on both Xpatch data [86] and measured RCS chamber data.

Chapter X concludes the dissertation document. After reviewing critical goals and accomplishments, it also suggests areas for future work. Following the conclusion, several brief appendices provide background on the FT and key `Matlab`® files for both point scatterer data simulation and SAR/ISAR image formation.

II. Wide-Angle Multistatic SAR: Benefits & Challenges

Increasingly complex battlefield environments are placing greater demands on tactical radar systems. Originally, Synthetic Aperture Radar (SAR) images were simply used to provide ground maps, illustrating the general terrain layout and localizing fixed targets. Today, users want SAR imaging systems capable of providing persistent, real-time surveillance of both stationary and moving targets over large ground swaths. Additionally, they want imagery of sufficient resolution to facilitate not only target detection but also target identification by image analysts and/or Automatic Target Recognition (ATR) algorithms.

Using traditional SAR imaging platforms and techniques, it is not feasible to simultaneously meet all user requirements. Radar platforms (e.g., Joint-STARS) often collect SAR imagery by time-multiplexing SAR data collection with Moving Target Indication (MTI) applications, limiting both synthetic aperture length (and therefore image resolution) and the MTI system's revisit rate. Other times, Unmanned Aerial Vehicles (UAVs) (e.g., Predator) collect SAR data where the small image area provides a narrow "soda-straw" target region view. While this approach is adequate for small, high-interest regions, it is inadequate for wide-area surveillance. In short, the required number of collection platforms, competing applications, finite frequency spectrum, and extensive processing requirements preclude high resolution persistent surveillance of large regions.

Addressing the inherent limitations of current SAR systems requires more than incremental improvements in data collection and processing methods. It requires an entirely new approach.

Such an approach has recently been proposed by Mr. Edmund Zelnio, chief of the Air Force Research Laboratory's (AFRL) Sensor ATR Technology Division (SNA). Mr. Zelnio has proposed using a wide-angle monostatic imaging paradigm that should be capable of addressing these issues [143]. This research effort takes this paradigm one step further, examining the multistatic case, where both monostatic

and/or bistatic radar echoes may be available. The resultant approach is termed Wide-Angle Multistatic Synthetic Aperture Radar (WAM-SAR).

This chapter continues by outlining WAM-SAR benefits. It also highlights specific implementation challenges, reviews the current literature status, and introduces the proposed solutions.

2.1 WAM-SAR

The key enabler of WAM-SAR is the use of wide-angle radar beams [143]. In general, a wide-angle SAR system can be defined as one whose angular extent $\Delta\theta$ is large enough that its cross range resolution is superior to its range resolution [105]. Angular extent denotes the span of azimuth angles, from the SAR platform to the scene, observed during the data collection. Setting range resolution δx (3.20) equal to cross range resolution δy (3.21) (after removing the small $\Delta\theta$ assumption) and solving for $\Delta\theta$ yields the following mathematical criterion for when $\Delta\theta$ is truly wide-angle [104][1]

$$\Delta\theta > 2\sin^{-1}\left(\frac{B}{2f_c}\right), \tag{2.1}$$

where B is waveform bandwidth and f_c is the center frequency. The $\Delta\theta$ values used in this document are large enough that the SAR sensor is wide-angle for any reasonable bandwidth.

Figure 2.1 depicts the monostatic wide-angle radar approach. A single radar platform transmits and extremely wide beam covering a large ground swath. The beam is transmitted in a *stripmap mode* (Sec. 3.4) fashion to gain maximum coverage area. When using stripmap mode, $\Delta\theta$ is equal to antenna beamwidth. The monostatic radar echoes are received, range-gated (establishing the ground swath width $\Delta R \triangleq R_{\max} - R_{\min}$), and digitally sampled. These digital samples are then processed to form

---

[1]In the narrow-angle case, range is traditionally defined in the x-direction and cross range is defined in the y-direction. Chapter V removes this assumption when examining the more general wide-angle case.

an arbitrary number of individual, high resolution, *spotlight mode* (Sec. 3.5) SAR images at arbitrary locations within the beam footprint.

Figure 2.2 illustrates the full WAM-SAR architecture. The wide-angle data collection principles remain identical to the monostatic case, but in WAM-SAR, more than one platform is present. Each platform may act as a transmitter, receiver, or both transmitter and receiver[2]. In the figure, both platforms act as transmitters and receivers, flooding the same ground swath with Radio Frequency (RF) energy. All three individual image regions are struck by RF energy from both platforms. Platform 1 is forming a monostatic image of the left-most target, while platform 2 is forming both a bistatic image of the center target and a monostatic image of the right-most target. The addition of bistatic imaging geometries adds a host of opportunities and challenges. Some of these opporunities/challenges are addressed throughout the reminder of this chapter and the rest of the document.

As a point of comparison, the theoretical benefits of the WAM-SAR approach will be compared with current Global Hawk parameters/capabilities. Table 2.1 lists a number of relevant Global Hawk parameters. Several of these parameters are used in the next section, illustrating the advantages of the WAM-SAR approach over current imaging radar capabilities. These comparisons are not intended to imply WAM-SAR could be directly ported to the existing Global Hawk platform. They are simply used as a point of reference for motivating WAM-SAR research efforts.

2.2   *WAM-SAR Benefits*

This section outlines the benefits achieved with the WAM-SAR approach. Many of the concepts in this section are taken from discussions with Mr. Zelnio [143].

2.2.1 Large Coverage Area.   One of the most significant advantages of the wide-angle approach is the vast ground swath available for imaging. The Global Hawk's field-of-regard is listed as $\pm 45°$, indicating the relatively narrow transmit beam

---

[2]The use of multiple platforms in this manner is also called netted radar [9].
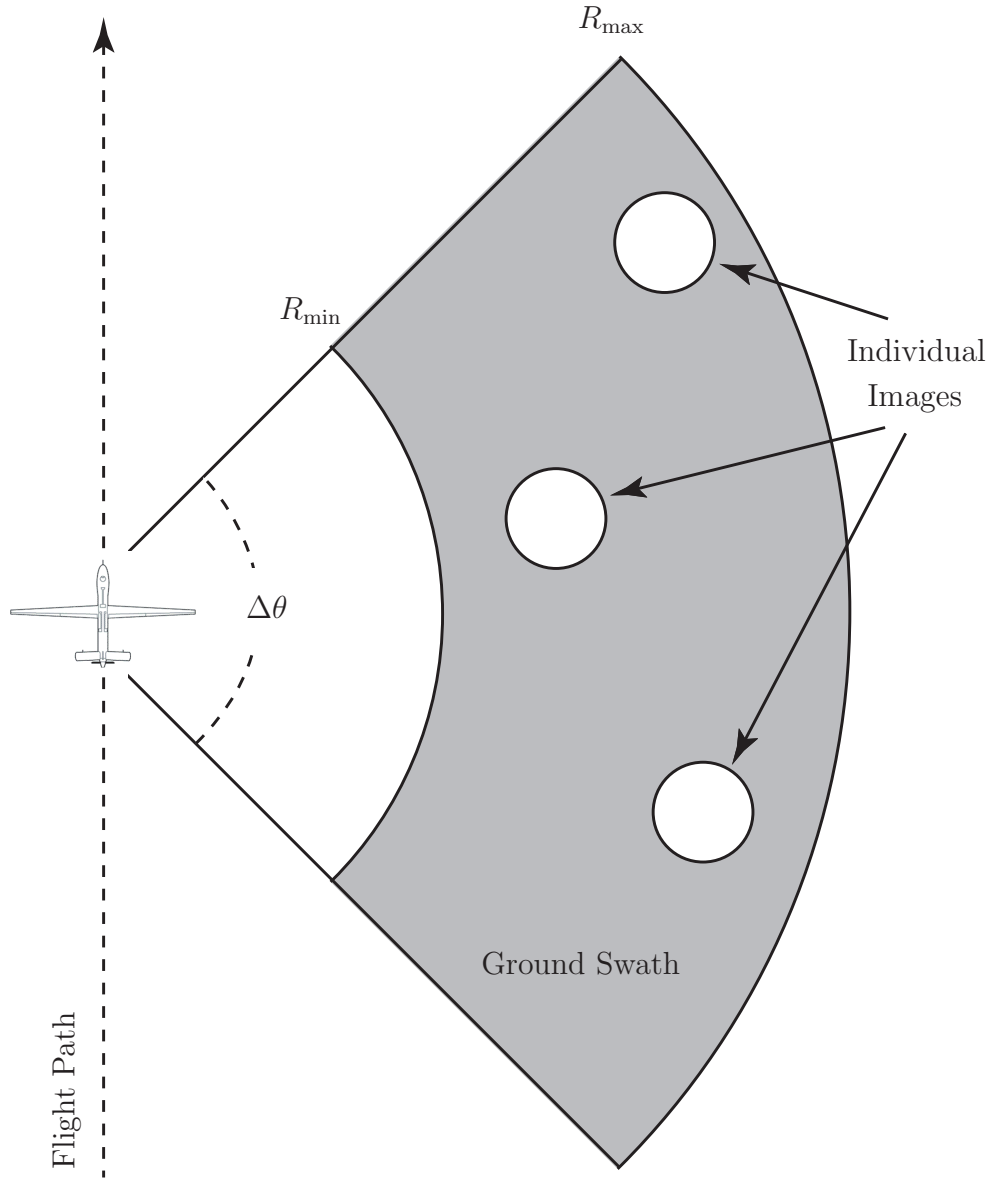
Figure 2.1: Monostatic wide-angle concept. A single radar platform transmits an extremely wide beam ($\Delta\theta \approx 90°$) over a large ground swath. Monostatic echoes are received and processed to form a number of small, high resolution, spotlight mode SAR images in parallel.
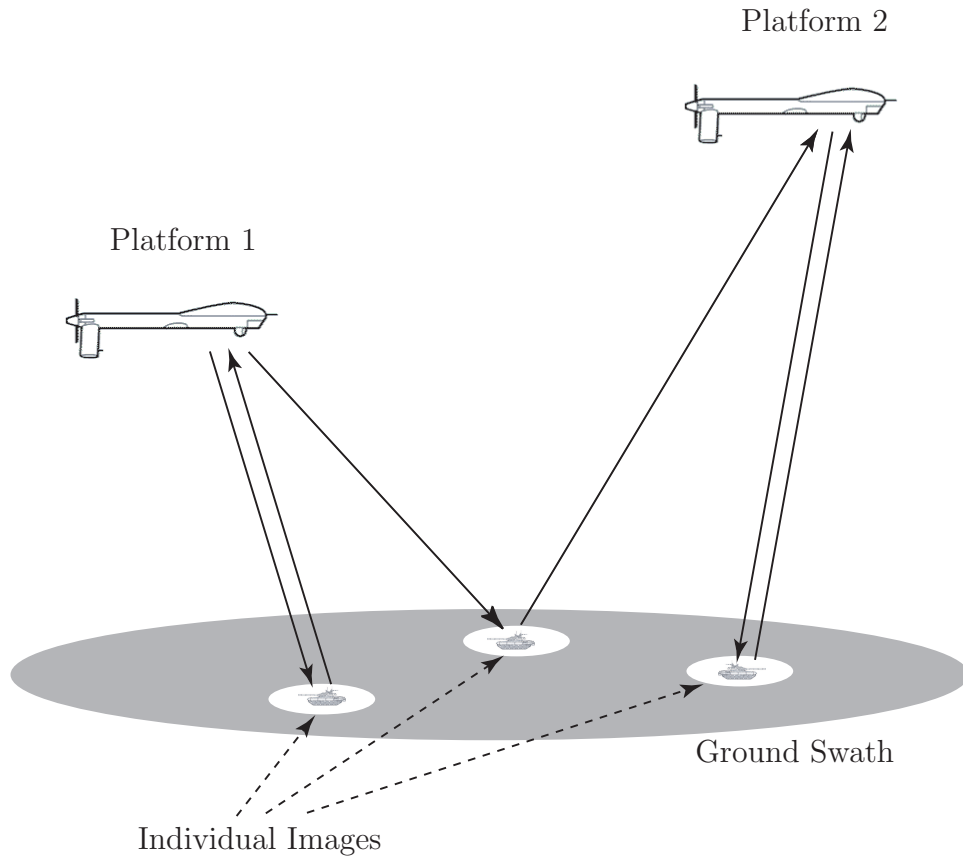
Figure 2.2: WAM-SAR concept. One or more radar platforms transmit an extremely wide beam ($\Delta\theta \approx 90°$) over a large ground swath. Monostatic and/or bistatic radar echoes are received and processed to form a number of small, high resolution, spotlight mode SAR images in parallel.

Table 2.1:   Global Hawk Parameters [32].

Parameter	Value
Frequency	X-band
Bandwidth	600 MHz
Peak Power	3.5 kW
Maximum Velocity	200 m/s
Maximum Ceiling	65,000 ft
Maximum Loiter Time	24 hours
Antenna Field-of-Regard	$\pm 45°$
Antenna Dimensions	14.4" x 49.5"
Stripmap Resolution	1 m
Strip Width	10 km
Spotlight Resolution	0.3 m
Maximum Range (for SAR)	200 km
Minimum Discernable Velocity (MDV)	2.1 m/s

can be steered up to 45° off boresight. WAM-SAR uses a 90° beamwidth to replicate this coverage without the need for beamsteering. Due to the stripmap data collection mode, this beamwidth translates directly to an angular coverage of $\Delta\theta = 90°$ and is significantly larger than any systems discussed in the literature [54, 118].

Another important consideration in establishing the coverage area is the maximum range swath width ΔR. Although the maximum Global Hawk stripmap image width is only 10 km, the goal of WAM-SAR is continuous surveillance of the entire ground swath. To accomplish this task, $R_{\max} = 200$ km while $R_{\min}$ falls between 20 and 50 km depending on the stand-off range needed to keep the radar platform safe from attack. These values place ΔR in a range between 150-180 km. Combining these values with the wide beamwidth give a total instantaneous ground swath area of approximately 30,000 km^2.

2.2.2   Persistent Coverage.   While the large instantaneous ground swath is certainly beneficial, another key advantage of the wide-angle approach is the persistent coverage maintained on targets within the beam [143]. Since the beam covers the entire ground swath simultaneously, the revisit rate is equal to the radar's Pulse

Repetition Frequency (PRF). This fact is especially important for MTI and tracking applications as discussed in Section 2.2.5.

Assuming a linear flight path and the maximum (i.e., worst-case) Global Hawk velocity of 200 m/s, a broadside target at a 50 km range remains in the beam for more than eight minutes. A target at the maximum range of 200 km is illuminated for more than 33 minutes. If the radar platform opted for a circular flight path, instead of the traditional linear flight path, the 50-200 km ground swath range dictates a circular swath with a 150 km diameter. The resulting 17,600 km^2 ground swath could be monitored continually for up to 24 hours, the maximum Global Hawk loiter time. This spotlight mode SAR collection scenario would result in $\Delta\theta = 360°$ while the actual beamwidth could be reduced to approximately 62° due to the smaller, circular ground patch.

2.2.3 High Resolution. WAM-SAR not only images vast ground swaths, but also produces extremely high resolution imagery. Section 3.9 presents a method for calculating the theoretical SAR image resolution using traditional approaches assuming small $\Delta\theta$. Chapter V extends the resolution derivation to the wide-angle case. In a typical SAR system, where $\Delta\theta$ is only a few degrees, the range and cross range resolutions are essentially independent since one is based on waveform bandwidth and the other is based on antenna beamwidth. However, the small angle assumption used in these calculations is not valid in the wide-angle case. The true resolution in each dimension is determined both by the waveform and beamwidth characteristics.

Figure 2.3 illustrates the Impulse Response (IPR) functions for a wide-angle $\Delta\theta = 90°$ SAR data collection. IPR functions represent the SAR image produced for a scene consisting of a single point scatterer located at the scene center. Ideally, IPR functions should be delta functions, but finite $\Delta\theta$ and B cause IPR broadening. Subfigure (a) shows the $B = 6$ GHz (e.g., wideband) IPR, while subfigure (b) illustrates the $B = 600$ MHz (e.g., narrowband) IPR. The ovals on top of each peak denote the -4.0 dB IPR boundary.
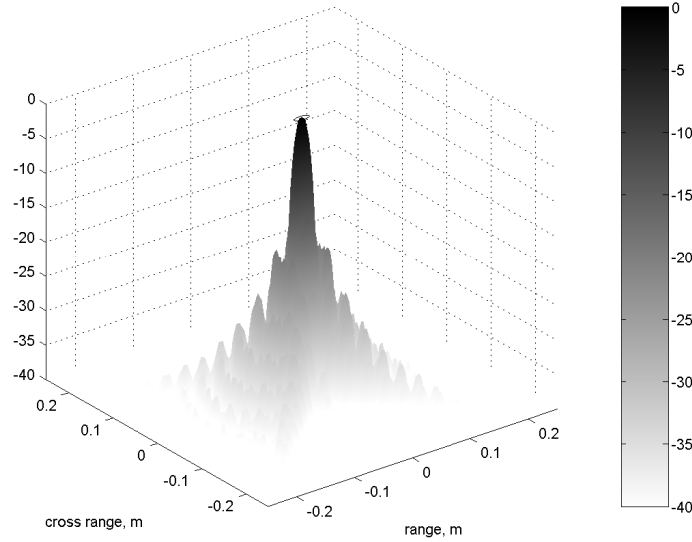
(a) $B = 6$ GHz
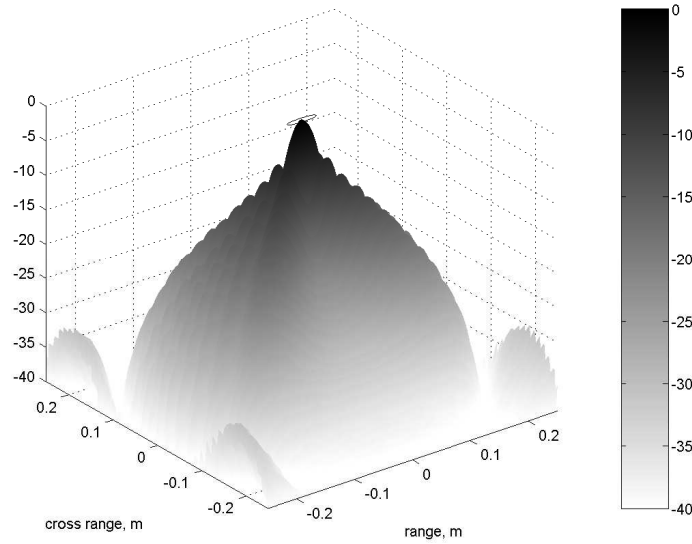
(b) $B = 600$ MHz

Figure 2.3: IPR functions for SAR data collections pictured in Fig. 3.8. The ovals on top of each peak denote the -4.0 dB contour lines. Note, while the -4.0 dB resolutions are similar, the reduction in bandwidth results in significantly higher sidelobe levels (40.0 dB dynamic range).

Table 2.2: Predicted vs. actual resolution for wide-angle SAR collections. Predictions use (3.20) and (3.21) which contain an inherent narrow angle assumption. Actual values are taken from IPR images in Fig. 2.3.

Relevant	Collection Parameters		Predicted Resolution		Actual Resolution	
Figures	B, GHz	$\Delta\theta$, deg	δx, cm	δy, cm	δx, cm	δy, cm
2.3(a)	6.0	90°	2.5	1.0	2.4	0.9
2.3(b)	0.6	90°	25.0	1.0	5.2	1.0

Table 2.2 illustrates the predicted and actual IPR resolutions (using the traditional resolution formulas in Sec. 3.9) for the wide-angle collections illustrated in Fig 2.3. In this example, range is defined in the x-direction while cross range is defined in the y-direction. This definition is consistent with an imaging target normal to the SAR platform's flight path.

The predicted resolution is quite accurate in the wideband ($B = 6$ GHz) case. However, the resolution formulas fail to predict the appropriate range resolution δx in the relatively narrowband ($B = 600$ MHz) case. In both cases, the resolutions are significantly better than the Global Hawk's 1.0 m stripmap and 0.3 m spotlight resolutions, demonstrating the wide-angle imaging approach's utility. It should also be noted, while reducing the bandwidth by a factor of ten only reduced the range resolution by a factor of two, it significantly increased the IPR sidelobe levels.

The ability to generate resolutions consistent with those in Tab. 2.2 requires the SAR platform collect radar echoes over extremely wide angular extents. One part of collecting this data involves using a wide beam, but the other part depends on the target itself. If the target does not reflect energy (i.e., persist) over the entire $\Delta\theta$ extent, the effective angular coverage of that particular target is reduced. This limited persistence can be caused by a number of different effects including individual target scattering characteristics and/or target shadowing. In fact, the only targets whose signatures typically persist over such large angles are point scatterer-like objects (e.g., dipole antennas, telephone poles, flag poles). More typically, scatterer returns in complex scenes do not persist for more than 20° in azimuth [98].

The limited persistence of real targets seems to limit the resolution, and thus the usefulness, of a wide-angle SAR platform. However, this observation is incorrect. Consider a flat metallic plate. The plate's peak monostatic Radar Cross Section (RCS) occurs when the wave propagation vector is perpendicular to the plate's surface. As the illumination angle changes, the RCS decreases based on the illumination wavelength and plate dimensions. It is well known the mainlobe width $\Delta\zeta$ of the plate's specular reflection (i.e., the plate's persistence) is given by [73]

$$\Delta\zeta = \frac{\lambda_c}{2W}, \tag{2.2}$$

where W is the plate width and λ_c is the center wavelength. The amount of angular data available to the SAR sensor is bounded by the scatterer persistence, thus $\Delta\theta \leq \Delta\zeta$ no matter what collection geometry is being used. Assuming the SAR sensor collects the full $\Delta\zeta$ scattering data, (3.21) may be rewritten as

$$\delta y = \frac{\lambda_c}{2\Delta\zeta} = W, \tag{2.3}$$

implying the cross range resolution is equal to the true plate width. This result indicates the imaging system still achieves sufficient resolution to resolve the scatterer, despite the limited scatterer persistence. In other words, high resolution is not needed to image a large target.

Despite this limited resolution, there is still an inherent advantage in setting $\Delta\theta \gg \Delta\zeta$. While the return from a given large scatterer may be confined to a few degrees, the user has no prior knowledge of what orientation angle allows reception of this limited target return. Large $\Delta\theta$ increases the odds the platform collects the critical few degrees of target return and thereby resolves the target.

In short, a wide-angle sensor with $\Delta\theta \approx 90°$ should produce images capable of resolving targets only a few centimeters in size, despite operating in stripmap

mode. This ability represents a significant improvement over existing SAR platform capabilities.

2.2.4 *Narrowband Waveforms.* In addition to producing extremely fine resolution over large coverage areas, the WAM-SAR approach holds promise for achieving these gains using relatively narrowband waveforms. As shown in Tab. 2.2, using wide-angle data collections, high range resolutions are still possible even with relatively narrow waveform bandwidth. Perhaps the greatest cost associated with this approach is higher sidelobe levels (Fig. 2.3).

There are many reasons why narrowband waveforms are desirable. One of the most significant is a dramatic simplification of radar operation. Wideband waveform transmission presents difficulties for an antenna designer. Perhaps most challenging is antenna pattern variability as a function of frequency [68].

Another key reason narrowband sensors are often preferred over wideband sensors is the frequency band is a finite resource [116]. In a battlefield environment, a collection of military and non-military systems broadcast signals at a range of different frequencies. If these frequencies interfere with those used by the SAR platform, extraneous signals may mask the radar echoes and degrade image quality. This problem is often encountered in FOliage PENetration (FOPEN) applications where the combination of relatively low radar frequencies (UHF/VHF) and wide percent bandwidths lead to significant interference from radio and television transmitters [118].

A final point in favor of narrowband waveforms is related to thermal noise. The SAR sensor must collect sufficient target energy to overcome detector's thermal noise. Since thermal noise is linearly related to the receiver bandwidth (and the receiver bandwidth is set based on the waveform bandwidth), a reduction of waveform bandwidth results in a reduction in noise power and thus an increase in Signal-to-Noise Ratio (SNR).

Despite the inherent advantages of narrowband waveforms, it should be reiterated that their use in wide-angle SAR results in sparse spatial frequency data (as

illustrated by Fig. 3.8(b)) and can result in high sidelobe levels. Further details about this problem as well as a taxonomy of possible solutions are discussed in [104].

2.2.5 *Simultaneous SAR/MTI.* Despite the clear advantages of wide-angle SAR imaging, a true multi-mode radar platform must also demonstrate a robust MTI capability. Unfortunately, the waveforms and processing techniques associated with traditional MTI systems are quite different than those used with SAR systems [116, 121]. Recent research in focusing moving targets within SAR images provides hope of implementing robust MTI within the WAM-SAR framework.

MTI systems traditionally transmit narrow RF beams into the environment, keeping the Doppler spread of the stationary ground clutter as small as possible. This approach allows moving target detection using a Doppler filter bank. Distinguishing targets from clutter becomes harder as a target's relative velocity becomes smaller. This relationship leads to a Minimum Discernable Velocity (MDV) criterion, setting a lower bound on detectable relative target velocities. However, WAM-SAR's wide transmit beam dramatically increases the clutter's Doppler spread, and thus increases the MDV achievable via traditional MTI processing. Clearly, the Doppler filter bank approach is inadequate.

Despite the limitations of traditional MTI approaches, it may be possible to perform simultaneous SAR/MTI processing. With relatively modest changes, the SAR processing algorithm's "fixed" target assumption (needed to image the stationary ground swath) can be replaced with a "moving" target assumption leading to focused moving target images against a blurred background [94, 143].

Recent work in the SAR field shows several techniques can form focused moving target images. These techniques include everything from time-frequency distributions [13] to Space Time Adaptive Processing (STAP) principles [44, 45]. One of the most promising approaches produces a series of SAR images focused to different motion parameters [66]. This method results in an image bank, similar to the Doppler filter bank used in traditional MTI. However the processing is performed, the ability

23

to detect and track moving targets using a SAR sensor provides an ideal zero MDV capability while achieving continuous coverage of a very large areas due to the large beamwidth.

The persistent coverage and high revisit rates implied by the wide-angle beam (Section 2.2.2) address another key MTI system limitation. Since typical MTI systems localize the target in azimuth and elevation using very fine beams, they must step between resolution cells over time. This stepping limits the amount of time the beam dwells on one particular target, increasing the likelihood a target track could be lost. However, WAM-SAR's continuous scene illumination allows simultaneous detection and tracking of targets in different locations.

While this research effort does not explicitly address the issues and challenges associated with successful simultaneous SAR/MTI implementation, the possible benefits help motivate the pursuit of more fundamental SAR image formation issues (Sec. 2.4 and Sec. 2.5).

2.2.6 Change Detection. Another significant SAR application made possible by a wide-angle data is known as change detection. While traditional approaches for SAR image analysis involve interpretation of a single SAR image, change detection assumes interesting objects change from one image to the next.

Change detection is performed by combining data from subsequent radar passes over the same ground swath. A collection of different change detection processing techniques are presented in [110]. Unfortunately, due to the angular variations in SAR imaging target signatures (especially those of natural features such as grass, trees, etc.), effective change detection requires multiple SAR collections traversing almost exactly the same flight path [127]. Even if it were possible to precisely replicate the data collection scenario, variability in image speckle limits performance. However, using a wide-angle collection promises to minimize these problems [143]. While it is impossible to fly exactly the same path on two subsequent collections, the extremely large WAM-SAR angular data diversity helps smooth out geometric variations, pro-

viding a more uniform data set. Additionally, use of large numbers of radar pulse echoes helps minimize speckle, increasing correlation between the two images and improving change detection performance.

2.2.7 Passive Reception. Up to this point, the perceived WAM-SAR benefits have been applicable to both monostatic and bistatic collection geometries. This section, as well as Sec. 2.2.8, is explicitly tied to a bistatic/multistatic geometry.

Radar platforms are inherently vulnerable to electronic or physical attack due to their use of active sensing technology, transmitting a radar waveform, broadcasting the sensor's location. Since radar wave amplitude decays as a function of propagation distance, a military target can often sense the transmitted radar beam long before the target echoes are strong enough to be sensed by the radar platform. This situation allows the target to engage the radar, hide beneath foliage, or otherwise interrupt the radar mission.

It is possible to dramatically reduce radar vulnerability using a stand-off transmitter and a passive short-range bistatic receiver. This concept uses a powerful, long-range radar transmitter to illuminate the given scene. A small, cheap, fast, low-altitude, receive-only radar platform can then be flown relatively close to the scene. Since the receive platform doesn't transmit, it is much less vulnerable to detection.

2.2.8 Multistatic Data Fusion. Another WAM-SAR advantage is the possibility of performing multistatic data fusion. With multiple transmitters broadcasting over the same ground swath, a collection of echoes, both monostatic and bistatic, are available to each radar receiver. Having simultaneous target echoes from multiple observation and/or bistatic angles is beneficial because targets have different monostatic and bistatic scattering characteristics. These returns could be combined coherently or non-coherently, producing more complete ground swath images than currently possible.

One straight forward application of monostatic/bistatic image fusion relates to SAR image shadowing effects. Since these shadows are dependent on collection geometry, having images from multiple geometries allows generation of composite images virtually free from shadow effects. Less intuitive are ATR applications where shadows provide some of the best target discrimination information. With multiple target shadows from multiple orientations, target identification could be greatly enhanced [18, 83].

Multistatic radar data fusion may be particularly beneficial for detection and imaging of stealthy targets. A large part of RCS reduction centers around reducing a target's monostatic RCS by reflecting incident radar energy in non-monostatic (i.e., bistatic) directions [73]. Placing a network of bistatic receivers around a target region increases the odds of intercepting larger stealthy target bistatic echoes, aiding in detection, tracking, identification, and imaging [9].

Finally, high resolution SAR images do not look like optical images of comparable resolution. Radar images tend to show an object's edges whereas optical images show "filled-in" targets. Various monostatic and bistatic collection angles provide high resolution images of different parts of the same target. It is possible that intelligently combining these images would make high resolution radar images could appear more "optical," simplifying the job of imagery analysts and/or ATR algorithms.

2.3 Implementation Challenges: Unaddressed Issues

The expected advantages of WAM-SAR are significant. This observation begs the question of why such an approach has not been previously implemented. Part of the reason may simply be due to radar culture [143]. The basic wide-angle concept is contrary to common thinking within the field. Yet culture is not the only thing standing in the way of wide-angle SAR platforms. There are also serious technical challenges. Some of these challenges form the core of this research effort. It is hoped that successfully addressing these challenges motivates WAM-SAR concept transition from theoretical research towards hardware implementation.

26

Before outlining the problems solved in this research effort, it is important to point out a few implementation issues not explicitly examined. These issues include the air-to-ground communication bandwidth requirements, data storage requirements, radar transmit power requirements, and synchronization procedures for bistatic data collections. Each of these issues are briefly addressed in the following several paragraphs.

The basic WAM-SAR approach will assume real-time processing is performed at a ground station. This assumption is beneficial for several reasons. First, it allows powerful ground-based computers to handle the processing load associated with multiple simultaneous missions. Second, it makes the raw data available for more advanced post-processing techniques. Third, it allows the ground station access to echoes from all operating platforms, facilitating data fusion. Unfortunately, down-linking the raw data to such a processing facility requires an extremely wideband communication system. Although communication system performance has been steadily improving, much work remains to be done in this area.

Related to the required communication bandwidth are the massive data storage requirements. Although this research does not directly address either the required communication bandwidth or data storage requirements, the results of this research remove the phased array antenna requirement (Chapter VI), dropping the communication bandwidth and data storage requirements by orders of magnitude.

Finally, a requirement for any bistatic radar is maintaining precise synchronization between the transmitter and receiver. The time standard provided by the Global Positioning System (GPS) holds promise for providing the required synchronization [131]. Recent success in narrow-angle bistatic imaging experiments indicates this problem is not intractable [129].

2.4 Implementation Challenges: Focused Image Formation

Section 2.2 provided an overview of potential WAM-SAR benefits, yet these applications presuppose the ability to collect and process radar data into high quality SAR imagery. Simply collecting and processing raw wide-angle data into high resolution images is a significant problem. Without a demonstrated ability to perform these basic, but critical tasks, the loftier goals of simultaneous SAR-MTI and change detection remain out of reach. For these reasons, this research focuses on addressing foundational imaging issues. The remainder of this chapter outlines these problems in greater detail, reviews previous work in these areas, and introduces solutions developed in the research effort.

One of the major challenges inhibiting wide-angle SAR image production is the basic image formation algorithm itself. The standard Fourier-based image formation algorithm (Section 3.11) is based on multiple idealistic assumptions which fall apart in the wide-angle collection scenario. The result is unfocused SAR imagery failing to achieve the resolutions in Tab. 2.2. Addressing these assumptions and providing a simple, practical algorithm for SAR data focusing is a critical step in demonstrating WAM-SAR feasibility.

2.4.1 Problem Introduction.   Perhaps the single most significant challenge to producing focused WAM-SAR imagery is dealing with Range Migration (RM). RM results from the curvature of the ElectroMagnetic (EM) wavefront and causes an overall reduction in image quality, contrast, and resolution. In the EM community, RM effects are more commonly known as radiative near-field effects since they relate directly to far-field assumption validity. This assumption is used to derive the definition of RCS as well as basic SAR and Inverse Synthetic Aperture Radar (ISAR) algorithms. Chapter V, which solves the radiative near-field/RM imaging challenge, examines this problem from the EM perspective, adopting the "near-field/far-field" terminology. None-the-less, since RM is the more common term within the SAR community, it is used throughout the remainder of this section.

RM is considered problematic when the difference in range between targets at the beam center and beam edge exceed the radar's range resolution δr [100]. From simple trigonometry, assuming a beam normal to the SAR flight path, this criterion mandates

$$r \leq \delta r \left[\frac{\cos(\Delta\theta/2)}{\cos(\Delta\theta/2) - 1} \right], \tag{2.4}$$

where r is the range to the scatterer from the synthetic aperture center. Using a 90° beamwidth and a range resolution of $\delta r = \delta x = 5.2$ cm (taken from Tab. 2.2), (2.4) gives a range of $r = 12.6$ cm. This value represents the maximum scatterer range where RM effects can be ignored, and is clearly impractical for any real SAR system. Not correcting for RM results in significant image degradation, causing smearing and inhibiting high resolution image formation.

Understanding the changing geometric relationships between the radar and the scatterers throughout the synthetic aperture is critical to quantifying and eliminating RM effects. Defining the mathematical relationship between the radar and individual scatterers requires selecting a suitable coordinate system. Consider an individual scatterer located at (x_0, y_0), where the x-coordinate refers to range and the y-coordinate refers to cross range. The coordinate system origin is located at the synthetic aperture center. If the radar flies a linear flight path, the radar location at any point in time can be specified by $(0, u)$ where u is the instantaneous cross range radar platform location. Using the pythagorean theorem, the range r can be calculated as

$$r = \sqrt{x_0^2 + (y_0 - u)^2}. \tag{2.5}$$

As shown in [117], this equation represents a half-hyperbola. Figure 2.4 shows several range/round trip delay hyperbolas for a collection of three point scatterers.

Equation (2.5) implies the energy reflected from an individual scatter throughout a SAR collection is spread over a range hyperbolic arc. Producing a well focused image requires correcting for this shape by collecting this hyperbolic energy arc into a single point at the true scatterer location. The ability (or inability) of a SAR pro-
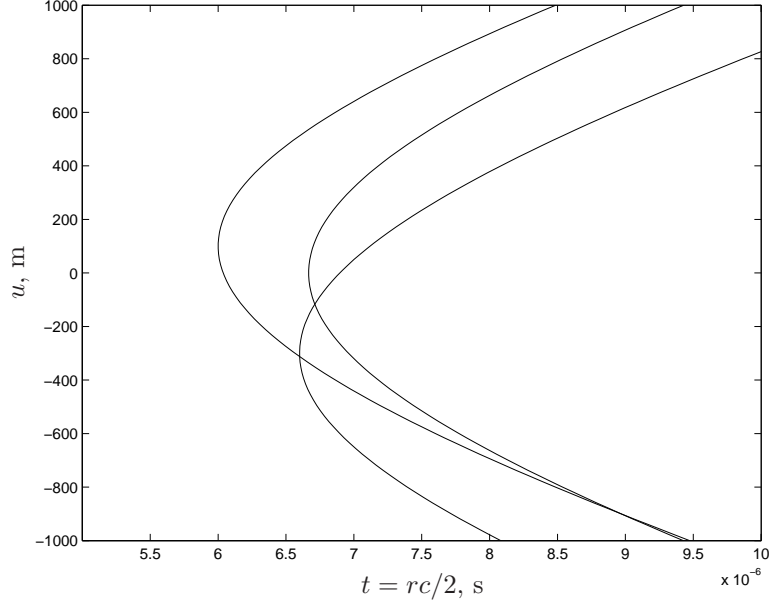
Figure 2.4:   Round trip delay (equivalent to range) for three point scatterers as a function of radar location along a linear flight path. The hyperbolic shape is determined by point scatterer location relative to the synthetic aperture.

cessing algorithm to produce imagery free from RM effects is directly tied to how well this hyperbolic relationship is modeled. Note, even the hyperbolic range relationship presupposes a linear flight path, making it inadequate for full WAM-SAR image focusing.

Development of SAR algorithm RM correction has been largely driven by the spaceborne SAR community. This motivation results from the large stand-off ranges and large ground swaths inherent in these applications, making RM a much larger problem. None-the-less, while space-based systems do have large footprints, they do not have beamwidths approaching 90° as desired in WAM-SAR. This fact shows why even spaceborne SAR algorithms are not adequate for WAM-SAR data processing.

RM is not the only defocusing problem plaguing a true wide-angle processor. By virtue of the long synthetic aperture resulting from the wide-angle collection, other long-held SAR image formation assumptions must be relaxed. Traditional SAR image formation often assumes the radar platform traverses a linear flight path over perfectly

30
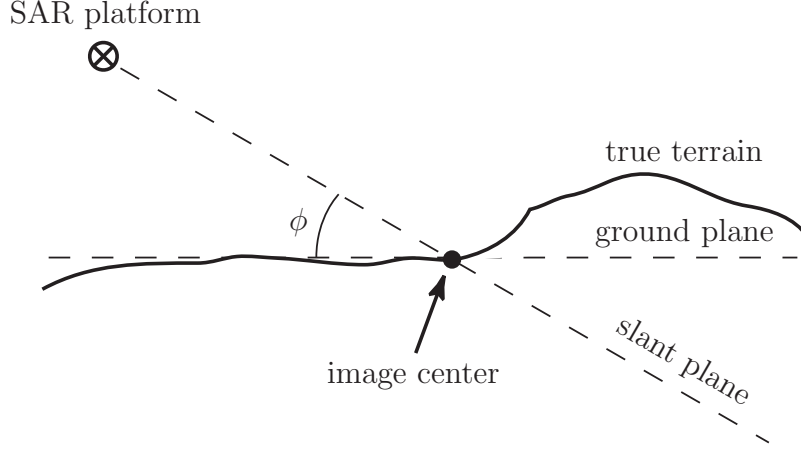
Figure 2.5: Data collection plane comparison. Platform flies a linear flight path into the page. Traditional SAR images are formed in the slant plane (defined by the flight path and image center) and then projected into the image plane. This process assumes the scene is flat, while the true terrain exhibits height variation.

flat ground. In this case, the resulting 2-D image is formed in the slant plane, defined by the linear flight path and the scene center [65]. The user usually desires a final result in the ground plane, representing the scene as it would appear from an overhead view. This requirement is typically met using a simple trigonometric correction, projecting the slant plane image into the ground plane. Figure 2.5 illustrates these relationships.

True SAR platforms do not fly perfectly linear paths, especially over the long distances needed to produce high resolution images. This non-linear flight path means the slant plane definition changes for each Coherent Processing Interval (CPI) pulse, leading to defocusing in both the slant plane and resulting ground plane imagery. These effects can be reduced through a procedure known as out-of-plane correction. Out-of-plane correction individually projects the spatial frequency domain data from each CPI pulse into the desired slant or ground plane prior to image formation, resulting in an orthographically correct image [65]. Unfortunately, the procedure assumes the imaged terrain is in the far-field and the Earth is perfectly flat.

In addition to defocusing, the flat-Earth assumption leads to an effect known as layover [36, 65]. For scatterers outside the ground plane, the range measured by

each CPI pulse is somewhat different than if the target was in the ground plane. In the typical airborne SAR scenario, a tall scatterer such as a hill or top of a building appears closer to the radar, causing the image of such structures to "lay over" towards the radar in the resulting imagery. Using the scenario depicted in Fig. 2.5, the amount of layover (range error) in the image plane may be estimated as

$$\epsilon = z \tan(\phi), \tag{2.6}$$

where ϵ denotes layover magnitude, ϕ is the elevation angle, and z is the height (i.e., z-coordinate) of a given scatterer. This layover effect means the apparent target location is somewhat incorrect and could inhibit the use of precision guided munitions. Given prior knowledge of ground contours (usually available from existing digital elevation maps or contour maps) there have been attempts to correct for layover using a collection of "tiepoints." These tiepoints define a polynomial used to warp and resample the slant plane image [42, 101]. Although these initial approaches have been somewhat streamlined, they still require significant operator interaction and computational resources [36].

2.4.2 Current Literature Status. WAM-SAR algorithm development requires examining the focusing problem from first principles, incorporating the non-ideal nature of a SAR collection stretching over more than a hundred kilometers. From the current literature, it is clear this approach requires careful attention to items such as the type of waveform transmitted, the domain where correction factors are applied, and the necessity/accuracy of any required interpolation schemes. It is also necessary to incorporate knowledge of Three-Dimensional (3-D) and bistatic geometry effects. The next several subsections introduce the benefits and limitations from a series wide-angle SAR data processing algorithms. Each method fails to address key WAM-SAR scenario components. The most promising approach, based on tomographic principles from the medical imaging community, is extended to meet all WAM-SAR requirements in Chapter V.

2.4.2.1 Range-Doppler Algorithm. Up until the early 1990s, most precision SAR processors relied on the "range-Doppler algorithm" with certain modifications to address varying RM levels [12]. The basic range-Doppler approach is similar to the Fourier Transform (FT) techniques introduced in Section 3.11. Instead of using data in the 2-D spatial frequency domain, the collected data is compressed (Fourier transformed) in the range dimension prior to any attempt at focusing. This operation results in a collected data set where the range coordinate is in the image domain and the cross range coordinate is in the transform (frequency) domain. These domains give the basic algorithm its name. Time-domain interpolation techniques are then used for partial RM correction. After interpolation, azimuth compression is performed resulting in a complex image. Unfortunately, the range-Doppler approach makes several assumptions, the most significant being scatterers are approximately normal to the SAR flight path [12]. Since wide-angle collection necessarily implies collecting data from large angular swaths, this approach is inadequate for WAM-SAR.

One method of alleviating range-Doppler algorithm assumptions is called Secondary Range Compression (SRC) [135]. This approach involves generating a new RM compensation kernel at each range value. Unfortunately, even with its substantial computational burden, SRC does not completely correct for RM effects, and therefore leads to defocusing in wide-angle imagery.

2.4.2.2 Wide Angle SAR Algorithm. In [49] and [50], Franceschetti, et al., developed algorithms explicitly for a wide-angle processor. They refer to their algorithm as the Wide-Angle Synthetic Aperture Radar (WASAR) algorithm. Their work uses a parabolic approximation to the hyperbolic relationship given in (2.5). While more accurate than the linear or quadratic approximations used in many lower precision systems [24, 100], the parabolic approach still lacks the complete rigor of the full hyperbolic correction and is therefore not appropriate for the extremely large beamwidths being examined in this document.

2.4.2.3 Range Migration Algorithm. In 1991, Cafforio, et al., used techniques from the seismic surveying community to address RM effects in a new way [26]. Common names for techniques using this approach include the $\omega - k$ algorithm [26], the wave-number domain algorithm [12], the wavefront reconstruction algorithm [119], and the Range Migration Algorithm (RMA). The RMA algorithm represents a significant departure from the range-Doppler approach. The idea recasts the basic SAR problem from one which uses a radar to transmit and receive radar echoes into one where the radar simply listens to transmissions from point "radiators" distributed throughout the scene. The scatterers within the scene are modeled as pulsed waveform emitters. The pulses, originating from the scatterers themselves, are assumed to travel at a velocity of *one-half* the speed of light [26]. These assumptions ensure the pulses received by the radar arrive at the same time they would in the true scenario. RMA's point radiator model assumes an inherently monostatic collection geometry.

RMA algorithm development was originally based on the 2-D wave equation to effectively model the spherical propagation of radar waves. In [12], the algorithm is derived without using the wave equation. The initial SAR processing projects the data into the spatial Fourier domain. A change of variables (interpolation) procedure called Stolt interpolation then implements RM corrections [122]. This mapping places the data on a rectangular grid where a simple 2-D FT produces the final image.

The key strength of the RMA approach is it provides exact correction for monostatic RM effects under a few key assumptions. These assumptions include a perfectly linear flight path and a fixed Earth. For the wide-angle collection geometry required by the target platform, neither assumption holds true. Over the long synthetic aperture required by WAM-SAR, the Earth's curvature produces a curvature in the "linear" flight path. Additionally, the long time it takes to traverse this aperture means Earth rotation effects must also be incorporated. Cafforio, et al., [26] mention these effects but do not provide a rigorous method for dealing with them. Also, RMA requires processing data in a stripmap-like fashion, referencing each pulse along the synthetic

aperture to a fixed radius (Section 3.4). This procedure imparts an azimuth frequency chirp to individual scatterers and can have negative impacts on the cross range sampling requirements (i.e., PRF requirements) for RMA-based SAR processors.

2.4.2.4 *Chirp Scaling Algorithm.* Another SAR processing technique deserving mention is chirp scaling [12, 107]. Unlike the range-Doppler or RMA approaches, chirp scaling does not begin by compressing the samples in range (i.e., matched filter application). It performs RM correction directly on uncompressed Linear Frequency Modulation (LFM) chirps using a phase multiply, and thus requires LFM waveforms. Chirp scaling's key advantage is its ability to address limited RM effects using only Fast Fourier Transforms (FFTs) and multiplies, forgoing the need for interpolation. As shown in [107], the accuracy of chirp scaling compares favorably with range-Doppler approaches using SRC methods. As with RMA, chirp scaling also uses the stripmap fixed range referencing procedure increasing cross range sampling requirements and complicating the aliasing problem (Sec. 2.5).

2.4.2.5 *Widefield Polar Format Algorithm.* In 2004, a modified form of the traditional Polar Format Algorithm (PFA) (Sec. 5.2.1) dubbed the Widefield Polar Format Algorithm (WPFA) was introduced [29]. Similar to RMA, WPFA claims the ability to perfectly correct for RM effects. Instead of using Stolt interpolation, WPFA uses a spatially varying data storage approach to account for RM. Since WPFA is merely an extension of PFA, it provides focusing to a point (i.e., spotlight processing), eliminating the azimuth chirp observed in radars which focus to a line (i.e., stripmap processing). This paradigm shift reduces the Doppler bandwidth of WPFA data relative to RMA data and produces RMA quality imagery without the RMA computational burden. Since WPFA's is to replicate RMA-quality imagery, WPFA suffers from many of RMA's limiting assumptions.

2.4.2.6 *Back-Projection Algorithms.* The final relevant category of SAR imaging algorithms are based on tomographic principles used by the medi-

cal imaging community. These techniques were first applied to SAR processing in 1983 by Munson et al. [99]. Unlike the algorithms presented previously, tomographic imaging techniques are applied on a pulse-to-pulse basis in the time (range) domain, making them ideal for incorporating non-uniformly spaced synthetic aperture samples. They work by serially processing a collection of One-Dimensional (1-D) range profiles, spreading or *back-projecting* them over the entire 2-D image. A 2-D image is formed by coherently summing the back-projected range profiles generated at each CPI pulse. These techniques are collectively termed Back-Projection Algorithms (BPAs) within the SAR community.

Standard derivation of 2-D BPA makes use of the projection-slice theorem to equate BPA with the more common PFA (i.e., range-Doppler) approach [65, 99]. Chapter V extends this derivation to the 3-D bistatic near-field scenario. Since the projection-slice theorem requires planar illumination wavefronts [64], the standard BPA suffers from the same RM problems as the unmodified PFA. More recent work demonstrates wavefront curvature effects can be accounted for using spherical shells to control the back-projection process [15, 137]. The utility of this correction has only been demonstrated through simulated data. It has also been suggested that BPA can be extended to process bistatic SAR data [16].

One unique aspect of BPA is its "real-time" nature [90]. All the previous SAR imaging methods require data from the entire synthetic aperture before processing. Back-projection methods, on the other hand, process individual samples along the aperture in a serial fashion, implying SAR data processing can begin during the data collection process. For WAM-SAR data, where the total CPI could be more then several minutes long, producing moderate resolution imagery with data is vital for minimizing the image production time.

Despite the apparent advantages of BPA, it is often criticized as being significantly slower then other methods. While 2-D PFA has a computational complexity of $O(N^2 \log_2 N)$, standard 2-D BPA exhibits $O(N^3)$ complexity [39]. Despite

this difference, BPA parallelizes very easily, making it much easier to integrate into large computing facilities. Also, there have been several recent papers on decreasing BPA's computational load using an approach termed "fast" back-projection. In these methods, computational complexity is reduced from $O(N^3)$ to $O(N^2 \log_2 N)$ at the expense of incorporating an additional interpolation step into the image formation routine [126, 137, 140].

2.4.3 Proposed Solution. As indicated above, this research effort builds on basic BPA to solve the focused image formation problem. The final algorithm, presented in Sec. 5.5, corrects both for RM (i.e., near-field) effects and arbitrary flight path/layover effects. Data collected in the Air Force Institute of Technology's (AFIT's) RCS chamber (Sec. 5.6) is used to test this algorithm.

2.5 Implementation Challenges: Aliasing Artifact Reduction

The appearance of aliasing artifacts (i.e., ambiguities) in radar data products is of significant concern to both the traditional radar and SAR communities. The basic problem concerns the inability to meet Nyquist sampling requirements when simultaneously determining the true range, cross range, and Doppler properties for a given target. These ambiguities manifest themselves as multiple copies of point target returns called aliasing artifacts. As this section illustrates, these problems are particularly challenging for WAM-SAR. Failure to address this issue means even if well focused imagery is produced, extraneous target energy throughout the transmit beam footprint is spread around the final images.

2.5.1 Problem Introduction. Since the individual pulses in a SAR collection provide spatial ground samples, the radar's PRF defines the sampling frequency along the SAR flight path. As a consequence of the sampling theorem, the sampling

rate must equal radar echoes' Doppler bandwidth to avoid Doppler aliasing[3]. This bandwidth is usually calculated as the difference between the Doppler shifts from the front and back edges of the radar's main beam. Although the clutter returns due to antenna sidelobes extend over a much broader Doppler frequency range, the returns are low enough in power that they are typically ignored when selecting the PRF [100].

In the monostatic scenario, the Doppler shift f_d imparted to a radar pulse echo is given by [116]

$$f_d = \frac{2v_r}{\lambda}, \tag{2.7}$$

where v_r is the relative velocity magnitude between the radar and the target [116]. For a broadside[4] airborne SAR imaging the fixed ground,

$$v_r = v_a \sin(\Delta\theta/2), \tag{2.8}$$

where v_a is the aircraft (i.e., SAR platform) velocity magnitude. Equation (2.8) assumes a 2-D monostatic scenario, ignoring the aircraft depression angle and bistatic collection geometry. While these effects are explicitly addressed in Chapter VIII they would needlessly complicate the discussion here.

Equation (2.8) allows calculation of the minimum PRF for avoiding ambiguous Doppler returns $\text{PRF}_{\min}$ as

$$\text{PRF}_{\min} = \frac{4v_a \sin(\Delta\theta/2)}{\lambda}, \tag{2.9}$$

where λ denotes wavelength and the broadside assumption ensures the Doppler shift at the front and back beam edges is of equal magnitude and opposite sign. This PRF requirement can also be expressed as the required distance between CPI pulses

---

[3]The actual Nyquist sampling theorem requires sampling at twice the bandwidth. Since SAR is a coherent process, both the real and imaginary components of the radar echoes are sampled, effectively doubling the sampling rate.

[4]A collection is termed "broadside" if the scene center has the same cross range location as the synthetic aperture center.

δu. Inverting (2.9) and multiplying by v_a gives the distance δu moved by the SAR platform between pulses

$$\delta u = \frac{\lambda}{4\sin(\Delta\theta/2)}.$$ (2.10)

This relationship is independent of v_a and indicates sampling requirements are determined entirely by collection scenario geometry. Spacing along the synthetic aperture determines the allowable cross range extent of the ground swath. This observation is consistent with the development in [65], where derivation of the SAR principle, usually done from the Doppler perspective, is accomplished via geometry. This redundancy in the relationship between Doppler and cross range aliasing is explored further in Chapter VI where the same PRF requirement is derived from an antenna theory perspective.

While avoiding Doppler (cross range) aliasing sets a minimum PRF value, avoiding range aliasing sets a maximum PRF value $\mathrm{PRF}_{\mathrm{max}}$. This PRF bound originates from the requirement that the range swath ΔR must be small enough for the radar to unambiguously distinguish between echoes from different CPI pulses. The formula for calculating $\mathrm{PRF}_{\mathrm{max}}$ is

$$\mathrm{PRF}_{\mathrm{max}} = \frac{c}{2\Delta R},$$ (2.11)

where c is the speed of light and the ground swath width ΔR is equivalent to the unambiguous slant plane range extent.

Equations (2.9) and (2.11) demonstrate one of the fundamental challenges to wide-angle SAR imaging. If one wishes to simultaneously collect SAR data over a large ground patch (i.e., with large extents in both the range and cross range dimensions), ambiguities result. This fact is illustrated graphically in the contour plot shown in Fig. 2.6. The contours are labeled with beamwidths in degrees (i.e., $\Delta\theta$ since stripmap geometry is assumed) and mark the boundaries of alias-free operation. To avoid aliasing artifacts, a platform's $(v_a, \Delta R)$ parameters must place it below the curve of the appropriate beamwidth $\Delta\theta$. This requirement is not challenging for a traditional narrow-angle radar, but for a wide-angle radar it becomes much more
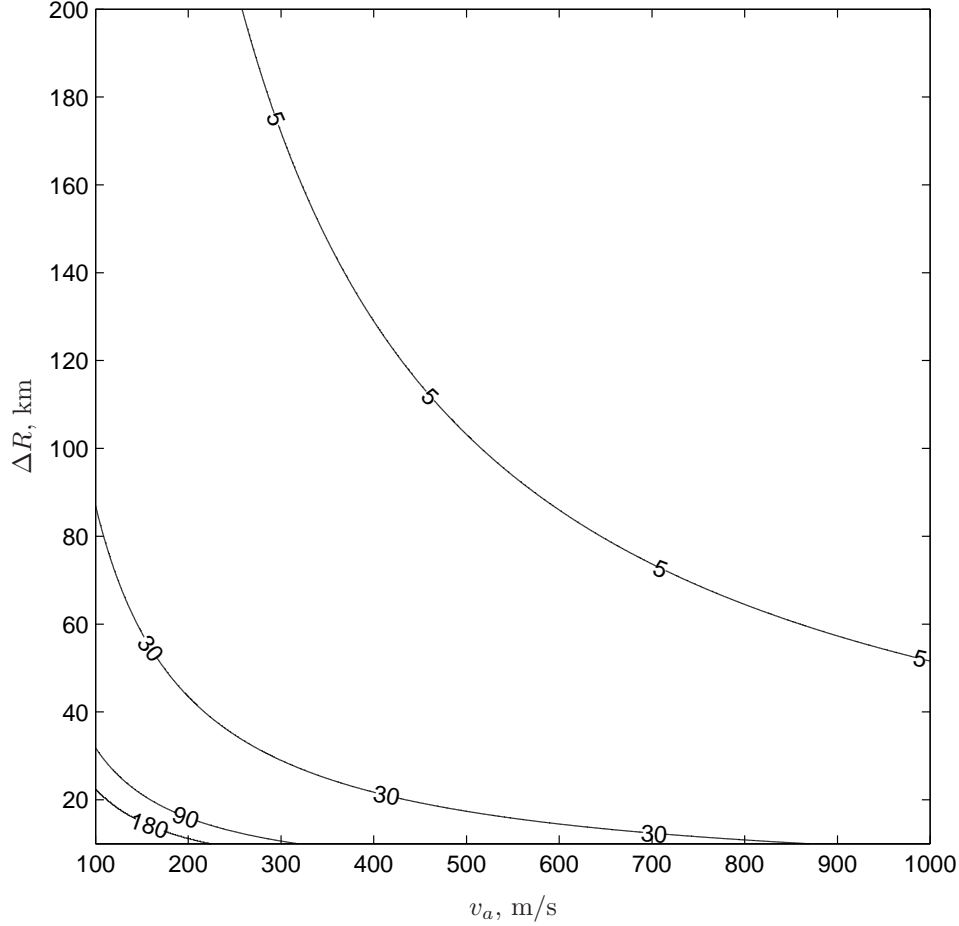
Figure 2.6:   Contour plot denoting appearance of aliasing artifacts for various beamwidths $\Delta\theta$ as functions of platform velocity v_a and range swath width ΔR. Contour labels denote beamwidth in degrees. Aliasing artifacts appear for $(v_a, \Delta R)$ pairs above the contour line denoting sensor beamwidth $\Delta\theta$.

problematic. Note, the use of a $\Delta\theta = 90°$ beam limits the unambiguous range to less than 20 km for the Global Hawk's 200 m/s velocity. This value is more than an order of magnitude below the ΔR goal of nearly 200 km. The problem is significantly more challenging if large Doppler shifts from moving targets are incorporated into the PRF_{min} requirements[5]. Addressing ways to break these ambiguities, thereby eliminating aliasing artifacts from the final imagery, is vital to the success of WAM-SAR.

---

[5]Ambiguities can also be understood as the ratio of ground swath area to resolution cell area. If the number of resolution cells within the ground swath exceeds the number of data samples, aliasing results [53].

2.5.2   Current Literature Status.   Although most SAR systems avoid cross range aliasing by employing narrow transmit beams, there have been some research efforts on wide-angle aliasing artifact mitigation. The first class of approaches uses phased array antennas to place spatial filters on top of aliasing artifacts. While theoretically possible, this method mandates extremely complex and expensive radar hardware, making implementation impractical. The second class of techniques centers on radar waveform modifications. Although, a large literature database exists for diverse waveform applications in traditional radar, relatively little work has been done in the SAR arena. Chapters VI-IX solve the aliasing problem using a waveform diversity approach, achieving excellent performance with minimal implementation difficulty.

2.5.2.1   Spatial Filtering Approaches.   As shown in Fig. 2.6, it is not possible to select a PRF simultaneously eliminating Doppler and range ambiguities in the wide-angle case. One class of approaches for dealing with these ambiguities applies a spatial filter to aliasing artifact locations during the image formation process. The spatial filter approach uses active phased array antennas along with element-level digitization. Before discussing ambiguity resolution using phased arrays, a few comments should be made about using these same arrays for the wide transmit beam production.

Antenna theory dictates simple linear antennas provide beamwidths proportional to λ/W. This relationship results in another often quoted formula for approximate cross range resolution in stripmap SAR [57]

$$\delta y = \frac{W}{2}.$$ (2.12)

Equation (2.12) implies generation of a beamwidth wide enough to get a cross range resolution on the order of a centimeter requires an antenna with a diameter no larger than about two centimeters. This diameter is clearly impractical since this value is less than a single wavelength (at X-band frequencies).

One possible method for wide-angle beam generation makes use of phased array antennas. Phased array antennas are actually a collection of tens, hundreds, or even thousands of individual wide-angle antennas (called elements), grouped together into a single (usually planar) array structure. Each element is connected to a phase shifter and attenuator controlling both the phase and amplitude of the transmitted waveform emanated from a given Transmit/Receive (T/R) module. Through proper phase shifter and attenuator control, the antenna pattern can be electronically steered (i.e., focused) in a wide variety of directions without mechanically turning the physical antenna structure.

Just as the phase shifters and attenuators can focus the beam to a fine point, they can also defocus the beam to cover a larger beamwidth than indicated by the antenna dimensions. This technique is referred to as "spoiling" the beam [70]. Appropriate phase and amplitude selection in the individual T/R modules provides this spoiling. Phase and amplitude weights are determined via the FT or the Woodward-Levinson method [116].

Producing a wide transmit beam does nothing to solve the ambiguity problem. However, the advantage of a digitally sampled phased array radar is phase and amplitude values used on *transmission* do not have to be used on *reception*. Ignoring mutual coupling effects between individual antenna elements, each T/R module is essentially an independent sample of the scene from a slightly different location. Once the received echoes are sampled digitally, the processing software introduces virtual phase shifts and attenuations, forming a receive pattern different than the transmit pattern. This digital beamforming on the received echoes provides one possible spatial filtering mechanism for ambiguity resolution [27, 37, 141, 143].

As discussed in the preceding paragraphs, achieving a wide-beam transmit pattern with any realistic phased array antenna requires beam spoiling. This approach enables focusing of sampled data on receive to form narrow-angle receive beams from wide-angle transmit beam data. As an example, consider the Global Hawk antenna.

From Table 2.1, the antenna width is known to be 1.26 meters. The best-case resolution for a phased array radar can be approximated by the resolution of an equivalently sized flat plate. This simplification allows calculation of the focused beamwidth via (2.2)

$$\Delta\theta = \frac{\lambda}{2W}. \tag{2.13}$$

Using a 10 GHz frequency (implying $\lambda = 0.03$ m) and $W = 1.26$ m gives a beamwidth of approximately 0.68°. Returning to the radar echo bandwidth calculations in (2.9), using such a narrow receive beamwidth decreases the PRF_{min} requirement by a factor of $\sin(90/2)/\sin(0.68/2) \approx 120$. This focusing dramatically reduces the Doppler ambiguities caused by selection of a PRF below the PRF_{min} wide-angle requirement. Similar results can be obtained using the element vertical spacing, forming multiple receive beams in elevation, and thereby increasing PRF_{max}. Since receive beam focusing is done digitally, the processor can form any number of receive beams simply by processing the same digitally sampled returns with a different set of phase and amplitude weights.

Figures 2.7 and 2.8 depict using multiple focused receive beams to resolve both range and Doppler ambiguities. The spoiled transmit beam illuminates a large ground patch. Through digital beamforming techniques, each receive beam covers a much smaller ground patch. The dimensions of the smaller receive patches determine PRF_{min} and PRF_{max} requirements.

In addition to the focused receive beam approach, Currie and Brown [37] theorize a different ambiguity resolution method using multiple defocused receive beams based on displaced phase center concepts (Fig. 2.9). This approach uses wide beams during transmit and receive. The receive beams, however, are formed from antennas displaced from each other in an along track direction (i.e., phased array subsets). Assuming the distance between the receive beam phase centers is "suitable," certain Doppler ambiguities can be resolved without raising the PRF. Hansen [58] proposes a similar approach for improving the Signal-to-Noise Ratio (SNR) of a SAR sensor.
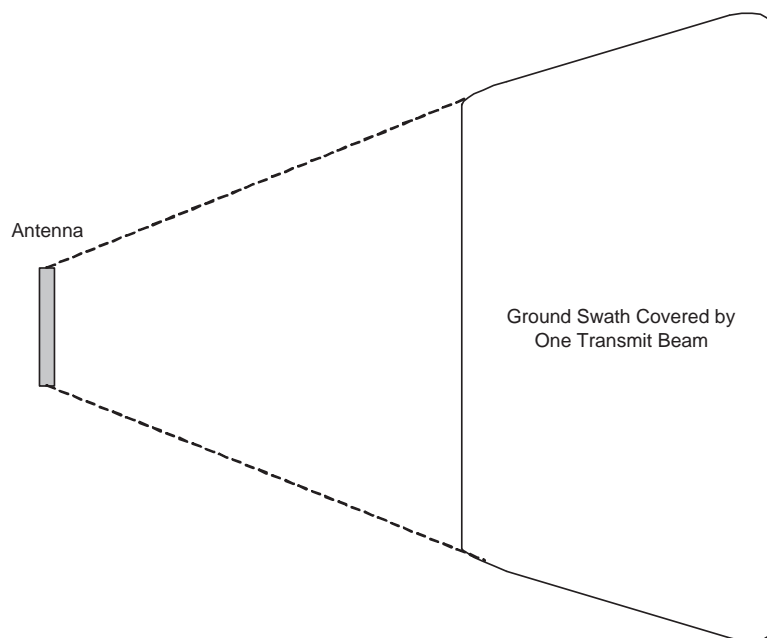
Figure 2.7: Spoiled phased array transmit beam. The beam has a large footprint causing many range and Doppler ambiguities.
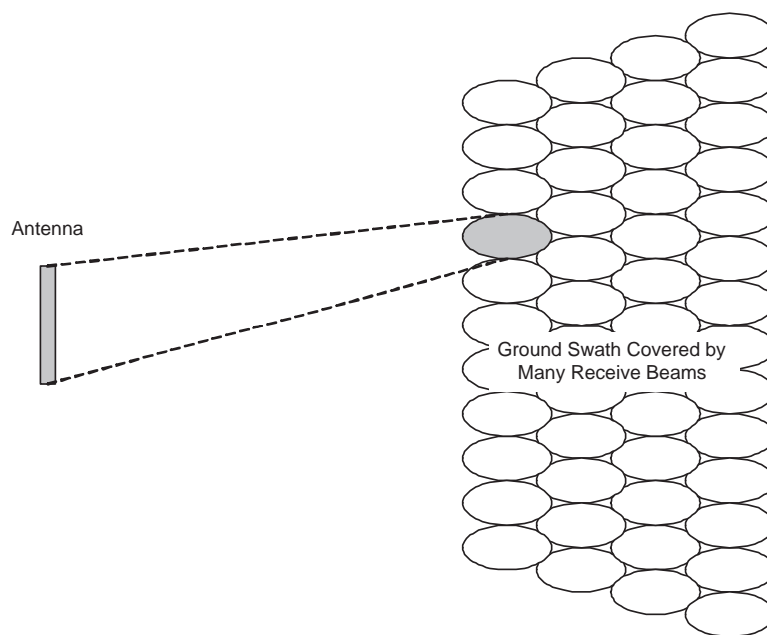
Figure 2.8: Multiple focused receive beams formed from the phased-array elements. Smaller receive beam dimensions determine the PRF requirement for alias-free operation.
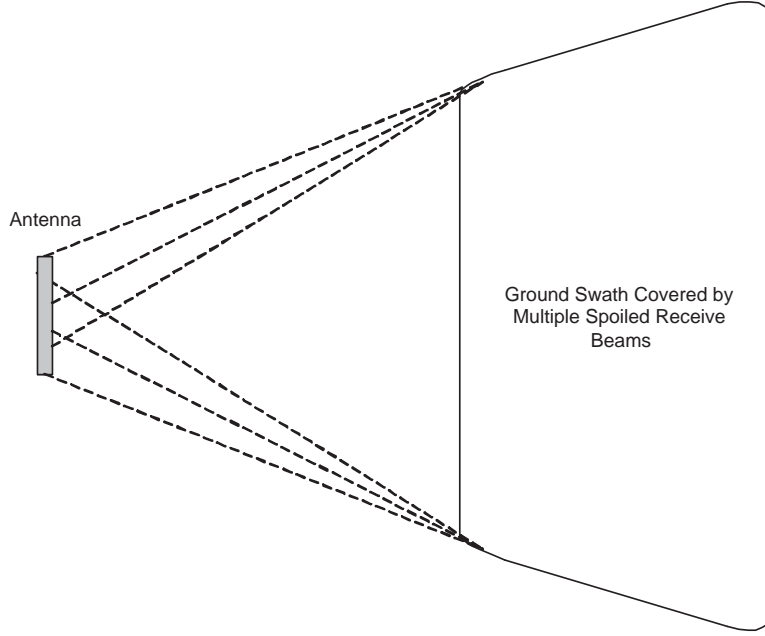
Figure 2.9: Use of multiple spoiled receive beams to defeat ambiguities. The displaced phase center effect allow ambiguity resolution with *multiple* wide beams.

Goodman, et al., address a similar problem when developing processing methods for sparse spaceborne receiver arrays [53]. Their work reformulates the ambiguity problem via correlation matrices and applies Maximum-Likelihood (ML) and Minimum Mean-Square Error (MMSE) methods, minimizing SAR ambiguities.

In addition to the non-adaptive digital beam forming techniques presented above, adaptive methods also provide an effective tool for ambiguity elimination. Griffiths and Mancini [56] propose a method involving an adaptive elevation-plane array to place nulls explicitly at range ambiguous locations. Callaghan and Longstaff [27] examine the use of STAP techniques to control antenna null placement.

A final technique meriting mention was developed by Moreira [96]. Although not explicitly related to spatial filter application, it uses the "ideal" filter concept to mitigate individual cross range ambiguities from SAR data through a deconvolution process. Unfortunately, the phase and amplitude histories of aliasing artifacts must

be precisely known. This limits effectiveness, especially in the face of large RM effects [96].

Phased array-based spatial filtering approaches to ambiguity resolution do not come without a price. Phased arrays are very complex and expensive. Furthermore, the requirement for digitized radar echoes means the amount of data scales linearly with the number of independent antenna elements N_a. Since this research effort assumes all image formation in ground-based facilities, phased array usage also increases the required communication bandwidth by a factor of N_a.

2.5.2.2 Waveform Diversity Approaches. The previous section approached solving the ambiguity problem using a collection of digital beam forming methods. This section reviews an approach based on modifying the transmitted waveform itself, not simply the phasing of the echoes received by individual antenna elements. Since the radar waveform itself is varied, this class of techniques is grouped under the umbrella of waveform diversity.

One of the oldest methods for resolving radar waveform ambiguities involves using multiple PRFs [121]. Transmitting two waveforms at different PRF values changes the ambiguity locations. If the PRF values are relatively prime, they do not share any common ambiguities and may be used together to recover ambiguity free data over larger ground swaths than is possible with either PRF alone. Unfortunately, using multiple PRFs causes irregular sample spacing along the synthetic aperture. Irregular spacing complicates the image formation process since traditional Fourier methods require uniform sampling. This approach also suffers from reduced SNR since the equivalent number of CPI pulses must be divided among two multiple image formation routines.

Waveform pulse coding provides another important ambiguity resolution method. These methods mark successive waveforms so they can be distinguished from one another when the echoes are received. There are a wide variety of pulse coding techniques present in the literature. One of the simplest transmits successive LFM chirps

in different "directions." The first chirp begins at the minimum frequency and linearly increases to the maximum frequency. The next chirp begins at the maximum frequency and linearly decreases until reaching the minimum frequency [27]. Assuming the two waveforms can be perfectly distinguished on receive, this process doubles the unambiguous range and maximum PRF[6]. More complex methods include superimposing binary codes on top of pre-existing waveforms. One popular approach uses Pseudo-Random Noise (PRN) codes. These methods employ shift registers, imparting a binary sequence of phase shifts on the waveform [116].

Regardless of the code type applied, effectiveness is linked to the waveform response to a matched filter. The user desires a coded waveform set yielding a maximum SNR when applying a matched filter constructed using this code. If the filter is "mismatched" using the incorrect code, a minimum SNR should result. Orthogonal codes are termed ideal since application of the incorrect code perfectly cancels the incoming signal energy.

A more advanced coding technique for ambiguity reduction is discussed in [6]. In this method, nonlinear suppression techniques add additional separation between the SNR of matched and mismatched responses. This approach modifies the received data, zeroing the pulse energy after mismatched filtering and results in waveform performance closely approximating the ideal orthogonal relationship.

Waveform diversity can also be achieved through frequency diversity [27]. This approach resolves range ambiguities but inserts Doppler additional ambiguities. Frequency diversity might also be of value in dealing with the excessive sidelobe levels in wide-angle imagery.

While there is an extensive literature database on waveform diversity techniques, there is relatively little information about applying these techniques to SAR (some examples are [77, 138] but they do not relate explicitly to ambiguity resolution). This

---

[6]Section 9.4 illustrates these waveforms are not perfectly distinguishable, limiting their usefulness for the anti-aliasing problem.

lack of research may stem from the relative lack of ambiguity problems in traditional narrow-angle SAR sensors, and indicates there is significant room for additional research.

Before closing this section, it should be mentioned that the SAR sensor's waveform type may effect the entire imaging process. While some image processing methods (e.g., chirp scaling) are explicitly linked to waveform type, others (e.g., backprojection) begin processing with matched filtered range profiles, making them less sensitive to waveform parameters. For this reason, the use of diverse waveforms must coincide with a clear understanding of the image formation process.

2.5.3 Proposed Solution. Chapter VI develops a new diverse waveform anti-aliasing technique. By combining radar echoes from randomized Stepped-Frequency (SF) waveforms, the technique forms a series of Doppler filter nulls coinciding with aliasing artifact Doppler values. Un-aliased scene components are unaffected by this approach. Unlike the phased-array methods discussed in Sec. 2.5.2.1, this SF waveform method does not require advanced hardware or specialized processing. Chapters VII and VIII demonstrates the technique using point scatterer simulations, while Chapter IX provides validation using high fidelity third party simulation software and measured RCS chamber data.

2.6 Summary

This chapter introduced the WAM-SAR radar architecture. WAM-SAR promises to solve some of the most vexing real-time radar surveillance problems faced on the modern battlefield, providing high resolution SAR imagery over vast ground swaths. The use of a multistatic data collection geometry helps prevent shadowing and increases platform survivability.

Unfortunately, as enticing as WAM-SAR's benefits sound, the wide-angle data collection geometry introduces significant problems, precluding SAR image formation using traditional methods. The first of these problems involves focusing wide-angle

data in the presence of RM (i.e., radiative near-field effects) and warped ground planes. While the literature contains several techniques which address certain aspects of these data focusing problems, none of these solutions fully corrects for these issues in the general WAM-SAR scenario. The SAR imaging algorithm presented in Chapter V provides complete data focusing in a 3-D monostaic/bistatic radiative near-field scenario. This algorithm is validated using ISAR data from AFIT's RCS chamber.

The second problem precluding WAM-SAR is the presence of aliasing artifacts in the resulting imagery. The large Doppler spread inherent in wide-angle radar ground echoes mandates an impractically large PRF. Failing to meet this requirement leading to undersampling along the synthetic aperture resulting in cross range (i.e., Doppler) aliasing. In theory, a fully digitized active phased array radar could solve this problem, but the expense and complexity of this approach precludes implementation. This research effort develops a new anti-aliasing approach based on waveform diversity principles. When combined with matched filter processing, the randomized SF radar waveforms place Doppler filter nulls at aliasing artifact locations, effectively removing the aliased energy from the imagery. The technique's theory is presented in Chapter VI. It is demonstrated using both simulated and measured data in Chapters VII-IX. In addition to only requiring a two channel antenna, the use of randomized CW SF waveforms allows simultaneous multi-platform operation and reduces platform vulnerability.

III. Synthetic Aperture Radar Overview

Chapter II provided a detailed introduction to the Wide-Angle Multistatic Synthetic Aperture Radar (WAM-SAR) concept, illustrating both benefits and challenges. Before discussing the dissertation's core research efforts and results, a more detailed overview of the Synthetic Aperture Radar (SAR) field is needed. This chapter provides such an overview, reviewing SAR history and applications as well as introducing basic processing approaches and implementation issues.

3.1   Brief SAR History

In 1951, Carl Wiley discovered that two fixed targets with an angular separation could be differentiated by a moving radar platform based on the difference between the targets' Doppler shifts. He called this technique Doppler beam sharpening, but today it is recognized as a specialized form of SAR [133, 134]. While Wiley formalized his Doppler beam sharpening technique, a group at the University of Illinois noticed the same Doppler effect in frequency spectra from a series of terrain samples. In 1953, they built a specialized X-band radar and produced a basic Two-Dimensional (2-D) radar image [8, 74, 114].

Since the 1950s, SAR processing techniques have matured dramatically. SAR imaging was first extended to three dimensions by Lee Graham in 1974 using interferometric processing [55]. One of the most significant advancements came with the advent of high-speed digital computers. Computers enabled the replacement of optical processors (used in most pre-1980 SAR imagery) with digital processors. John Kirk first demonstrated this advance in 1975 [71].

In 1980, Jack Walker corrected significant focusing errors in SAR imagery by recognizing the polar nature of SAR data collection. This discovery also helped solidify the foundations of Inverse Synthetic Aperture Radar (ISAR) [128]. ISAR uses target motion (as opposed to the radar motion) to form a high resolution multi-dimensional image. Walker's work also forms the basis for the Polar Reformatting Algorithm (PFA) still used in many modern SAR systems. Another significant discovery was

made by David Munson in 1983, when he showed tomographic techniques from the medical imaging community could also be used to form SAR images [99]. This discovery led to the development of the Back-Projection Algorithm (BPA). Chapter V demonstrates a specialized BPA approach, developed for a general Three-Dimensional (3-D) near-field bistatic collection geometry.

3.2 *Basic SAR Principle*

The first SAR algorithms were derived from a Doppler shift paradigm [114,133]. These algorithms exploit the fact that radar targets at the same range but different angular locations have different Doppler shifts as observed by a moving radar platform. More recently, SAR imaging has been reexamined from the antenna theory perspective [121]. This approach makes uses the fact that antenna main beam width is inversely proportional to antenna size [68]. Thus, achieving a very narrow beamwidth requires a very large antenna. In many applications, the desired antenna beamwidth, which correlates directly to image angular resolution, demands an impractically large antenna. SAR allows the radar designer to achieve very fine angular resolution using a relatively small antenna by coherently combining radar echoes received by a small antenna located at a collection of different spatial locations. These echoes are collected over a period of time known as the Coherent Processing Interval (CPI), during which the transmitted waveform phase cannot drift significantly. The spatial extent of these locations determines the "synthetic" antenna length and thus the angular (i.e. cross range) resolution[1]. Combining the SAR principle with high range resolution techniques (e.g., pulse compression [41]) produces high resolution, multi-dimensional radar imagery.

---

[1]The synthetic antenna beamwidth is half the beamwidth of an equal-length real antenna, and provides better angular resolution by a factor of two [121]. This effect results from the two-way propagation of the radar echoes forming the synthetic aperture.

3.3 Role of SAR

Since the initial discovery of the basic SAR principle in the 1950s, the number and importance of SAR applications has grown considerably. While in no way exhaustive, this section highlights major applications of SAR systems with relevant citations.

The most well known applications for SAR systems are the production of terrain maps. The ability to map large ground patches, even while in darkness and through cloud cover, has made SAR imagery vitally important for many military and non-military applications. SAR maps can be used for everything from classification of terrain type [17] to real-time surveillance and reconnaissance of a battlefield [46,119]. With the advent of spaceborne SAR systems, the remote sensing community gained a powerful tool for creating maps to monitor environmental changes in the Earth's surface [124]. The future plans of the National Aeronautics and Space Administration (NASA) include launching a SAR system called LightSAR, capable of producing near-global interferometric maps of the Earth for monitoring surface changes [61]. Yet satellite SAR systems are not limited to remote sensing of geophysical characteristics of the Earth. Considerable effort has also been put into the use of SAR for mapping other planets. One of the best examples of this application was the Magellan mission to the planet Venus [68].

Extensive research has begun into SAR systems capable of penetrating either the ground or dense foliage canopies. One promising application of ground penetrating SAR is the ability to detect land mines [7]. FOliage PENetration (FOPEN) applications also hold promise, allowing SAR systems to view manmade objects (such as tanks) beneath vegetation [138].

A very active SAR research area is Automatic Target Recognition (ATR). These techniques allow computer algorithms to identify targets of interest with minimal human intervention. This ability is useful because the volume of data produced by a SAR system can overwhelm human operators. ATR methods are based on a variety

of techniques. One of the most popular involves modeling targets as collections of discrete point scatterers and fitting these models to the data [20,31,105]. Other ATR approaches are based on everything from Hidden Markov models to template matching and neural networks. Another ATR-related application uses ship wake imagery for ship identification [113].

Even the archeology field has benefitted from SAR. In 1999, an ancient city in the Honduran rain forest was discovered using SAR imagery [139]. The radar did not locate the ruins directly, but observed variations in the jungle canopy above the ruins, localizing the ancient city.

Another important military SAR application deals with the challenge of integrating SAR and Moving Target Indication (MTI) systems. Combining these missions into a single platform (or even a single waveform) holds great promise for improving effectiveness on the battlefield. Several recent papers address the issues associated with moving targets as observed by SAR systems [33,66,97].

In SAR, a moving radar samples a fixed target region. The same principle can be applied by fixed radars to image moving (especially rotating) targets is a technique known as ISAR. In addition to aiding in target recognition schemes, ISAR methods can produce radar images using Radar Cross Section (RCS) chamber data. These images help engineers identify and perhaps control the prominent scatters on a given object, lowering the overall RCS [73,93].

A final application deals with bistatic radar concepts. Most SAR systems operate in a monostatic mode, both transmitting and receiving from a single radar antenna. Bistatic systems, on the other hand, transmit from one antenna and receive echoes from a different antenna. These antennas can be located on entirely different radar platforms and separated by substantial distances. This configuration could add substantial new capabilities to radar and SAR applications, such as the ability to operate in a passive mode, decreasing the odds of radar platform detection. Bistatic

SAR systems could be built which do not use explicit radar waveforms, but rather radio and television signals already present in the environment [62, 106].

3.4 Stripmap SAR Geometry

SAR systems generally operate in one of two modes: stripmap and spotlight. Stripmap SAR systems produce relatively low resolution images over large regions. Spotlight SAR systems produce high resolution imagery over small regions. This section outlines the basic geometry behind stripmap mode SAR. Section 3.5 details spotlight SAR.

As the name suggests, stripmap SAR systems produce images of large ground strips. The width of these strips is defined by the radar's range swath while the length is governed by the aircraft's flight path extent [117]. The literature covers stripmap SAR systems extensively [8, 23, 100]. Typical stripmap platforms fly a linear path parallel to the ground while the radar beam is pointed at some *fixed* angle relative to the radar flight path. Many systems operate with the radar beam pointed normal to this flight path, resulting in a "broadside" collection. If the beam is not normal to the flight path, the collection geometry is termed "squinted."

Figure 3.1 shows a broadside stripmap SAR geometry. The term "ground swath" refers to the intersection between the ground and the radar's mainbeam. It defines one dimension (the range extent ΔR) of the maximum image size. The vertical axis (parallel to the radar's flight path) is known as the cross range dimension. The horizontal axis is called the range or slant range dimension depending on the author or situation [36, 100, 117]. Ground range is the distance between a target and a point in the ground plane directly beneath the radar. Slant range refers to the true distance between the radar and the target. Since the radar is usually aboard an aircraft or other elevated platform, the slant range is somewhat larger than the ground range. For 2-D collection scenarios, when collection platform altitude is defined as zero, ground range is equivalent to slant range. Radar data is always collected and often processed in the slant range plane (defined by the aircraft flight path and a point on the ground
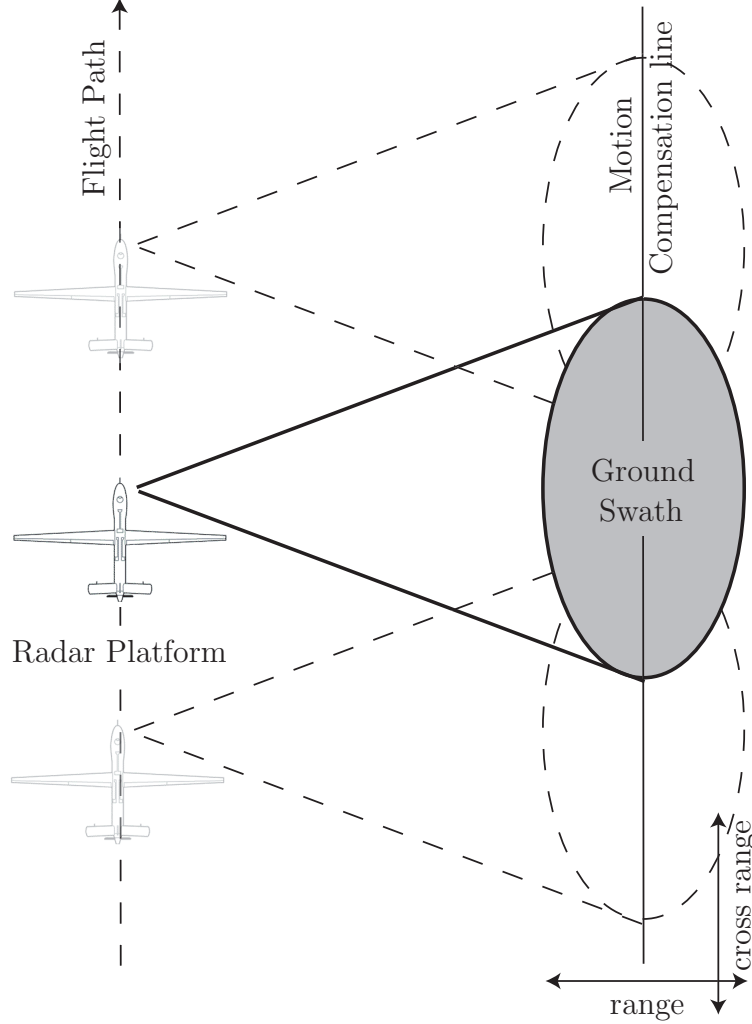
Figure 3.1:   Broadside stripmap SAR geometry.

marking the imaged scene center). The resulting imagery is usually projected into the ground plane to create images as though the viewer is located directly overhead [65]. Figure 3.2 illustrates the different types of range.

As discussed in Section 3.9, the span of azimuth angles (denoted $\Delta\theta$) observed by the SAR platform determines the cross range resolution. The larger the angular span, the better the resolution achieved. In stripmap mode, $\Delta\theta$ is equal to the beamwidth, since the beam is fixed relative to the radar platform.

Stripmap systems also usually share a common processing method. As individual radar echoes are processed, they are referenced to a fixed range, usually the
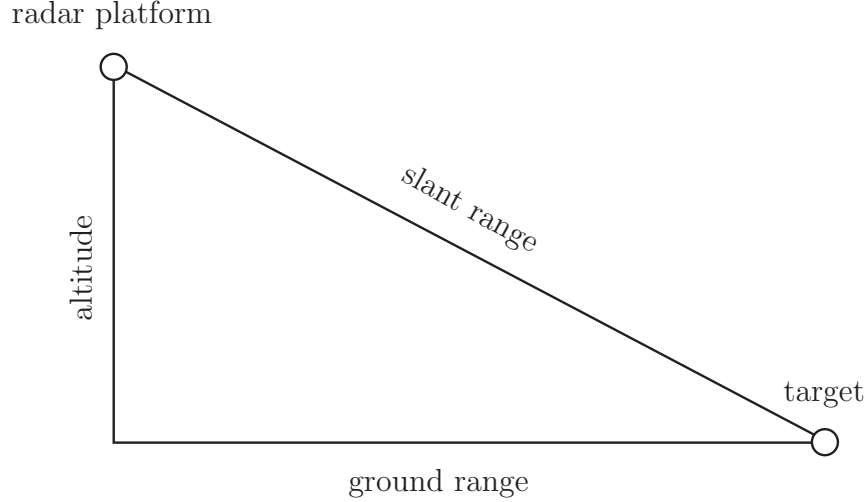
Figure 3.2: Depiction of various range terms. The radar platform is flying into the page. The term "range" can refer to either "slant range" or "ground range" depending on the author.

range swath's midpoint. This referencing procedure, called "motion compensation to a line," ensures the demodulated echoes from a given point scatterer exhibit a frequency shift depending on its instantaneous cross range location. Often referred to as an azimuth chirp, this behavior can have significant impact on the sampling requirements and processing methods used by SAR imaging algorithms [36, 100].

3.5 Spotlight SAR Geometry

Spotlight SAR systems are a more recent SAR operating mode, and are also addressed extensively in the literature [8, 28, 99]. In stripmap SAR, the radar platform motion moves the beam over different ground sections. Conversely, in spotlight SAR, radar platform motion and/or beam steering continually illuminates the *same* ground patch. This approach necessarily limits the scene (i.e., image) size, but also results in higher resolution imagery. This procedure makes $\Delta\theta$ larger than the beamwidth, leading to high resolution.

Figure 3.3 shows a typical spotlight collection geometry. Note, the flight path is identical to the stripmap case. This time, however, the beam illuminates the same
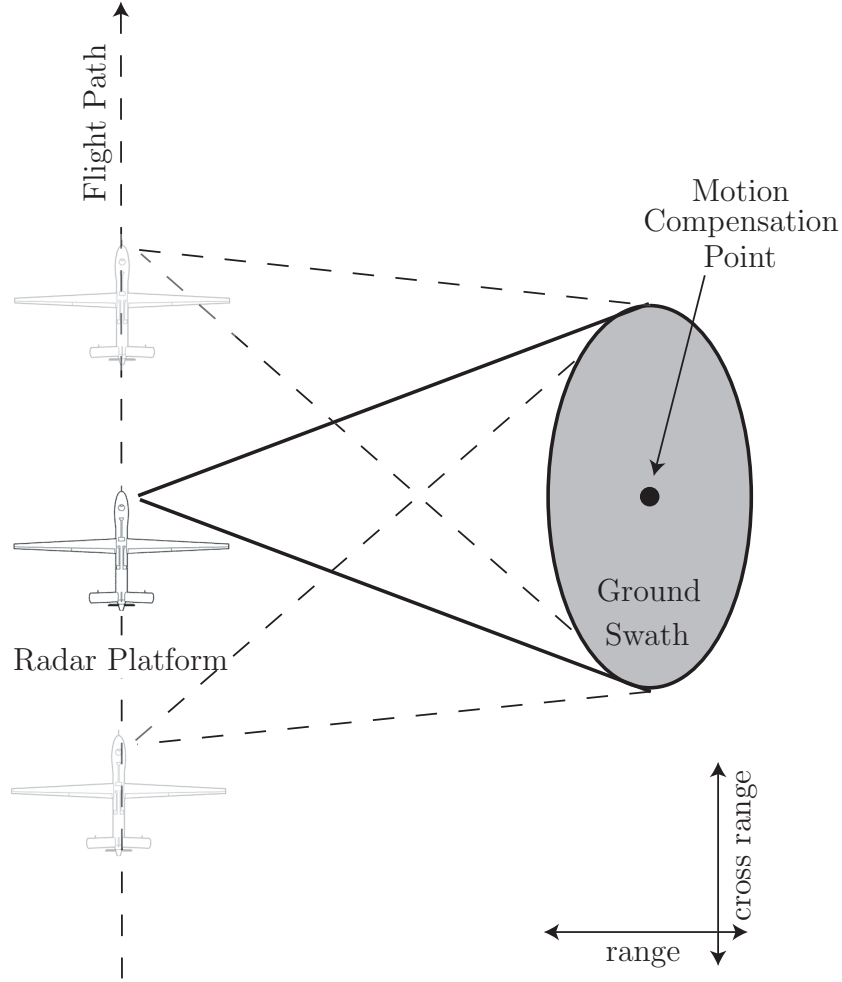
Figure 3.3:   Broadside spotlight SAR geometry.

ground patch throughout the collection. Since the ground patch center's cross range location is the same as the middle of the radar platform flight path (i.e., middle of the synthetic aperture), this collection is still referred to as broadside. Shifting the ground swath's cross range location results in a squinted collection.

Another common spotlight SAR operating mode requires flying a circular path about the scene. In this mode, beam steering is unnecessary as the circular flight path keeps the beam pointed at the same ground patch throughout the flight. Again, the beam must illuminate the same ground patch throughout the collection.

spotlight mode processing is also different than stripmap processing. Instead of being referenced to a fixed range during the demodulation process, spotlight SAR

signals are referenced to the ground swath center. This absolute referencing is called "motion compensation to a point" and effectively removes the azimuth chirp found in demodulated stripmap data. In fact it is often possible to use spotlight processing methods on stripmap data, resulting in some ambiguity in determining which mode a SAR system is using [100]. In this research effort, data is simulated/collected in both stripmap and spotlight geometries, but the processing always uses spotlight's "motion compensation to a point" approach. This decision enables the construction of SAR imaging algorithms insensitive to the data collection mode. WAM-SAR itself uses stripmap data collection and spotlight processing.

3.6   Matched Filtering

Whether operating in a stripmap or spotlight mode, most SAR systems transmit a series of pulses into the environment at regular time intervals spanning the CPI. The pulse echoes during the CPI are collected and processed into SAR images. Assuming the SAR platform velocity is small compared to the wave propagation velocity c, SAR echoes may be processed using the start-stop assumption. This approach assumes the SAR platform is fixed during transmission/reception of each CPI pulse. Platform motion is assumed to occur instantaneously between pulses. The start-stop assumption is used extensively in the SAR community and is valid for most airborne data collection scenarios [25, 65, 100, 117].

Invoking the start-stop assumption allows each CPI pulse to be processed individually. This section introduces one of the most popular processing methods, matched filtering. It illustrates how waveform pulse echoes are used to form One-Dimensional (1-D) range profiles. Later sections describe how SAR imaging algorithms combine range profiles from the entire CPI to produce multi-dimensional SAR imagery.

At each CPI point, the radar transmits a waveform $w_{\mathrm{TX}}(t)$. As a consequence of the constant waveform propagation velocity, the relationship between range r and

time delay t can be written as

$$r = \frac{ct}{2},$$ (3.1)

where c is the speed of light. Using this linear relationship, the receive radar echo $w_{\text{RX}}(r)$ may be written as

$$w_{\text{RX}}(r) = w_{\text{TX}}(r) * p_\theta(r),$$ (3.2)

where $*$ denotes convolution. Doppler shift may be ignored for the moment due to the start-stop approximation. The function $p_\theta(r)$ is the scene's true range profile as observed from the radar's instantaneous location. Assuming the scene is contained in the radar's far-field (where plane wave propagation is assumed), the scene's Radon transform determines its range profile [60]

$$p_\theta(r) = \int_{-\infty}^{\infty} \int_{-\infty}^{\infty} f(x, y)\delta(x \cos \theta + y \sin \theta - r) \mathrm{d}x\mathrm{d}y,$$ (3.3)

where $\delta(\cdot)$ is the delta function. The function $f(x, y)$ is the scene's 2-D complex reflectivity function. Assuming the scene center is defined at $(0, 0)$, the range r and angle θ are defined by the instantaneous SAR platform location (x_p, y_p) via

$$r = \sqrt{x_p^2 + y_p^2},$$ (3.4)

$$\theta = \tan^{-1}\left(\frac{y}{x}\right).$$ (3.5)

Note the $\tan^{-1}(\cdot)$ assumes both x and y are positive. When this is not the case, care must to ensure θ is placed in the correct quadrant.

Generating an accurate estimate $\hat{f}(x, y)$ of $f(x, y)$ is the SAR system's primary goal. Unfortunately, as dictated by (3.3), the scene is projected onto a line defined by the instantaneous platform location and scene center. The range profile $p_\theta(r)$ defines the integrated contribution from scatterers at a given range r from the radar's current

location. At each CPI point, the platform's new location (x_p, y_p) defines a new θ value, resulting in a new true range profile $p_\theta(r)$.

The returning radar echo $w_{\mathrm{RX}}(r)$ is "matched filtered," generating the range profile estimate $\hat{p}_\theta(r)$

$$\hat{p}_\theta(r) = w_{\mathrm{RX}}(r) * h_{\mathrm{MF}}(r) = [w_{\mathrm{TX}}(r) * p_\theta(r)] * h_{\mathrm{MF}}(r), \tag{3.6}$$

where $h_{\mathrm{MF}}(r)$ is the matched filter's impulse response. By definition, the matched filter maximizes the ratio of peak signal power to mean noise power (i.e., Signal to Noise Ratio (SNR)) [63]. Assuming the radar echoes are corrupted by white Gaussian noise (e.g., thermal noise), $h_{\mathrm{MF}}(r)$ is defined by [117]

$$h_{\mathrm{MF}}(r) = w_{\mathrm{TX}}^*(-r), \tag{3.7}$$

where the superscripted $*$ denotes conjugation. Equation (3.7) allows (3.6) to be rewritten as

$$\hat{p}_\theta(r) = [w_{\mathrm{TX}}(r) * p_\theta(r)] * w_{\mathrm{TX}}^*(-r). \tag{3.8}$$

Using the convolution and conjugation Fourier Transform (FT) properties (Appendix A), (3.8) becomes

$$\hat{p}_\theta(r) = \mathcal{F}^{-1}\left[|W_{\mathrm{TX}}(k_r)|^2 P_\theta(k_r)\right], \tag{3.9}$$

where

$$k_r = \frac{4\pi}{\lambda}, \tag{3.10}$$

is the radial spatial frequency (i.e., wave number) defined by λ, the transmitted wavelength[2] and $\mathcal{F}^{-1}$ denotes the Inverse Fourier Transform (IFT). Taking the range

---

[2]Equation (3.10) contains an additional factor of two compared to the traditional wave number definition $k_r = 2\pi/\lambda$. The functions $W_{\mathrm{TX}}(k_r)$ and $P_\theta(k_r)$ are the Fourier transforms of $w_{\mathrm{TX}}(r)$ and $p_\theta(r)$, respectively. This additional factor of two results from the two-way propagation inherent in radar applications. Unless stated otherwise, this factor of two is always assumed.

profile estimate's FT, yields

$$\hat{P}_\theta(k_r) = \mathcal{F}[\hat{p}_\theta(k_r)] = |W_{\text{TX}}(k_r)|^2 P_\theta(k_r). \tag{3.11}$$

Equation (3.11) shows Fourier transforming the matched filter output $\hat{p}_\theta(r)$ results in a windowed estimate $\hat{P}_\theta(k_r)$ of the scene's spatial frequency data $P_\theta(k_r)$. The windowing function $|W_{\text{TX}}(k_r)|^2$ determines the spatial frequency values available to the SAR sensor.

An "ideal" bandlimited waveform provides uniform frequency coverage over a bandwidth B. Analytically, this frequency coverage is

$$|W_{\text{TX}}(k_r)|^2 = \begin{cases} 1, & \min(k_r) \leq k_r \leq \max(k_r) \\ 0, & \text{otherwise,} \end{cases} \tag{3.12}$$

where $\min(k_r)$ is the minimum k_r value (corresponding to the minimum transmit frequency) and $\max(k_r)$ is the maximum k_r value (corresponding to the maximum transmit frequency). In this case, the estimate $\hat{P}_\theta(k_r)$ is simply a subset of $P_\theta(k_r)$. The specific spatial frequency samples acquired are determined by the waveform bandwidth B. In the limit of $\min(k_r) \to 0$ and $\max(k_r) \to \infty$ (i.e., infinite waveform bandwidth), $\hat{P}_\theta(k_r) = P_\theta(k_r)$ and $\hat{p}_\theta(r) = p_\theta(r)$, yielding a perfect range profile estimates (assuming noise-free measurements).

Prior to closing this section, it should be noted that matched filtering is not the only SAR data processing method. Many older SAR systems use "deramp processing" where Linear Frequency Modulation (LFM) waveform echoes are mixed with the original transmit waveform, producing 2-D spatial frequency samples without the need for an explicit FT operation [65]. Deramp processing was particularly attractive to older systems because it can be easily implemented in analog radar hardware. Unfortunately, deramp processing mandates the use of LFM waveforms, and is therefore inappropriate for the waveform diversity-based anti-aliasing technique introduced in Chapter VI. Also, deramp processing is not appropriate for wide-angle focused image

formation since it inherently assumes plane wave illumination [65]. For these reasons, in addition to their optimal SNR matched filter properties, matched filters process all WAM-SAR data.

3.7 Point Scatterer Model for Scene Reflectivity

As stated in the previous section, SAR/ISAR imaging produces an estimate $\hat{f}(x, y)$ of the scene's spatial reflectivity function $f(x, y)$. This "image" is different from, but related to, an optical image or photograph of the same region. An in-depth analysis of these differences is beyond the scope of this section, but these differences arise from several important effects. First, the SAR system's wavelengths are much longer than those of light. Second, SAR is a coherent imaging system (magnitude and phase) while optical images use non-coherent collections (magnitude only). Also, radar systems directly measure range whereas optical systems do not.

The point scatterer model is commonly used throughout the SAR community as a basis for imaging algorithm development [8, 65, 117]. It consists of modeling the scene's reflectivity function $f(x, y)$ as a superposition of ideal point scatterers. The mth point scatterer $s_m(x, y)$ is defined as

$$s_m(x, y) = A_m \delta(x - x_m, y - y_m), \tag{3.13}$$

where A_m is the complex scatterer amplitude, $\delta(\cdot, \cdot)$ is the 2-D delta function, and the scatterer location is defined by the coordinates (x_m, y_m). Note the amplitude A_m is a complex constant. More robust point scatterer models allow A_m to vary as a function of look angle and illumination frequency [119].

The point scatterer model makes several inherent scene assumptions. Perhaps most significantly, it doesn't allow for the interaction among individual point scatterers. This assumption means real targets, exhibiting interactions due to cavities, multipath effects, etc., will not be correctly modeled. None-the-less, the assumption's limitations are not an issue for SAR image formation. Since this model is used to

develop imaging algorithms, the point scatterer model only focuses energy from radar echoes as though it was reflected from a point scatterer. The echoes from a more complicated target, such as a cavity, simply appear as a point scatterer further away from the radar. One approach for dealing with this effect is including a much more complex model in the imaging algorithm, but the complexity and computational effort involved is unlikely to yield beneficial results. Instead, one can simply treat the excess energy from a cavity echo as an additional feature in a point scatterer model-based image. Although not present in an optical image, this additional feature can be exploited by imagery analysts, enabling better scene/target characterization [111].

3.8   The Spatial Frequency Paradigm

Section 3.6 illustrated how each Fourier transformed matched filtered radar echo $\mathcal{F}[\hat{f}_\theta(r)]$ generates a series of spatial frequency samples $\hat{F}_\theta(k_r)$ covering all available orientation angles θ. Due to the Fourier transform's rotational property (see Appendix A), the orientation angle θ in the spatial (image) domain (x, y) is the same as the orientation angle in the transform domain (k_x, k_y). This fact allows the user to map spatial frequency samples from individual CPI pulse echoes onto the 2-D spatial frequency domain using a simple polar-to-cartesian conversion

$$k_x = k_r \cos\theta \qquad\qquad (3.14)$$

and

$$k_y = k_r \sin\theta, \qquad\qquad (3.15)$$

where k_x is the spatial frequency coordinate in the k_x-direction and k_y is the spatial frequency coordinate in the k_y-direction. These conversions allow examination of the scene's 2-D complex reflectivity function $f(x, y)$ in the 2-D spatial frequency domain $F(k_x, k_y)$. This paradigm for understanding SAR data collection and processing forms the basis for many modern SAR image generation algorithms.

Using the point scatterer assumption from Sec. 3.7, a scene's 2-D complex reflectivity function $f(x, y)$ can be represented as

$$f(x, y) = \sum_{m=0}^{M-1} s_m(x_m, y_m), \tag{3.16}$$

where M is the number of scatterers. Figure 3.4(a) illustrates such a scene containing $M = 4$ unit amplitude point scatterers located at arbitrary locations. The equivalent spatial frequency domain data $F(k_x, k_y)$ is found by taking the scene's 2-D FT to obtain

$$F(k_x, k_y) = \mathcal{F}\left[f(x, y)\right]. \tag{3.17}$$

Figure 3.4(b) shows $|F(k_x, k_y)|$ for the scene in Fig. 3.4(a).

Using the linearity of the Fourier transform, (3.17) can be rewritten as

$$F(k_x, k_y) = \sum_{m=0}^{M-1} S_m(k_x, k_y), \tag{3.18}$$

where

$$S_m(k_x, k_y) = \mathcal{F}\left[s_m(x, y)\right] = A_m \exp[-j(k_x x_m + k_y y_m)]. \tag{3.19}$$

As shown in Sec. 3.6, the SAR data collection process obtains a subset of the scene's spatial frequency data $F(k_x, k_y)$. For typical narrow-angle SAR sensors, the available spatial frequency data is roughly rectangular in shape. Figure 3.4(c) displays this available data and represents the radar's estimate $\hat{F}(k_x, k_y)$ of $F(k_x, k_y)$.

When the available data is subjected to a 2-D IFT, the result is Figure 3.4(d) containing the estimate $\hat{f}(x, y)$ of the true reflectivity function $f(x, y)$. Although the scene estimate has placed all 4 scatterers at their correct locations, the limited amount of available data has degraded the resolution of $\hat{f}(x, y)$ and introduced a cross-shaped sidelobe structure around each scatterer.

Figure 3.5 illustrates a different approach to the spatial frequency paradigm. Inherent data collection process limitations mean $\hat{F}(k_x, k_y)$ is acquired by multiplying
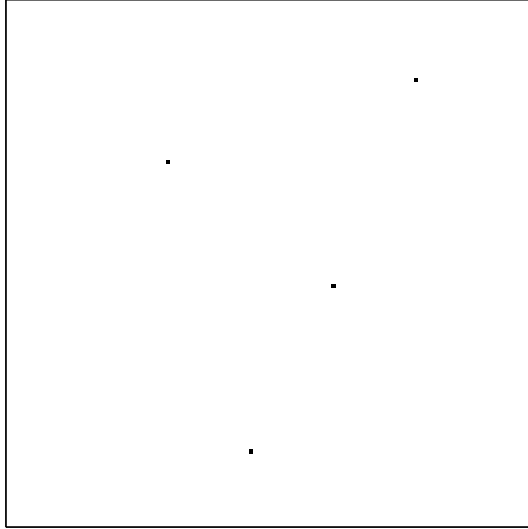
(a) True reflectivity function.
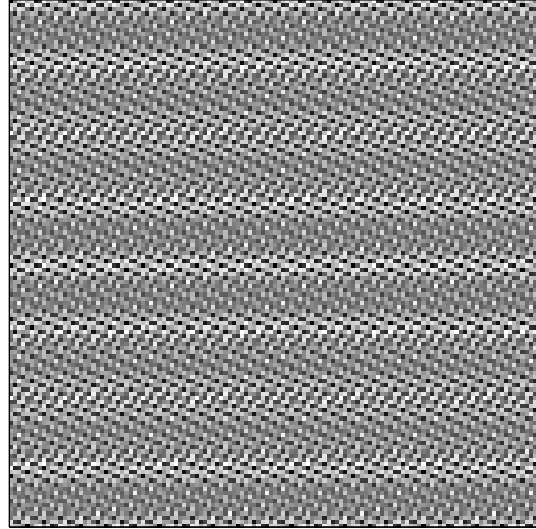
(b) 2-D FT of true reflectivity function.
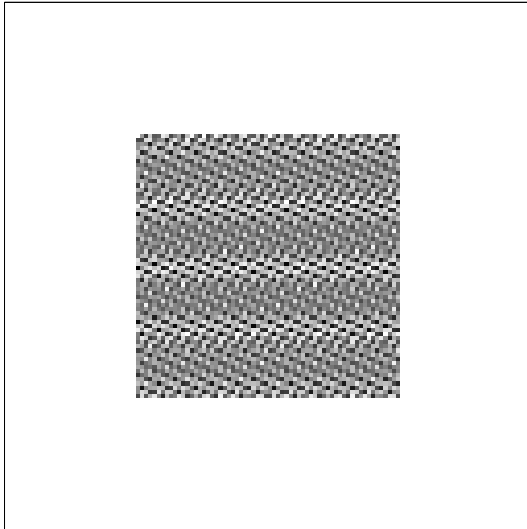
(c) Available data.
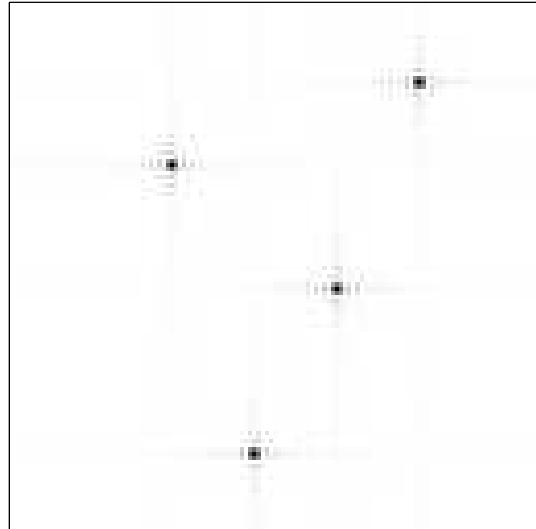
(d) Reflectivity function estimate.

Figure 3.4:   Conceptual depiction of SAR imaging process using spatial frequency paradigm.
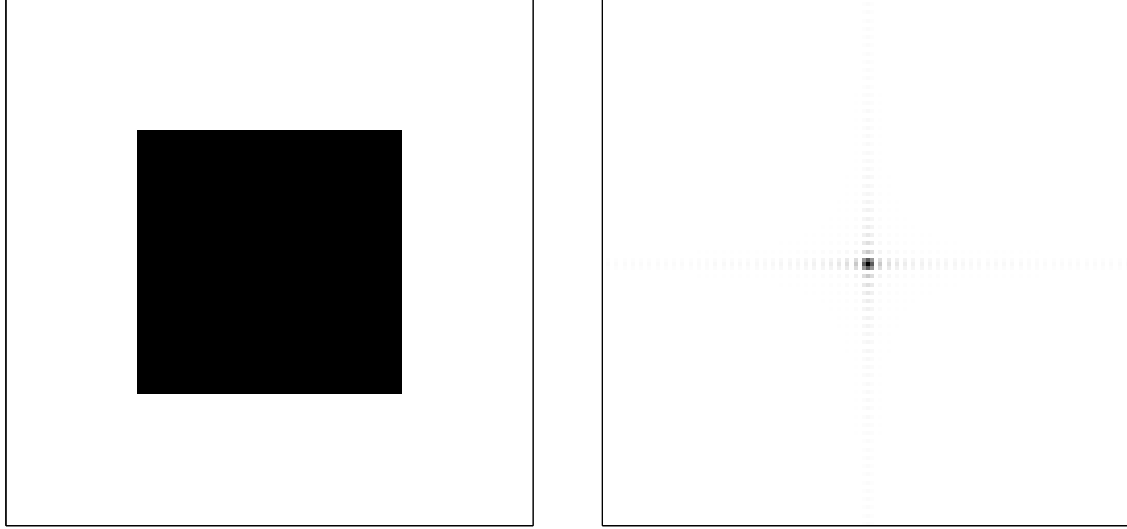
(a) Data support region in 2-D spatial frequency domain.

(b) Image (spatial) domain IPR defined by the 2-D FT of the data support region.

Figure 3.5:   Relationship between data support region and SAR IPR function.

$F(k_x, k_y)$ by a masking function defining the specific (k_x, k_y) values available to the SAR system. Figure 3.5(a) shows such a mask. Since the mask defines the available data, it is also referred to as a data support region [65].

Taking the mask's 2-D IFT results in the ImPulse Response (IPR) function shown in Fig. 3.5(b). This function represents the scene estimate $\hat{f}(x, y)$ resulting from a scene consisting of a single, unit-amplitude point scatterer appearing at the scene center. Using the FT convolution property, the estimate $\hat{f}(x, y)$ of a more complicated scene can be obtained by performing a 2-D convolution of the IPR with the true scene $f(x, y)$.

3.9   Image Resolution

Perhaps the most fundamental qualifier for establishing SAR/ISAR image quality is resolution. Conceptually, resolution refers to the minimum spacing between objects for both objects to be distinguished (i.e., resolved). Image resolution is normally divided into range and cross range components. This distinct terminology is used because in traditional narrow-angle SAR systems range and cross range resolu-

tion are essentially independent. In wide-angle systems, these factors are not independent. This section develops methodology for calculating achievable narrow-angle SAR/ISAR image resolution based on data coverage extent in the spatial frequency plane. Chapter V extends these results to the wide-angle bistatic 3-D case.

From basic Fourier analysis, it is well known that resolution in one domain is determined by the extent in the other domain. For example, the FT of an infinite duration single-frequency sinusoid, is a delta function $\delta(\cdot)$. As the sinusoid's temporal support is reduced, the delta function expands into a $\mathrm{sinc}(x) \triangleq \sin(\pi x)/\pi x$ function. The shorter the signal, the wider the $\mathrm{sinc}(\cdot)$ function's main lobe. Extending this analogy to the spatial frequency domain, the data support region extent in the k_x-direction (Δk_x) determines the final image resolution in the x-direction (δx). Similarly, Δk_y determines δy. Assuming the scene is normal to the platform flight path, the x-direction corresponds to range, while the y-direction corresponds to cross range.

Calculating the predicted resolution only requires a little geometry. As shown in [65], Fourier analysis provides the range and cross range resolutions as

$$\delta x = \frac{2\pi}{\Delta k_x} \tag{3.20}$$

and

$$\delta y = \frac{2\pi}{\Delta k_y}, \tag{3.21}$$

where Δk_x and Δk_y are the extents of available spatial frequency data in the k_x and k_y-directions, respectively. To this point, the term resolution has been used rather loosely, without specifying whether it refers to null-to-null resolution, -3.0 dB resolution, etc. To be more precise, (3.20) and (3.21) should be multiplied by a broadening factor b_w determined by the amplitude window used to weight the available data.

Under uniform weighting, multiplying the resolution equations by $b_w \approx 0.88$ gives -3.0 dB resolution. Under the more typical 40.0 dB Taylor weighting, $b_w \approx 1.24$

gives the -3.0 dB resolution [65]. To avoid introducing unnecessary complexity, unless otherwise specified, this document uses $b_w = 1$ (allowing it to be ignored). Choosing $b_w = 1$ and using uniform weighting results in a -4.0 dB resolution criterion.

Equations (3.20) and (3.21) demonstrate determining image resolution becomes a question of calculating the data support region dimensions in the 2-D spatial frequency plane. Given the SAR collection parameters, this calculation is not difficult. As discussed in Sec. 3.6, each CPI pulse samples a radial "spoke" of the 2-D spatial frequency plane $F(k_x, k_y)$.

Figure 3.6 shows the data support of a hypothetical SAR data collection. The waveform bandwidth determines the annulus width. The dots within the circles correspond to radar waveform samples. Each spoke corresponds to data from a single CPI pulse. The sampled region's angular extent $\Delta\theta$ is determined by the set of look angles, from the radar, to the scene center, throughout the collection. A close-up of Fig. 3.6 is shown in Fig. 3.7. The dimensions of the rectangular box approximately bounding the data $(\Delta k_x \times \Delta k_y)$ determine the best-case image resolution.

The hypothetical collection shown in Figs. 3.6 and 3.7 illustrates a typical narrow-angle SAR collection. In this case, the bounding box width is determined by the signal bandwidth and the height is determined by the collection's angular extent and mean wavelength. Under these conditions, the resolution formulas become

$$\delta x = \frac{c}{2B} \tag{3.22}$$

and

$$\delta y = \frac{\lambda_c}{2\Delta\theta}, \tag{3.23}$$

where B is the waveform bandwidth and λ_c is the center wavelength. These formulas are equivalent to typical SAR resolution formulas found in many SAR texts [36, 65, 130]. Note, these equations were derived using small angle approximations for $\Delta\theta$.
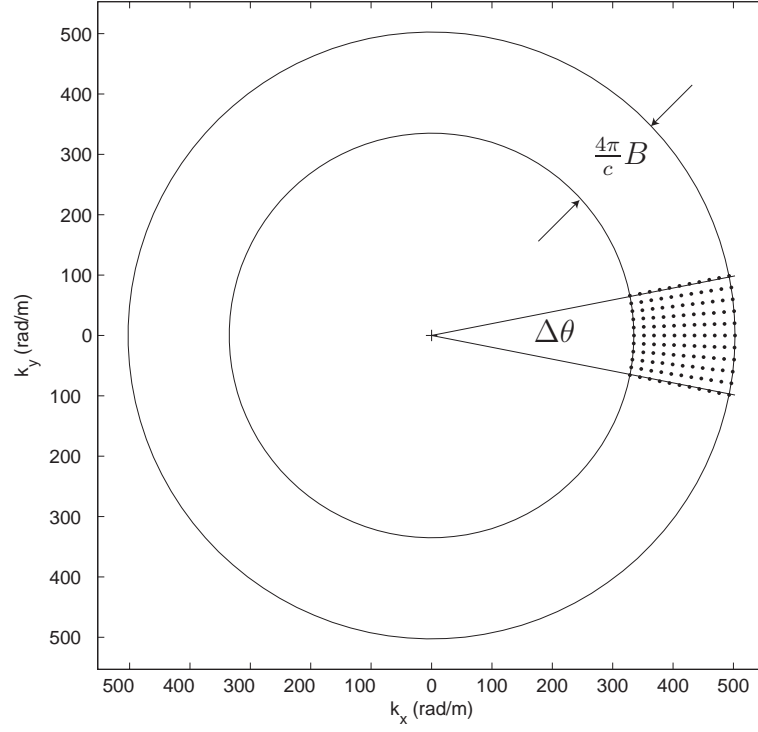
Figure 3.6: 2-D spatial frequency domain SAR data collection representation. Each point represents a single digital sample. Waveform bandwidth B determines the annulus width. The look angles define the angular extent $\Delta\theta$.
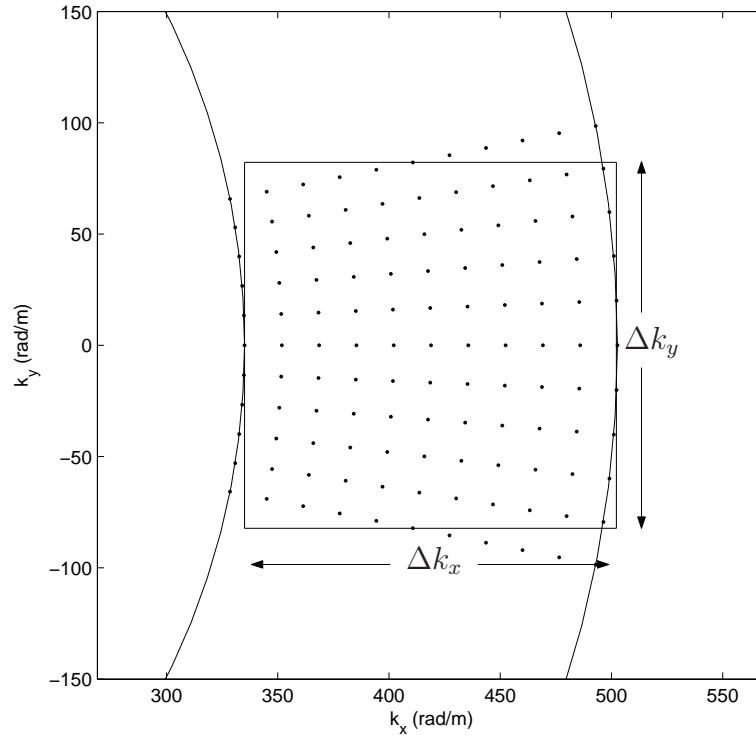
Figure 3.7: Close-up of Fig. 3.6. The rectangular bounding box dimensions ($\Delta k_x \times \Delta k_y$) determine the best-case image resolution.

Figure 3.8 shows the data support regions (gray arcs) for two $\Delta\theta = 90°$ collections. Subfigure (a) illustrates a $B = 6$ GHz collection, while subfigure (b) uses the Global Hawk bandwidth of $B = 600$ MHz. The rectangular box circumscribing the data arcs serves as a quantitative indicator of the resulting image resolution. While the width along the k_x-axis is determined primarily by waveform bandwidth in the narrow-angle case (Figs. 3.6 and 3.7), both B and $\Delta\theta$ contribute in the wide-angle case illustrated here. Taking the 2-D FT of these data support regions results in the IPR functions presented in Fig. 2.3. Resolution values are in Tab. 2.2.

3.10   Sampling Requirements

The previous section calculated expected SAR image resolution using the principle that frequency domain extent determines image domain resolution. The same principle can be used to determine sampling requirements by reversing the domains. Sampling density in the spatial frequency domain determines the maximum alias-free image domain size.

Using (3.20) and (3.21) and reversing the domains gives the following relations

$$\delta k_x = \frac{2\pi}{\Delta x}, \tag{3.24}$$

and

$$\delta k_y = \frac{2\pi}{\Delta y}, \tag{3.25}$$

where δk_x and δk_y represent the maximum allowable sample spacing in the spatial frequency domain. The variables Δx and Δy define the maximum allowable image extent in range and cross range directions (i.e., the maximum ground swath dimensions).

The maximum sample spacing along the k_x-axis occurs at $\theta = 0$, when the target is broadside to the radar. In this case, the spacing is determined by dividing the total waveform bandwidth B by the number of samples N across the bandwidth.

71
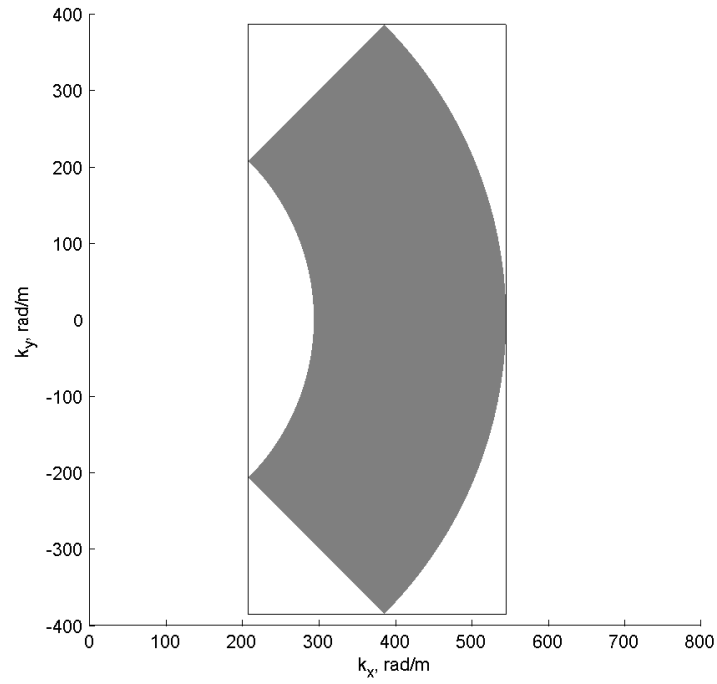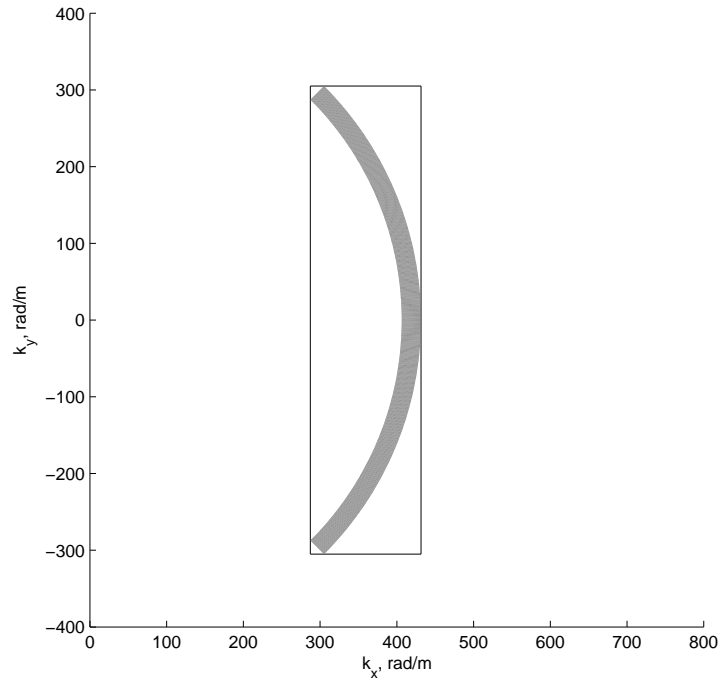
(a) $B = 6$ GHz

(b) $B = 600$ MHz

Figure 3.8: Data support regions (gray arcs) for two wide-angle SAR data collections ($\Delta\theta = 90°$, $f_c = 10$ GHz). Subfigure (a) has $B = 6$ GHz with 60% relative bandwidth. Subfigure (b) has $B = 600$ MHz with 6% relative bandwidth. The circumscribed rectangle area is inversely proportional to the resulting image resolution.

Thus, for a waveform of bandwidth B,

$$\delta k_x = \frac{4\pi}{cN}B. \tag{3.26}$$

This equation implies the total allowable range extent Δx for a given waveform is simply

$$\Delta x = N\frac{c}{2B}, \tag{3.27}$$

where N is the number of frequency samples. Equation 3.27 is simply the number of frequency samples times the approximate -4.0 dB range resolution δx from (3.20). This development assumes only discrete frequency samples are available. While valid for some data collection scenarios, a more common approach in real SAR systems is transmitting a waveform with its energy spread uniformly across its bandwidth (e.g., LFM waveforms). In this case, the number of frequency samples N is essentially infinite, implying that range aliasing due to undersampling will not occur. Another type of range aliasing is caused by having multiple pulses "in the air" simultaneously, creating an ambiguity as to which pulse caused individual radar echoes. Section 2.5.1 introduced this effect.

Similar to k_x, the maximum spacing of k_y samples occurs at $\theta = 0$. In this case, k_y can be well approximated as the height of a right triangle whose hypotenuse is equal to mean(k_x) (the mean value of k_x) and where the angle between the base and hypotenuse is $\delta\theta$, the angular difference between subsequent CPI pulses. Under these conditions

$$\delta k_y = \text{mean}(k_x)\sin(\delta\theta). \tag{3.28}$$

Substituting the definition of $k_x = k_r$ (for $\theta = 0$) and assuming P uniformly spaced azimuth samples gives

$$\delta k_y = \frac{4\pi}{c}f_c\sin\left(\frac{\Delta\theta}{P}\right), \tag{3.29}$$

where f_c is the center frequency. Using the small angle approximation for $\sin(\cdot)$ produces

$$\delta k_y = \frac{4\pi\Delta\theta}{cP}f_c.$$

(3.30)

Using (3.21), (3.30) implies the total alias-free cross range extent Δy is

$$\Delta y = P\frac{\lambda_c}{2\Delta\theta}.$$

(3.31)

Equation (3.31) is simply the number of azimuth samples P times the cross range resolution δy.

3.11 *Image Formation via Fourier Transform Methods*

Previous sections reviewed the basic ideas behind SAR data collection, image resolution, and sampling requirements. This section addresses one class of image formation algorithms based on 2-D FT techniques.

Fourier transforming matched filtered of SAR radar echoes yields radial samples of the scene's 2-D spatial frequency plane data. Thus, the most obvious image formation approach is simply taking the inverse 2-D Fourier transform of this data. Since SAR data sets are typically very large, computational load is always an image formation issue. For this reason, early digital SAR processors sought to make use of Fast Fourier Transform (FFT) techniques. FFTs are extremely fast methods for taking Fourier transforms. They can be performed in multiple dimensions assuming the data samples are arrayed on a rectangular grid. Although SAR samples are collected on an approximately polar grid [128], FFT processing can be performed by *assuming* the data was collected on a rectangular grid. This assumption is reasonable for small $\Delta\theta$ only (i.e., low resolution stripmap SAR systems). Imagery formed without correcting for error due to this non-rectangular sampling is referred to as "unfocused" [121].
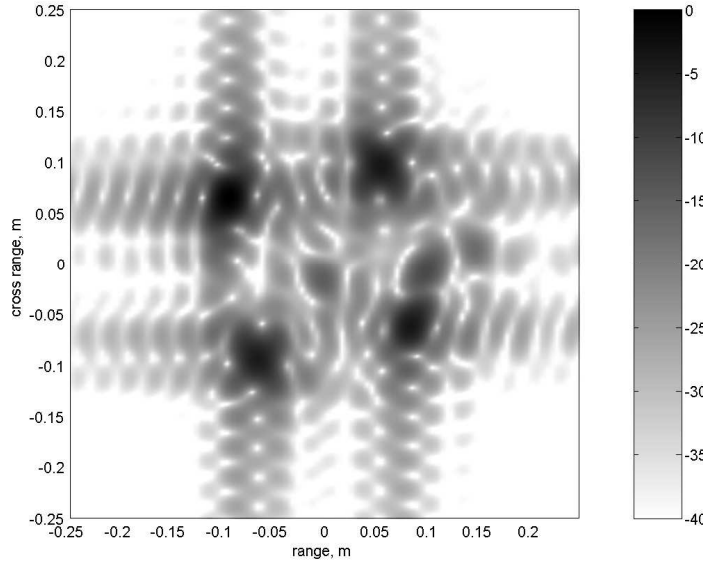
Figure 3.9:   Unfocused ISAR image of four point scatterers. Scatterers are not well focused. Sidelobes are perfectly vertical/horizontal due to the assumption data is collected on a rectangular grid ($\Delta\theta = 20°$, $B = 6$ GHz, 40.0 dB dynamic range).

Figures 3.9 and 3.10 illustrate two ISAR images formed from the same spatial frequency data[3]. The target consisted of four thin vertical wires approximating four point scatterers. The scatterers in the unfocused image (Fig. 3.9) are somewhat larger and more irregular than scatterers in the focused image (Fig. 3.10). Note, the unfocused sidelobes are perfectly vertical/horizontal due to the assumption that the data was collected on a rectangular grid. The focused sidelobes reflect the true polar nature of the data collection. As $\Delta\theta$ becomes larger, these sidelobes acquire a bow-tie shape [90, 132].

While Fig. 3.10 is well focused, this result does not imply simply accounting for non-rectangular sampling is the only requirement for producing focused WAM-SAR imagery. The data in Fig. 3.10 is 2-D, monostatic, and uniformly spaced. The target was in the radar's far-field and confined to a planar target mount. The WAM-SAR

---

[3]The data was taken in the RCS chamber at the Air Force Institute of Technology (AFIT). Procedures for ISAR data collection and calibration are covered in Chapter IV.
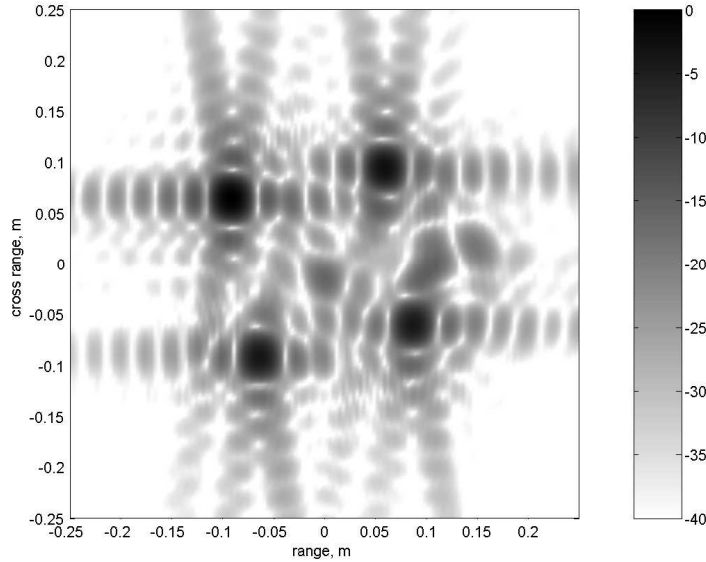
Figure 3.10: Focused ISAR image of four point scatterers. Scatterers are well focused. Sidelobes reflect the polar nature of the collected data ($\Delta\theta = 20°$, $B = 6$ GHz, 40.0 dB dynamic range).

scenario mandates focusing of radar echoes from 3-D monstatic/bistatic near-field targets on non-planar surfaces. These factors dramatically complicate the image formation process. The algorithm developed and validated in Chapter V accounts for all these effects.

The sidelobe strength illustrated in Figs. 3.9 and 3.10 is a significant issue in SAR imaging. Most SAR images consist of large regions with relatively low-level ground returns combined with a few very bright returns from man-made objects. This situation gives the resulting images a large dynamic range. High sidelobe levels therefore cause the energy from strong scatters to bleed over large portions of an image. This energy bleeding, in-turn, can mask returns from objects of interest at lower energy levels. For this reason amplitude windows are usually applied to SAR data during processing. However, in this document no windows are used for sidelobe control. This decision allows unhindered observation of the full sidelobe structure.

3.12 Summary

This chapter provided a detailed overview of 2-D SAR image generation. It began by highlighting key events in SAR history and introducing key role's played by SAR systems today. The basic principles of SAR data processing, resolution, sampling, and 2-D image generation were presented using the relatively new, but increasing popular spatial frequency paradigm. These principles are built around Fourier transform theory. While many of concepts introduced here employ narrow-angle approximations (e.g., the far-field assumption), they serve as a good basis for Chapter V which solves the image focusing problem for arbitrary 3-D bistatic geometries.

IV. ISAR Data Collection and Calibration

Inverse Synthetic Aperture Radar (ISAR) is similar to Synthetic Aperture Radar (SAR) in that it forms high resolution, multi-dimensional radar images. Unlike SAR, ISAR uses target motion (instead of radar motion) to achieve high resolution, but the basic principle is the same: the changing angular relationship between the radar and the target adds a second dimension to the 1-D range profiles generated by matched filtered waveform echoes.

ISAR has many useful applications. It can be used by fixed ground-based radars to produce images of aircraft flying through the radar's beam. It can be also be used to make high resolution images of ships as these ships rock back and forth on ocean waves. But most importantly for this research, ISAR can be used within a Radar Cross Section (RCS) radar chamber to produce high resolution radar imagery of complex targets without the need for an airborne SAR mission. This application provides cost-effective laboratory environment for SAR/ISAR algorithm validation.

Fundamentally, RCS chambers exist to measure the RCS of complex targets. Target RCS (usually represented by σ) is defined as [73]

$$\sigma = \lim_{r \to \infty} 4\pi r^2 \frac{|\bar{e} \cdot \bar{E}_s|^2}{|\bar{E}_i|^2}, \qquad (4.1)$$

where r represents the target range, $\bar{e}$ is the receiver's polarization vector, $\bar{E}_s$ is the scattered electric field, and $\bar{E}_i$ is the incident electric field. The incident field is treated as a scaler since it refers to the electric field strength which impinges on the scattering target. RCS information allows designers to identify (and perhaps modify) a target's geometric features which scatter radar energy in a given (usually monostatic) direction. By reducing the scattered energy, the enemy radar's probability of target detection falls. However, this research is focused not on controlling target scattering, but developing high-quality imaging algorithms applicable to Wide-Angle Multistatic Synthetic Aperture Radar (WAM-SAR).

The remainder of this chapter focuses on data collection and calibration processes in the Air Force Institute of Technology's (AFIT's) RCS chamber. The resultant data is used to form ISAR images, providing laboratory-based validation of WAM-SAR research efforts in both the focused image formation (Chapter V) and anti-aliasing (Chapter IX) arenas.

4.1 RCS Range Types

The RCS range provides an approximation to a free space environment for measuring target scattering of ElectroMagnetic (EM) waves. In order to approximate a free space environment, the RCS range must ensure received radar echoes come only from the interactions between the incident wave and the target. Any scattering from the range itself, or multipath echoes from interactions between the target and the range, corrupt the measurements.

There are four major types of RCS ranges [136]. The simplest and cheapest variety, the type owned by AFIT, is the static indoor far-field range. These ranges have their walls, floor, and ceiling coated with broadband pyramidal and/or wedge-shaped absorber to minimize reflections. The target is typically mounted on a pylon, keeping it as far away from the absorber as possible, minimizing target/absorber interactions. An antenna is mounted as far from the target as practical. The antenna emits a series of spherical wave pulses, which are approximately planar over a small volume centered on top of the target mount. This volume defines the chamber's "quiet zone" and determines the maximum target dimensions allowable when assuming far-field illumination [136]. Section 4.2 derives quite zone specifications.

The second major RCS range type is the static indoor compact range. The chamber design is nearly identical to a static indoor far-field range, but in this case one or more reflectors collimate the incident radar beam. This configuration creates a much larger quiet zone without increasing the distance between the radar and target. The additional reflectors add substantially to the chamber's cost and complexity. The Air Force Research Laboratory (AFRL) operates such a chamber at Wright Patterson
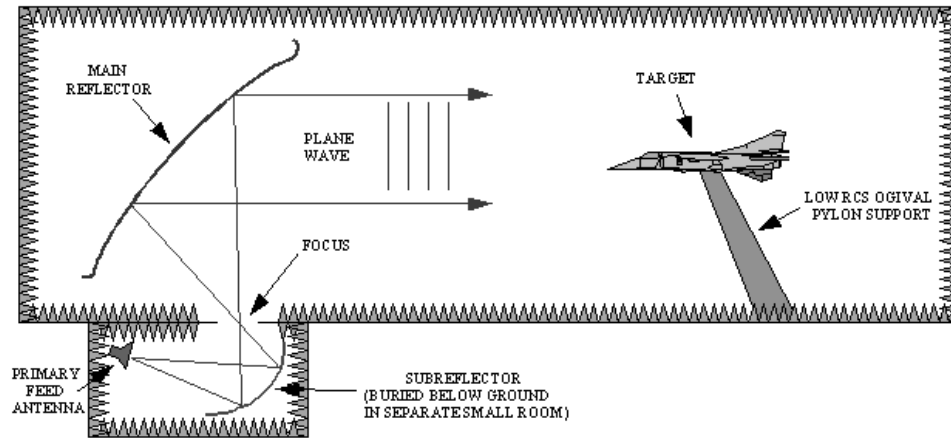
Figure 4.1: AFRL RCS Chamber Diagram. The two reflectors collimate the EM waves increasing quiet zone size [4].

Air Force Base (AFB). Figure 4.1 shows a diagram of AFRL's static indoor compact range. Figure 4.2 shows a photograph of the same chamber. The radar is located in a small room beneath the main chamber. A set of two reflectors redirect and collimate the transmitted/reflected EM waves, illuminating the target with approximately planar wavefronts. The target rotates on its mount, providing automated measurements at multiple orientation angles.

The final two RCS range types are built outdoors. A static outdoor far-field range is similar to its indoor counterpart except it does not have an enclosing structure. Outdoor ranges must deal with multipath echoes due to the reflection of target energy off the ground plane. Such a range must also periodically characterize the outdoor environment to account for changes in the target background. The primary advantage of a static outdoor far-field range, relative to its indoor counterpart, is the ability to use much larger targets. This utility comes at much greater expense and complexity. The National RCS Test Facility (NRTF) at Holloman AFB operates several ranges of this type. The second outdoor range type is the dynamic outdoor far-field range. Target RCS is measured in flight by a fixed radar on the ground. Air-dropped spheres provide calibration. This type of test is much more expensive than any of the three previous RCS data collections.

Figure 4.2:   AFRL RCS Chamber Photograph. The main reflector is visible in front of the target aircraft. The two people at the reflector's lower left corner indicate approximate scale [4].

4.2   Quiet Zone

The quiet zone is the RCS chamber region giving reliable far-field target RCS measurements [11, 73]. The approximately planar incident waves have the desirable properties of a uniform phase front and uniform amplitude independent of both angle and range. These properties greatly simplify the RCS measurement and ISAR imaging processes. The derivations in this section are only applicable to far-field RCS chambers like AFIT's.

The derivation of quiet zone dimensions requires a brief introduction to EM wave propagation principles. It is well known the Green's function Ψ describing the free-space electric field contribution from an elemental charge or source current is given by

$$\Psi = \frac{e^{-jkr}}{4\pi r},\tag{4.2}$$

where k (wave number) has the usual $k = 2\pi/\lambda$ definition and the radius r denotes the distance between the source and the observation point [10, 73]. The electric field

magnitude $|\bar{E}|$ is proportional to the product of this Green's function and the intensity of the source current I

$$|\bar{E}| \propto \frac{I}{r}. \tag{4.3}$$

This equation assumes $r \gg \lambda$, ensuring the field is composed of a purely radiated field.

In order to generate a plane wave, it is necessary to drive both $r \to \infty$ and $I \to \infty$. It is not possible to generate a plane wave within the confines of a finite chamber. None-the-less, it is possible to generate a good plane wave approximation over a finite region. Assuming the contributions from the chamber itself have been minimized, the size of this region is determined by a number of effects including:

1. Range attenuation of the incident wave

2. Non-uniform antenna pattern (e.g., finite beamwidth) of the radar antenna

3. Spherical phase variation of the incident wave

Figure 4.3 shows the top view of a hypothetical target in an ISAR chamber. Illumination is from the left. The quite zone dimensions determine maximum target depth D and width W, as explained in the following paragraphs.

The first non-ideal characteristic of RCS chamber radar waves is the range attenuation of the incident wave. As shown in (4.3), EM wave amplitude is proportional to $1/r$. Within an RCS chamber, a large target diameter may be a significant fraction of the range to the illuminating radar. In this case, the amplitude of the incident wave striking the target's front and back edges can be significantly different, artificially weighting the RCS measurements and scaling the eventual ISAR image. To keep this variation minimal, the maximum target depth D is usually kept small enough to ensure amplitude variation due to range differences is less than 1.0 dB [136].

Using this criterion, it is possible to derive the relationship between the range to the target center r_c and the target depth D. The first derivation step involves setting the ratio of the field magnitudes $|\bar{E}(r)|$ at the front and back of the target equal to
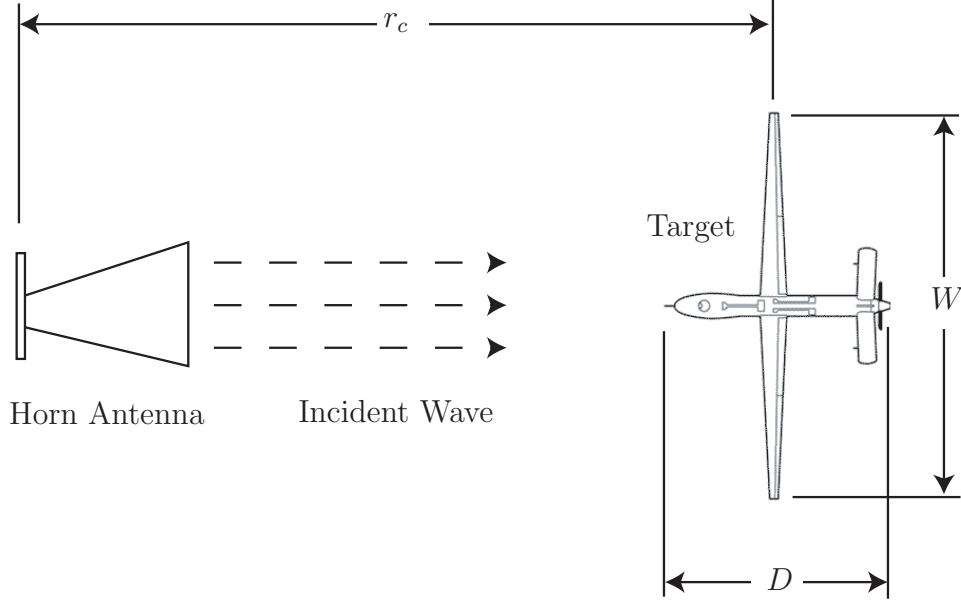
Figure 4.3: ISAR target depth D and width W viewed from above.

an arbitrary variable x. That is,

$$x = \frac{\left| \bar{E} \left(r_c - \frac{D}{2} \right) \right|}{\left| \bar{E} \left(r_c + \frac{D}{2} \right) \right|}. \tag{4.4}$$

Since $|\bar{E}(r)| \propto 1/r$ this equation can be rewritten as

$$x = \frac{r_c + \frac{D}{2}}{r_c - \frac{D}{2}}. \tag{4.5}$$

Solving for r_c yields

$$r_c = \frac{D}{2} \left(\frac{x+1}{x-1} \right). \tag{4.6}$$

Equation (4.4) is the ratio of the electric field strength between the front and back of the target. For a 1.0 dB allowable variation, the numerical value of x is given by $10^{0.05} \approx 1.13$, allowing evaluation of (4.6)

$$r_c \approx 8.7D. \tag{4.7}$$

Equation (4.7) implies the target's total range extent must be less 8.7 times the distance from the radar to the target center. AFIT's RCS chamber has $r_c = 27$ ft (8.23 m) implying D must be less than about 37 in (0.95 m).

The second effect that must be accounted for when determining quiet zone size is the non-uniform beamwidth of the illumination antenna. Because there is no known antenna structure which radiates uniformly in all directions, the transmitted amplitude varies as a function of angle [11]. Similar to the range amplitude variation, the angular amplitude variation must be less than a specified tolerance to assume plane wave target illumination. The angular variation limits the target width W. This effect is usually small compared to the cross range phase variation. For this reason, the angular antenna pattern is often ignored when deriving the quite zone.

The expected phase variation across the wavefront is usually the limitation factor on quite zone dimensions. The plane wave assumption used in traditional RCS chambers means waves striking two scattering elements at the same range location are assumed to be in phase regardless of the scatterers' cross range locations. However, the spherical nature of the Green's function Ψ indicates true phase varies according to both range and cross range locations.

Figure 4.4 illustrates the geometry used to derive phase variation effects. Total target width is denoted W and the range from the radar to the target center is denoted r_c. Using the Pythagorean Theorem, the range to the target's edge r_e is given by

$$r_e = \sqrt{r_c^2 + \left(\frac{W}{2}\right)^2}. \tag{4.8}$$

The range difference between the target center and target edge is

$$r_e - r_c = \sqrt{r_c^2 + \left(\frac{W}{2}\right)^2} - r_c. \tag{4.9}$$

Multiplying by $2\pi/\lambda$ converts this difference from distance to spatial frequency,

$$\frac{2\pi}{\lambda}(r_e - r_c) = \frac{2\pi}{\lambda}\left[\sqrt{r_c^2 + \left(\frac{W}{2}\right)^2}\right] - \frac{2\pi}{\lambda}r_c. \tag{4.10}$$

The left hand side is simply the maximum phase variation ϕ_{max}

$$\phi_{\mathrm{max}} = \frac{2\pi}{\lambda}\left[\sqrt{r_c^2 + \left(\frac{W}{2}\right)^2}\right] - \frac{2\pi}{\lambda}r_c. \tag{4.11}$$

Extracting r_c^2 from the square root operation gives

$$\phi_{\mathrm{max}} = \frac{2\pi}{\lambda}r_c\left[\sqrt{1 + \left(\frac{W}{2r_c}\right)^2} - 1\right]. \tag{4.12}$$

Assuming $r_c \gg W$ and using

$$\sqrt{1 + x} \approx 1 + \frac{x}{2}, \tag{4.13}$$

for small x gives

$$\phi_{\mathrm{max}} = \frac{2\pi}{\lambda}r_c\left[\frac{1}{8}\left(\frac{W}{r_c}\right)^2\right]. \tag{4.14}$$

Solving for r_c results in

$$r_c = \frac{\pi W^2}{4\lambda\phi_{\mathrm{max}}}. \tag{4.15}$$

Although the selection of ϕ_{max} is somewhat arbitrary, for most antennas, setting $\phi_{\mathrm{max}} = \pi/8$ rad gives good results over a wide variety of conditions [11, 73]. This value allows (4.15) to be simplified to

$$r_c = \frac{2W^2}{\lambda}. \tag{4.16}$$

Equation (4.16) is also known as the far-field requirement and states for a given target cross range width W, plane wave illumination may be assumed when $r_c \geq 2W^2/\lambda$ [73].

The same result applies in the vertical dimension, indicating maximum target height (H) is also determined by (4.16).

Combining the results of (4.7) and (4.16) defines the quiet zone dimensions as a box of depth D, width W, and height $H = W$. As long as the target is confined to this box, it is safe to assume plane wave illumination. For AFIT's RCS chamber, assuming a maximum frequency of 18 GHz and $r_c = 27$ ft (8.23 m) gives nominal quiet zone dimensions of $37.2 \times 10.3 \times 10.3$ in ($0.95D \times 0.26W \times 0.26H$ m). However, ISAR works by taking measurements over a collection of angles. Thus, guaranteeing the target remains confined to the quiet zone for any possible rotation angle in the range/cross range plane requires the true quiet zone be a cylinder inscribed within the rectangular box. Since $W < D$, the dimensions of this final quiet zone are cylindrical with both a height and diameter of $W = 10.3$ in (0.26 m).

4.3   AFIT's Indoor Far-Field RCS Chamber

The previous section derived the quiet zone size, determining the maximum target dimensions. This section introduces the RCS chamber hardware itself.

The radar system used in AFIT's chamber is the Lintek 4000. The Lintek 4000 system produces a series of single-frequency sinusoidal pulses used to sample the target response to individual frequencies. Table 4.1 lists critical Lintex 4000 radar parameters. The frequency range is 6-18 GHz. The radar has two channels, one used for monostatic collections, the other placed on a movable arm capable of receiving bistatic radar echoes. In the monostatic configuration, only Vertical transmit/Vertical receive (VV) and Horizontal transmit/Horizontal receive (HH) polarizations are possible (i.e., co-polarization), but using the bistatic configuration Vertical transmit/Horizontal receive (VH) and Horizontal transmit/Vertical receive (HV) polarization measurements are also possible (i.e., cross-polarization)[1]. The Pulse Repetition Frequency (PRF), range gate delay, and gate width are software selectable.

---

[1]Although the chamber can collect bistatic cross-polarization data, the calibration procedures introduced in this chapter are not applicable to the cross-polarization case.

Target Edge

r_e

$W/2$

Spherical Phase Front

r_c

Antenna

Target Center

$W/2$
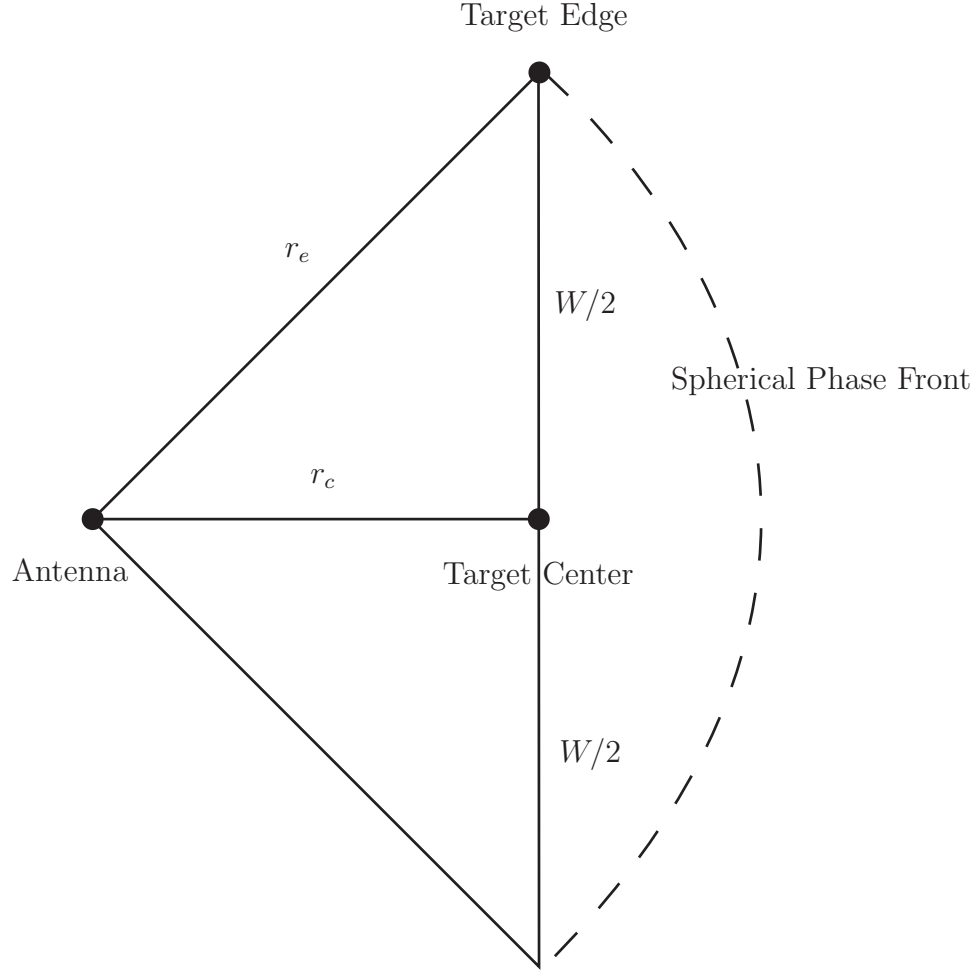
Figure 4.4:   Relationship between the range to target center r_c and the range to target edge r_e. The plane wave/far-field assumption used to derive the cross range quiet zone extent assumes $r_c \approx r_e$. However, as target width W increases, the true spherical nature of the EM waves/phase fronts invalidates this assumption, defining the quite zone boundary.

Table 4.1:   Lintek 4000 Parameters [2].

Parameter	Value
Frequency	6-18 GHz
Number of Channels	2
TX/RX Polarization	VV, HH, VH, HV
PRF	1.5 kHz - 10 MHz
Noise Figure	< 4.0 dB
Range Gate Delays	0-2.56 μsec
Gate Widths	5-1000 nsec
Rise Time	2 nsec
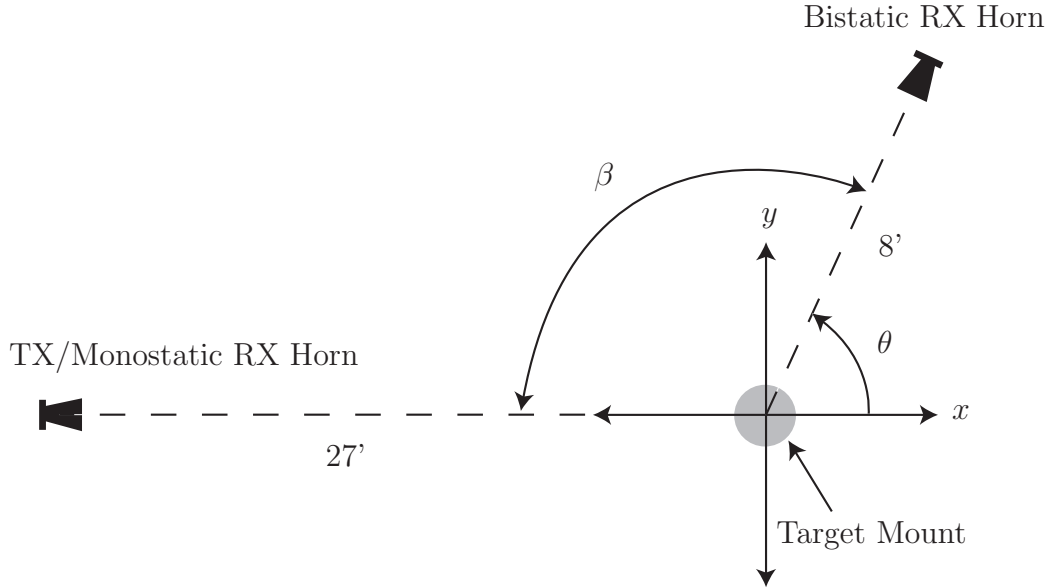
Figure 4.5: Top view of RCS chamber coordinate system. 2-D images are produced in the xy-plane, defined relative to the target mount center. The TX/Monostatic RX horn is at a fixed angle of 180° while the bistatic RX horn may be positioned at any angle θ in the xy-plane. The bistatic angle β is critical for determining the target's scatterer characteristics.

Figure 4.5 illustrates the coordinate system used to collect and process RCS data. The origin is at the target mount center. Angles are calculated relative to the x-axis. The Transmit (TX) / Monostatic Receive (RX) horn is fixed in both range (27') and angle (180°). The Bistatic RX horn is fixed in range (8') but can be rotated to an arbitrary angle θ in the xy-plane. The bistatic angle β denotes the angle between the TX and bistatic RX antennas.

Figure 4.6 shows the RCS chamber interior. The target is located on top of the ogive target pylon in the chamber's center. The target is mounted on a styrofoam block. Styrofoam is used because it is essentially invisible to the radar, allowing the target to appear as though it is simply floating above the pylon. The pylon's cross-section has an ogive (football-like) shape and is tipped towards the TX antenna. These two features minimize the pylon's RCS. The pylon also contains a stepper-motor used to rotate the target (and the styrofoam mount) during the data collection process. Towards the left side of the image is the bistatic arm topped with its horn

receiver[2]. This arm can be positioned anywhere in a 360° arc around the target mount, although care must be taken to minimize reflections from the arm itself, especially when $\theta \approx 180°$ and the bistatic arm shadows the target from transmitter illumination. Note, the target shown is significantly larger than the quiet zone, invalidating the far-field illumination assumption. This situation is addressed in Chapter V.

Figure 4.7 shows the horn used for transmission and monostatic reception. The horn is oriented diagonally to create a more narrow beam in the azimuth plane (i.e., range/cross range plane or xy-plane), keeping more of the radar energy away from the side walls. This horn is identical to the bistatic reception horn shown in Fig. 4.6.

Figures 4.8 and 4.9 illustrate the operator terminal and radar hardware respectively. The operator terminal provides the user interface to the Lintek 4000 software. The TV monitor provides a live video feed from the RCS chamber. The small black control box is used to control the monostatic antenna polarization. The computer rack contains the Hewlett-Packard signal generators and network analyzers used to generate and sample the radar waveforms. They are controlled from the operator terminal.

Pulse width and PRF are selected based on two competing requirements. First, the pulse must be short enough and the PRF must be low enough to prevent simultaneous transmission and reception. Second, the pulse must be long enough to simultaneously cover the entire target. Figure 4.10 shows how these requirements are balanced for a monostatic radar located a distance r_c from the target center with a target depth D. At time 0, the radar transmits pulse of duration τ. Time t_f corresponds to the beginning of the pulse echo from the target's front edge (closest to the radar). From times t_f to $t_f + \tau$, the echo from the target's front edge returns to the radar. To prevent simultaneous TX/RX, $\tau < t_f$. Times t_b to $t_b + \tau$ indicate when the echo from the target's back edge returns to the radar. Finally, at time $T = 1/\text{PRF}$, the entire process repeats. Again, to prevent simultaneous TX/RX, $t_b + \tau < T$. Note,

---

[2]The bistatic arm is capable of reception only, not transmission.
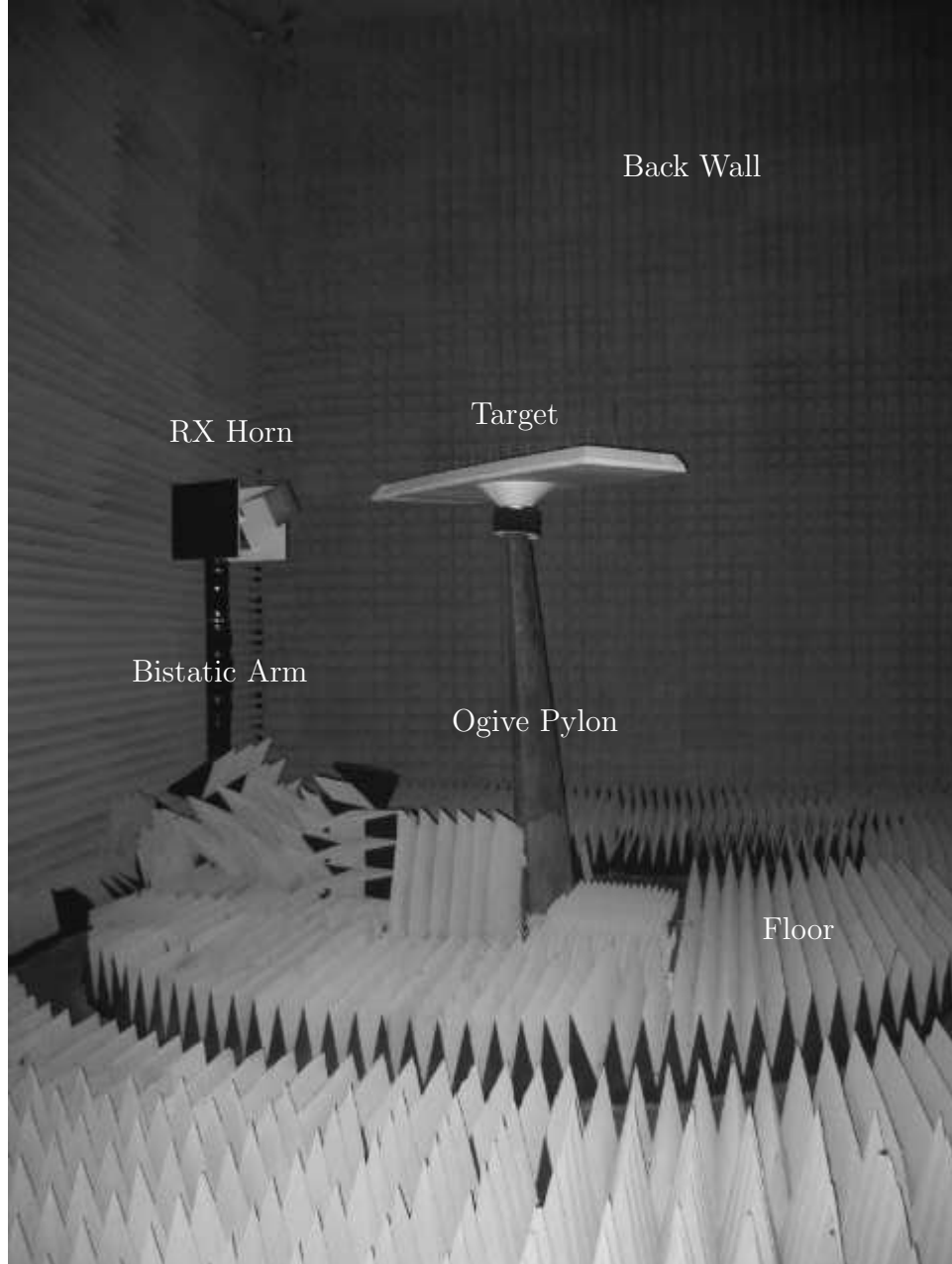
Figure 4.6:   AFIT's RCS chamber. Bistatic arm and horn receiver
at left. Sample target on styrofoam mount shown on top of ogive py-
lon. Chamber walls and floor covered by absorber. Note, the target
shown ($D \approx 5$ ft) is significantly larger than the quiet zone, invalidat-
ing the far-field illumination assumption. This situation is addressed
in Chapter V.
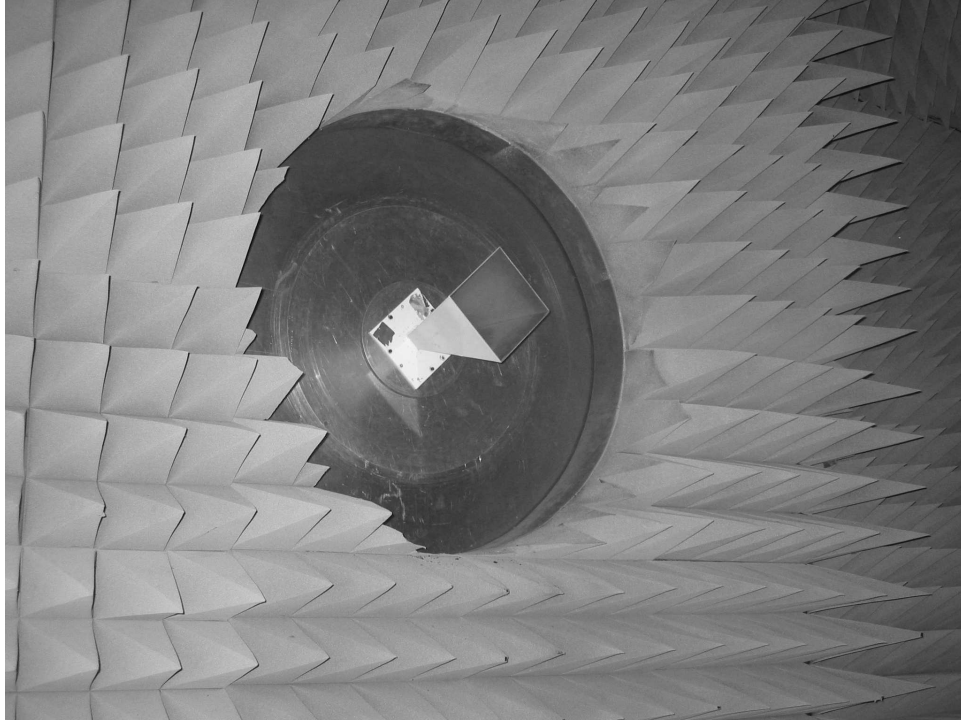
Figure 4.7: TX/monostatic RX horn for AFIT's RCS chamber. Diagonal orientation narrows the mainbeam in the xy-plane. Pyramidal absorber surrounds the antenna structure.

Figure 4.8:   Operator terminal for AFIT's RCS chamber. Computer screen display shows Lintek 4000 software. TV monitor shows live picture of RCS chamber. Black control box used to set TX horn polarization.
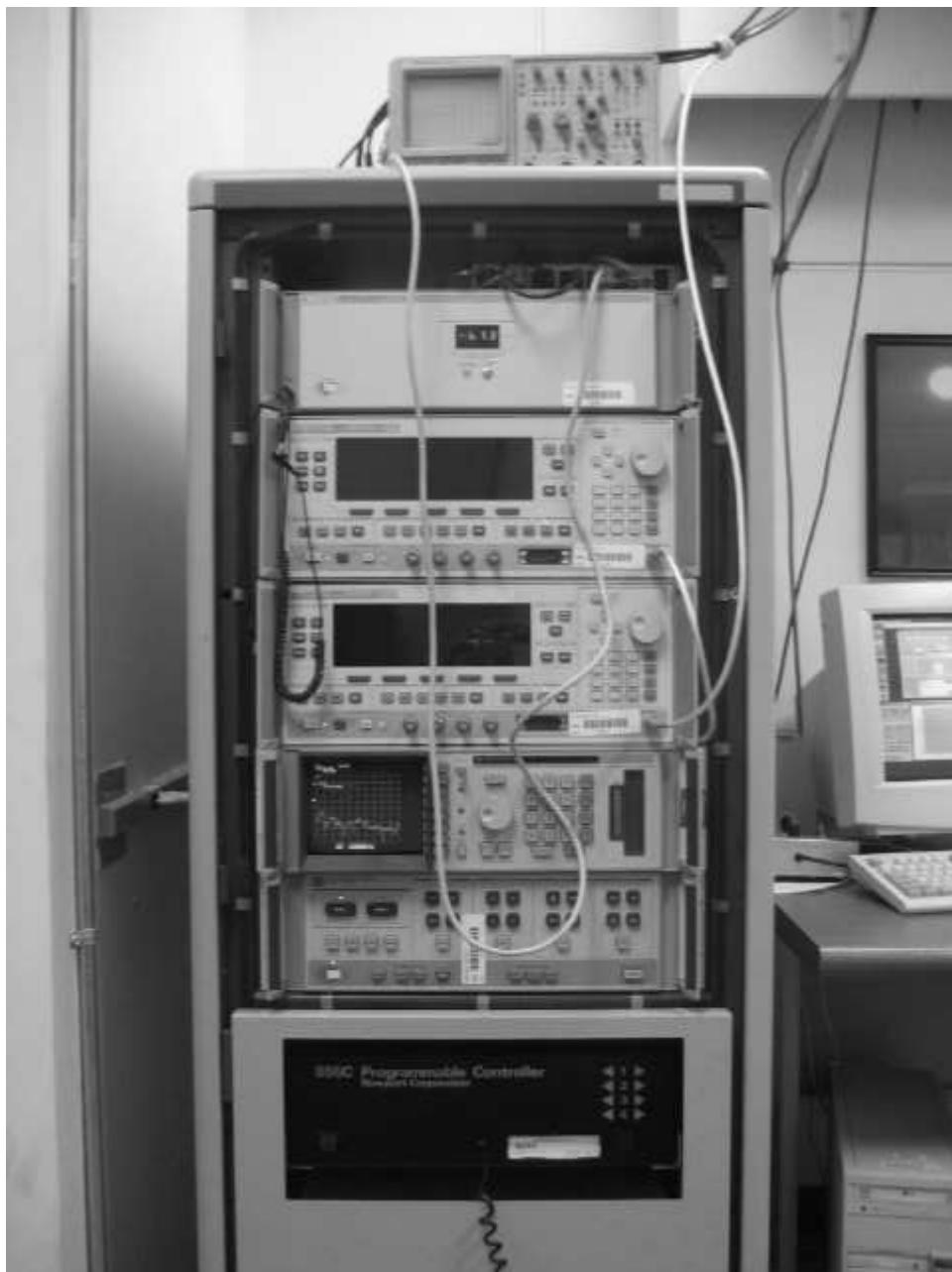
Figure 4.9:   HP signal generators for AFIT's RCS chamber.
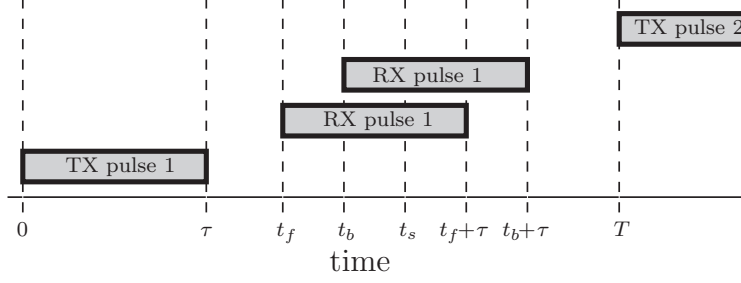
Figure 4.10:   RCS chamber timing requirements.

there is a period of time when echoes from the front and back of the target overlap. This overlap is critical since samples taken during this time provide the target response to Continuous Wave (CW) illumination at the given frequency. The radar collects a single complex sample of the echo at t_s, roughly the mid-point of the overlap, representing the target response to the given frequency with a single complex number. To ensure such an overlap exists, the total target length must not exceed $c\tau/2$. Table 4.2 shows the calculation of critical times in Fig. 4.10 in terms of r_c and D. The default setting of pulse width τ is 10 nsec. This selection supports a maximum depth of $D = c\tau/2 = 1.5$ meters. Note, D is significantly larger than the quiet zone depth implying any target within the quiet zone is simultaneously illuminated by a single radar pulse, ensuring a CW measurement for an appropriately chosen t_s.

Once the pulse width and PRF are selected, the user sets the gate width and range gate delay. The gate width controls the size of the hardware range gate, and it tells the receiver how long to record data from the target echoes. The range gate must be wide enough to capture sufficient return from the entire target, but short enough to reject unwanted echoes from the chamber's walls. The default value is 10 nsec, the same as the pulse width τ. The range gate delay determines how long after pulse transmission the radar begins recording data. The default value for monostatic collections is 87 nsec. This value is based not only on the round trip propagation time of the transmitted waveform ($\approx$ 55 nsec), but also on inherent delays in the radar hardware.

94

Table 4.2:   RCS Chamber timing requirements. Events must occur in the order listed. Figure 4.10 depicts these times graphically.

Time	Formula	Significance
0	n/a	begin pulse TX
τ	n/a	end pulse TX
t_f	$\frac{2r_c - D}{c}$	begin RX from target front
t_b	$\frac{2r_c + D}{c}$	begin RX from target back
t_s	$t_b < t_s < t_f + \tau$	radar samples target response
$t_f + \tau$	$\frac{2r_c - D}{c} + \tau$	end RX from target front
$t_b + \tau$	$\frac{2r_c + D}{c} + \tau$	end RX from target back
T	$\frac{1}{\text{PRF}}$	begin next pulse TX

With the basic hardware requirements and software settings determined, data collection can then proceed. This process, along with the associated calibration procedure, is covered in the next section.

4.4   Data Collection and Calibration

Section 4.1 indicated the goal of an RCS range is providing an approximation to free space where the given target's RCS characteristics can be measured without interference from the surrounding environment. In AFIT's indoor far-field range, a primary way of reducing the contribution from the floor, walls, and ceiling is coating them with appropriately shaped absorbing material to try and minimize reflections from these sources. This absorbing material is visible in Fig. 4.6. Despite these efforts, reflections from these sources still contribute significantly to the overall radar echoes. The use of hardware range gating also eliminates unwanted echo energy, but is only effective against radar echoes reaching the radar significantly before or after target echoes. Elimination of residual unwanted echo energy is accomplished using

a procedure called background subtraction [136]. This procedure drives the data collection process.

4.4.1 Data Collection Overview. RCS data collection begins by placing the target/styrofoam mount on the pylon. The desired frequency and azimuth values are programmed into the Lintek software before initiating the collection. Once started, the radar transmits a series of pulses at each frequency. Each pulse echo is sampled using In-phase Quadrature (I/Q) sampling to provide a complex sample. These pulse echoes are then integrated[3] to produce a single complex number proportional the target's scattered electric field E_s^{tar}. The radar performs the same procedure for each specified frequency.

After completing the frequency sweep, the radar must change its orientation with respect to the target. For monostatic or fixed bistatic collections (i.e., when β is constant throughout the collection), this orientation change is accomplished using the pylon's stepper motor to rotate the target directly. However, the Lintek software also precisely controls the bistatic arm's location, allowing data collection using a variable bistatic angle. Chapter V uses all three data collection geometries: monostatic, fixed bistatic, and variable bistatic.

Unfortunately, the E_s^{tar} measurements contain more than just scattered target energy. Despite the pains taken to minimize the contribution from the chamber, the background still forms a significant component of the E_s^{tar} measurements. To minimize this effect, an identical set of measurements are taken, this time with only the styrofoam mount, not the target. These measurements (E_s^{bkg}) represent the scattered electric field from the chamber background. Another pair of target/background measurements are then collected using a calibration target (E_s^{cal} and E_s^{cbk}) with an analytically known scattered field E_s^{ext}. These four files: target, target background, calibration target, and calibration target background, along with the calibration tar-

---

[3]The effects of thermal noise are greatly reduced by integrating the echoes from a number of pulses since target echoes add coherently while noise adds incoherently.

get's known scattering characteristics, provide the necessary data needed for RCS data calibration. The calibrated data can then be used for ISAR imaging.

4.4.2 Background Subtraction Procedure. Understanding the background subtraction process used for data calibration requires a more in-depth investigation of the interactions between the radar waves and the RCS chamber/target. This section examines the bistatic data calibration problem in the frequency domain since it allows scattering characteristics of the target and chamber to be treated as transfer functions.

Figure 4.11 (adapted from [67]) illustrates the frequency domain relationship between the transmitted and received radar pulses. This relationship applies to each of the four files: target, target background, calibration target, and calibration target background. The radar generates an initial transmitted electric field $E_{TX}(f)$. This field is passed through the transmission antenna, whose transfer function $H_{TX}(f)$ defines the incident field $E_i(f) = H_{TX}(f)E_{TX}(f)$. This incident field interacts with the target/chamber through three different transfer functions:

1. $H_T(f)$: the target's transfer function containing the desired target scattering information.

2. $H_B(f)$: the chamber background transfer function including returns from the chamber itself, the styrofoam target mount, and the ogive pylon.

3. $H_{TB}(f)$: the transfer function describing interactions between the target and the chamber background.

Note, the "target" in the $H_T(f)$ or $H_{TB}(f)$ transfer functions could refer either to the true ISAR imaging target or the calibration target depending on which file is being collected.

The scattered field $E_s(f)$, required for RCS measurement (see (4.1)), is defined as

$$E_s(f) = H_T(f)E_i(f) = H_T(f)H_{TX}(f)E_{TX}(f). \tag{4.17}$$
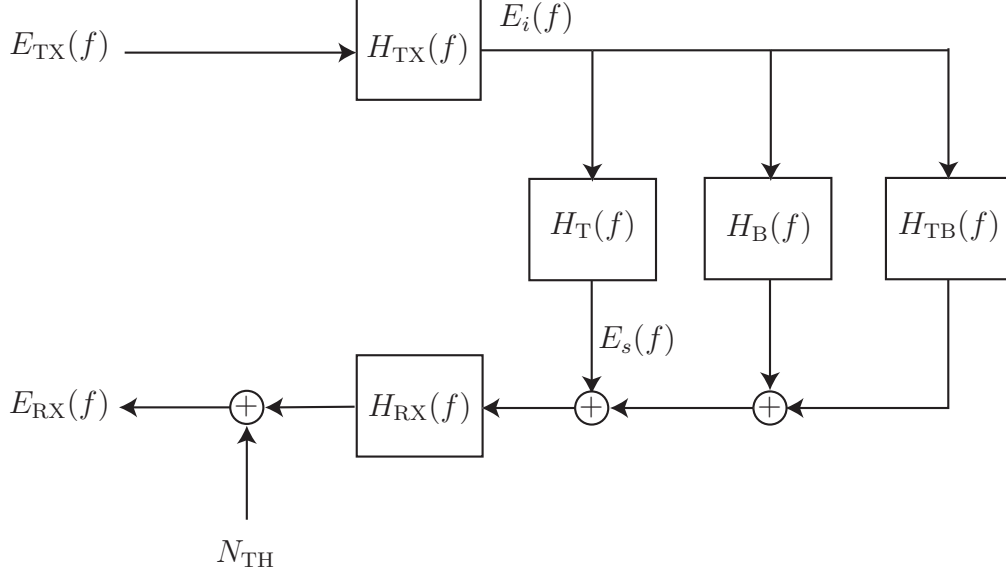
Figure 4.11: Frequency domain schematic of RCS data collection illustrating the relationship between the transmitted and received waveforms. Target scattering information is contained in the transfer function $H_T(f) = E_s(f)/E_i(f)$ (Adapted from [67]).

Unfortunately, the scattered field is combined with the results of the other two transfer functions $H_B(f)$ and $H_{TB}(f)$ before passing through the receive antenna transfer function $H_{RX}(f)$. Receiver thermal noise N_{TH} then corrupts the signal before the final field measurement $E_{RX}(f)$ is taken. Note, Fig. 4.11 ignores coupling between the transmit and receive antennas.

Using the schematic in Fig. 4.11, the measured data from each of the four files can be represented as

$$E_{RX}^{tar}(f) = \left[H_T^{tar}(f) + H_B^{tar}(f) + H_{TB}^{tar}(f) \right] H_{TX}(f) H_{RX}(f) E_{TX}(f) + N_{TH}^{tar}, \quad (4.18)$$

$$E_{RX}^{bkg}(f) = \left[H_T^{bkg}(f) + H_B^{bkg}(f) + H_{TB}^{bkg}(f) \right] H_{TX}(f) H_{RX}(f) E_{TX}(f) + N_{TH}^{bkg}, \quad (4.19)$$

$$E_{RX}^{cal}(f) = \left[H_T^{cal}(f) + H_B^{cal}(f) + H_{TB}^{cal}(f) \right] H_{TX}(f) H_{RX}(f) E_{TX}(f) + N_{TH}^{cal}, \quad (4.20)$$

$$E_{RX}^{cbk}(f) = \left[H_T^{cbk}(f) + H_B^{cbk}(f) + H_{TB}^{cbk}(f) \right] H_{TX}(f) H_{RX}(f) E_{TX}(f) + N_{TH}^{cbk}, \quad (4.21)$$

where the superscripts "tar," "bkg," "cal," and "cbk" refer to the target, target background, calibration target, and calibration target background files respectively. The functions $E_{\text{TX}}(f)$, $H_{\text{TX}}(f)$, and $H_{\text{RX}}(f)$ are assumed constant over all four files.

The calibration process begins by assuming thermal noise is negligible. This assumption is reasonable, since an arbitrary number of radar pulse echoes may be integrated during data collection. Typically, the use of 64 pulses (increasing the Signal-to-Noise Ratio (SNR) by $20 \log_{10}(\sqrt{64}) = 18.1$ dB) is sufficient for AFIT's chamber. The process proceeds by calculating the complex ratio ϑ for each complex I/Q value

$$\vartheta = \frac{E_{\text{RX}}^{\text{tar}}(f) - E_{\text{RX}}^{\text{bkg}}(f)}{E_{\text{RX}}^{\text{cal}}(f) - E_{\text{RX}}^{\text{cbk}}(f)}. \tag{4.22}$$

Plugging in the appropriate definitions from (4.18)-(4.21) yields

$$\vartheta = \frac{[H_{\text{T}}^{\text{tar}}(f) + H_{\text{B}}^{\text{tar}}(f) + H_{\text{TB}}^{\text{tar}}(f)] - \left[H_{\text{T}}^{\text{bkg}}(f) + H_{\text{B}}^{\text{bkg}}(f) + H_{\text{TB}}^{\text{bkg}}(f)\right]}{\left[H_{\text{T}}^{\text{cal}}(f) + H_{\text{B}}^{\text{cal}}(f) + H_{\text{TB}}^{\text{cal}}(f)\right] - \left[H_{\text{T}}^{\text{cbk}}(f) + H_{\text{B}}^{\text{cbk}}(f) + H_{\text{TB}}^{\text{cbk}}(f)\right]}, \tag{4.23}$$

where the common $E_{\text{TX}}(f)H_{\text{TX}}(f)H_{\text{RX}}(f)$ term has been canceled and noise terms ignored. Note,

$$H_{\text{T}}^{\text{bkg}}(f) = H_{\text{T}}^{\text{cbk}}(f) = 0. \tag{4.24}$$

$$H_{\text{TB}}^{\text{bkg}}(f) = H_{\text{TB}}^{\text{cbk}}(f) = 0, \tag{4.25}$$

since no "targets" are present during either background measurement. This result allows ϑ to be simplified to

$$\vartheta = \frac{[H_{\text{T}}^{\text{tar}}(f) + H_{\text{B}}^{\text{tar}}(f) + H_{\text{TB}}^{\text{tar}}(f)] - H_{\text{B}}^{\text{bkg}}(f)}{\left[H_{\text{T}}^{\text{cal}}(f) + H_{\text{B}}^{\text{cal}}(f) + H_{\text{TB}}^{\text{cal}}(f)\right] - H_{\text{B}}^{\text{cbk}}(f)}, \tag{4.26}$$

Furthermore,

$$H_{\text{B}}^{\text{tar}}(f) = H_{\text{B}}^{\text{bkg}}(f) \neq H_{\text{B}}^{\text{cal}}(f) = H_{\text{B}}^{\text{cbk}}(f). \tag{4.27}$$

Equation (4.27) states the chamber background transfer functions may differ between the true target and calibration target files since these targets may have different

styrofoam mounts. Using (4.27), (4.26) simplifies to

$$\vartheta = \frac{H_{\mathrm{T}}^{\mathrm{tar}}(f) + H_{\mathrm{TB}}^{\mathrm{tar}}(f)}{H_{\mathrm{T}}^{\mathrm{cal}}(f) + H_{\mathrm{TB}}^{\mathrm{cal}}(f)}. \tag{4.28}$$

The final and most critical assumption of the background subtraction process is that target/backround interactions may be ignored:

$$H_{\mathrm{TB}}^{\mathrm{tar}}(f) = H_{\mathrm{TB}}^{\mathrm{cal}}(f) = 0. \tag{4.29}$$

This assumption precludes accounting for any multipath interactions between the target and the mount. This limitation does not include multipath interactions between the target and the chamber walls, since the additional propagation distance for these paths places the multipath echoes outside the hardware range gate.

Applying (4.29), ϑ becomes

$$\vartheta = \frac{H_{\mathrm{T}}^{\mathrm{tar}}(f)}{H_{\mathrm{T}}^{\mathrm{cal}}(f)}. \tag{4.30}$$

The target transfer function definition, $H_{\mathrm{T}}(f) = E_s(f)/E_i(f)$, allows (4.30) to be rewritten as

$$\vartheta = \frac{E_s^{\mathrm{tar}}(f)}{E_s^{\mathrm{cal}}(f)}. \tag{4.31}$$

Recall that a target's RCS is defined as

$$\sigma = \lim_{r \to \infty} 4\pi r^2 \frac{|\bar{e} \cdot \bar{E}_s|^2}{|\bar{E}_i|^2}. \tag{4.32}$$

Using this definition, obtaining RCS measurements using the results of the background substraction process is simply a matter of multiplying (4.31) by an appropriately scaled version of the known calibration target scattering characteristics

$$\sigma = \lim_{r \to \infty} \left| 2\sqrt{\pi} r \vartheta \frac{E_s^{\mathrm{ext}}(f)}{E_i^{\mathrm{ext}}(f)} \right|^2, \tag{4.33}$$

where $E_s^{\text{ext}}(f)$ is the exact value of the calibration target's scattered field and $E_i^{\text{ext}}(f)$ is the incident field assumed during derivation of $E_s^{\text{ext}}(f)$ ($E_i^{\text{ext}}(f)$ is not necessarily equal to $E_i(f)$, the incident field strength used during data collection).

ISAR imaging requires complex data, but the definition of σ takes the magnitude of the appropriately scaled electric field ratios. This observation means the required scaled I/Q data output from the calibration process (denoted φ) is actually

$$\varphi = \lim_{r \to \infty} \left[2\sqrt{\pi} r \vartheta \, \frac{E_s^{\text{ext}}(f)}{E_i^{\text{ext}}(f)} \right], \tag{4.34}$$

where RCS is available as

$$\sigma = |\varphi|^2. \tag{4.35}$$

4.4.3   Calibration with a Conducting Sphere.   Having obtained ϑ from measured data, the final step in the calibration process is analytically determining $E_s^{\text{ext}}/E_i^{\text{ext}}$ for the calibration target. First and foremost, this requirement mandates a suitable calibration target. Although different calibration targets are used for many different circumstances, two key requirements dominate for the purposed of this research: availability of an exact scattering solution and insensitivity to calibration target misalignment errors. In both cases, the ideal solution is a conducting sphere. The bistatic scattered field can be analytically determined and its rotational invariance removes any concerns about sphere "orientation" during calibration data collection. The most significant limitation resulting from using a sphere for calibration is only co-polarization (i.e., HH and VV) measurements are possible. Cross-polarization measurements (i.e., HV and VH) are not feasible. The following analysis demonstrates this fact.

4.4.3.1   Scattered Field for a Plane Wave Illuminated Conducting Sphere. Scattered field equations for interactions between a plane wave and conducting sphere are derived in a number of sources [10, 59, 123]. The development presented here is excerpted from [59].
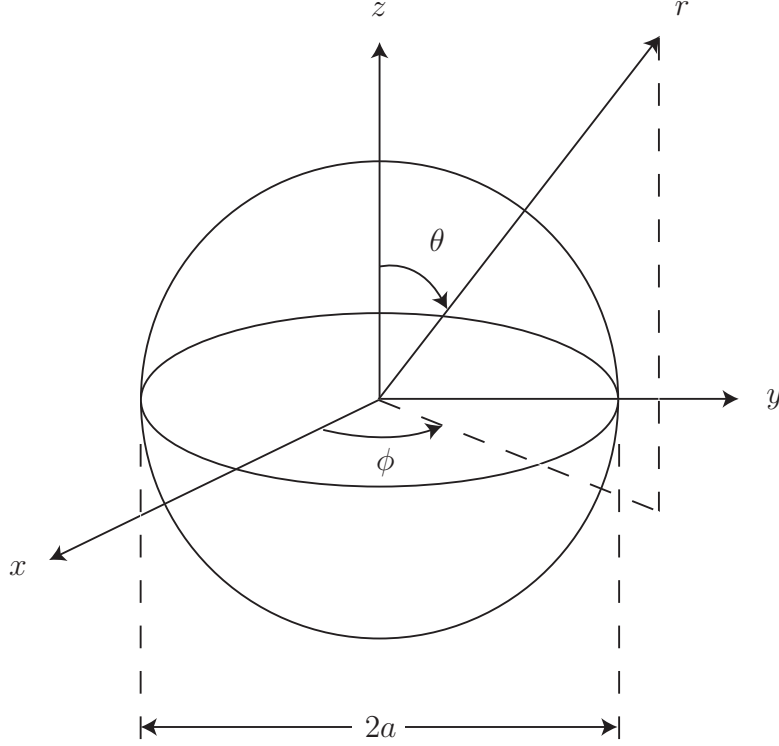
Figure 4.12: Spherical coordinate system for calculation of $\bar{E}_s$ from a conducting sphere of radius a illuminated by a plane wave whose electric field is x-directed and propagates in the z-direction.

First, it is necessary to define the relevant coordinate system. The scatter electric field vector $\bar{E}_s$ is presented in the spherical coordinate system illustrated by Fig. 4.12. An incident plane wave whose electric field orientation is defined in the x-direction and magnetic field orientation is defined in the y-direction illuminates a conducting sphere of radius a. These conventions lead to incident wave propagation in the $\bar{x} \times \bar{y} = \bar{z}$-direction, where $\times$ denotes cross product. The scattered field vector $\bar{E}_s$ at an arbitrary location (r, θ, ϕ) is defined by its spherical components $\bar{E}_s = [E_{s_r}, E_{s_\theta}, E_{s_\phi}]^{\mathrm{T}}$, where $[\cdot]^{\mathrm{T}}$ denotes a matrix transpose.

A complete scattered field derivation would unnecessarily complicate this section, but it is important to note, the scattered field solution is built around spherical

Bessel functions. Standard (e.g., cylindrical) Bessel functions are solutions to

$$x\frac{d}{dx}\left(x\frac{dy}{dx}\right) + (x^2 - n^2)y = 0, \tag{4.36}$$

where n denotes the equation's "order." Solutions to this equation are grouped into categories called "kinds." Solutions of the first kind are denoted $J_n(x)$, while solutions of the second kind are denoted $Y_n(x)$. For the scattering problem at hand, it is also useful into introduce Hankel functions of the second kind, defined as

$$H_n^{(2)}(x) = J_n(x) - jY_n(x). \tag{4.37}$$

The derivative of these solutions is given by

$$J_n'(x) = J_{n-1}(x) - \frac{n}{x}J_n(x) = -J_{n+1}(x) + \frac{n}{x}J_n(x) \tag{4.38}$$

and

$$H_n^{(2)'}(x) = H_{n-1}^{(2)}(x) - \frac{n}{x}H_n^{(2)}(x) = -H_{n+1}^{(2)}(x) + \frac{n}{x}H_n^{(2)}(x), \tag{4.39}$$

where the prime is used to indicate a derivative.

Since the scattering problem involved a spherical object, spherical Bessel functions are more appropriate than the cylindrical versions introduced thus far. Traditionally, spherical Bessel functions are written using the lowercase letters $j_n(x)$ and $h_n^{(2)}(x)$, respectively [1]. However, electromagnetics problems often use a slightly modified form of the spherical Bessel functions denoted [10, 59]

$$\hat{J}_n(x) = xj_n(x) = \sqrt{\frac{\pi x}{2}}J_{n+1/2}(x) \tag{4.40}$$

and

$$\hat{H}_n^{(2)}(x) = xh_n^{(2)}(x) = \sqrt{\frac{\pi x}{2}}H_{n+1/2}^{(2)}(x). \tag{4.41}$$

103

Another differential equation used in the scattered field derivation is the associated Legendré equation

$$\frac{1}{\sin\theta}\frac{d}{d\theta}\left(\sin\theta\frac{dy}{d\theta}\right) + \left[n(n+1) - \frac{m^2}{\sin^2\theta}\right]y = 0, \qquad (4.42)$$

for $0 \le \theta \le \pi$. The scattered field solution makes use of this equation's solutions, termed associated Legendré functions of the first kind. These solutions can be expressed as polynomials $P_n^m(u)$, determined recursively via

$$P_n^m(u) = (-1)^m(1-u^2)^{m/2}\frac{d^m P_n(u)}{du^m}, \qquad (4.43)$$

where

$$P_n(u) = \frac{1}{2^n n!}\frac{d^n}{du^n}(u^2-1)^n \qquad (4.44)$$

and ! indicates a factorial. Derivatives of these solutions are also required and can be calculated via

$$P_n^{m'}(u) = \frac{1}{1-u^2}\left[-nuP_n^m(u) + (n+m)P_{n-1}^m(u)\right]. \qquad (4.45)$$

Armed with the preceding mathematical machinery, it becomes possible to derive the asymptotic solution for the scattered field $\bar{E}_s = [E_{s_r}, E_{s_\theta}, E_{s_\phi}]^{\mathrm{T}}$ as [59]

$$\bar{E}_s^{\mathrm{ext}} = \begin{bmatrix} 0 \\ \frac{jE_i^{\mathrm{ext}}}{kr}e^{-jkr}\cos\phi\sum_{n=1}^{\infty}j^n\left[b_n\sin\theta P_n^{1'}(\cos\theta) - c_n\frac{P_n^1(\cos\theta)}{\sin\theta}\right] \\ \frac{jE_i^{\mathrm{ext}}}{kr}e^{-jkr}\sin\phi\sum_{n=1}^{\infty}j^n\left[b_n\frac{P_n^1(\cos\theta)}{\sin\theta} - c_n\sin\theta P_n^{1'}(\cos\theta)\right] \end{bmatrix}. \qquad (4.46)$$

where

$$b_n = -a_n\frac{\hat{J}_n'(ka)}{\hat{H}_n^{(2)'}(ka)}, \qquad (4.47)$$

$$c_n = -a_n\frac{\hat{J}_n(ka)}{\hat{H}_n^{(2)}(ka)}, \qquad (4.48)$$

104

and

$$a_n = \frac{j^{-n}(2n+1)}{n(n+1)}.$$ (4.49)

Using (4.46), the scattered electric field components at an arbitrary location can be found by plugging in the appropriate (r, θ, ϕ) values. Under the special case of monostatic illumination, when $\theta = \pi$, the $\sin \theta$ term evaluates to zero giving [59]

$$\lim_{\theta \to \pi} \frac{P_n^1(\cos \theta)}{\sin \theta} = \frac{(-1)^n}{2} n(n+1)$$ (4.50)

and

$$\lim_{\theta \to \pi} \sin \theta P_n^{1'}(\cos \theta) = \frac{(-1)^n}{2} n(n+1).$$ (4.51)

These relationships keep the scattered field equations well behaved in the monostatic case.

4.4.3.2 Co-polarization and Cross-polarization Conditions. Having obtained a generic expression for the scattered field vector $\bar{E}_s^{\text{ext}}$ at an arbitrary location, it now becomes possible to determine the *scalar* scattered field to the incident field ratio, as required by the calibration process

$$\frac{E_s^{\text{ext}}}{E_i^{\text{ext}}} = \frac{\bar{e} \cdot \bar{E}_s^{\text{ext}}}{E_i^{\text{ext}}}.$$ (4.52)

Each of the four polarization values (HH, HV, VV, VH) results in a different $\bar{e} \cdot \bar{E}_s^{\text{ext}}$ value.

Given a far-field conducting sphere of radius a, the *vector* scattered field $\bar{E}_s^{\text{ext}}$ is determined entirely by the incident (i.e., transmit) polarization. This result implies HH and HV polarizations share a common $\bar{E}_s^{\text{ext}}$ as do VV and VH polarizations. Figure 4.13 is adapted from Fig. 4.5 to illustrate the calibration scenario when the incident wave is horizontally polarized. This horizontal polarization defines the *xyz*-

105
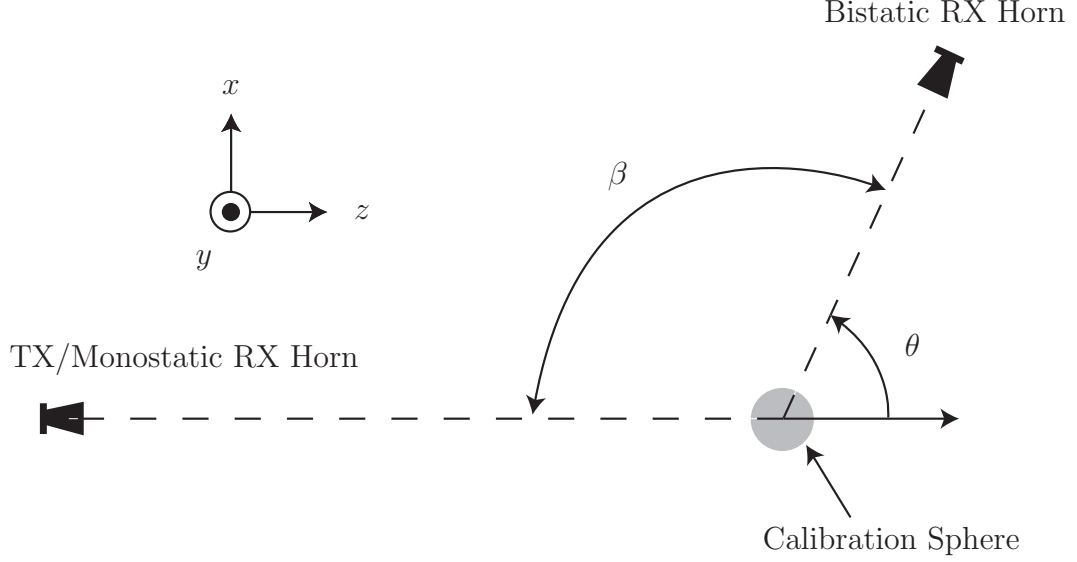
Figure 4.13: Calibration coordinate system for horizontally polarized incident waves. Incident wave propagation defines z-direction while incident wave E-field polarization defines x-direction. Co-planar relationship between the antennas and calibration sphere ensures $\phi = 0°$.

coordinate system with respect to the antennas and calibration target[4]. The incident field propagates in the z-direction and its E-field points in the x-direction. Using the definitions of θ and ϕ from Fig. 4.12, the fact the receive horn is confined to the xz-plane guarantees $\phi = 0°$. The angle θ, used here to define determine $\bar{E}_s$, is equivalent to the θ defining the angle between the image domain's x-axis and the bistatic horn location (Fig. 4.5).

Since $\phi = 0°$ for a horizontally polarized transmit wave, $\bar{E}_s^{\text{ext}} = [E_{s_r}^{\text{ext}}, E_{s_\theta}^{\text{ext}}, E_{s_\phi}^{\text{ext}}]^{\text{T}}$ immediately simplifies to

$$\bar{E}_s^{\text{ext}} = \begin{bmatrix} 0 \\ \frac{jE_i^{\text{ext}}}{kr}e^{-jkr}\sum_{n=1}^{\infty} j^n \left[b_n \sin\theta P_n^{1'}(\cos\theta) - c_n \frac{P_n^1(\cos\theta)}{\sin\theta} \right] \\ 0 \end{bmatrix}. \tag{4.53}$$

---

[4]This coordinate system, used only for calibration purposes, is different than the system shown in Fig. 4.5. Figure 4.5's definition is used throughout this document to define the image domain coordinates. Chapter V extends the image domain coordinate system to three dimensions.

The final piece of information needed to determine the scattered $E-$field collected at the receiver is the receiver's polarization vector $\bar{e} = [e_r, e_\theta, e_\phi]^\mathrm{T}$. In the co-polarized case (i.e., HH)

$$\bar{e} = \begin{bmatrix} 0 \\ 1 \\ 0 \end{bmatrix}, \tag{4.54}$$

indicating

$$\frac{E_s^{\mathrm{ext}}}{E_i^{\mathrm{ext}}} = \frac{j}{kr} e^{-jkr} \sum_{n=1}^{\infty} j^n \left[b_n \sin\theta P_n^{1\prime}(\cos\theta) - c_n \frac{P_n^1(\cos\theta)}{\sin\theta} \right]. \tag{4.55}$$

In the cross-polarized case (i.e., HV)

$$\bar{e} = \begin{bmatrix} 0 \\ 0 \\ 1 \end{bmatrix}, \tag{4.56}$$

indicating

$$\frac{E_s^{\mathrm{ext}}}{E_i^{\mathrm{ext}}} = 0. \tag{4.57}$$

Equation (4.57) says there is no scattered E-field energy received in HV polarization indicating calibration of HV data is not possible using a conducting sphere calibration target.

The calibration scenario for vertically polarized incident waves requires definition of a new coordinate system. As before, the incident wave propagation is in the z-direction and the E-field is x-directed, but this time $\phi = 90°$. The scattered field $\bar{E}_s^{\mathrm{ext}}$ becomes

$$\bar{E}_s^{\mathrm{ext}} = \begin{bmatrix} 0 \\ 0 \\ \frac{j E_i^{\mathrm{ext}}}{kr} e^{-jkr} \sum_{n=1}^{\infty} j^n \left[b_n \frac{P_n^1(\cos\theta)}{\sin\theta} - c_n \sin\theta P_n^{1\prime}(\cos\theta) \right] \end{bmatrix}. \tag{4.58}$$

The receiver's polarization vector $\bar{e}$ in the co-polarization case (i.e., VV) is

$$\bar{e} = \begin{bmatrix} 0 \\ 0 \\ -1 \end{bmatrix}, \tag{4.59}$$

resulting in

$$\frac{E_s^{\text{ext}}}{E_i^{\text{ext}}} = \frac{-j}{kr} e^{-jkr} \sum_{n=1}^{\infty} j^n \left[b_n \frac{P_n^1(\cos\theta)}{\sin\theta} - c_n \sin\theta P_n^{1'}(\cos\theta) \right]. \tag{4.60}$$

However, the angle θ used to define the angle between the bistatic horn and image domain x-axis is now equal to the negative of the angle θ used to calculate $\bar{E}_s^{\text{ext}}$. To rectify this situation a change of variables is performed. Making use of

$$\sin(-\theta) = -\sin\theta \tag{4.61}$$

and

$$\cos(-\theta) = \cos\theta, \tag{4.62}$$

the new expression for $\bar{E}_s^{\text{ext}}$ is given by

$$\frac{E_s^{\text{ext}}}{E_i^{\text{ext}}} = \frac{j}{kr} e^{-jkr} \sum_{n=1}^{\infty} j^n \left[b_n \frac{P_n^1(\cos\theta)}{\sin\theta} - c_n \sin\theta P_n^{1'}(\cos\theta) \right]. \tag{4.63}$$

In the cross-polarization case (i.e., VH)

$$\bar{e} = \begin{bmatrix} 0 \\ -1 \\ 0 \end{bmatrix}, \tag{4.64}$$

leading to

$$\frac{E_s^{\text{ext}}}{E_i^{\text{ext}}} = 0. \tag{4.65}$$

108
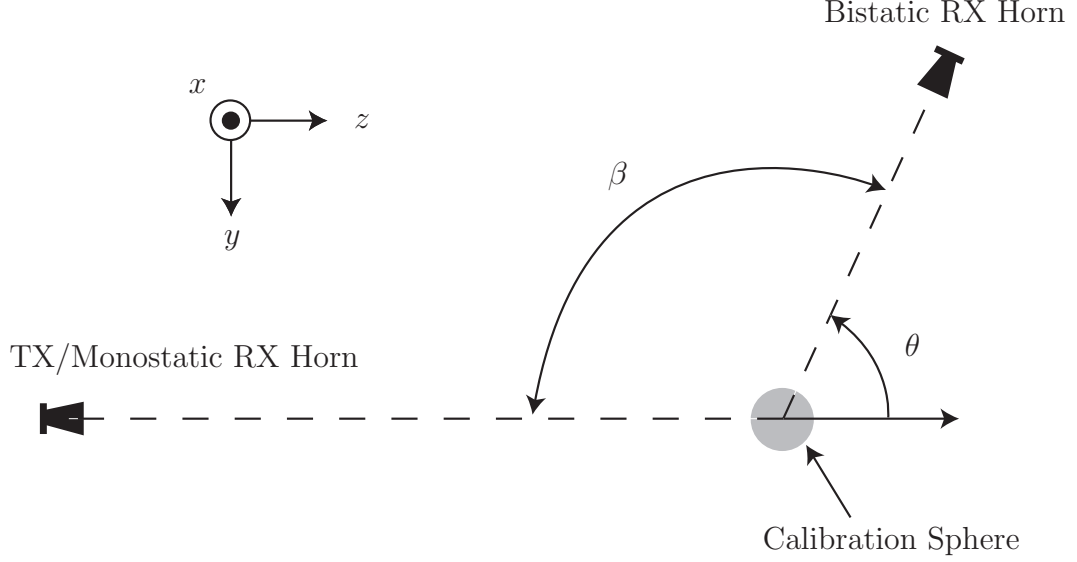
Figure 4.14: Calibration coordinate system for vertically polarized incident waves. Incident wave propagation defines z-direction while incident wave E-field is x-directed. Co-planar relationship between the antennas and calibration sphere ensures $\phi = 90°$.

As in the HV case, VH polarization measurements cannot be calibrated using a conducting sphere calibration target. Figure 4.14 illustrates the coordinate system for vertically polarized incident waves.

In summary, the calibration process begins by collecting four I/Q data files. These files contain complex scalar values representing the received fields for the target $E_{\mathrm{RX}}^{\mathrm{tar}}$, target background $E_{\mathrm{RX}}^{\mathrm{bkg}}$, spherical calibration target $E_{\mathrm{RX}}^{\mathrm{cal}}$, and calibration target background $E_{\mathrm{RX}}^{\mathrm{cbk}}$. These samples are combined via (from (4.22) and (4.34))

$$\varphi = \lim_{r \to \infty} \left[2\sqrt{\pi} r \cdot \frac{E_{\mathrm{RX}}^{\mathrm{tar}} - E_{\mathrm{RX}}^{\mathrm{bkg}}}{E_{\mathrm{RX}}^{\mathrm{cal}} - E_{\mathrm{RX}}^{\mathrm{cbk}}} \cdot \frac{E_s^{\mathrm{ext}}}{E_i^{\mathrm{ext}}} \right], \tag{4.66}$$

where $E_s^{\mathrm{ext}}/E_i^{\mathrm{ext}}$ is determined by (4.55) for HH polarization and by (4.63) for VV polarization. In both cases the r in (4.66) cancels the $1/r$ term in $E_s^{\mathrm{ext}}/E_i^{\mathrm{ext}}$. Combining this realization with the fact that the $\exp(-jkr)$ factor in $E_s^{\mathrm{ext}}/E_i^{\mathrm{ext}}$ represents a unit-amplitude phase constant, the limit in (4.66) may be ignored, yielding calibrated complex I/Q data. The real RCS value σ at a given frequency/orientation is available

as the magnitude squared of φ (4.35). Calibration of cross-polarization measurements is not possible using these procedures and calibration targets. Cross-polarization calibration information is available in [21, 95].

4.5 Summary

Data collection and calibration is a major component of the research validation process. This chapter develops these methods for AFIT's RCS chamber, used to collect all the research effort's ISAR data. It began by reviewing the major RCS data collection facility types. It then focused on AFIT's indoor far-field range, highlighting the specific facility capabilities and limitations. The chapter then detailed the background subtraction process used to calibrate the target scattering data. While the calibration procedures are not new to the RCS measurement community, they are new to AFIT, and correct for more than 10.0 dB of error in previous bistatic calibration methods. Appendix B contains the `Matlab`® code used for data calibration. In addition to the ISAR images shown in Chapters V and IX, this code produced the calibrated data previously reported in [43, 76].

V. 3-D Near-Field Bistatic SAR/ISAR Image Formation

The primary goal of this chapter is developing and demonstrating new Synthetic Aperture Radar (SAR)/Inverse Synthetic Aperture Radar (ISAR) data processing techniques capable of focusing Two-Dimensional (2-D) or Three-Dimensional (3-D) SAR/ISAR images using a general radiative near-field bistatic data collection scenario. Defocusing caused by radiative near-field effects is simply another name for the Range Migration (RM) issue introduced in Chapter II. In addition to solving the radiative near-field problem, the algorithm presented accounts for non-uniform data collection geometries and warped ground planes. The result is a SAR/ISAR algorithm capable of precisely focusing Wide-Angle Multistatic Synthetic Aperture Radar (WAM-SAR) data.

This chapter begins by rigorously deriving the relationship between the image domain (containing the scene or target) and the spatial frequency domain. This development uses an arbitrary 3-D far-field bistatic collection geometry. Section 5.2 derives a 3-D SAR/ISAR image generation technique based on tomographic back-projection principles. Unlike other methods, this approach fully accounts for variable bistatic geometries where the spatial relationship between the transmitter and receiver changes on a pulse-to-pulse basis. Section 5.3 derives 3-D SAR/ISAR resolutions from a spatial frequency perspective. This derivation corrects errors in the current literature [108][1]. It also develops a resolution-like metric which quantifies expected image quality without resorting to traditional narrow-angle or narrowband assumptions. The derivations in Sec. 5.1-5.3 are validated using actual ISAR data in Sec. 5.4. A sample target's theoretical spatial frequency response is compared to the measured results using a variety of collection geometries. ISAR images are also examined along with their resolutions. Section 5.5 removes the restrictive far-field assumptions resulting in the final 3-D near-field bistatic imaging algorithm. This

---

[1] The relevant citation correctly accounts for bistatic effects on range resolution, but not in horizontal or vertical cross range resolution.

algorithm is validated in Sec. 5.6 using three different ISAR collections representing three distinct SAR/ISAR scenarios.

It should be noted near-field Radar Cross Section (RCS) chamber effects can only be observed in a far-field-type RCS chamber, similar to the one operated by the Air Force Institute of Technology (AFIT). The additional reflectors present in a compact RCS chamber eliminate the spherical wave near-field effects. While helpful for traditional RCS measurement purposes, this feature is inappropriate for the research effort, since it removes ability to test RM correction using laboratory-based ISAR processing.

5.1 Spatial Frequency Domain Data Representation

The SAR/ISAR scene exists in the 3-D image domain represented by $f(x, y, z)$. SAR image formation has traditionally been based on a Doppler perspective using the Doppler shift in radar echoes caused by radar platform motion to derive SAR processing techniques [23]. However, for RCS chamber-based ISAR, data is usually collected when neither the radar nor the target are moving. The target is rotated between transmission/reception of radar waveforms. Under these circumstances, there is no Doppler shift, necessitating a different processing paradigm. Unifying both SAR and ISAR is possible using the tomographic paradigm from the medical imaging community [99]. This approach lends itself to representation of radar data in the 3-D spatial frequency domain $F(k_x, k_y, k_z)$ defined as the 3-D Fourier Transform (FT) of $f(x, y, z)$ [65]. This section examines a how data collected from a general 3-D bistatic SAR/ISAR geometry can be mapped into the spatial frequency domain, leading to SAR/ISAR processing techniques built around the Fourier transform.

5.1.1 SAR/ISAR Data Collection Geometry. Using the start-stop approximation, the SAR/ISAR data collection geometry for a single Coherent Processing Interval (CPI) pulse can be represented as in Fig. 5.1. The scene center is defined as $(0, 0, 0)$ in a right-hand cartesian coordinate system. Unit vectors $\bar{u}_{\text{TX}}$ and $\bar{u}_{\text{RX}}$

point from the origin to the radar transmission and reception platforms, respectively. Analytically, these unit vectors are

$$\bar{u}_{\text{TX}} = \begin{bmatrix} \cos(\theta_{\text{TX}}) \cos(\phi_{\text{TX}}) \\ \sin(\theta_{\text{TX}}) \cos(\phi_{\text{TX}}) \\ \sin(\phi_{\text{TX}}) \end{bmatrix} \tag{5.1}$$

and

$$\bar{u}_{\text{RX}} = \begin{bmatrix} \cos(\theta_{\text{RX}}) \cos(\phi_{\text{RX}}) \\ \sin(\theta_{\text{RX}}) \cos(\phi_{\text{RX}}) \\ \sin(\phi_{\text{RX}}) \end{bmatrix}, \tag{5.2}$$

where θ_{TX} (θ_{RX}) is the azimuth angle to the transmission (reception) platform, measured relative to the x-axis, and ϕ_{TX} (ϕ_{RX}) is the elevation angle to the transmission (reception) platform, measured from the xy-plane. The angle between $\bar{u}_{\text{TX}}$ and $\bar{u}_{\text{RX}}$ is known as the bistatic angle β. The unit vector $\bar{u}_b$ bisects β and is given by

$$\bar{u}_b = a\left(\bar{u}_{\text{TX}} + \bar{u}_{\text{RX}}\right) = \begin{bmatrix} \cos(\theta_b) \cos(\phi_b) \\ \sin(\theta_b) \cos(\phi_b) \\ \sin(\phi_b) \end{bmatrix}, \tag{5.3}$$

where a is a normalization constant. In general, $\theta_b \neq (\theta_{\text{TX}} + \theta_{\text{RX}})/2$ and $\phi_b \neq (\phi_{\text{TX}} + \phi_{\text{RX}})/2$.

5.1.2 Bistatic Angle Effects on Far-Field Range. Under the far-field assumption, the radar platform transmits (receives) a uniform plane wave at the same orientation angles θ and ϕ to (from) every point (x, y, z) in the scene. This approximation allows the far-field range r_{TX} (r_{RX}) from the origin to each point (x, y, z) to be calculated as the dot product of the vector $\bar{\rho} = [x, y, z]^{\text{T}}$ (note $[\cdot]^{\text{T}}$ denotes a matrix transpose) with the unit vector $\bar{u}_{\text{TX}}$ ($\bar{u}_{\text{RX}}$),

$$r_{\text{TX}} = \bar{\rho} \cdot \bar{u}_{\text{TX}} = [x \cos(\theta_{\text{TX}}) \cos(\phi_{\text{TX}}) + y \sin(\theta_{\text{TX}}) \cos(\phi_{\text{TX}}) + z \sin(\phi_{\text{TX}})] \tag{5.4}$$
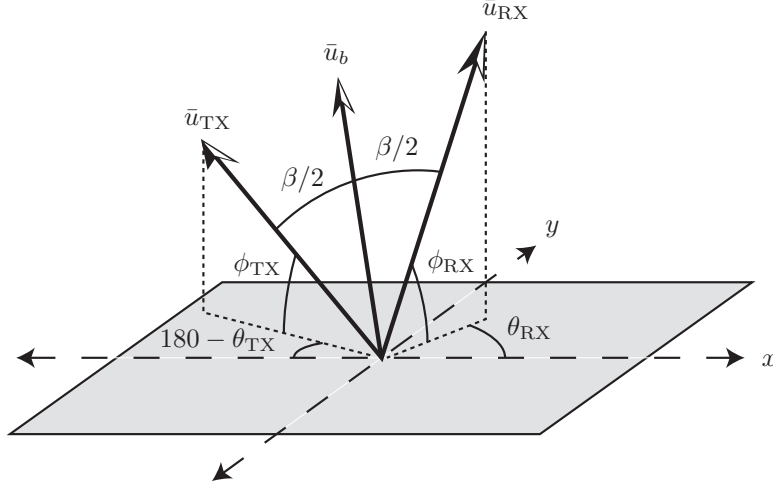
Figure 5.1:   3-D bistatic SAR/ISAR collection geometry. The unit vectors $\bar{u}_\text{TX}$ and $\bar{u}_\text{RX}$ point from the scene center towards the transmission and reception platforms, respectively. The bistatic angle β between these two vectors is bisected by the unit vector $\bar{u}_b$.

and

$$r_\text{RX} = \bar{\rho} \cdot \bar{u}_\text{RX} = \left[x \cos(\theta_\text{RX})\cos(\phi_\text{RX}) + y\sin(\theta_\text{RX})\cos(\phi_\text{RX}) + z\sin(\phi_\text{RX})\right], \qquad (5.5)$$

where $\cdot$ indicates the dot product. The set of points sharing a common r_TX (r_RX) value form a plane defined by the unit normal $\bar{u}_\text{TX}$ ($\bar{u}_\text{RX}$).

Using (5.1)-(5.3), along with dot product and cross product definitions, allows calculation of the triple product of $\bar{u}_{TX}$, $\bar{u}_{RX}$, and $\bar{u}_b$ as

$$
\begin{aligned}
\bar{u}_{TX} \times \bar{u}_{RX} \cdot \bar{u}_b \;=\; & a\,[\sin(\theta_{TX})\cos(\phi_{TX})\sin(\phi_{RX})\cos(\theta_{TX})\cos(\phi_{TX}) \\
& + \sin(\theta_{TX})\cos(\phi_{TX})\sin(\phi_{RX})\cos(\theta_{RX})\cos(\phi_{RX}) \\
& - \sin(\phi_{TX})\sin(\theta_{RX})\cos(\phi_{RX})\cos(\theta_{TX})\cos(\phi_{TX}) \\
& - \sin(\phi_{TX})\sin(\theta_{RX})\cos(\phi_{RX})\cos(\theta_{RX})\cos(\phi_{RX}) \\
& + \sin(\phi_{TX})\cos(\theta_{RX})\cos(\phi_{RX})\sin(\theta_{TX})\cos(\phi_{TX}) \\
& + \sin(\phi_{TX})\cos(\theta_{RX})\cos(\phi_{RX})\sin(\theta_{RX})\cos(\phi_{RX}) \\
& - \cos(\theta_{TX})\cos(\phi_{TX})\sin(\phi_{RX})\sin(\theta_{TX})\cos(\phi_{TX}) \\
& - \cos(\theta_{TX})\cos(\phi_{TX})\sin(\phi_{RX})\sin(\theta_{RX})\cos(\phi_{RX}) \\
& + \cos(\theta_{TX})\cos(\phi_{TX})\sin(\theta_{RX})\cos(\phi_{RX})\sin(\phi_{TX}) \\
& + \cos(\theta_{TX})\cos(\phi_{TX})\sin(\theta_{RX})\cos(\phi_{RX})\sin(\phi_{RX}) \\
& - \sin(\theta_{TX})\cos(\phi_{TX})\cos(\theta_{RX})\cos(\phi_{RX})\sin(\phi_{TX}) \\
& - \sin(\theta_{TX})\cos(\phi_{TX})\cos(\theta_{RX})\cos(\phi_{RX})\sin(\phi_{RX})]= 0, \quad (5.6)
\end{aligned}
$$

where $\times$ denotes the cross product. Equation (5.6) guarantees $\bar{u}_{TX}$, $\bar{u}_{RX}$, and $\bar{u}_b$ are coplanar. This observation implies the relationship between $\bar{u}_{TX}$, $\bar{u}_{RX}$, and $\bar{u}_b$ can be studied in the 2-D plane defined by $\bar{u}_{TX} \times \bar{u}_{RX}$ without loss of generality. Using this new $x'y'$-plane, the corresponding 2-D unit vectors $\bar{u}'_{TX}$, $\bar{u}'_{RX}$, and $\bar{u}'_b$ allow definition of r'_{TX} and r'_{RX} as

$$
r'_{TX} = x'\cos(\varphi_{TX}) + y'\sin(\varphi_{TX}) \tag{5.7}
$$

and

$$
r'_{RX} = x'\cos(\varphi_{RX}) + y'\sin(\varphi_{RX}), \tag{5.8}
$$

where the φ_{TX} and φ_{RX} are measured with respect to the x'-axis.

Calculating bistatic angle β effects on the observed far-field range r_b' begins by defining r_b' as one half the total distance traveled by the radar waveform

$$r_b' = \frac{1}{2}\left(r_{\mathrm{TX}}' + r_{\mathrm{RX}}'\right). \tag{5.9}$$

Substitution of (5.7) and (5.8) into (5.9) and collecting terms gives

$$r_b' = \frac{1}{2}\left\{ x'\left[\cos\left(\varphi_{\mathrm{TX}}\right) + \cos\left(\varphi_{\mathrm{RX}}\right)\right] + y'\left[\sin\left(\varphi_{\mathrm{TX}}\right) + \sin\left(\varphi_{\mathrm{RX}}\right)\right]\right\}. \tag{5.10}$$

Note that [145]

$$\cos(\alpha) + \cos(\gamma) = 2\cos\left(\frac{\alpha + \gamma}{2}\right)\cos\left(\frac{\alpha - \gamma}{2}\right) \tag{5.11}$$

and

$$\sin(\alpha) + \sin(\gamma) = 2\sin\left(\frac{\alpha + \gamma}{2}\right)\cos\left(\frac{\alpha - \gamma}{2}\right). \tag{5.12}$$

Applying (5.11) and (5.12) to (5.10) gives

$$r_b' = \left[x'\cos\left(\frac{\varphi_{\mathrm{TX}} + \varphi_{\mathrm{RX}}}{2}\right) + y'\sin\left(\frac{\varphi_{\mathrm{TX}} + \varphi_{\mathrm{RX}}}{2}\right)\right]\cos\left(\frac{\varphi_{\mathrm{TX}} - \varphi_{\mathrm{RX}}}{2}\right). \tag{5.13}$$

Unlike the general 3-D case, in two dimensions $\varphi_b = (\varphi_{\mathrm{TX}} + \varphi_{\mathrm{RX}})/2$. This fact, combined with the definition of the bistatic angle β, allows (5.13) to be rewritten as

$$r_b' = \left[x'\cos(\varphi_b) + y'\sin(\varphi_b)\right]\cos(\beta/2). \tag{5.14}$$

Generalizing to three dimensions, the apparent far-field range r_b from a vantage point defined by $\bar{u}_b$ to any location (x, y, z), may be calculated as

$$r_b = \left[x\cos(\theta_b)\cos(\phi_b) + y\sin(\theta_b)\cos(\phi_b) + z\sin(\phi_b)\right]\cos(\beta/2). \tag{5.15}$$

This result can also be derived graphically [65] or using a Taylor expansion [30]. The effective compression of range values by the bistatic angle has significant consequences

for both the image formation process and the eventual image resolution. Subsequent sections demonstrate these effects.

5.1.3 Spatial Frequency Domain.   At each CPI location, a matched filter-based SAR system generates a complex-valued range profile $p(r)$ denoting the strength of the radar waveform echoes as a function of range[2]. On the other hand, RCS chamber-based ISAR systems usually provide data directly in the frequency domain $P(k_r)$. These data products are related through the One-Dimensional (1-D) FT

$$P(k_r) = \mathcal{F}\left[p(r)\right] = \int_{-\infty}^{\infty} p(r) \exp\left(-jk_r r\right) \mathrm{d}r, \qquad (5.16)$$

where $\mathcal{F}$ denotes the FT, r is the range in meters, $k_r = 4\pi/\lambda$ is the spatial frequency value in radians/meter (twice the typical $2\pi/\lambda$ definition to account for two-way wave propagation), and λ is transmitted/received wavelength in meters.

According to (5.15), using a bistatic collection geometry compresses the range r_b. Undoing this compression, and thus obtaining the equivalent monostatic far-field range, involves scaling r_b by the constant $a = 1/\cos(\beta/2)$. However, it is well known that scaling the data in one domain by the constant a scales the data in the other domain by the constant $1/a$ [64]. This relationship indicates even though the transmitted/received frequencies determine the k_r values, the actual data acquired corresponds to spatial frequency values $k_r \cos(\beta/2)$.

Under the start-stop approximation, each CPI pulse provides a range profile for a specific look direction $\bar{u}_b$. As $\bar{u}_b$ changes throughout the CPI, subsequent pulses provide scene information from other angles. Representing this data in the spatial frequency domain requires extending the 1-D FT in (5.16) to a 3-D version,

$$F(k_x, k_y, k_z) = \int_{-\infty}^{\infty} \int_{-\infty}^{\infty} \int_{-\infty}^{\infty} f(x, y, z) \exp\left[-j(k_x x + k_y y + k_z z)\right] \mathrm{d}x \mathrm{d}y \mathrm{d}z. \quad (5.17)$$

---

[2]Chapter III used $\hat{p}(r)$ to denote the radar's estimate of the true range profile $p(r)$. In this chapter, all data is estimated. The ˆ notation is dropped for convenience.

Given a range profile $p(r)$ and the corresponding spatial frequency data $P(k_r)$, the goal is to represent this information in the full 3-D spatial frequency domain $F(k_x, k_y, k_z)$. The rotational property of Fourier transforms states rotation by an arbitrary angle in the image domain $f(x, y, z)$ is equivalent to rotation by the same angle in the transform domain $F(k_x, k_y, k_z)$ [64]. This property means for a sample at a given (k_r, θ_b, ϕ_b) value, the corresponding frequency domain location (k_x, k_y, k_z) is determined by

$$k_x = k_r \cos(\theta_b) \cos(\phi_b) \cos(\beta/2), \tag{5.18}$$

$$k_y = k_r \sin(\theta_b) \cos(\phi_b) \cos(\beta/2), \tag{5.19}$$

and

$$k_z = k_r \sin(\phi_b) \cos(\beta/2). \tag{5.20}$$

Thus, range profiles from individual CPI pulses can be mapped into the spatial frequency domain by first taking their 1-D Fourier transform and mapping the resultant $P(k_r)$ data samples onto the 3-D domain using (5.18)-(5.20).

5.2 Far-Field SAR/ISAR Image Formation

Section 5.1 showed how to map SAR/ISAR data into the 3-D spatial frequency domain. This section demonstrates how this data can be converted into a far-field scene estimate $f(x, y, z)$.

The FT relationship between $f(x, y, z)$ and $F(k_x, k_y, k_z)$ suggests effective imaging algorithms can be built using multidimensional FT techniques. While the two imaging techniques highlighted in this section are based on Fourier processing principles, it is important to mention that many non-Fourier-based SAR/ISAR processing methods exist (e.g., [19, 38, 80]). Many of these approaches are based on spectral estimation methods and, while they hold the promise of producing images with better resolution than Fourier-based methods, they often do so at the expense of vastly

higher computational loads and/or through the use of explicit scattering models for scene objects.

5.2.1 Polar-Format Algorithm. Perhaps the most obvious approach for obtaining an estimate of $f(x, y, z)$ from $F(k_x, k_y, k_z)$ is through the application of a 3-D Inverse Fourier Transform (IFT),

$$f(x, y, z) = \int_{-\infty}^{\infty} \int_{-\infty}^{\infty} \int_{-\infty}^{\infty} F(k_x, k_y, k_z) \exp\left[j(k_x x + k_y y + k_z z)\right] dk_x dk_y dk_z. \quad (5.21)$$

The computationally expedient method of performing this calculation uses multi-dimensional Fast Fourier Transform (FFT) techniques. The rectangular coordinates of (5.17) allow separable computation in each of the three dimensions giving an over-all computational complexity of $O(N^3 \log_2 N)$ for converting N^3 spatial frequency samples into a 3-D image with N^3 voxels (i.e., N^3 3-D pixels). However, this process assumes the spatial frequency samples are collected on a rectangular grid. Accepting this assumption and performing a 3-D Inverse Fast Fourier Transform (IFFT) on the raw spatial frequency data results in an *unfocused* SAR/ISAR image [121].

While unfocused SAR processing was adequate for many early low resolution SAR systems, higher resolutions demand correcting for the non-rectangular data collection geometries. In most collection scenarios, the collection geometry can be well approximated by a polar data collection grid. This observation is central to the Polar-Format Algorithm (PFA) initially introduced in [128]. PFA produces a SAR image by first interpolating the approximately polar data samples onto a rectangular grid and then applying a 3-D IFFT to the interpolated data. The computational burden for the complete PFA algorithm is essentially the sum of the frequency domain interpolator and the 3-D IFFT [39]. A recent extension of 2-D bistatic PFA uses a modified version of $\bar{u}_b'$ where $\varphi_b \neq (\varphi_{\text{TX}} + \varphi_{\text{RX}})/2$ in order to account for spatial frequency data warping effects [109].

5.2.2 Back-Projection Algorithm. While PFA is an intuitively attractive approach, it suffers from several implementation challenges. These challenges include: artifacts caused by multi-dimensional frequency domain interpolation, the need to collect all data before processing can begin, and the "corner-turn" operations required by multidimensional Fourier transforms which preclude parallel computing implementations [140]. The basic Back-Projection algorithm (BPA) removes these limitations.

Initially developed for use in the medical imaging community, BPA was first proposed for 2-D monostatic SAR processing [99]. Since this time, it has seen steadily increasing interest in the SAR/ISAR community. Using the spatial frequency paradigm, BPA can be extended to perform 3-D bistatic imaging. However, prior to deriving 3-D BPA, it is important to briefly return to the data collection scenario.

At each CPI location, the transmitter and receiver work together to produce a range profile $p_{\theta,\phi}(r)$ which represents a 3-D scene projection into a 1-D function. Assuming the scene is in the far-field, the resulting range profile $p_{\theta,\phi}(r)$ can be written as

$$p_{\theta,\phi}(r) = \int_{-\infty}^{\infty} \int_{-\infty}^{\infty} \int_{-\infty}^{\infty} f(x,y,z)\delta\left(r_b - r\right) \mathrm{d}x\mathrm{d}y\mathrm{d}z. \tag{5.22}$$

Equation (5.22) is a 3-D bistatic version of the Radon transform. Another important relationship, the projection-slice theorem, states the FT of $p_{\theta,\phi}(r)$ equals the scene's 3-D FT evaluated along a line with the same orientation [64]. Analytically, the projection-slice theorem proves

$$P_{\theta,\phi}(k_r) \equiv \mathcal{F}\left[p_{\theta,\phi}(r)\right] = F(k_r, \theta, \phi). \tag{5.23}$$

This relationship is critical to BPA.

Derivation of 3-D BPA itself begins by recognizing even though the output data $f(x,y,z)$ is usually desired in cartesian coordinates, the available spatial frequency data is collected in the (k_r, θ_b, ϕ_b) coordinate system. Modification of (5.21) to reflect

this fact results in

$$f(x, y, z) = \int_{-\pi/2}^{\pi/2} \int_{-\pi}^{\pi} \int_{0}^{\infty} F(k_r, \theta_b, \phi_b) \exp\left(jk_r r_b\right) \left[k_r \cos(\beta/2)\right]^2 \cos(\phi_b) \mathrm{d}k_r \mathrm{d}\theta_b \mathrm{d}\phi_b.$$
(5.24)

Note, β can be a function of both θ and ϕ if the geometric relationship between the transmitter and receiver changes throughout the CPI. This variability is likely in WAM-SAR data collections (e.g., Sec. 8.3.1). Using (5.23), (5.24) becomes

$$f(x, y, z) = \int_{-\pi/2}^{\pi/2} \int_{-\pi}^{\pi} \int_{0}^{\infty} P_{\theta_b, \phi_b}(k_r) \exp\left(jk_r r_b\right) \left[k_r \cos(\beta/2)\right]^2 \cos(\phi_b) \mathrm{d}k_r \mathrm{d}\theta_b \mathrm{d}\phi_b.$$
(5.25)

Since $k_r > 0$ (there is no "negative" frequency data), the inner integral of (5.25) is recognizable as the 1-D IFT of a function

$$Q_{\theta_b, \phi_b}(k_r) = \left[k_r \cos(\beta/2)\right]^2 \cos(\phi_b) P_{\theta_b, \phi_b}(k_r),$$
(5.26)

evaluated at r_b. The term $\left[k_r \cos(\beta/2)\right]^2 \cos(\phi_b)$ is the "back-projection filter" since it can be interpreted as the transfer function of a range profile filter. Defining $q_{\theta_b, \phi_b}(r)$ as the IFT of $Q_{\theta_b, \phi_b}(k_r)$ allows (5.25) to be rewritten as

$$f(x, y, z) = \int_{-\pi/2}^{\pi/2} \int_{-\pi}^{\pi} q_{\theta_b, \phi_b}(r_b) \mathrm{d}\theta_b \mathrm{d}\phi_b.$$
(5.27)

Equation (5.27) constitutes the 3-D far-field bistatic back-projection approach to SAR/ISAR image formation. Implementation of (5.27) can be accomplished in a few simple steps:

1. Declare a matrix of zeros $f(x, y, z)$ where each element corresponds to a single voxel.

2. Obtain $P_{\theta_b, \phi_b}(k_r) = \mathcal{F}[p_{\theta_b, \phi_b}(r)]$ for a given CPI pulse either directly (for an ISAR system) or via the FT (for a SAR system).

3. Multiply $P_{\theta_b, \phi_b}(k_r)$ by $\left[k_r \cos(\beta/2)\right]^2 \cos(\phi_b)$ to obtain $Q_{\theta_b, \phi_b}(k_r)$.

4. Take the IFT of $Q_{\theta_b,\phi_b}(k_r)$ (usually with zero-padding) to obtain $q_{\theta_b,\phi_b}(r)$.

5. Calculate the r_b value for each voxel.

6. Using a 1-D interpolator, calculate the value of $q_{\theta_b,\phi_b}(r)$ for each voxel based on its r_b value.

7. Multiply the interpolated values by $\exp[-j\min(k_r)r_b]$.

8. Add the resulting voxel values to $f(x,y,z)$.

9. Repeat steps 2-8 for each CPI pulse.

The Fourier domain multiplication in step 2 filters the data to account for the relative weight of a given sample based on the volume it occupies in the spatial frequency domain [69]. The act of calculating r_b values in step 5 is called "back-projection" since it has the effect of spreading the 1-D data collected by a single CPI pulse across the entire image domain. Step 7 corrects for the fact that the IFFT in step 4 is a low-pass filter. Ensuring the individual back-projected filtered range profiles add coherently requires restoring them to the appropriate frequency. The function $\min(\cdot)$ takes the minimum value of its argument. If desired, temporal windows for sidelobe control may be applied to the frequency domain data in step 2.

The proceeding development can be reduced to the 2-D imaging scenario by choosing $\phi_b = 0$ and performing the multiplication in step 2 using $k_r \cos(\beta/2)$. If the bistatic angle β is constant throughout the CPI, the $\cos(\beta/2)$ term simply acts as a constant over the entire image and may be ignored since most SAR/ISAR images are normalized prior to display. This observation further simplifies the back-projection filter, resulting in a value of k_r, the value normally reported in the literature [22, 39, 65, 99].

Equation (5.27) also inherently assumes the differential terms $d\theta_b$ and $d\phi_b$ are constant throughout the data collection. While this fact is usually true for ISAR data, it may not be true for a wide-angle SAR collection. In this case, the imaging algorithm may be modified to multiply each filtered range profile $q_{\theta_b,\phi_b}(r_b)$ by the

instantaneous differential $\mathrm{d}\theta_b\mathrm{d}\phi_b$, calculated using flight path data from the transmission and reception platforms.

While BPA corrects many issues associated with PFA (and can also be generalized to the near-field scenario as demonstrated in Section 5.5.3), the implementation of BPA comes at the substantially higher computation cost of $O(N^5)$ due to the need to explicitly determine the contributions to each voxel from each CPI pulse. However, recent developments have yielded a modified BPA form with a computation complexity of $O(N^3 \log_2 N)$, identical to the PFA algorithm [14, 126, 140]. This simplification results from a hierarchical decomposition of the actual back-projection step and is often called "fast" back-projection.

5.3 *Bistatic Resolution Criteria*

In addition to motivating Fourier transform-based imaging algorithms, the spatial frequency domain paradigm also dictates the expected resolution of a given SAR/ISAR image. The approach in this section is similar to [108] but achieves different results. In this section, the term "resolution" refers to the distance between the peak and first null of a $\operatorname{sinc}(x) \triangleq \sin(\pi x)/\pi x$ function (i.e., half the mainlobe null-to-null width). This convention defines a -4.0 dB resolution criterion for unwindowed data.

5.3.1 Resolution.   The resolution derivation begins by defining $\bar{u}_r$ as the unit vector $\bar{u}_b$ at the CPI's midpoint. It points opposite the range direction. The associated azimuth, elevation, and bistatic angles are θ_r, ϕ_r, and β_r respectively. The vector $\bar{u}_h$ defines the horizontal cross range direction (defined parallel to the xy-plane) while $\bar{u}_v$ defines the vertical cross range direction. Taken together, $\bar{u}_r$, $\bar{u}_h$, and $\bar{u}_v$ define a right-handed cartesian (r, h, v) coordinate system. The vectors $\bar{u}_r$ and $\bar{u}_h$ define the traditional slant plane often to derive traditional 2-D SAR imaging algorithms [65, 108].

Defining resolution according to a separable 3-D coordinate system inherently assumes the region containing available spatial frequency data is cubic in shape. In general, this assumption is accurate for data collections spanning relatively small sections of the spatial frequency domain (i.e., narrow-angle data), but degrades for larger SAR/ISAR collections. This degradation is more significant when β is also changing. In any case, multidimensional image resolutions are approximations and should be treated as such.

The resolution derivation approach comes from basic Fourier transform principles stating data extent in one domain determines the data resolution in the other domain. Using this approach, the spatial frequency data extent in the $\bar{u}_r$-direction is denoted Δk_r and defined by

$$\Delta k_r = [\max(k_r) - \min(k_r)] \cos(\beta_r/2), \tag{5.28}$$

where the functions $\max(\cdot)$ and $\min(\cdot)$ take the maximum and minimum values of their respective arguments. In a similar fashion, data extent in the $\bar{u}_h$ and $\bar{u}_v$-directions (Δk_h and Δk_v) can be determined by

$$\Delta k_h = 2 \operatorname{mean}(k_r) \sin\left[\frac{\max(\theta_b) - \min(\theta_b)}{2}\right] \cos(\phi_r) \cos(\beta_r/2) \tag{5.29}$$

and

$$\Delta k_v = 2 \operatorname{mean}(k_r) \sin\left[\frac{\max(\phi_b) - \min(\phi_b)}{2}\right] \cos(\beta_r/2), \tag{5.30}$$

where $\operatorname{mean}(\cdot)$ denotes the argument's mean. A more conservative calculation can be made using the minimum, instead of the mean, k_r values.

Having obtained the spatial frequency spans in the desired coordinate system, the resolutions in the transform (image) domain are calculated via

$$\delta\rho = \frac{2\pi}{\Delta k_\rho}, \tag{5.31}$$

124

where the variable ρ is replaced by the letter indicating the desired direction (i.e., r, h, or v). When determining δr, substituting in the definition of k_r gives

$$\delta r = \frac{2\pi}{\Delta k_r} = \frac{c}{2B\cos(\beta_r/2)}, \tag{5.32}$$

where c is the propagation velocity and B is the waveform bandwidth. This result matches traditional bistatic range resolution definitions [30, 108].

The user often desires resolution information not in the (r, h, v) coordinate system but in the (x, y, z) system. Unfortunately, this conversion is not possible using a simple coordinate transformation but requires an understanding of the SAR/ISAR collection's ImPulse Response (IPR).

The IPR of a particular collection geometry is defined as the SAR/ISAR image obtained from the specified collection geometry when $f(x, y, z) = \delta(x, y, z)$. The associated spatial frequency data is simply $F(k_x, k_y, k_z) = 1$. Assuming the collection's angular extent is relatively small, the shape of the available spatial frequency data (i.e., the data support region) is roughly cubic. In this case, the collection's IPR is a 3-D sinc($\cdot$) function. The -4.0 dB boundary of such a function is well approximated by an ellipsoid whose semi-axes (traditionally denoted a, b, and c [145]) are equal to the values $\delta r/2$, $\delta h/2$, and $\delta v/2$. This ellipsoid is defined analytically as

$$\frac{r^2}{(\delta r/2)^2} + \frac{h^2}{(\delta h/2)^2} + \frac{v^2}{(\delta v/2)^2} = 1. \tag{5.33}$$

In order to calculate the resolution $\delta\rho$ at an arbitrary orientation (θ, ϕ), (5.33) must be converted to polar coordinates using

$$r = \frac{\delta\rho}{2}\cos(\theta)\cos(\phi), \tag{5.34}$$

$$h = \frac{\delta\rho}{2}\sin(\theta)\cos(\phi), \tag{5.35}$$

and

$$v = \frac{\delta\rho}{2}\sin(\phi). \tag{5.36}$$

Making these substitutions and solving for $\delta\rho$ yields

$$\delta\rho = \frac{\delta r \delta h \delta v}{\sqrt{\delta h^2 \delta v^2 \cos^2(\theta)\cos^2(\phi) + \delta r^2 \delta v^2 \sin^2(\theta)\cos^2(\phi) + \delta r^2 \delta h^2 \sin^2(\phi)}}. \tag{5.37}$$

Finding δx, δy, and δz requires rotating from the (r, h, v) system back to the (x, y, z) system. The required (θ, ϕ) values for each direction are $\delta x : (-\theta_r, -\phi_r)$, $\delta y : (-\theta_r - 90°, -\phi_r)$, and $\delta z : (-\theta_r, -\phi_r - 90°)$. Substituting these values into (5.37) gives

$$\delta x = \frac{\delta r \delta h \delta v}{\sqrt{\delta h^2 \delta v^2 \cos^2(\theta_r)\cos^2(\phi_r) + \delta r^2 \delta v^2 \sin^2(\theta_r)\cos^2(\phi_r) + \delta r^2 \delta h^2 \sin^2(\phi_r)}}, \tag{5.38}$$

$$\delta y = \frac{\delta r \delta h \delta v}{\sqrt{\delta h^2 \delta v^2 \sin^2(\theta_r)\cos^2(\phi_r) + \delta r^2 \delta v^2 \cos^2(\theta_r)\cos^2(\phi_r) + \delta r^2 \delta h^2 \sin^2(\phi_r)}}, \tag{5.39}$$

and

$$\delta z = \frac{\delta r \delta h \delta v}{\sqrt{\delta h^2 \delta v^2 \cos^2(\theta_r)\sin^2(\phi_r) + \delta r^2 \delta v^2 \sin^2(\theta_r)\sin^2(\phi_r) + \delta r^2 \delta h^2 \cos^2(\phi_r)}}. \tag{5.40}$$

To better understand the relationship between $(\delta r, \delta h, \delta v)$ and $(\delta x, \delta y, \delta z)$, consider Fig. 5.2. It illustrates the relationship between δr, δv, and δx when $\theta_r = 0$. This geometry represents a linear flight path SAR data collection scenario when the platform velocity is in the $\bar{u}_h = \bar{u}_y$-direction. The vectors $\bar{u}_r$ and $\bar{u}_h$ define the slant plane. Most airborne 2-D SAR systems assume the scene is contained within the xy-plane, thus while the scene may be processed in the slant plane, it is projected in the xy-plane using simple trigonometry. This projection causes a degradation of the range resolution δr, thus while the slant plane image has resolution $(\delta r, \delta h)$, the final xy-plane image has resolution $(\delta x' = \delta r / \cos(\phi_r), \delta y = \delta h)$. However, if data is
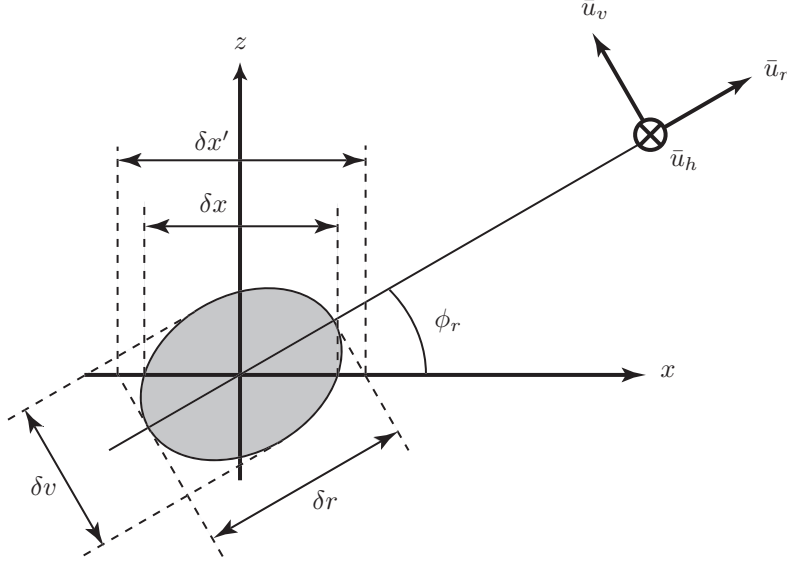
Figure 5.2:   Relationship between δr, δv and δx when $\theta_r = 0$. As δv approaches ∞ (i.e., no vertical resolution), δx approaches $\delta x' = \delta r / \cos(\phi_r)$.

available in the $\bar{u}_v$-direction[3], the resulting non-infinite value of δv helps improve δx according to (5.38).

5.3.2   Resolution Cell Volume.   The concept of resolution is widely used as a SAR/ISAR image metric because it provides a simple numerical method for predicting SAR/ISAR image quality. Yet as the collection's angular span increases, the assumptions built into the resolution calculation lose their validity.

One method of dealing with these inaccuracies was presented in [30] which suggested an alternative metric based on the total 2-D image area occupied the mainlobe return from a point scatterer. Extending this concept to three dimensions, one can define the total volume of a resolution cell without needing to assume the available spatial frequency data is confined to a cube. Unfortunately, deriving such volumes analytically for an arbitrary collection geometry is challenging.

---

[3]This data might be collected using multiple passes of the SAR platform at slightly different altitudes. Such a collection facilitates the use of technique called multi-pass interferometric SAR [65].

As an alternative to attempting a full analytical solution, it is possible to easily calculate Resolution Cell Volume (RCV) numerically. This approach is based on the IPR function, calculated numerically by assuming $F(k_r, \theta_b, \phi_b) = 1$ and evaluating (5.27) with the appropriate set of $(k_r, \theta_b, \phi_b, \beta)$ values denoting the data acquired during the data collection. This understanding leads to the following method for calculating RCV:

1. Calculate and normalize $|f(x, y, z)|$ via (5.27) assuming $F(k_r, \theta_b, \phi_b) = 1$.

2. Determine the number of $|f(x, y, z)|$ voxels exceeding a desired threshold (e.g. -4.0 dB).

3. Multiply the number of voxels by the single voxel volume.

The result is the resolution-like RCV metric, encompassing all available data and independent of orientation angle. The 2-D version of RCV is Resolution Cell Area (RCA) and is defined relative to a 2-D image plane within the 3-D scene.

If the user desires a quick estimate of -4.0 dB RCV or RCA without resorting to numerical computation, the IPR's assumed ellipsoidal shape may be used instead. Under these conditions the ellipsoid volume formula gives [145]

$$\text{RCV} \approx \frac{\pi}{6} \delta r \delta h \delta v. \tag{5.41}$$

Estimation of RCA in the 2-D rh-plane uses the ellipse area formula [145]

$$\text{RCA}_{rh} \approx \frac{\pi}{4} \delta r \delta h. \tag{5.42}$$

The accuracy of (5.41) and (5.42) are directly related to the values of $\Delta\theta$ and $\Delta\phi$. For smaller values, the spatial frequency data is nearly rectangular giving highly accurate RCV/RCA estimates. For larger values, the non-rectangular shape tends to make RCV and RCA estimates more conservative.

In the most common 2-D SAR imaging scenario, the user collects 2-D data and forms 2-D images when $\phi_b > 0$. In this case, RCA should be calculated in the xy-plane via

$$\text{RCA}_{xy} \approx \frac{\pi}{4}\delta x \delta y. \tag{5.43}$$

Note, $\text{RCA}_{rh} \geq \text{RCA}_{xy}$. The difference between the two is related to the angular difference between the orientation of these planes and the eccentricity of the ellipse defined by δr and δh. If these differences are great enough, the estimate of RCA_{xy} may become smaller than the true RCA_{xy} value, overestimating SAR/ISAR image quality.

5.4 Validation Using ISAR Data

Previous sections have derived several results including the spatial frequency domain relationship between monostatic and bistatic data, methods of SAR/ISAR image formation, and resolution derivations using the spatial frequency perspective. While some aspects of these derivations appear in the literature, they are not thoroughly validated with SAR/ISAR data collections. In this section, these relationships are validated using actual ISAR data. The data was collected in AFIT's RCS chamber and calibrated using the procedures outlined in Chapter IV.

5.4.1 Twin Wires Target. For a general ISAR scene, the differences between scattering from a monostatic and bistatic collection scenario can be separated into two categories. First, as derived in Section 5.1.3, the bistatic collection geometry warps the spatial frequency data, making the target behave as though it were illuminated using different frequencies. Second, the scattering characteristics of real scenes change dramatically as a function of illumination angle, illumination frequency, and bistatic observation angle. These variations are defined by the interactions of the ElectroMagnetic (EM) waves with the scene elements. In order to validate the bistatic collection geometry effects, the scene/target must be free of the second category of scattering effects.

A scene composed of independent ideal point scatterers has the desired properties. By definition, point scatterers illuminated by a given EM wave reflect that wave in an axially symmetric pattern, giving the same response to an observer located at any orientation angle. Such scatterers are termed independent if there are no interactions between a collection of such scatterers. For a scene consisting of a collection of M independent ideal point scatterers, the image plane $f(x, y, z)$ is given by

$$f(x, y, z) = \sum_{m=0}^{M-1} A_m \delta(x - x_m, y - y_m, z - z_m), \qquad (5.44)$$

where the mth scatterer has a complex amplitude A_m and is located at (x_m, y_m, z_m). Using the sifting property, the spatial frequency domain representation for a collection of M point scatterers is

$$F(k_x, k_y, k_z) = \sum_{m=0}^{M-1} \exp\left[-j\left(k_x x_m + k_y y_m + k_z z_m\right)\right]. \qquad (5.45)$$

According to (5.6), the frequency domain effects of a bistatic collection geometry may be verified, without loss of generality, by examining the 2-D case. A target consisting of two vertical wires, illuminated using Vertical transmit / Vertical receive (VV) polarization, can be approximated as two independent ideal point scatterers of equal amplitudes A_m as long as the wire diameter is much less than the illumination wavelength. Placing such wires at locations $(\pm 0.05, 0, 0)$ allows (5.45) to be rewritten as

$$F(k_x, k_y) = A_m \exp\left(j\frac{k_x}{20}\right) + A_m \exp\left(-j\frac{k_x}{20}\right). \qquad (5.46)$$

Using Euler's relationship, $\exp(j\theta) = \cos(\theta) + j\sin(\theta)$, gives

$$F(k_x, k_y) = 2A \cos\left(\frac{k_x}{20}\right). \qquad (5.47)$$

130

Table 5.1:   ISAR data collection parameters: twin wires target.

Type	f, GHz	N	θ_{TX}, deg	θ_{RX}, deg	θ_b, deg	β, deg	P
Monostatic	6-18	101	180-270	180-270	180-270	0	181
Fixed Bistatic	6-18	101	90-180	180-270	135-225	90	181
Variable Bistatic	6-18	101	180	225-315	202.5-247.5	45-135	181

When $k_x = 10\pi(2m + 1)$,

$$|F(k_x, k_y)| = 2|A|\cos\left[\frac{\pi(2m+1)}{2}\right] = 0, \tag{5.48}$$

for all integers m.

Interrogation of the twin wires ISAR target was performed using three independent data collections. The collection parameters are presented in Tab. 5.1. The first collection geometry was monostatic, rotating the target to collect data over the range $180° \leq \theta_b \leq 270°$. The second collection geometry used a fixed bistatic angle of $\beta = 90°$, rotating the target to achieve $135° \leq \theta_b \leq 225°$. The final collection used a variable bistatic geometry, fixing both the target and transmit antenna while moving the receive antenna during the collection, resulting in $45° \leq \beta \leq 135°$ and $202.5° \leq \theta_b \leq 247.5°$.

5.4.2   Spatial Frequency Data Representation.   Using the data collection outlined in Sec. 5.4.1, it is possible to validate the spatial frequency domain relationship between monostatic and bistatic data (Sec. 5.1.3). Figures 5.3-5.5 present this comparison. Each subfigure is plotted on a normalized 40.0 dB dynamic range. Subfigure (a) (for each figure) shows the magnitude of the raw $N \times P$ data matrix for each collection geometry (i.e., $|F(\theta_b, f)|$). While each of these subfigures shows a series of peaks (dark regions) and nulls (white lines), the individual collection geometries have warped these features in different ways. At first glance these collections would not appear to represent the same ISAR scene.
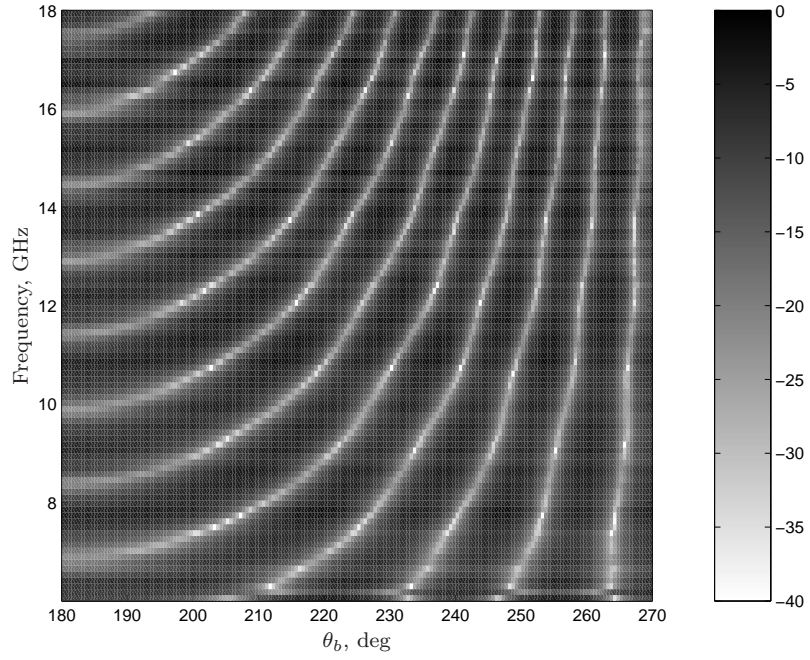
(a) Raw data magnitude
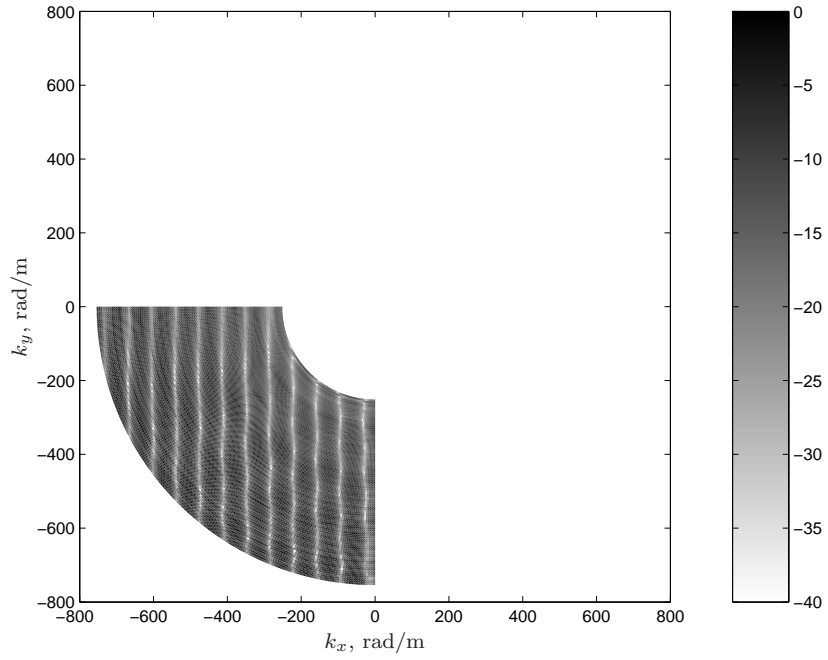
(b) Spatial frequency data magnitude

Figure 5.3:   Magnitude of full monostatic ISAR dataset for twin vertical wires target (40.0 dB dynamic range). Subfigure (a) shows the raw 2-D data matrix. Subfigure (b) shows this data mapped onto the spatial frequency plane.
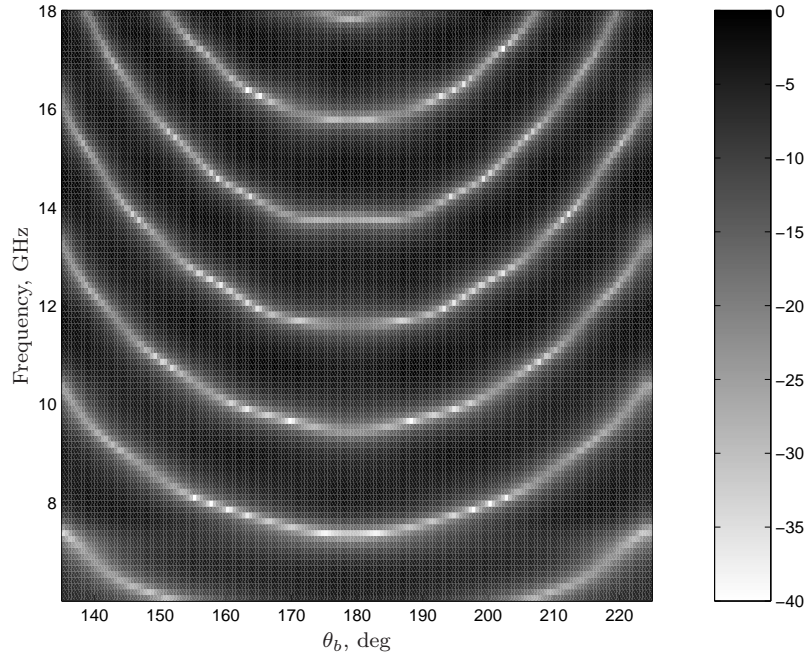
(a) Raw data magnitude $(\beta = 90°)$
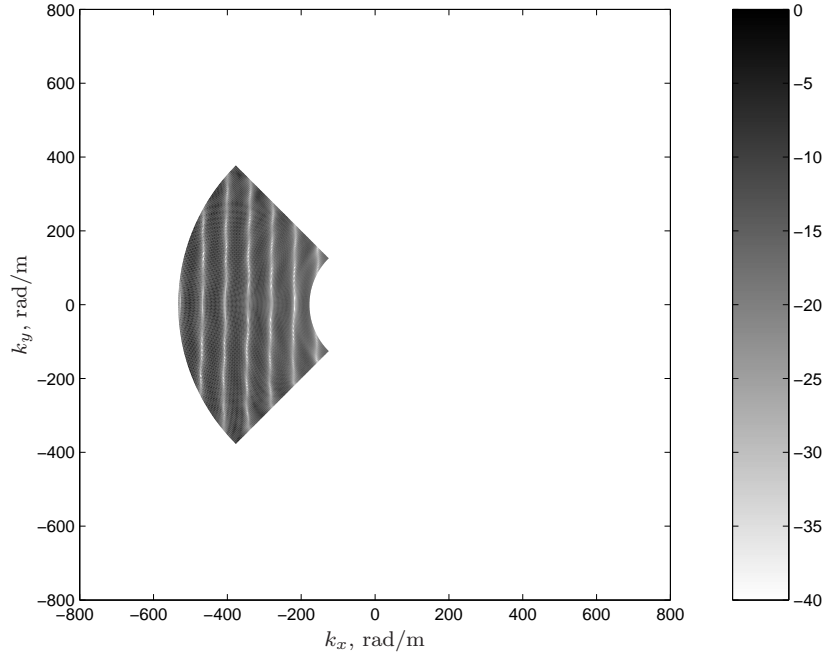
(b) Spatial frequency data magnitude

Figure 5.4:   Magnitude of full bistatic $(\beta = 90°)$ ISAR dataset for twin vertical wires target (40.0 dB log scale). Subfigure (a) shows the raw 2-D data matrix. Subfigure (b) shows this data mapped onto the spatial frequency plane.
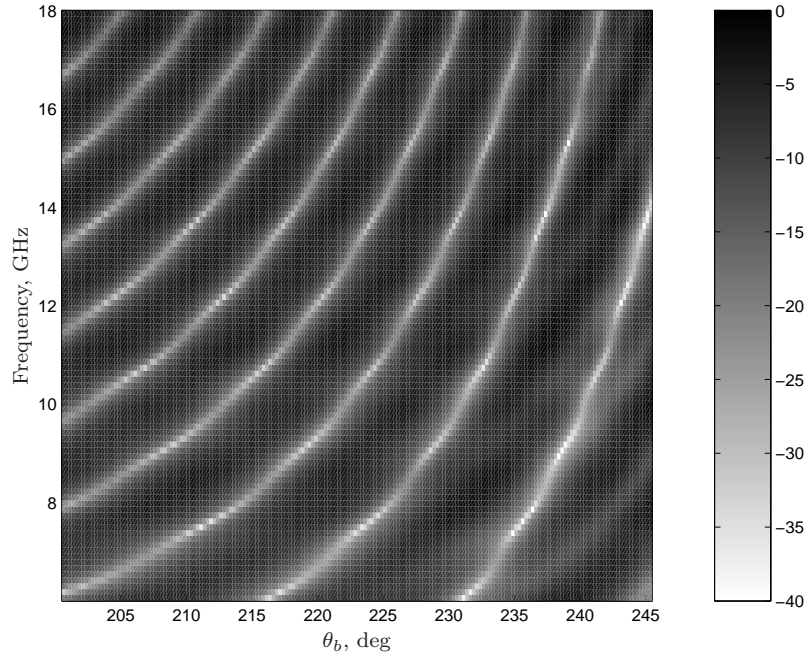
(a) Raw data magnitude
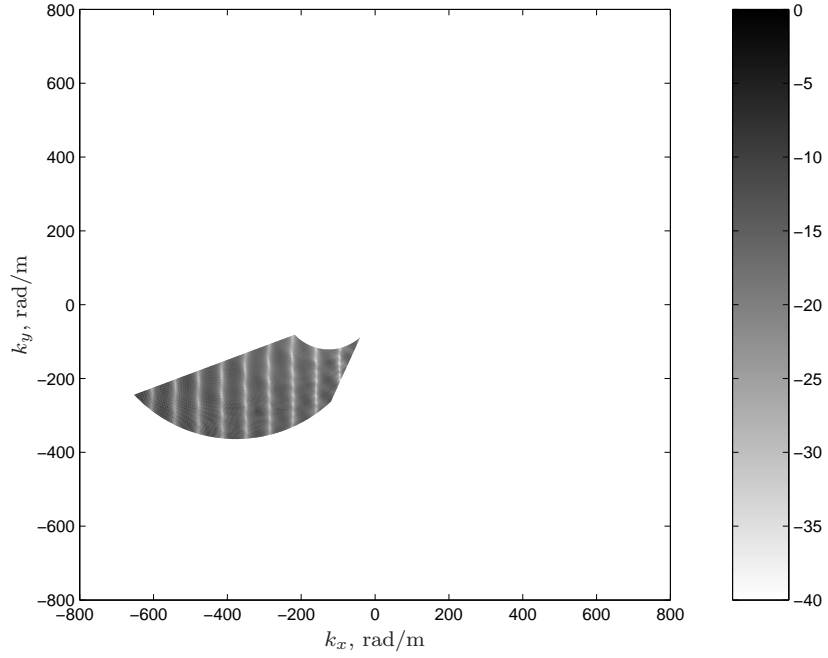
(b) Spatial frequency data magnitude

Figure 5.5: Magnitude of full bistatic ($45° \leq \beta \leq 135°$) ISAR dataset for twin vertical wires target (40.0 dB log scale). Subfigure (a) shows the raw 2-D data matrix. Subfigure (b) shows this data mapped onto the spatial frequency plane.

Subfigure (b) of Figs. 5.3-5.5 shows the same data transferred the spatial frequency domain. The original $|F(\theta_b, f)|$ data has been mapped to

$$|F(k_x, k_y)| = |F(k_r \cos(\beta/2) \cos(\theta_b), k_r \cos(\beta/2) \sin(\theta_b)|. \tag{5.49}$$

In the spatial frequency domain, is it obvious that all three collections are merely different segments of the same $|F(k_x, k_y)|$ function specified by (5.47). The nulls appear at the same k_x values in all three collections. According to (5.48), the tenth null counting backwards from $k_x = 0$ ($m = -10$) should appear at

$$k_x = 10\pi[2(-10) + 1] \approx -600. \tag{5.50}$$

This null may be observed in Figs. 5.3(b) and 5.5(b). Even though the same number of data samples were available for each collection, the dimensions of the frequency domain data differ significantly. The monostatic collection occupies the largest area and should therefore have the best resolution, while the fixed bistatic collection has a smaller area yielding degraded resolution.

Using the spatial frequency domain mapping, it is also possible to determine which (k_x, k_y) pairs were sampled by all three collections. The portion of θ_b common to all collections is $202.5° \leq \theta_b \leq 225°$. For each θ_b value in this range, the maximum common k_r is determined by the collection with the largest β and the minimum common k_r value is determined by the collection with the smallest β. Using this information, the data from Figs. 5.3-5.5 was trimmed to produce Figs. 5.6-5.8.

Subfigure (a) of Figs. 5.6-5.8 shows the union of the available raw data. Each block shows the same number of nulls, but represents a different segment of the original data collection. The differing sizes of the raw data blocks relate to the eventual sample density in the spatial frequency domain and are therefore inversely proportional to the maximum alias-free scene dimensions. Subfigure (b) appears virtually identical in all three figures, indicating ISAR images produced from this data should also be

135
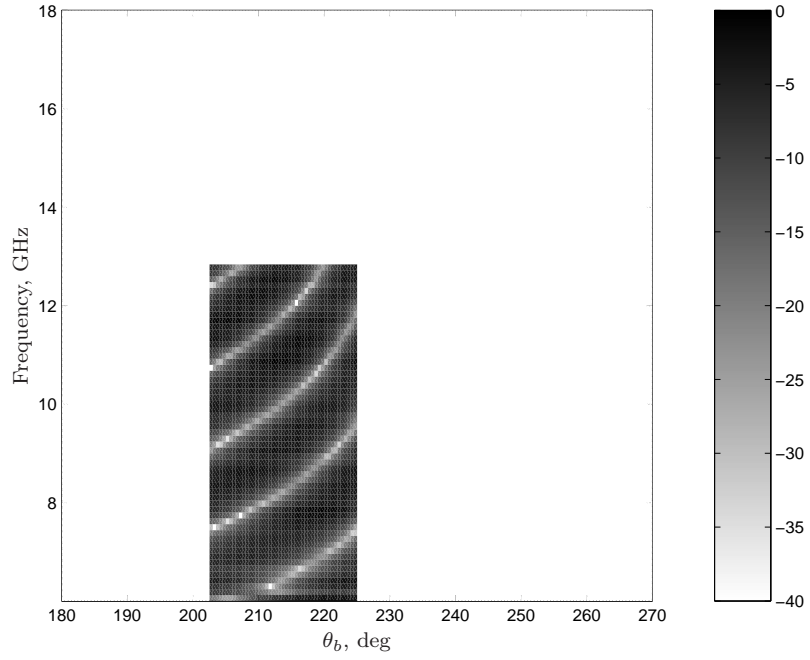
(a) Raw data magnitude
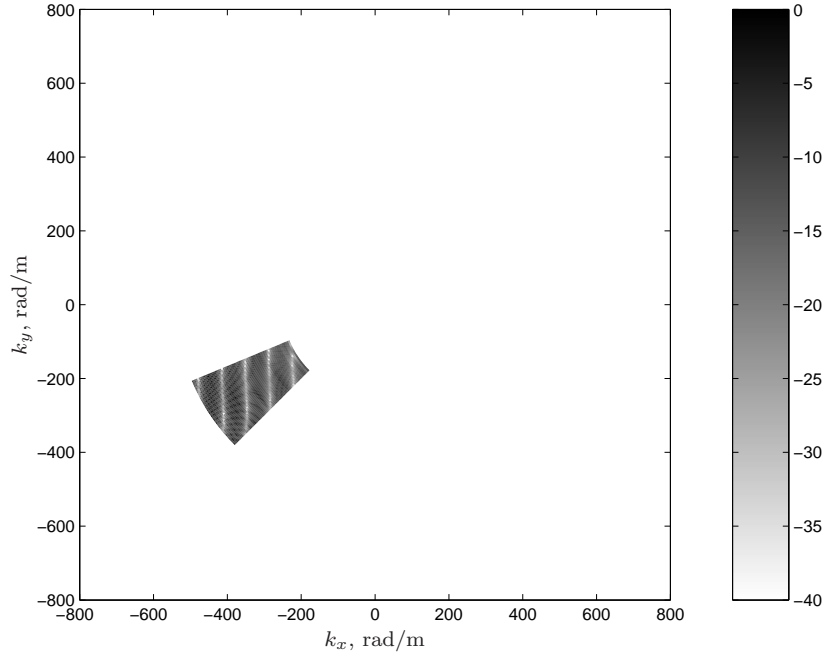
(b) Spatial frequency data magnitude

Figure 5.6: Magnitude of truncated monostatic ISAR dataset for twin vertical wires target (40.0 dB log scale). Bistatic scaling term used to remove data not common to all three collections. Subfigure (a) shows the raw 2-D data matrix. Subfigure (b) shows this data mapped onto the spatial frequency plane.
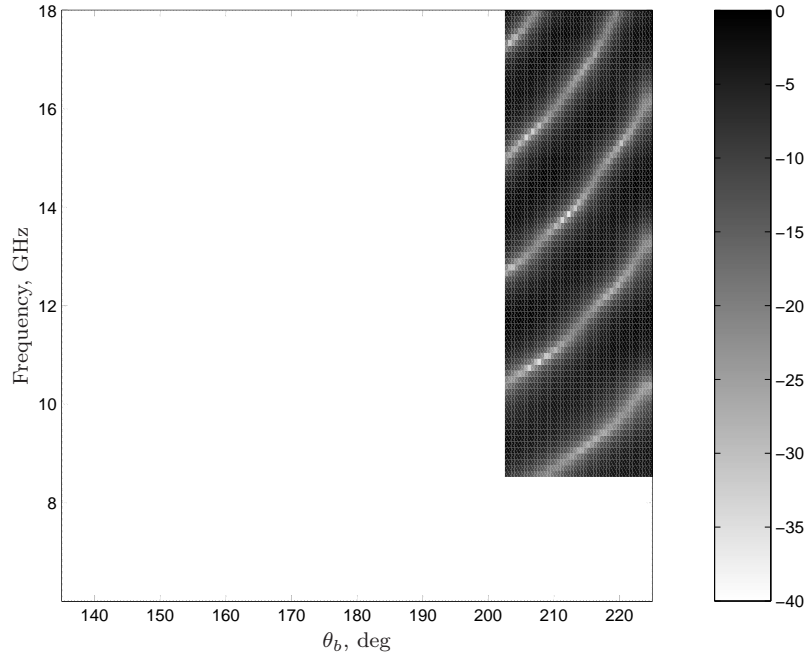
(a) Raw data magnitude $(\beta = 90°)$
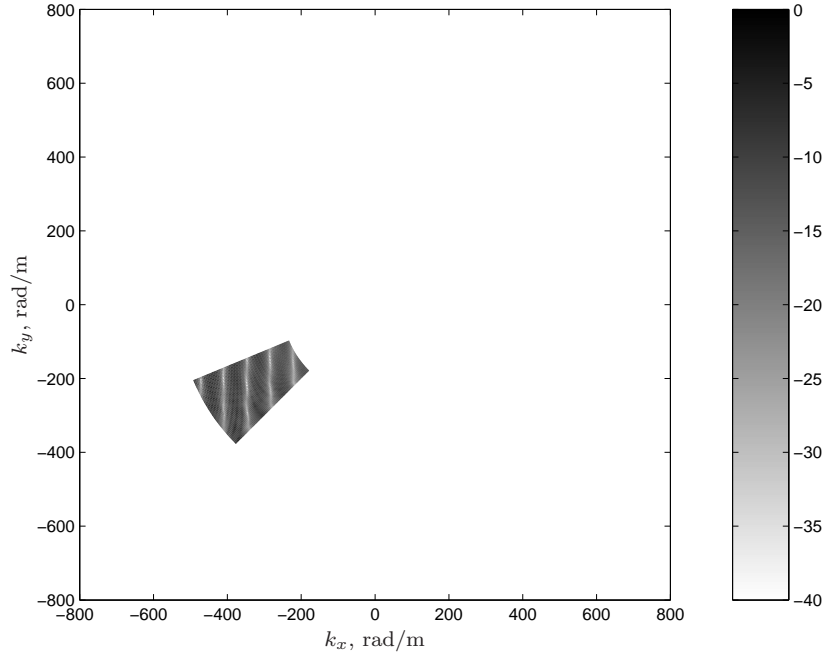
(b) Spatial frequency data magnitude

Figure 5.7: Magnitude of truncated bistatic $(\beta = 90°)$ ISAR dataset for twin vertical wires target (40.0 dB log scale). Bistatic scaling term used to remove data not common to all three collections. Subfigure (a) shows the raw 2-D data matrix. Subfigure (b) shows this data mapped onto the spatial frequency plane.

137
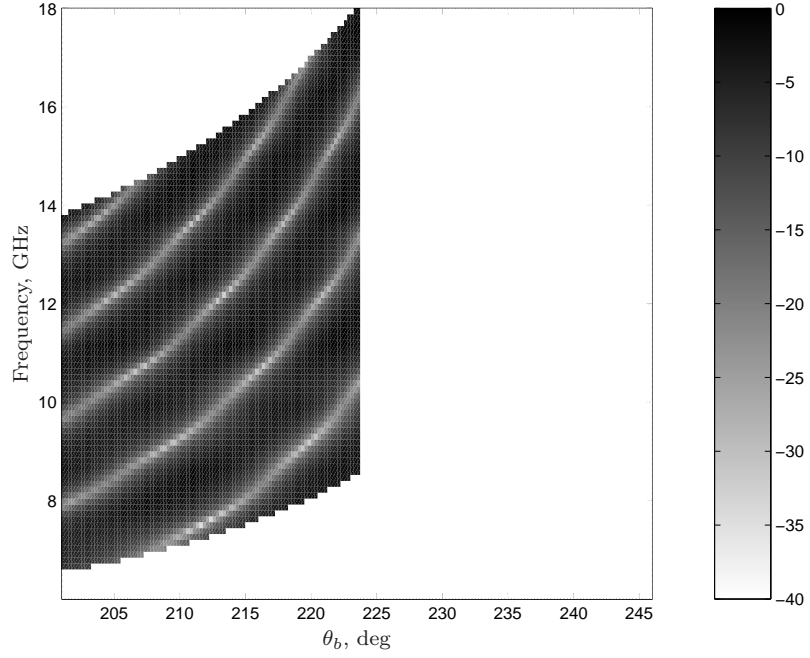
(a) Raw data magnitude $(45° \leq \beta \leq 135°)$
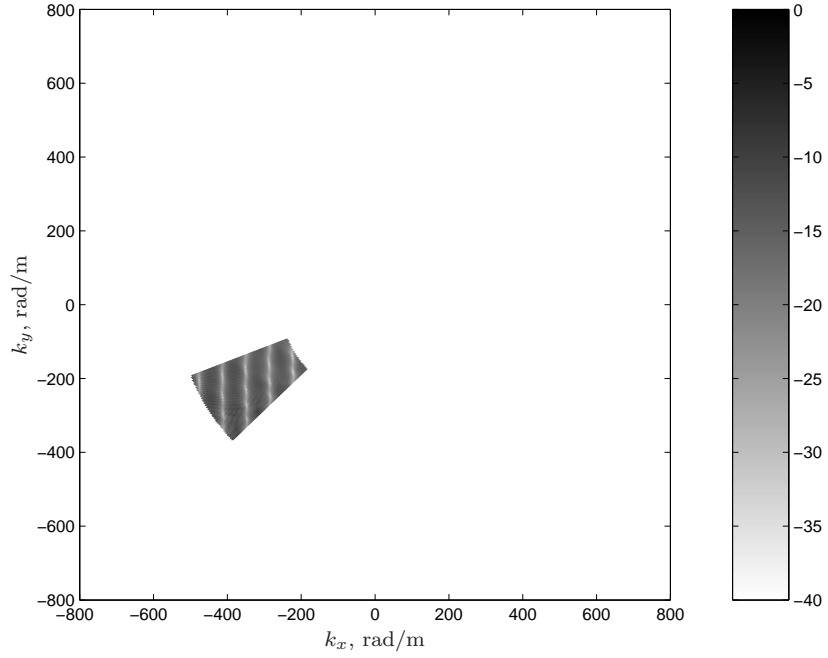
(b) Spatial frequency data magnitude

Figure 5.8: Magnitude of truncated bistatic $(45° \leq \beta \leq 135°)$ ISAR dataset for twin vertical wires target (40.0 dB log scale). Bistatic scaling term used to remove data not common to all three collections. Subfigure (a) shows the raw 2-D data matrix. Subfigure (b) shows this data mapped onto the spatial frequency plane.

very similar, despite the fact that the data was obtained using drastically different collection geometries.

5.4.3 ISAR Images.   Using the BPA algorithm presented in Sec. 5.2.2, the complex In-phase and Quadrature (I/Q) sampled data from Figs. 5.3-5.8 was processed into ISAR images. Since the data was collected in a 2-D geometry, the resulting images are processed using the 2-D version of BPA with the back-projection filter equal to $k_r \cos(\beta)$. These images are shown in Figs. 5.9-5.11. Subfigure (a) in each of these figures illustrates the images formed from the data in Figs. 5.3-5.5 (the full data sets) while subfigure (b) in each figure was made from the data in Figs. 5.6-5.8 (data set unions).

The resolution and RCA calculations (Section 5.3) for each image are presented in Tab. 5.2. The first two columns define the basic collection geometry and give the figure numbers of the respective images. The second three columns give the specific collection parameters which define resolution. The next two columns contain the predicted resolutions in both the rh-plane (the data collection plane) and the xy-plane (the image plane). Since the radar is in the image region plane (i.e., $\phi_r = 0$), these two planes differ only by a rotation in azimuth. The next three columns give the estimated RCA values in the rh and xy-planes followed by the true (numerically determined) -4.0 dB RCA value. The final column contains the ratio of RCA_{rh} to RCA illustrating how accuracy of the RCA_{rh} estimate is linked to $\Delta\theta_b$.

The full monostatic image, Fig. 5.9(a), shows two well focused point scatterers at the appropriate $(\pm 0.05, 0)$ locations. The bowtie-like shape of each scatterer is consistent with that predicted by [132]. From the rotational property of Fourier transforms, the presence of the associated spatial frequency data in quadrant 3 (Fig. 5.3(b)) indicates the illumination came from the same quadrant in the image domain.

Figure 5.9(a) also reveals that while the scene is well approximated as a collection of independent, ideal point scatterers, the true scattering relationships are somewhat more complex. This fact is illustrated by the light gray arc above and to

139
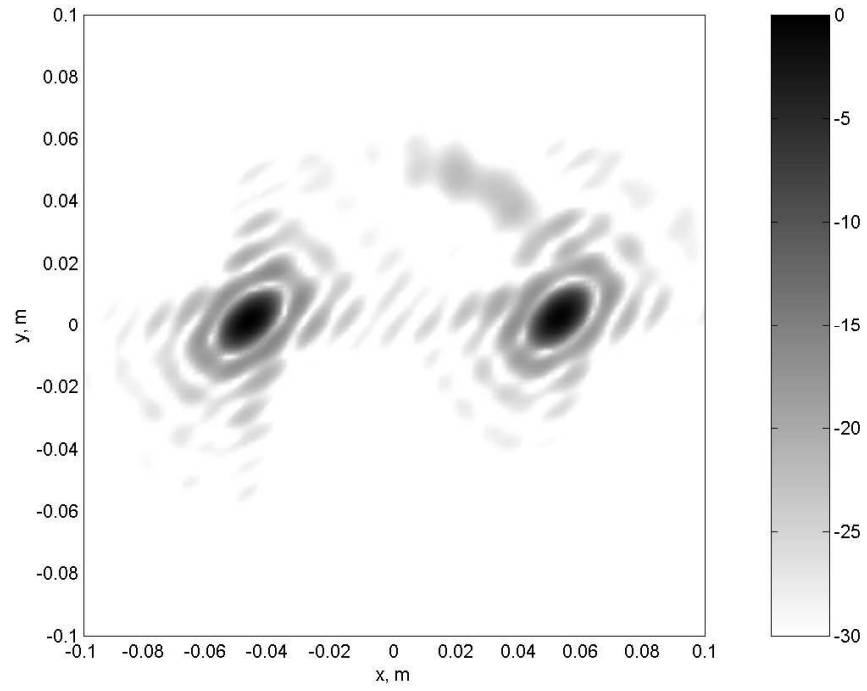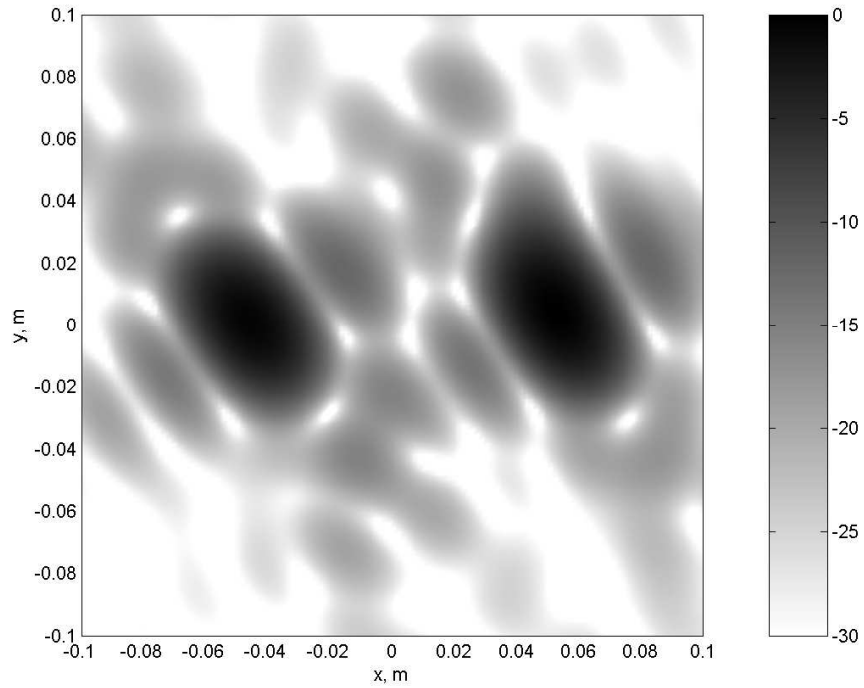
(a) Full image

(b) Truncated image

Figure 5.9:   Monostatic ISAR images for twin vertical wires target (30.0 dB log scale). Subfigure (a) shows full dataset image (data from Fig. 5.3). Subfigure (b) shows truncated dataset image (data from Fig. 5.6).

140
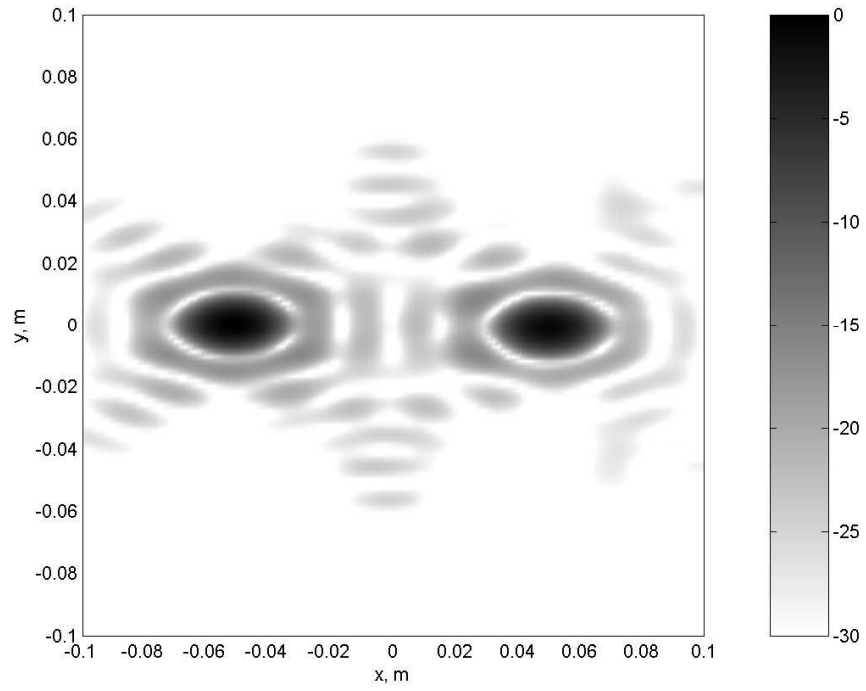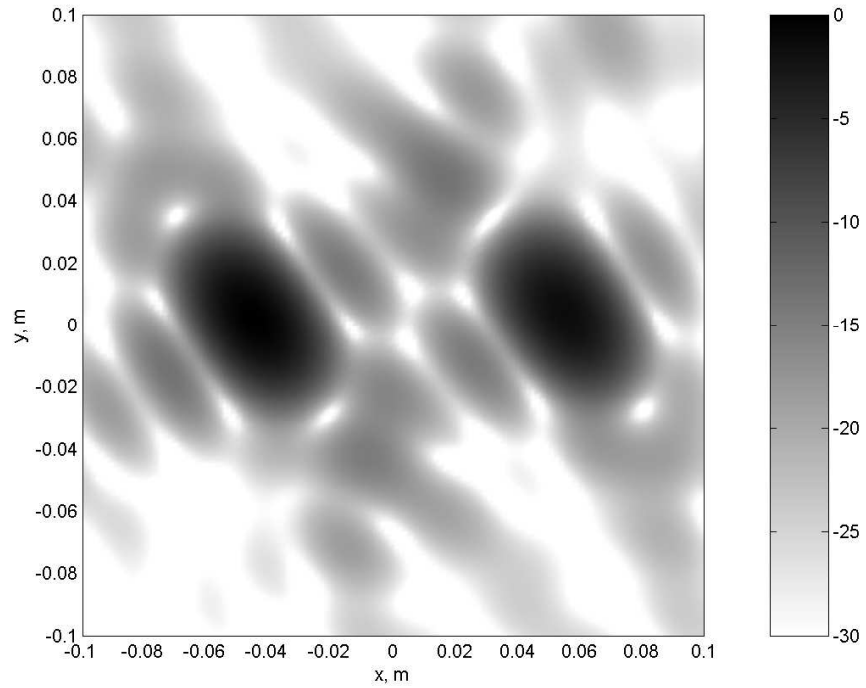
(a) Full image ($\beta = 90°$)

(b) Truncated image

Figure 5.10:   Bistatic ($\beta = 90°$) ISAR images for twin vertical wires target (30.0 dB log scale). Subfigure (a) shows full dataset image (data from Fig. 5.4). Subfigure (b) shows truncated dataset image (data from Fig. 5.7).

141
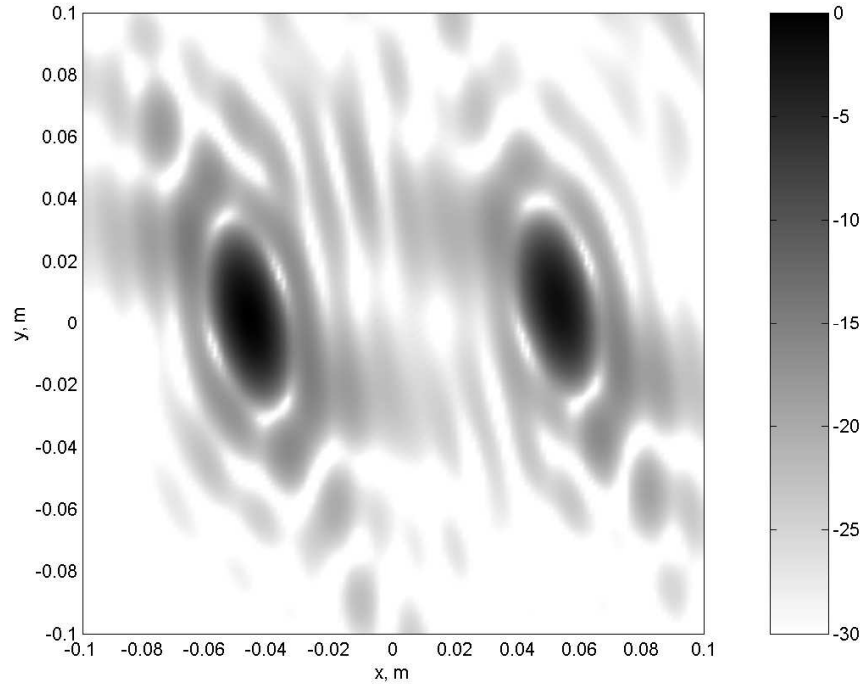
(a) Full image ($45° \leq \beta \leq 135°$)
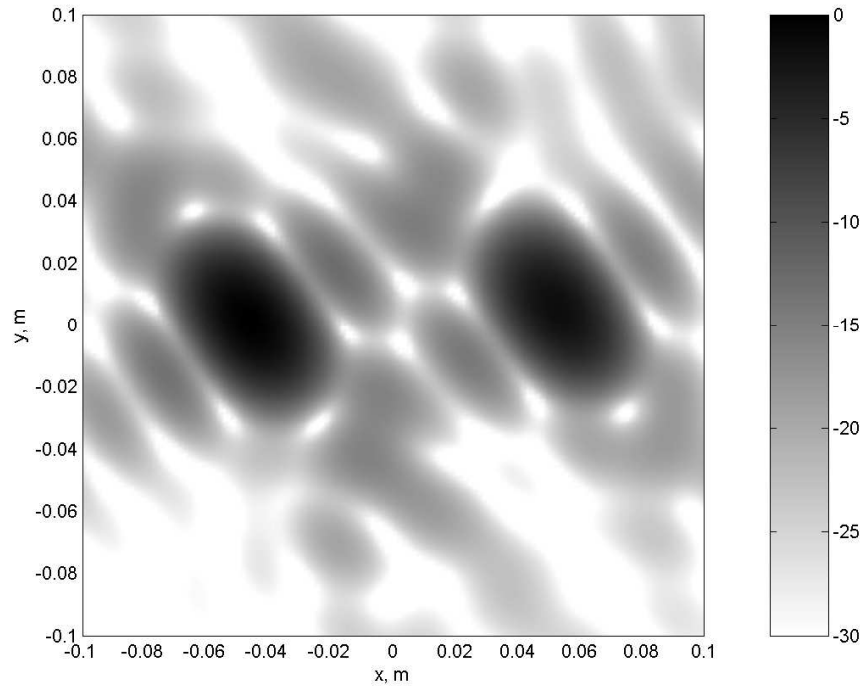
(b) Truncated image

Figure 5.11:   Bistatic ($45° \leq \beta \leq 135°$) ISAR images for twin vertical wires target (30.0 dB log scale). Subfigure (a) shows full dataset image (data from Fig. 5.5). Subfigure (b) shows truncated dataset image (data from Fig. 5.8).

Table 5.2: ISAR resolution predictions: twin wires target. Resolutions calculated using equations in Sec. 5.3.1. RCA estimates (RCA$_{rh}$, RCA$_{xy}$) calculated using (5.42) and (5.43). True -4.0 dB RCA is calculated using the procedure outlined in Sec. 5.3.2. The entry "var" denotes various values depending on collection geometry. The bottom row contains information common to Figs. 5.9(b), 5.10(b), and 5.11(b).

| Fig. | Angles, deg | | | Resolutions, cm | | Est. & True, cm^2 | | | $\frac{\text{RCA}_{rh}}{\text{RCA}}$ |
	θ_r	β_r	$\Delta\theta_b$	$(\delta r, \delta h)$	$(\delta x, \delta y)$	RCA$_{rh}$	RCA$_{xy}$	RCA	
5.9(a)	225	0	90	$(1.25, 0.88)$	$(1.02, 1.02)$	0.87	0.82	0.81	1.07
5.10(a)	180	90	90	$(1.77, 1.25)$	$(1.77, 1.25)$	1.74	1.74	1.62	1.07
5.11(a)	225	90	45	$(1.77, 2.31)$	$(1.99, 1.99)$	3.21	3.10	3.15	1.02
var	213.75	var	22.5	$(2.23, 4.11)$	$(2.52, 3.11)$	7.19	6.17	7.15	1.01

the left of the right-hand scatterer. This arc is the result of scatterer interactions and is caused by radar energy which first strikes one scatterer and then the other before returning to the antenna. In this case, the radar energy travels an additional 10 cm (the distance between the scatterers), leading to an apparent additional range of $10/2 = 5$ cm. These interactions manifest themselves as low-level returns at a radius of 5 cm and an angle 180° away from the monostatic radar location.

The monostatic image resolutions in the data collection plane $(\delta r, \delta h)$ predict superior performance in the horizontal cross-range direction $\bar{u}_h$ compared to the range direction $\bar{u}_r$. However, due to θ_r, the resolutions in the $\bar{u}_x$ and $\bar{u}_y$-directions are equal. The RCA$_{rh}$ estimate is somewhat conservative due to the large $\Delta\theta_b$ value (RCA$_{rh}$/RCA $= 1.07$). The RCA$_{xy}$ value is nearly identical to the true RCA value.

Figure 5.10(a) shows the image obtained from the fixed bistatic collection. The overall shape of the scatterers is essentially the same as the monostatic case, but the change in θ_r from 225° to 180° has also rotated the responses from each scatterer. The scatterer interaction effects seen in Fig. 5.9(a) are not visible. This absence results, since scatterer interactions are not independent of collection geometry. Resolutions in the data collection plane are a factor of $\cos(\beta/2)$ worse than the monostatic collection case, leading to the larger scatterer images. Since $\theta_r = 180°$, $\delta r = \delta x$ and $\delta h = \delta y$ leading to equal (and somewhat conservative) RCA estimates RCA$_{rh}$ and RCA$_{xy}$.

Figure 5.11(a) illustrates the image from the variable bistatic collection. Again, the variation in θ_r has caused a rotation in the scatterers. However, the sidelobe response appears less regular. This irregularity is caused by the variation in β, leading to the irregularly shaped spatial frequency data in Fig. 5.5(b). Despite this irregularity, the sidelobe levels are significantly lower than those obtained using the standard back-projection filter k_r. Unlike the previous images, Fig. 5.11(a) has better range resolution than cross-range resolution due to the $\Delta\theta_b$ reduction (only the RX antenna is moving). The reduction in $\Delta\theta_b$ also increases the accuracy of the RCA_{rh} estimate but pushes the RCA_{xy} value below the true RCA measure, slightly overestimating the resulting image quality.

Subfigure (b) in Figs. 5.9-5.11 shows the ISAR images obtained using the data in Figs. 5.6-5.8, respectively. As expected, despite significant variations in collection geometry, the resulting ISAR images are virtually identical. The scatterer images are in the same location, have the same orientation, and same resolutions. Some minor differences do appear in the image sidelobes, caused by different scatterer interactions and independent noise realizations in the each of the three collections. Since the spatial frequency domain extent of the data union is less than any of the individual collections, the image domain resolutions are also worse. The small $\Delta\theta_b$ value makes $\mathrm{RCA}_{rh}/\mathrm{RCA} \approx 1$ but pushes RCA_{xy} even further below the true value.

Figures 5.12 and 5.13 illustrate the minimal differences between Figs. 5.9(b), 5.10(b), and 5.11(b). Figure 5.12(a) shows the magnitude of the pixel-by-pixel differences between Fig. 5.9(b) (the monostatic image) and Fig. 5.10(b) (the fixed bistatic angle image). Over most of the image, the differences are quite small, indicating good agreement. Figure 5.12(b) shows only those pixels with differences of 10.0 dB or more. As expected, only a few pixels in the sidelobe regions exhibit significant differences. The worst-case difference is roughly 15.0 dB. These differences all occur in the upper right-hand quadrant. This quadrant contains monostatic multipath effects, which are expected to differ from bistatic multipath. Figure 5.13 compares the monostatic case (Fig. 5.9(b)) to the variable bistatic case (Fig. 5.11(b)). As in the fixed bistatic case,

144

the variable case shows very little difference across the majority of the image. Again, differences show up in the sidelobe region dominated by monostatic multipath.

Figure 5.14 demonstrates the utility of using a back-projection filter which takes the bistatic angle into account. Subfigure (a) is simply of copy of Fig. 5.11(a), repeated for convenience. It made use of the full $k_r \cos(\beta/2)$ filter. Subfigure (b) was made using the traditional k_r value. While the overall resolution is essentially the same, the sidelobes in subfigure (b) are significantly worse, demonstrating the utility of the new back-projection filter. In total, the images throughout this section serve to validate the spatial frequency paradigm and far-field bistatic back-projection algorithm. The remainder of the chapter extends this approach to incorporate near-field effect corrections (i.e., RM) as well as warped image planes.

5.5   Near-Field SAR/ISAR Image Formation

Up to this point, this document has used the far-field approximation, assuming all transmitted/received waveforms are uniform plane waves of infinite extent. This assumption contains three important components, each degrading SAR/ISAR image quality when they become invalid. These assumptions are:

1. The phase of the field is constant over a plane whose normal is defined by the wave propagation direction.

2. The amplitude is not a function of range since the plane wave is theoretically of infinite extent and therefore does not expand as it propagates.

3. The amplitude is uniform over this entire planar surface at a given range.

In practice, it is not possible to generate a uniform plane wave. However, when the target region is sufficiently small compared to the range of the transmitter/receiver, the effects of these assumptions are small enough to be ignored and the target is therefore assumed to be in the "far-field". These assumptions are identical to those used to derive the quiet zone (Chapter IV). Removing them allows imaging of targets extending beyond the traditional quiet zone boundaries.
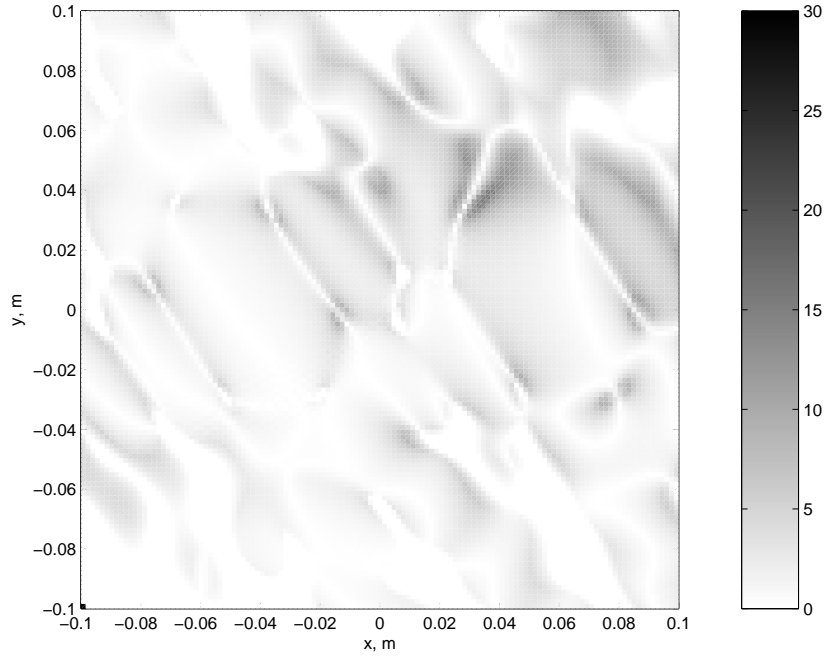
(a) All pixel difference values.
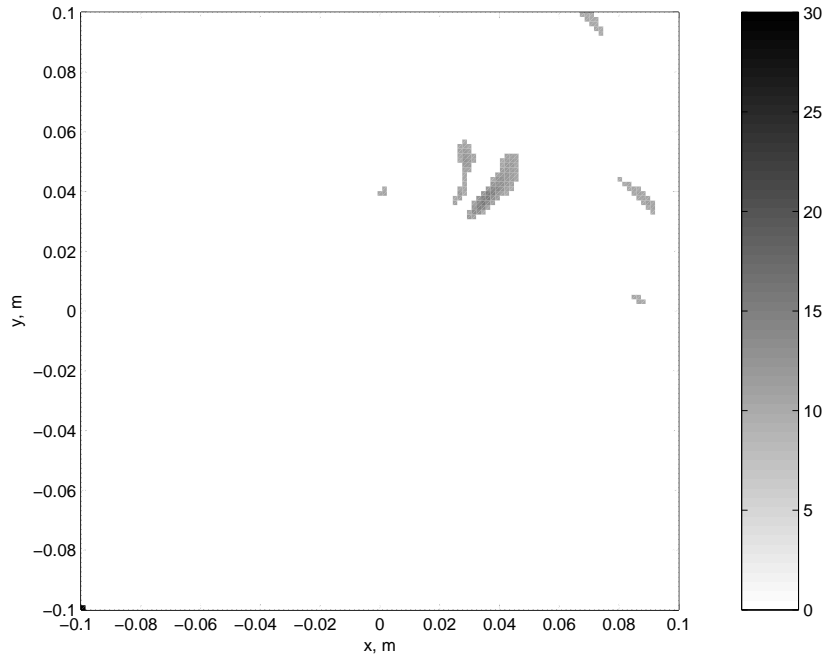
(b) Pixel differences > 10.0 dB.

Figure 5.12:   Magnitude of pixel differences (30.0 dB dynamic range) between Fig. 5.9(b) (monostatic collection geometry) and Fig. 5.10(b) (fixed bistatic collection geometry). The observed differences are due primarily to multipath effects and are therefore not problematic.
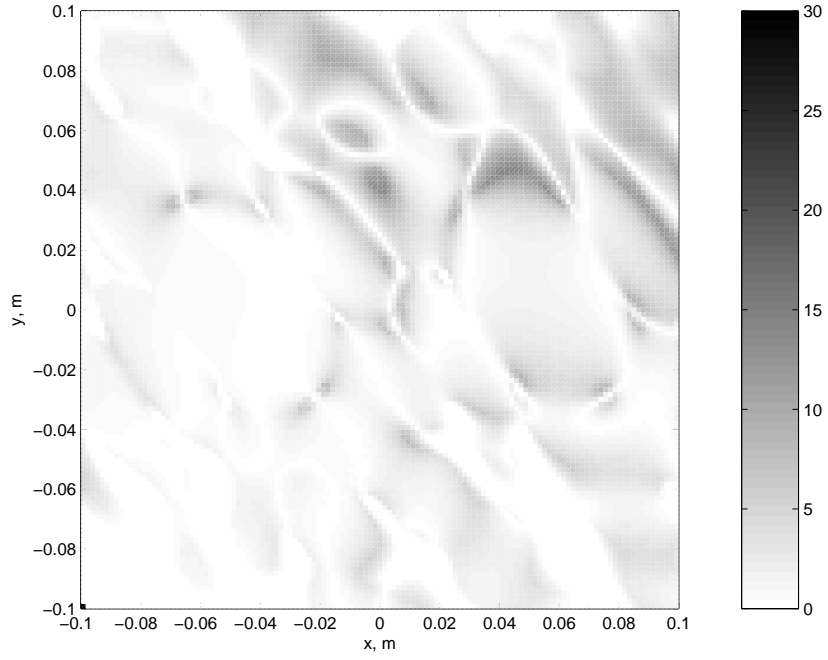
(a) All pixel difference values.
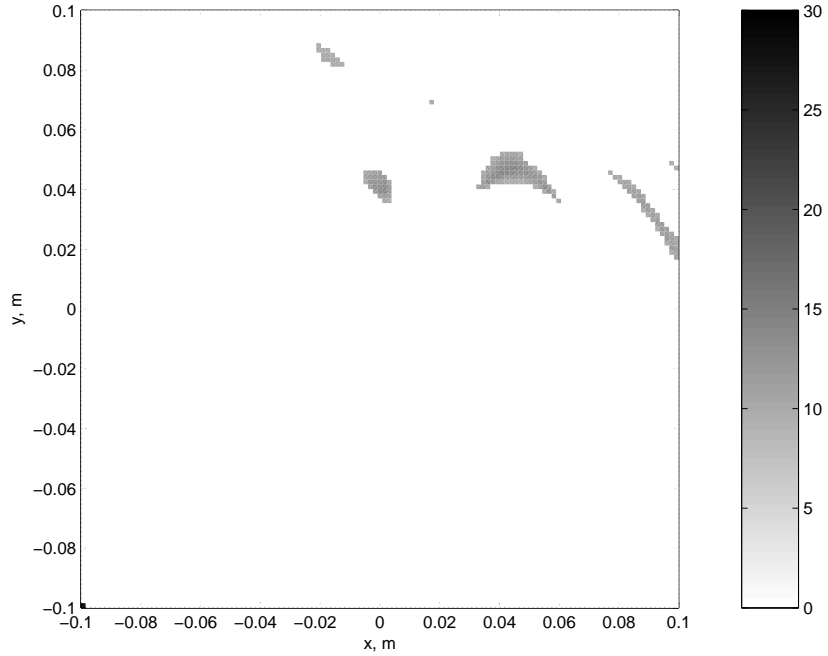
(b) Pixel differences > 10.0 dB.

Figure 5.13:   Magnitude of pixel differences (30.0 dB dynamic range) between Fig. 5.9(b) (monostatic collection geometry) and Fig. 5.11(b) (variable bistatic collection geometry). The observed differences are due primarily to multipath effects and are therefore not problematic.

147
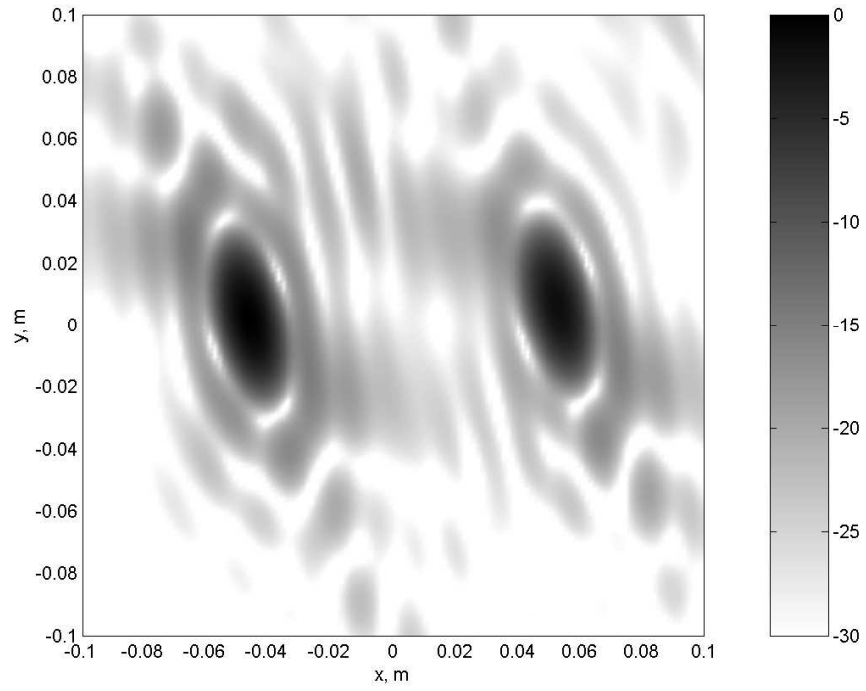
(a) New filter $k_r \cos(\beta/2)$. Image copied from Fig. 5.11(a) for convenience.
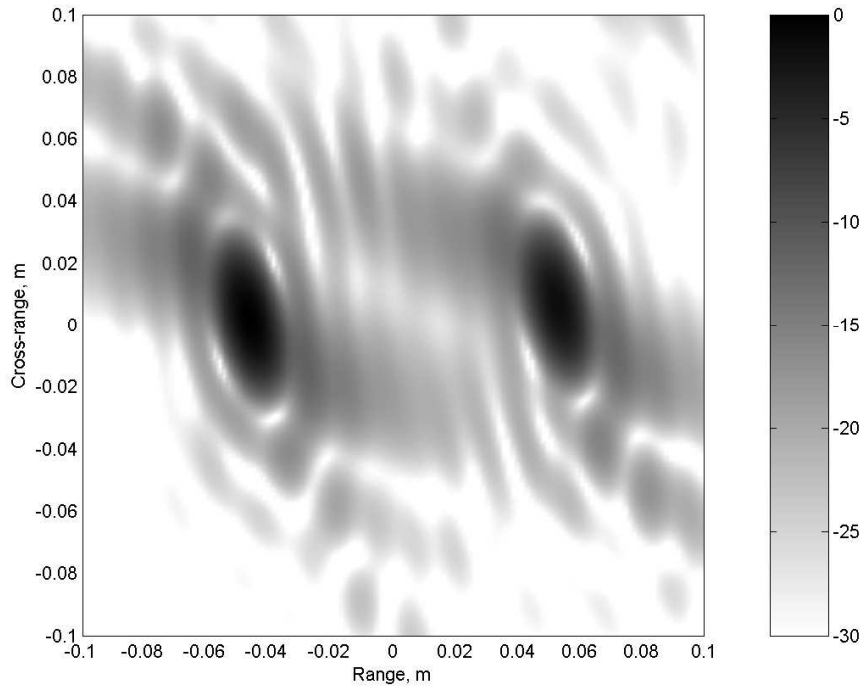
(b) Traditional filter k_r.

Figure 5.14: New and traditional back-projection filter comparison (30.0 dB dynamic range). Use of the new filter causes a reduction in sidelobe levels.

5.5.1 Radiative Near-Field Region. Traditionally, determination of the radar-to-target range required to place the target in the far-field has been based on the first assumption since it is usually the most restrictive. If the antenna is small compared to the maximum target width W (i.e., the scene's cross range extent) the range r_c from the antenna phase center to the scene center is related to the maximum allowable phase deviation ϕ_{max} across the EM wave and is given by (4.15) [72]

$$r_c = \frac{\pi W^2}{4\lambda\phi_{\mathrm{max}}},\tag{5.51}$$

where λ is the illumination wavelength. The far-field criterion is usually derived by limiting the allowable phase deviation to $\pi/8$ radians, (4.16)

$$r_c \geq \frac{2W^2}{\lambda}.\tag{5.52}$$

In practice, certain complex scattering objects require a distance of more than five times the standard far-field criteria to give accurate imaging results [72].

Assuming the scene is located many wavelengths from the finite transmission/reception antennas (i.e., $r \gg \lambda$) the locus of points with equal phases form a spherical shell. This spherical shape is a direct consequence of the uniform EM wave propagation velocity, dictating that points at equal ranges also share equal phases. Thus, the region

$$\lambda \ll r < \frac{2\Delta h^2}{\lambda},\tag{5.53}$$

is defined as the radiative near-field where the r is large enough that radiation fields dominate (as opposed to induction or quasi-static fields [59]), but the target region is large enough to require accounting for the spherical curvature of the EM waves. Even for wide-angle SAR/ISAR collection scenarios, the target is almost always contained in the radiative zone.

The literature contains several algorithms addressing SAR/ISAR imaging in the radiative near-field scenario. One of the earliest discusses removal of the first as-

sumption in the 2-D monstatic/bistatic scenario [16]. Another paper uses a 3-D scenario, but only addresses the first two assumptions and limits itself to the monostatic case [48]. In [22], all three far-field assumptions are addressed, but in a 2-D geometry using a tomographic approach. This chapter uses the most generic 3-D bistatic geometry, including corrections for all three far-field assumptions. Note, while all of these approaches attempt to localize radar echoes from near-field sources, this is not the same as using near-field radar signatures to predict far-field signatures. Various techniques to address the near-field to far-field signature problem are reviewed in [75].

5.5.2 Near-Field Range Profiles. Removing the three far-field assumption components allows the expression for the far-field range profile $p_{\theta,\phi}(r)$ from (5.22) to be rewritten in the radiative near-field $p_{\theta,\phi}^n(r)$ as

$$p_{\theta,\phi}^n(r) = \int_{-\infty}^{\infty} \int_{-\infty}^{\infty} \int_{-\infty}^{\infty} A_{\mathrm{TX}}(\theta,\phi) A_{\mathrm{RX}}(\theta,\phi) \frac{|\bar{\rho}_{\mathrm{TX}}|}{|\bar{\rho}_{\mathrm{TX}} - \bar{\rho}|} \frac{|\bar{\rho}_{\mathrm{RX}}|}{|\bar{\rho}_{\mathrm{RX}} - \bar{\rho}|} f(x,y,z) \delta(r_b^n - r) \mathrm{d}x \mathrm{d}y \mathrm{d}z.$$
(5.54)

The new terms in (5.54) are addressed individually.

Amplitude terms $A_{\mathrm{TX}}(\theta,\phi)$ and $A_{\mathrm{RX}}(\theta,\phi)$ in (5.54) denote the antenna gain patterns for the transmission and reception platforms, respectively. They act as amplitude weights, scaling the overall scene $f(x,y,z)$. During the SAR/ISAR collection, the antenna patterns themselves are assumed constant, but due to changes in position and orientation of the radar platforms, the actual gains seen by a specific voxel location may change for each CPI pulse. The inclusion of these terms removes the third far-field assumption. Note (5.54) assumes $A_{\mathrm{TX}}(\theta,\phi)$ and $A_{\mathrm{RX}}(\theta,\phi)$ are non-dispersive, giving the same gain pattern for all waveform frequencies.

The vectors $\bar{\rho} = [x,y,z]^{\mathrm{T}}$, $\bar{\rho}_{\mathrm{TX}} = [x_{\mathrm{TX}}, y_{\mathrm{TX}}, z_{\mathrm{TX}}]^{\mathrm{T}}$, and $\bar{\rho}_{\mathrm{RX}} = [x_{\mathrm{RX}}, y_{\mathrm{RX}}, z_{\mathrm{RX}}]^{\mathrm{T}}$ are cartesian vectors pointing from the origin to the locations of a specific voxel, the transmitter, and the receiver, respectively. The two ratio terms in (5.54) account for the reduction of EM wave amplitude as a function of range (proportional to $1/r$ [59])

and are normalized to the coordinate system origin. These terms account for the second far-field assumption.

The final difference between (5.54) and its far-field equivalent (5.22) concerns the replacement of the far-field range r_b with the near-field (i.e., "true") range r_b^n

$$r_b^n = \frac{1}{2}(r_{\text{TX}}^n + r_{\text{RX}}^n), \tag{5.55}$$

where

$$r_{\text{TX}}^n = |\bar{\rho}_{\text{TX}} - \bar{\rho}| - |\bar{\rho}| \tag{5.56}$$

and

$$r_{\text{RX}}^n = |\bar{\rho}_{\text{RX}} - \bar{\rho}| - |\bar{\rho}|. \tag{5.57}$$

Inclusion of r_b^n accounts for the first, and most important, of the far-field assumptions, modeling the effects of wavefront curvature.

5.5.3   Modification of BPA for Near-Field Imaging.   Incorporation of near-field corrections into BPA is relatively simple and computationally inexpensive since BPA processes individual range profiles directly in the image domain. This relative ease stands in sharp contrast to the non-tomographic RM correction methods reviewed in Sec. 2.4.1 where only partial RM correction demanded substantial algorithm modifications. The algorithm begins with the same four steps as far-field BPA. The superscript n denotes data collected in the radiative near-field.

1. Declare a matrix of zeros $f(x, y, z)$ where each element corresponds to a single voxel.

2. Obtain $P_{\theta_b,\phi_b}^n(k_r) = \mathcal{F}[p_{\theta_b,\phi_b}^n(r)]$ for a given CPI pulse either directly (for an ISAR system) or via the FT (for a SAR system).

3. Multiply $P_{\theta_b,\phi_b}^n(k_r)$ by $[k_r \cos(\beta/2)]^2 \cos(\phi_b)$ to obtain $Q_{\theta_b,\phi_b}^n(k_r)$.

4. Take the IFT of $Q_{\theta_b,\phi_b}^n(k_r)$ (usually with zero-padding) to obtain $q_{\theta_b,\phi_b}^n(r)$.

The function $q_{\theta_b,\phi_b}^n(r)$ represents the filtered version of the near-field range profile $p_{\theta_b,\phi_b}^n(r)$. The δ-function in (5.54) ensures the value of $p_{\theta_b,\phi_b}^n(r)$ (and therefore $q_{\theta_b,\phi_b}^n(r)$) at a given r value is only a function of scene elements at the same r value. Furthermore, since the terms $|\bar{\rho}_{\mathrm{TX}}|/|\bar{\rho}_{\mathrm{TX}} - \bar{\rho}|$ and $|\bar{\rho}_{\mathrm{RX}}|/|\bar{\rho}_{\mathrm{RX}} - \bar{\rho}|$ are constant as a function of r, they can be pulled through the integrals in (5.54) allowing the second component of the far-field assumption to be corrected via division by these terms. This division creates an amplitude corrected function

$$s_{\theta_b,\phi_b}^n(r) = \frac{|\bar{\rho}_{\mathrm{TX}} - \bar{\rho}|}{|\bar{\rho}_{\mathrm{TX}}|} \frac{|\bar{\rho}_{\mathrm{RX}} - \bar{\rho}|}{|\bar{\rho}_{\mathrm{RX}}|} q_{\theta_b,\phi_b}^n(r). \tag{5.58}$$

Using this new function, the algorithm proceeds by calculating the near-field range r_b^n to each voxel and then using a 1-D interpolator to estimate $s_{\theta_b,\phi_b}^n(r)$ at each value, back-projecting the scene over an ellipsoid and correcting for the first far-field assumption. The back-projection operation results in an estimate of the function $A_{\mathrm{TX}}A_{\mathrm{RX}}f(x,y,z)$ from a single CPI pulse. Recovering an estimate of $f(x,y,z)$ entails dividing these back-projected results by $A_{\mathrm{TX}}A_{\mathrm{RX}}$, correcting for the third and final far-field assumption component. These actions allow the remaining steps of the near-field BPA to be written as

5) Obtain $s_{\theta_b,\phi_b}^n(r)$ from $q_{\theta_b,\phi_b}^n(r)$ using (5.58).

6) Calculate the r_b^n value for each voxel in the scene $f(x,y,z)$ using (5.55).

7) Using a 1-D interpolator, calculate the value of s_{θ_b,ϕ_b}^n for each voxel based on its r_b^n value.

8) Divide the interpolation results by $A_{\mathrm{TX}}A_{\mathrm{RX}}$.

9) Multiply the interpolated values by $\exp[-j\min(k_r)r_b]$.

10) Add the resulting voxel values to $f(x,y,z)$.

11) Repeat steps 2-10 for each CPI pulse.

The additional computation burden carried by near-field BPA is relatively minor. The range amplitude correction in step 5 can be calculated once for the entire

CPI. The back-projection over ellipses instead of planes (step 7) simply involves taking true vector magnitudes instead of using the trigonometric functions in (5.15). The most expensive operation is the correction for the antenna pattern (step 8) since the antenna pattern mapping to the xyz image domain changes for each pulse. None-the-less, this operation does not change the overall computational complexity, it simply adds additional overhead to the existing $O(N^5)$ algorithm.

The reader may note, the derivation of far-field BPA made use of the projection-slice theorem to relate the spatial frequency data obtained by each CPI pulse to the image domain. The projection-slice theorem itself assumes planar wavefronts. This observation seems to invalidate the near-field BPA approach. However, the problem is not with the far-field nature of the projection-slice theorem, but the assumption that the near-field data represents spatial frequency domain samples. Since each sample in the spatial frequency domain is defined to represent the response of the scene to a single frequency at a *single* orientation angle, the near-field data is not pure spatial frequency domain data. What is important, is that by back-projecting the range profiles over ellipsoids, the reflected radar energy is placed at the "true" range in the SAR/ISAR image, allowing the returns from near-field scatterers to add coherently despite wavefront curvature effects.

The near-field amplitude corrections as well as the back-projection filter use an "inverse filter" approach. This inversion process amplifies not only the scene data, but the noise as well. For a small Signal-to-Noise Ratio (SNR) (as occurs outside the nominal antenna beamwidth), the noise amplification effects of inverse filter application may actually degrade image quality. To counteract this effect, the user may use either a pseudo-inverse filter which places a fixed limit on the gain of the inversion process, or a Wiener filter which uses SNR data to balance amplitude correction and noise minimization [64].

Finally, it is important to recognize a couple of inaccuracies in the near-field BPA algorithm caused by wavefront curvature effects. First, wavefront curvature

Table 5.3: Near-Field ISAR data collection parameters. Data from "pillars" target consists of 10 independent collections using the parameters below, each at slightly different elevation angles.

Target	Type	f, GHz	N	θ_b, deg	β, deg	P
Bed-of-Nails	Monostatic	12-18	201	135-225	0	451
Bed-of-Nails	Bistatic	12-18	201	88.5-178.5	93	451
Pyramid	Monostatic	12-18	101	97-180	0	141
Pyramid	Bistatic	12-18	101	85-126.5	107	141
Pillars	Monostatic	12-18	101	0-60	0	121

affects the differential volume swept out by the total data collection for each voxel, causing slight spatial variability in the ideal back-projection filter. Second, the IPR function (and therefore the associated image resolution) becomes spatially varying. In practice, the variations in the ideal filter and IPR functions are quite minor and may be safely ignored.

5.6 Near-Field 2-D/3-D ISAR Imagery

A series of 2-D and 3-D ISAR data sets were collected to validate the near-field imaging algorithms. This section presents the results of each experiment. Data collection parameters are listed in Tab. 5.3.

5.6.1 Bed-of-Nails Target. To test the effectiveness of near-field BPA, a large rectangular "bed-of-nails" target was constructed consisting of eleven rows with three vertical wires each. The wires were separated by 15.24 cm (6.0 inches) in each direction. Figure 5.15 contains a target photograph. Illuminated using VV polarization, the wires approximate a series of independent ideal point scatterers. Both monostatic and bistatic geometries were used in the data collection (Tab. 5.3).

Determination of the boundary between the near-field and far-field via (5.52) requires knowledge of the range r between the scene and the antenna phase centers. For the ISAR chamber, the transmission (and monostatic reception) antenna range is 8.23 m (27 ft) while the range to the bistatic reception antenna is 2.43 m (8 ft). Using the less conservative monostatic antenna range, (5.52) gives a maximum cross-

154

Figure 5.15:   Bed-of-Nails target consisting of 33 vertical wires.

range extent of $\Delta h = 0.26$ m using the worst case λ value. However, the target has $\Delta h = 1.524$ m clearly placing it within the near-field of the monostatic and bistatic antennas.

Figure 5.16 shows the far-field BPA and near-field BPA images of the "bed-of-nails" target under monostatic illumination. Illumination is from the left. Subfigure (a) shows the far-field algorithm image. The scene appears to bend away from the monostatic antenna due to the wavefront curvature. Also, wires at the top and bottom edges of the image are defocused due to these same curvature effects. Subfigure (b) illustrates the near-field algorithm image, produced from the same data used to form subfigure (a). Correcting for wavefront curvature has restored the rectangular target shape, while the amplitude corrections have ensured roughly uniform point scatterer amplitudes, independent of spatial location. Scatterers near the image top and bottom also show higher noise levels since the division by $A_{TX}A_{RX}$ amplifies both target echoes and noise.
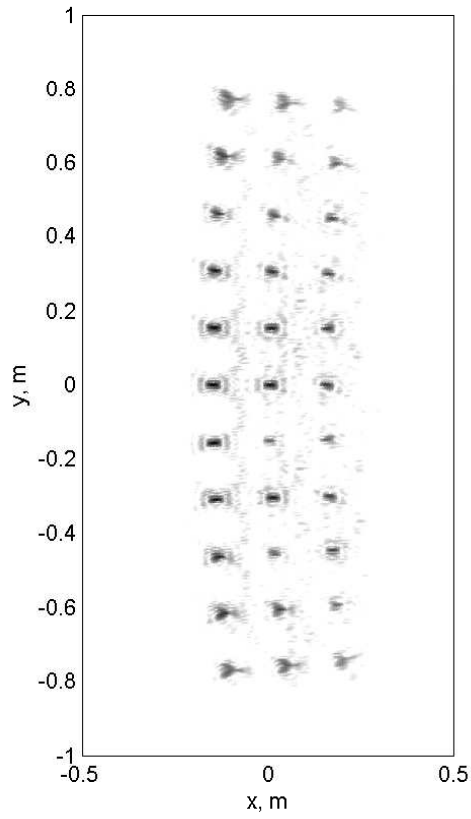
(a) Far-field bed-of-nails image.
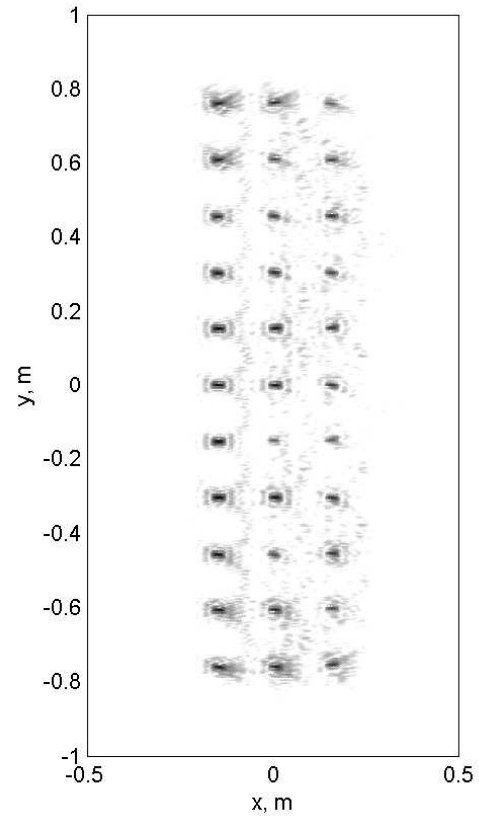
(b) Near-field bed-of-nails image.

Figure 5.16:   Monostatic ISAR Images of the "bed-of-nails" target illustrating the effectiveness of the near-field corrections (30.0 dB dynamic range).

The bistatic images of the "bed-of-nails" target are shown in Fig. 5.17. The transmitter was located at the left, while the receiver was at the top. The far-field image, subfigure (a), shows both defocusing and amplitude effects. Those scatterers at the image top are closer to the receive antenna and thus are much stronger than those at the image bottom. The near-field image, subfigure (b), refocuses all the scatterers. Notice the images of the three topmost scatterers appear to be rotated at slightly different angles. These three scatterers are so close to the reception antenna (< 1.7 m) that they are being imaged from measurably different observation angles. At this short range, these scatterers are close to being in the reactive (as opposed to radiative) near-field, where the spherical wave propagation assumption begins to breakdown.

5.6.2 *Pyramid Target.* While demonstrating the effects of near-field BPA corrections, the images in Sec. 5.6.1 used a strictly 2-D geometry, confining both the radar and the target to the xy-plane. True SAR systems usually collect that data by flying above the ground plane. This situation makes the collection geometry inherently 3-D, even if only 2-D images are produced.

Traditional SAR image formation assumes the radar platform traverses a linear flight path over perfectly flat ground. In this case, the resulting 2-D image is formed in the slant plane defined by the linear flight path and the scene center [65]. The user usually desires a final result in the ground plane, representing the scene as it would appear from an overhead view. A simple trigonometric function makes this correction, projecting the slant plane image into the ground plane. Figure 5.18 illustrates these relationships.

True SAR platforms do not fly perfectly linear paths, especially over the long distances needed to produce high resolution images. This non-linear flight path means the slant plane definition changes for each CPI pulse, leading to distortions in both the slant plane and resulting ground plane imagery. These effects can be removed through a procedure known as out-of-plane correction. The basic idea is to individually project

(a) Far-field bed-of-nails image.   (b) Near-field bed-of-nails image.
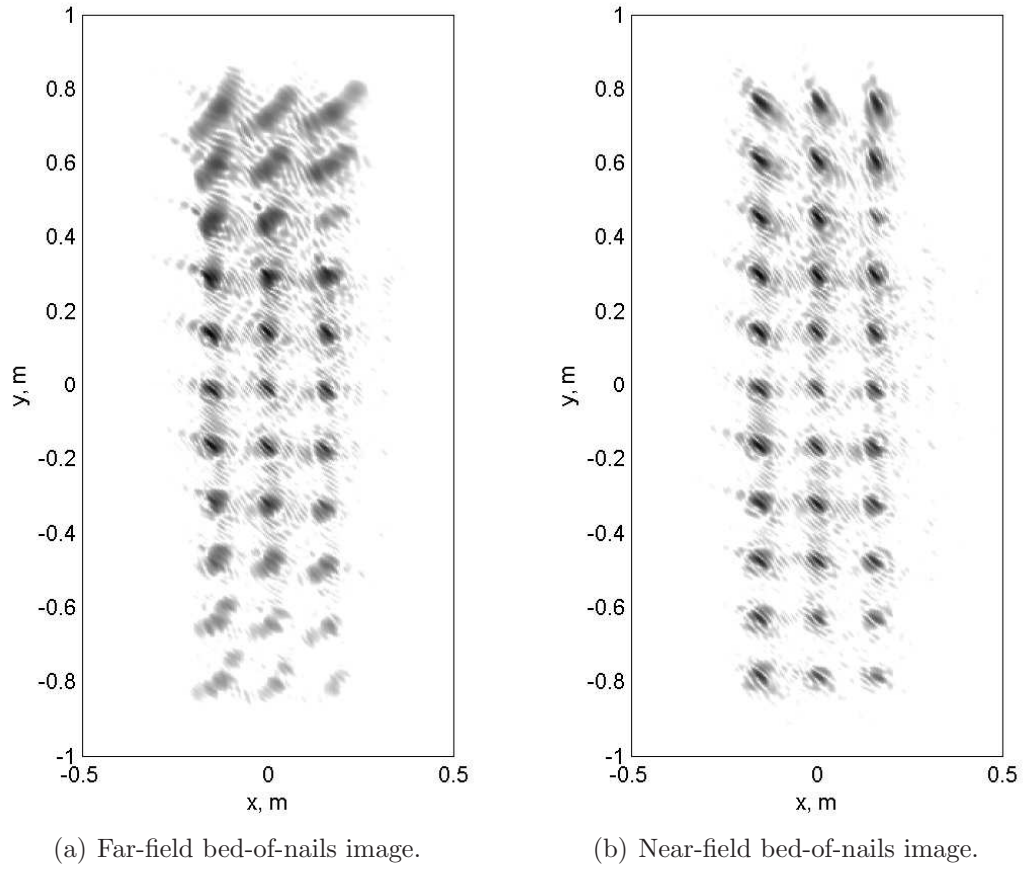
Figure 5.17:   Bistatic ($\beta = 93°$) ISAR Images of the "bed-of-nails" target illustrating the effectiveness of the near-field corrections (30.0 dB dynamic range).
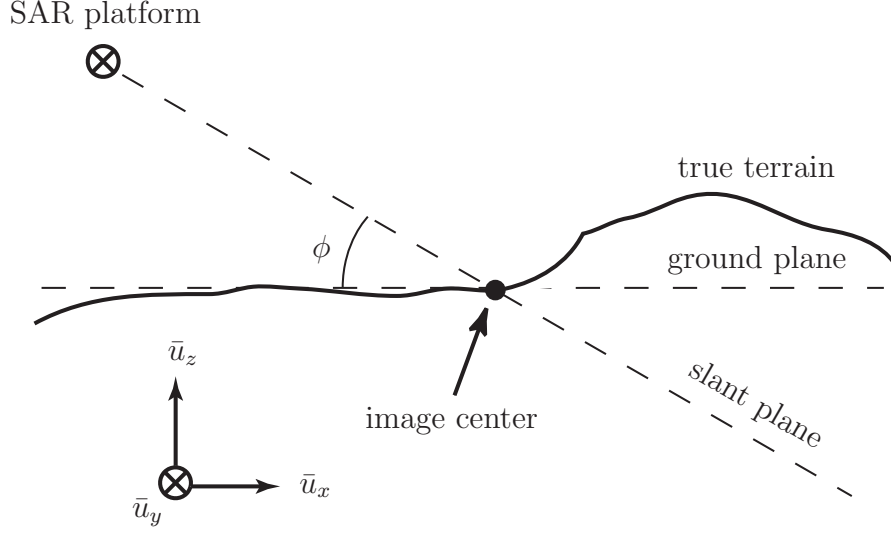
Figure 5.18:   Data collection plane comparison. Platform flies a linear flight path into the page. Traditional SAR images are formed in the slant plane (defined by the flight path and image center) and then projected into the image plane. This process assumes the scene is flat, while the true terrain exhibits height variation. Reprinted from Fig. 2.5.

the spatial frequency domain data from each CPI pulse into the desired slant or ground plane prior to image formation, resulting in an orthographically correct image [65]. Unfortunately, the out-of-plane correction procedure assumes the imaged terrain is in the far-field and perfectly planar, making it inappropriate for WAM-SAR.

The planar-terrain assumption leads to an effect known as layover [36, 65]. For scatterers outside the ground plane (i.e., $z \neq 0$) the range measured by each CPI pulse is somewhat different than if the target were in the ground plane. In the typical airborne SAR scenario, a tall scatterer such as a hill or the top of a building appears closer to the radar, causing such structures to "lay over" towards the radar in the resulting imagery. Using the scenario depicted in Fig. 5.18, the amount of layover (range error) in the image plane may be estimated as

$$\epsilon = z \tan(\phi), \tag{5.59}$$

where ϵ denotes layover and z is the height (i.e., z-coordinate) of a given scatterer.

159

Previous attempts at eliminating layover have used a series of tie-points representing a dense grid known locations to warp SAR images in a post-processing fashion [36]. Unfortunately, this method require high levels of operator interaction and computational complexity. However, using the same terrain information, the BPA allows elimination of layover effects without requiring either operator interaction or post-processing efforts.

The far-field and layover limitations of the out-of-plane correction procedure can be eliminated using near-field BPA combined with knowledge of the actual terrain contours. Unlike traditional PFA, near-field BPA calculates voxel values in parallel, allowing the user to specify any desired set of voxels. For 2-D SAR image formation using a 3-D collection geometry, the user simply selects a set of voxels (x, y, z) forming a 2-D skin covering the terrain. Near-field BPA is then used to estimate $f(x, y, z)$ for each of these points. By ensuring each voxel has a unique xy-value, the resulting voxels form an orthographically correct image of the terrain contours. Ignoring the z-component and viewing the results as a 2-D image projects the voxels into the xy-ground plane. Obviously, correcting for the layover effect requires knowledge of the true terrain profile. This knowledge (the same knowledge used to define the "tie-points" mentioned above) might come from simply assuming ellipsoidal Earth curvature, or by incorporating knowledge from an independent source such as a contour map. In either case, the strength of near-field BPA to address this issue comes not from an ability to collect this information, but to incorporate it in the image generation processes without significant algorithm modifications or additional assumptions.

To illustrate the layover correcting abilities of near-field BPA, a styrofoam pyramid was covered with a series of 25 0.64 cm (0.25 in) diameter ball bearings designed to approximate 3-D ideal point scatterers. The pyramid's base was 50×50 cm and had a height of 40 cm. Figure 5.19 contains a target photograph. The target was illuminated with VV-polarization using the parameters given in Tab. 5.3. Both the transmission and reception antennas were confined to the xy-plane (i.e., $z = 0$).

Figure 5.19: Pyramid target. Ball bearings placed on each of the four styrofoam blocks.
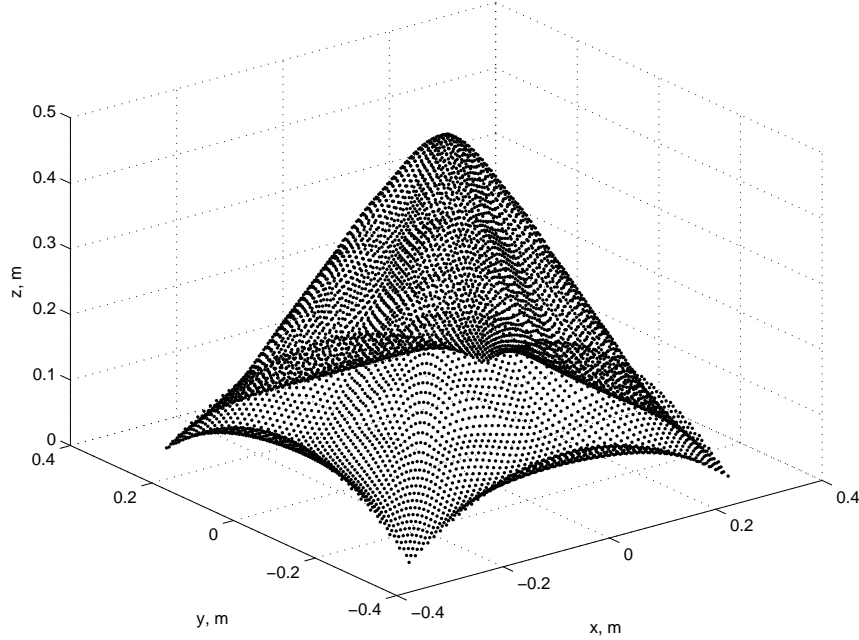
Figure 5.20:   3-D target contour map. Built using an interpo-
lation of known target contour points.

A cubic interpolator calculated a 3-D target contour map using knowledge of
the true scatterer locations. The result defined the corresponding z value used for
each (x, y) pixel in the resulting 2-D near-field BPA ISAR image. Fig. 5.20 illustrates
this 3-D contour map.

Figure 5.21 shows the ISAR images resulting from the monostatic collection,
both with and without the contour map corrections. Subfigure (a) contains the near-
field monostatic BPA image assuming $z = 0$ for all pixels. A slight bowing is visible as
though the pyramid's top has been pulled towards the lower right hand corner of the
image. This effect is layover. Since the target is above the antenna, the layover occurs
away from the antenna. In traditional SAR imagery, where the antenna is above
the target, the layover direction reverses. Some defocusing of the center (highest)
scatterer is also visible in that the sidelobes are blurred into the mainlobe response.
Subfigure (b) contains the near-field BPA monostatic image when the z-coordinate is
defined by the 3-D skin. Injection of true height information has removed the layover

162

effect. Also, the mainlobe and sidelobe responses are clearly delineated, indicating better focusing of the center scatterer.

The $z \neq 0$ effects are not severe in the monostatic case due to the relatively large monostatic antenna range compared to the target height. In the bistatic case (Fig. 5.22), the effects are more noticeable. Subfigure (a) illustrates the $z = 0$ near-field bistatic BPA results. The layover effect is much more dramatic as the top of the pyramid appears to be pulled towards the image bottom. Also, scatterer amplitude decreases as a function of height. This decrease results from the antenna pattern's amplitude fall-off in the vertical dimension. Traditional SAR processing ignores this fall-off due to the $z = 0$ assumption. Subfigure (b) shows the effect of injecting the $z \neq 0$ surface into near-field BPA. This action corrects the layover problem and restores appropriate scatterer amplitudes.

In both the monostatic and bistatic cases, the addition of prior height knowledge has been shown to improve the image quality, removing effects on warped ground planes. This prior knowledge is increasingly available from outside sources, but is difficult to incorporate using traditional SAR/ISAR imaging techniques. However, near-field BPA allows incorporation of this data without any increased computational complexity. The result is imagery with highly focused scatterers appearing at orthographically correct locations.

5.6.3 Pillars Target. Due to the inherent limitations of the available ISAR chamber, pure 3-D ISAR imagery production is challenging. While the target and bistatic reception antenna can be precisely rotated in the xy-plane, no automated capability exists to vary the height of either the target or antennas during the data collection process. To add a rudimentary height variation capability, a series of nine 5 cm thick styrofoam plates were constructed. These plates allow a given target to be raised in 5 cm increments from the standard $z = 0$ position to $z = 45$ cm. The resulting series of ten independent ISAR collections is then combined using near-field BPA to produce 3-D imagery. Unfortunately, the act of inserting these styrofoam
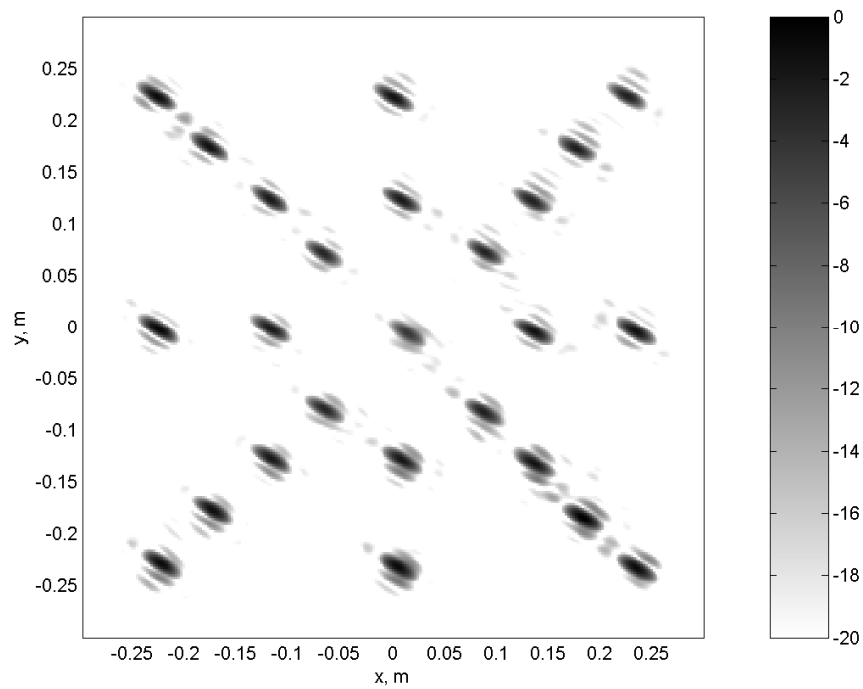
(a) Image w/o contour corrections
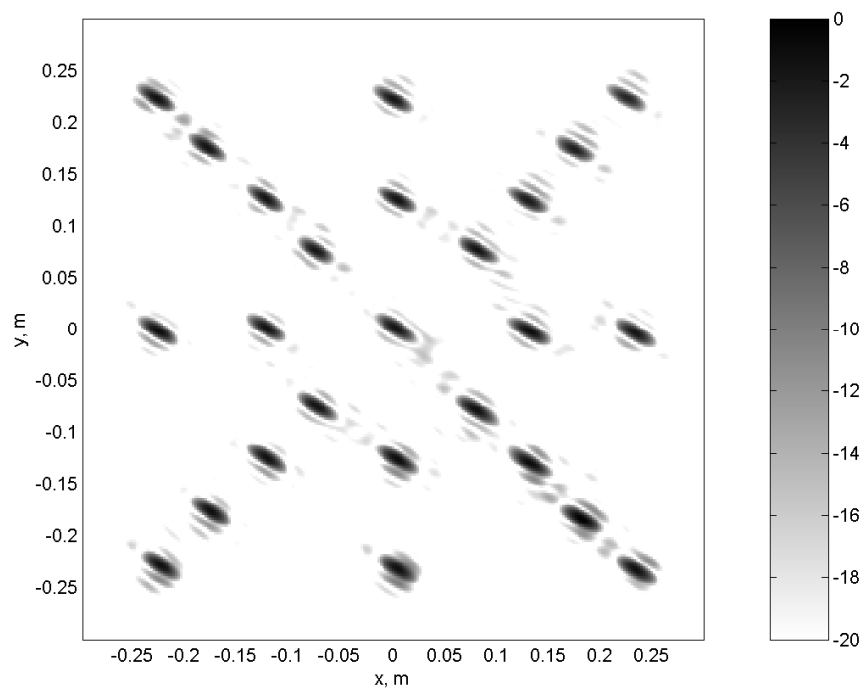
(b) Monostatic Image w/contour corrections

Figure 5.21: Monostatic contour map ISAR images (20.0 dB dynamic range).
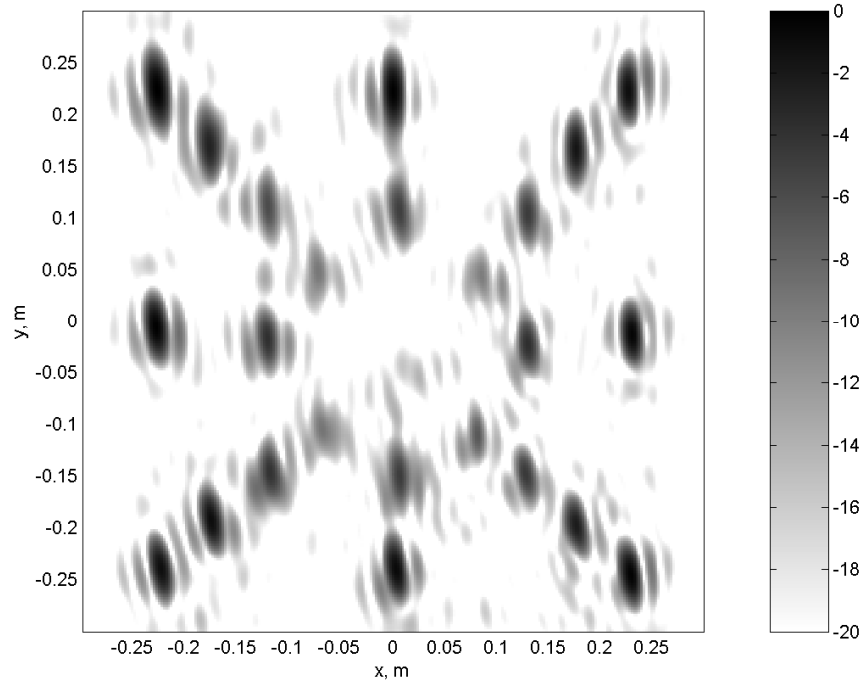
(a) Image w/o contour corrections ($\beta = 107°$)
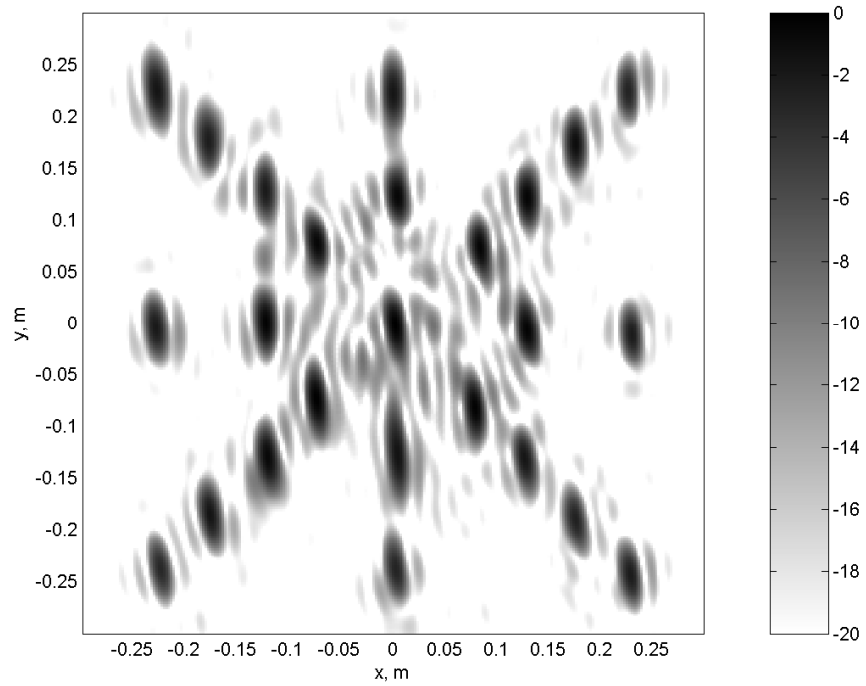
(b) Image w/ contour corrections

Figure 5.22:   Bistatic ($\beta = 107°$) contour map ISAR images (20.0 dB dynamic range).

plates requires removing and replacing the target. This procedure leads to subtle, unknown changes in target position and prevents perfect coherent combination of the ten independent ISAR collections into a single 3-D ISAR image[4]. Despite these limitations, the following results demonstrate the 3-D imaging capabilities of near-field BPA.

The ISAR target in this section consists of four 0.64 cm (0.25 in) ball bearings placed on the end of four narrow styrofoam pillars of heights 10, 20, 30, and 40 cm. The pillars were arrayed around the edges of a 40 cm diameter styrofoam column. Figure 5.23 is a target photograph. As viewed from this perspective, scatterer height increases from left to right (the second scatter *appears* lowest because it is further away from the camera). The collection parameters are listed in the final row of Tab. 5.3 (pg. 154). Only a monostatic collection was possible because the combined height of the target and the mount was well outside the bistatic receiver's vertical beamwidth.

Figure 5.24 demonstrates the effectiveness of 3-D near-field BPA. Figure 5.24 (a) shows the 2-D image produced when no styrofoam plates were used to raise the target. The algorithm assumed $z = 40$ cm, consistent with the tallest (bottom left) scatterer. Due to the lack of vertical diversity in the ISAR collection, all four scatterers appear at approximately the same amplitude. However, the sidelobes of the two highest scatterers (image bottom) are much better structured than the lowest scatterers (image top). This difference results from the validity of the height assumption used to form the image, but is not sufficient to provide a reliable scatterer height estimate.

The ISAR data from all ten collections was combined to produce a 3-D image. Subfigure (b) is the 2-D $z = 40$ cm slice of that 3-D image. The addition of vertical diversity has left the highest scatterer essentially untouched, but significantly reduced the amplitude of the remaining scatterers. The lowest scatterer is virtually eliminated.

---

[4]This problem is also encountered in airborne SAR collections where radar platform locations cannot be known precisely. These errors can be minimized using various "autofocus" algorithms [28, 65]
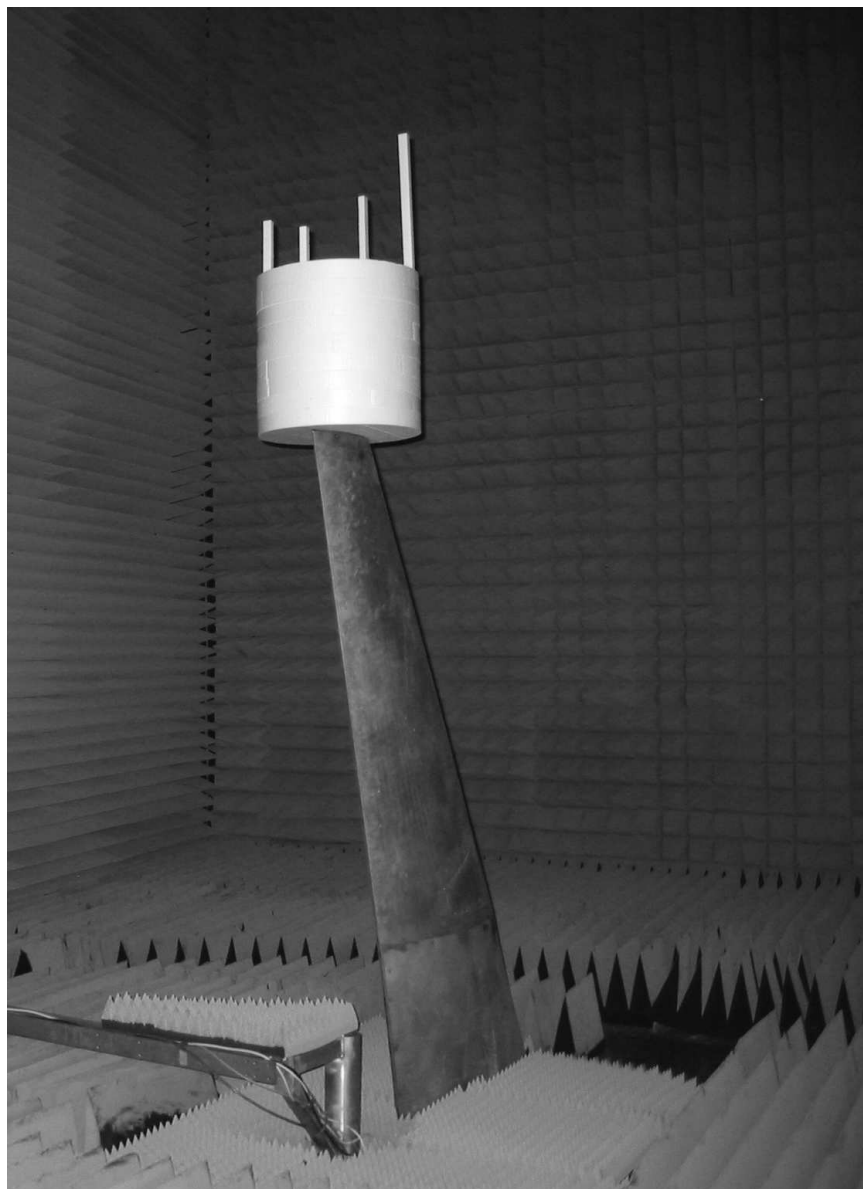
Figure 5.23:   Pillars target mounted on ogive pylon. Pillar heights from left to right are 10, 20, 30, and 40 cm. Several styrofoam disks, used to vary target elevation, are also visible.
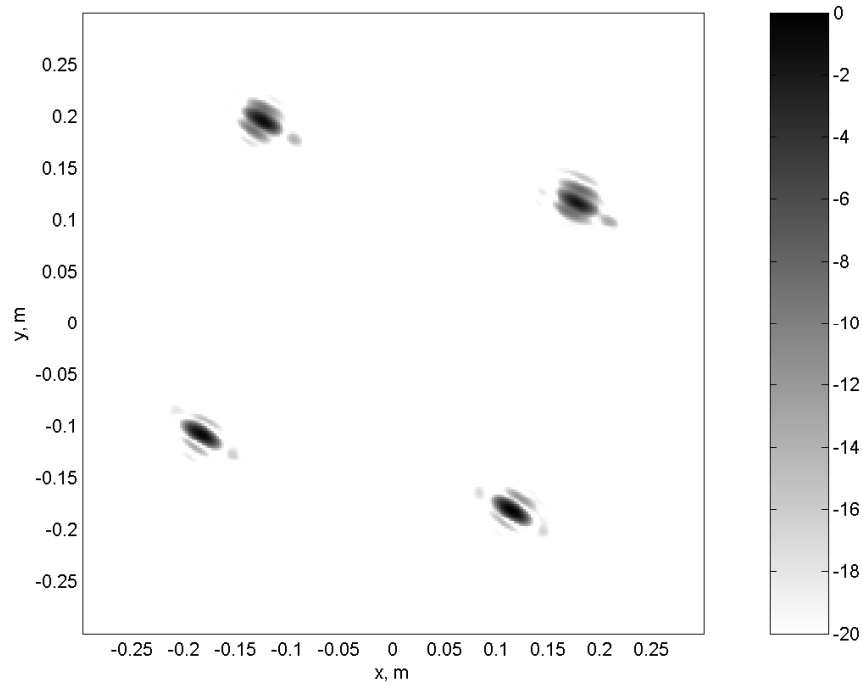
(a) 2-D Image focused on highest (bottom left) scatterer
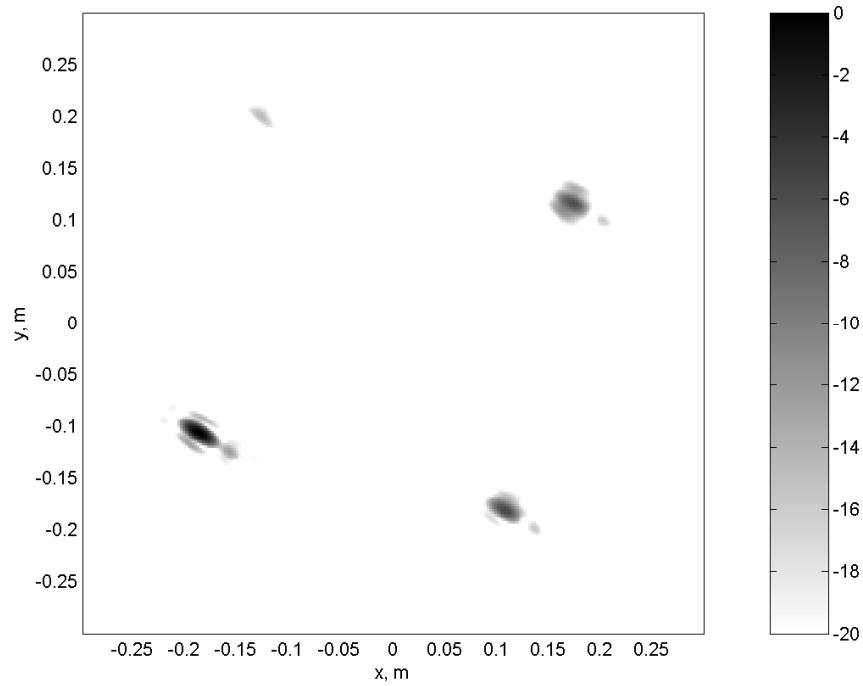
(b) 2-D slice of 3-D Image at height of highest (bottom left) scatterer

Figure 5.24:   ISAR Images of the pillars target (20.0 dB dynamic range). Addition of vertical data diversity allows vertical filtering.

Table 5.4: Peak scatterer values for pillars target. The peak values are listed for the images in Fig. 5.24.

Scatterer Attributes			Peak Scatterer Value, dB		
Number	Location	Height, cm	2-D	3-D	Predicted
1	top left	10	-0.7	-14.7	-20.5
2	top right	20	-1.5	-6.1	-15.8
3	bottom right	30	0.0	-5.6	-6.1
4	bottom left	40	-0.4	0.0	0.0

Table 5.4 quantifies the observed and predicted vertical filtering performance. In the 2-D image (Fig. 5.24(a)), the amplitudes are roughly equal. These small variations could be caused by several effects including noise and target-mount interactions. When the 2-D slice from the full 3-D image is analyzed (Fig. 5.24(b)), the scatterer amplitudes decrease dramatically as a function of height.

Given an antenna range of 8.23 m and the vertical data span of 0.5 m, the total elevation span is 3.1°. Equations (5.30) and (5.31) allow calculation of the vertical -4.0 dB resolution as $\delta v = \delta z = 0.165$ m. Using an appropriately scaled sinc($\cdot$) function to approximate the vertical point scatterer IPR allows calculation of the predicted amplitudes in the last column of Tab. 5.4. The predicted and actual 3-D values for the 30 cm high scatterer are quite accurate, especially when accounting for scatterer three's stronger 2-D image response. This fact demonstrates the accuracy of the resolution prediction. Subsequent scatterer amplitudes continue to fall, but not as quickly as predicted. This effect is likely related to the subtle target misalignment caused by adding styrofoam plates between collections. These small differences prevent the near-perfect coherent phasing required to form a sinc-like null structure.

5.7 Summary

This chapter introduced a technique for solving the WAM-SAR data focusing problem. The relationship between traditional monostatic range measurements and bistatic measurements in an arbitrary 3-D geometry is first derived. While this result was not new, the derivation methodology and accompanying validation with measured

data were. The 3-D bistatic spatial frequency paradigm was used to derive new 3-D resolution and resolution-like metrics applicable to wide-angle data collected in arbitrarily oriented coordinate systems. The chapter contains a new back projection filter capable of accounting for the variable bistatic angles likely to occur in WAM-SAR data collections. The 2-D traditional BPA was also extended to the 3-D near-field bistatic case, correcting for RM effects. While specific components of this extension are present in the literature, they have not been combined and tested with measured data. Additionally, the use of a tomographic algorithm enabled seamless inclusion of ground contour data. This technique has not been observed in the literature. Appendix C includes the `Matlab`® code used to produce the pyramid target images (Sec. 5.6.2) since this represents the most likely data collection scenario for WAM-SAR. While specific SAR and ISAR applications may require additional processing to perform functions such as autofocusing, speckle reduction, or sidelobe control, the algorithm presented here forms the core of wide-angle SAR/ISAR processing routines.

VI. Theory of Anti-Aliasing with Randomized Stepped-Frequency Waveforms

Having solved the challenge of wide-angle focused Synthetic Aperture Radar (SAR) image formation with Chapter V's near-field Back-Projection Algorithm (BPA), focus shifts towards addressing the second Wide-Angle Multistatic SAR (WAM-SAR) implementation problem, anti-aliasing of focused SAR imagery.

This chapter examines the aliasing problem from a Two-Dimensional (2-D) monostatic perspective, consistent with the monostatic wide-angle architecture (Sec. 2.1). As opposed to the hundreds of channels required by the proposed phased-array implementation, the anti-aliasing technique developed here requires only a two-channel system (one transmit and one receive channel), dramatically simplifying the radar hardware and processing [143]. Chapter VIII presents anti-aliasing technique application to 3-D monostatic/bistatic scenarios needed for full WAM-SAR implementation.

Figure 6.1 (reprinted from Fig. 2.1 for convenience) illustrates a wide-angle monostatic SAR data collection. It consists of a SAR aircraft traversing a linear flight path with a velocity magnitude v_a, transmitting an extremely wide beam normal to its flight path. The beam illuminates a large ground swath, using range gating to establish minimum and maximum range values ($R_{\min}$ and $R_{\max}$). From this stripmap transmit pattern, the user desires the ability to form alias-free SAR images over an arbitrary ground patch illuminated by the beam while significantly undersampling the scene along the synthetic aperture.

Most SAR systems use Linear Frequency Modulated (LFM) waveforms due, in large part, to the ease of their generation and processing [28, 65, 100]. LFM waveforms are extremely Doppler tolerant, exhibiting roughly uniform gain over a wide Doppler frequency range. While this property is very useful in certain applications (e.g., Moving Target Indication (MTI)), it causes significant challenges in wide-angle SAR imaging. This chapter introduces a new anti-aliasing technique using continuously transmitted sets of Stepped-Frequency (SF) waveforms. The SF waveform echoes are digitally sampled and then match-filtered to perform pulse compression.
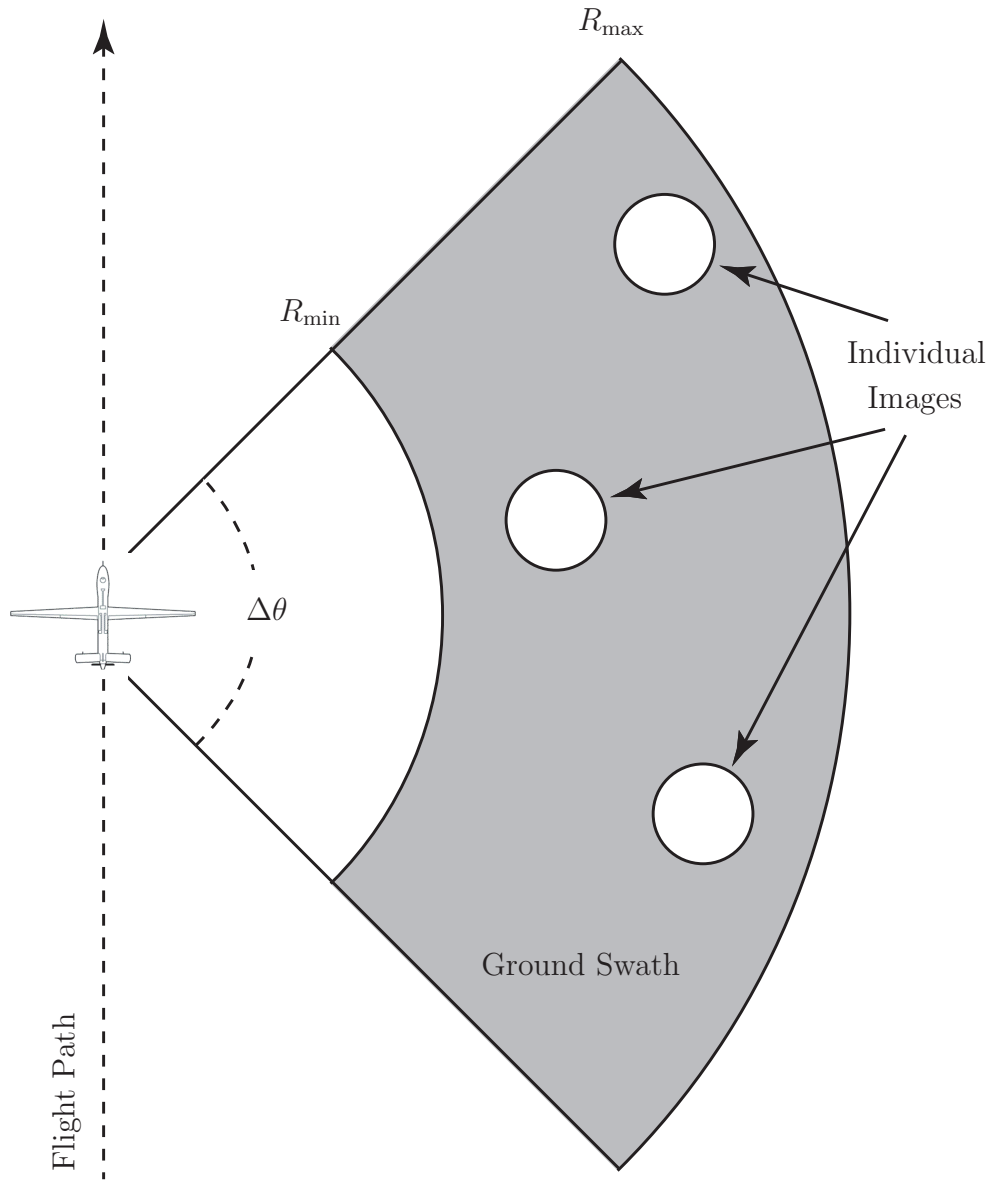
Figure 6.1: Anti-aliasing scenario. A single radar platform transmits an extremely wide beam ($\Delta\theta \approx 90°$) over a large ground swath. Monostatic echoes are received and processed to form a number of small, high resolution, spotlight mode SAR images in parallel. Reprinted from Fig. 2.1.

172

The integration time (i.e., matched filter length) is determined by the length of the artificial Pulse Repetition Frequency (PRF) used to encode the continuous transmission. The SF waveform's Doppler filtering properties mitigate cross range aliasing artifacts. Note, the use of Doppler filters for beamforming in space-based MTI radar was proposed by [120].

The remainder of this chapter is divided into four sections. Section 6.1 characterizes the cross range (Doppler) aliasing problem in terms of antenna theory. The basic anti-aliasing principle is introduced in Section 6.2. Section 6.3 discusses LFM waveforms, showing how their ambiguity function permits aliasing to occur. Section 6.4 discusses SF waveforms and illustrates how sets of these waveforms can be used to approximate the desired rectangular data support region. Finally, selection of subpulse frequency order is reviewed in Section 6.5. This chapter forms the basis for [89] (with contributions from [87, 88]) which addresses the the anti-aliasing technique's theory. Chapter VII validates the theory using a point scatterer simulation. These simulation results are also contained in [85, 87–89].

6.1   *Grating Lobe View of Cross Range Aliasing*

Although usually derived using a Doppler paradigm (Sec. 2.5.1), the relationship between PRF and cross range aliasing is perhaps most easily understood from an array theory perspective [121]. This perspective is depicted in Figure 6.2. The three dots (labeled A, B, and C) correspond to the locations of three sequential samples along the synthetic aperture, spaced by uniform distance δu. The points are collinear indicating a linear SAR flight path. The three solid arrows point in the imaging target direction. To form a synthetic radar beam in a desired direction, the radar echoes from this direction must add constructively. This condition occurs when the total distance traveled by target echoes from each point along the aperture differs by integer multiples of a wavelength λ. Assuming the scatterer of interest is in the synthetic antenna's far-field, the rays connecting the three aperture samples to the

173

target are parallel, making an angle θ with respect to a vector normal to the linear flight path.

The one-way distance traversed between successive synthetic aperture samples differs by a distance d where

$$d = \delta u \sin \theta. \tag{6.1}$$

Since radar echoes travel a two-way path, constructive interference angles between consecutive samples occurs when

$$d = n\frac{\lambda}{2}, \tag{6.2}$$

for some integer n. Combining (6.1) and (6.2) allows calculation of the angles θ_m corresponding to constructive interference for a synthetic array spaced by uniform distance δu

$$\sin \theta_m = m\frac{\lambda}{2\delta u}. \tag{6.3}$$

For $m = 0$, $\theta_m = 0$ and a synthetic beam is formed normal to the SAR flight path. The $m = 0$ beam is often referred to as the array main beam (or mainlobe) and corresponds to the array look direction. Additional beams, referred to as grating lobes, are formed for all other values of m such that $|\theta_m| < 90°$ [121]. Thus, grating lobes only exist when $\delta u > \lambda/2$ and the synthetic aperture is deemed undersampled. This condition is common in SAR systems. Targets within these grating lobes are spatially indistinguishable from targets within the main beam (assuming the antenna gains are the same) resulting in cross range aliasing. SAR systems usually eliminate cross range aliasing artifacts by applying an amplitude taper on the transmit/receive beam (i.e., transmitting a "narrow" beam), placing a spacial filter on the grating lobes. From the array theory perspective, this amplitude taper is equivalent to an element pattern $e(\theta)$. Such an element pattern destroys wide-angle system utility, hence this development assumes an extremely wide element pattern indicating a *real*
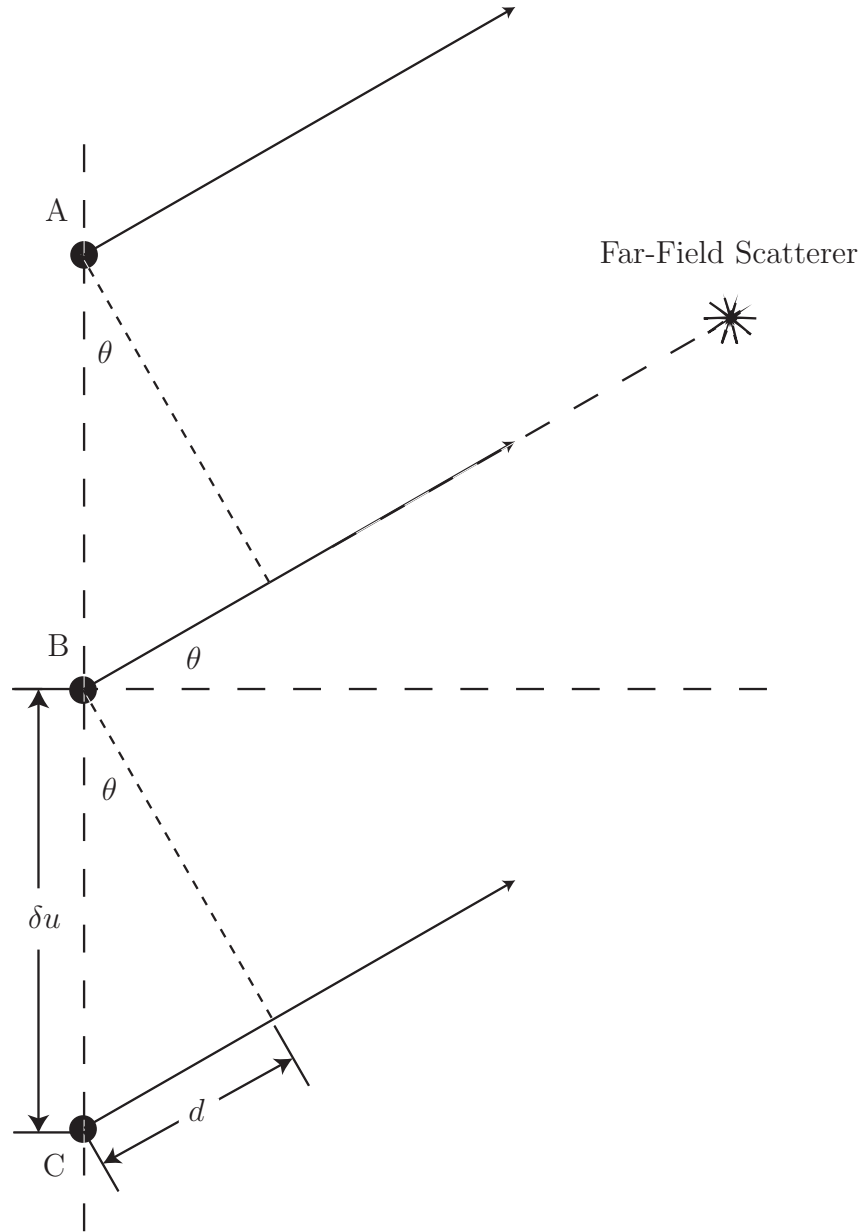
Figure 6.2: Linear antenna array paradigm for SAR image formation. The three dots (labeled A, B, and C) correspond to the locations for three sequential samples along the linear synthetic aperture. The three large arrows point to the imaging target. They are parallel as long as the target is in the synthetic antenna's far-field. The variable δu represents the distance between consecutive aperture samples and d denotes the one-way distance difference from consecutive synthetic aperture samples for a far-field target located an angle θ relative to the figure's horizontal axis.

instantaneous beamwidth of up to 180°

$$e(\theta) = \begin{cases} 1 & |\theta| < 90° \\ 0 & \text{otherwise.} \end{cases} \qquad (6.4)$$

Equation (6.3) would be adequate for characterizing the cross range aliasing problem if SAR systems only formed target images normal to their flight path. However, one of the major advantages of wide angle SAR is its large coverage area. Leveraging this feature requires main beam steering (i.e., squinting [117]) away from the broadside direction. In array theory, a phased array antenna is steered by placing an incremental phase shift on successive antenna elements, effectively introducing a sequential delay in the returns for a narrowband signal. SAR processing steers its *synthetic* beam in the same fashion. Accounting for the effects of this incremental phase shift, (6.3) can be rewritten as

$$\sin \theta_m = m \frac{\lambda}{2 \delta u} + \sin \theta_0, \qquad (6.5)$$

where θ_m is the direction of the mth grating lobe and θ_0 corresponds to the mainlobe direction.

While cross range aliasing artifacts cannot be distinguished spatially, they can be distinguished through Doppler shift. The distance δu between each Coherent Processing Interval (CPI) pulse (i.e., element of the synthetic array being formed) is

$$\delta u = \frac{v_a}{\text{PRF}}, \qquad (6.6)$$

where v_a is the SAR platform velocity magnitude. Substituting this relationship into (6.5) yields

$$\sin \theta_m = m \text{PRF} \frac{\lambda}{2 v_a} + \sin \theta_0. \qquad (6.7)$$

Multiplying through by $2v_a/\lambda$ gives

$$\frac{2v_a \sin\theta_m}{\lambda} = m\mathrm{PRF} + \frac{2v_a \sin\theta_0}{\lambda}. \tag{6.8}$$

Recall the monostatic Doppler frequency shift f_d of a given scatterer is defined by (2.7)

$$f_d = \frac{2v_r}{\lambda}, \tag{6.9}$$

where v_r is the relative velocity magnitude between the radar and the scatterer. Assuming the scatterer is stationary and located in the mth grating lobe, the relative velocity is simply defined by $v_r = v_a \sin\theta_m$ (2.8) and (6.8) can be rewritten as

$$f_{d_m} - f_{d_0} = m\mathrm{PRF}, \tag{6.10}$$

where f_{d_m} and f_{d_0} are the Doppler shifts of scatterers in the mth grating lobe and mainlobe respectively. In words, (6.10) shows the difference in Doppler shift of a target within the mainlobe and a target within the mth grating lobe is $m\mathrm{PRF}$. This result indicates for a SAR image of a relatively small scene (i.e., with a small Doppler frequency spread), cross range aliasing artifacts only arise from scatterers having Doppler shifts which differ from the scene Doppler shift by integer PRF multiples.

6.2   Anti-Aliasing with Rectangular Data Support Regions

This section outlines a theoretical approach for cross range aliasing artifact elimination. It begins by demonstrating how the data support region's shape effects individual range profile generation. These effects can used to eliminate aliasing artifacts from SAR images. The aliasing problem is approached here from an "information only" perspective, determining which scene information is required to eliminate aliasing artifacts without explicitly defining the waveform used to collect that information.

177

6.2.1 Range Profile Generation. At a single location along the synthetic aperture, a SAR system illuminates a ground patch $p(t, f_d)$ consisting of M scatterers at widely varied locations. Assuming the ground patch is composed of ideal point scatterers, it can be represented by

$$p(t, f_d) = \sum_{m=0}^{M-1} A_m \delta(t - t_m, f_d - f_{d_m}), \tag{6.11}$$

where $\delta(\cdot, \cdot)$ is a 2-D delta function and A_m, t_m, and f_{d_m} are the complex amplitude, time delay, and Doppler shift of the mth scatterer, respectively. The 2-D Fourier transform of (6.11) is given by

$$P(f, t_d) = \mathcal{F}\left[p\left(t, f_d\right)\right], \tag{6.12}$$

where $\mathcal{F}$ denotes the Fourier transform. Note, the dual of t, a time delay, is the frequency f, and the dual of f_d, a Doppler frequency shift, is the time t_d.

Assuming $p(t, f_d)$ is a continuous function of both t and f_d, $P(f, t_d)$ has infinite extent in both variables. Thus, accurate estimation of $p(t, f_d)$ requires knowledge of $P(f, t_d)$ over an infinite frequency band and infinite time duration. Since it is impractical to acquire such information, it is assumed a measurement method exists to acquire frequency information over a bandwidth B and time information over a duration τ. With these limitations, the measured estimate of $P(f, t_d)$, denoted $\hat{P}(f, t_d)$, is given by

$$\hat{P}(f, t_d) = \text{rect}\left(\frac{f}{B}\right) \text{rect}\left(\frac{t}{\tau}\right) P(f, t_d), \tag{6.13}$$

where

$$\text{rect}\left(\frac{x}{X}\right) = \begin{cases} 1, & -\frac{X}{2} \leq x \leq \frac{X}{2} \\ 0, & \text{otherwise.} \end{cases} \tag{6.14}$$

Offsets due to the carrier frequency (leading to phase shifts in the transform domain) are ignored as they do not effect the analysis. The product of the two rect functions

in (6.13) forms a 2-D uniform amplitude rectangular mask in (f, t_d) space, the extent of which is termed the *data support region.*

Using (6.13) and 2-D Fourier processing, the estimate of the scene $\hat{p}(t, f_d)$ is given by

$$\hat{p}(t, f_d) = \mathcal{F}^{-1} \left[\text{rect}\left(\frac{f}{B}\right) \text{rect}\left(\frac{t_d}{\tau}\right) P(f, t_d) \right], \tag{6.15}$$

where $\mathcal{F}^{-1}$ denotes the inverse Fourier transform. Applying the convolution property and evaluating the inverse Fourier transforms of the two rect functions results in

$$\hat{p}(t, f_d) = [B\tau\text{sinc}(Bt)\text{sinc}(f_d\tau)] * p(t, f_d), \tag{6.16}$$

where $\text{sinc}(x) \triangleq \sin(\pi x)/\pi x$ and $*$ denotes 2-D convolution. The first term on the right side of (6.16) is a scaled 2-D sinc function and represents the system impulse response. Its sinc-shape results from the uniform rectangular shape of the $B \times \tau$ support region.

To limit the computational workload, when processing the echo from a single CPI pulse, the SAR system filters the data using a fixed Doppler shift corresponding to the Doppler shift f_{d_c} of the ground patch (i.e., scene) center[1]. The resulting One-Dimensional (1-D) range profile $\hat{p}(r)$ is simply a 1-D cut of $\hat{p}(t, f_d)$ denoted

$$\hat{p}(r) = \hat{p}\left(\frac{c}{2}t, f_{d_c}\right), \tag{6.17}$$

where $r = ct/2$ denotes range.

6.2.2 Eliminating Cross Range Aliasing Artifacts. Using the definition and commutative property of convolution, (6.16) can be rewritten as

$$\hat{p}(t, f_d) = B\tau \int_{-\infty}^{\infty} \int_{-\infty}^{\infty} p(t', f_d')\text{sinc}\left[B\left(t' - t\right)\right] \text{sinc}[(f_d' - f_d)\tau] dt' df_d', \tag{6.18}$$

---

[1]The use of matched filter parameters linked to a specific ground patch location indicates spotlight mode data processing. spotlight mode processing may be used on SAR data regardless of whether it was collected using a stripmap or spotlight antenna pointing scheme [100].

where t' and f'_d are introduced as integration variables. To examine the 1-D range profiles generated by matched filtering, the definition of $p(t, f_d)$ (given by (6.11)) is substituted into (6.18), yielding

$$\hat{p}(t, f_d) = B\tau \int_{-\infty}^{\infty} \int_{-\infty}^{\infty} \left[\sum_{m=0}^{M-1} A_m \delta(t' - t_m, f'_d - f_{d_m}) \right]$$
$$\cdot \operatorname{sinc}\left[B\left(t' - t\right) \right] \operatorname{sinc}[(f'_d - f_d)\tau] \mathrm{d}t' \mathrm{d}f'_d. \qquad (6.19)$$

The integrals can be evaluated using the sifting property of delta functions giving

$$\hat{p}(t, f_d) = B\tau \sum_{m=0}^{M-1} A_m \operatorname{sinc}[B(t_m - t)] \operatorname{sinc}[(f_{d_m} - f_d)\tau]. \qquad (6.20)$$

Setting $f_d = f_{d_c}$ and converting the time delays to ranges yields the following matched filtered range profile expression

$$\hat{p}(r) = B\tau \sum_{m=0}^{M-1} A_m \operatorname{sinc}[B(r_m - r)] \operatorname{sinc}[(f_{d_m} - f_{d_c})\tau], \qquad (6.21)$$

where $r_m = ct_m/2$ is the range to the mth scatterer. Equation (6.21) shows the matched filter output for a given CPI pulse is simply a sum of appropriately scaled and delayed $\operatorname{sinc}[B(r_m - r)]$ functions. The amplitude of each sinc is determined by the mismatch between the Doppler shift of the mth scatterer f_{d_m} and the ground patch center f_{d_c} according to the term $\operatorname{sinc}[(f_{d_m} - f_{d_c})\tau]$. When $(f_{d_m} - f_{d_c})$ equals a non-zero integer multiple of $1/\tau$, $\operatorname{sinc}[(f_{d_m} - f_{d_c})\tau] = 0$ and the mth scatterer is effectively filtered out of range profile $\hat{p}(r)$.

Recall from (6.10) that cross range (i.e., Doppler) aliasing artifacts only appear at integer PRF multiples. This uniform aliasing artifact spacing can be combined with the uniformly spaced Doppler filter nulls generated by the $\operatorname{sinc}[(f_{d_m} - f_{d_c})\tau]$ term of (6.21) to remove aliasing artifacts. Choosing

$$\text{PRF} = \frac{1}{\tau}, \qquad (6.22)$$

180

achieves this goal, ensuring the Doppler values of cross range aliasing artifacts coincide with Doppler nulls in the range profile generation process. This precise Doppler null positioning is the fundamental concept of the cross range aliasing reduction technique.

Since the scene information is collected using a waveform of duration τ, the PRF $= 1/\tau$ requirement of (6.22) implies Continuous Wave (CW) transmitter operation. An artificial PRF is formed on receive by independently matched filtering the radar echoes with each of the individual duration τ waveforms. Additionally, claiming PRF $= 1/\tau$ filters aliasing artifacts from a given SAR image assumes the individual region being imaged (not the full scene intercepted by antenna beamwidth, see Fig. 6.1) has a small Doppler spread. Since the system architecture specifies the formation of many relatively small spotlight mode images, this assumption is valid. Simulation results in Chapter VII and Chapter VIII demonstrate this claim.

6.3   Linear Frequency Modulation Waveforms

As discussed previously, most SAR systems use LFM waveforms. Analytically, an LFM waveform is written

$$x(t) = \text{rect}\left(\frac{t}{\tau}\right)\exp[2\pi j(f_c t + \alpha t^2)], \tag{6.23}$$

where τ is the pulse width, f_c is the center frequency and α is the chirp rate.

Assuming radar waveform echoes are processed using matched filtering, the waveform impulse response is given by the time-frequency auto-correlation function $\chi(t_e, f_e)$. The squared magnitude $|\chi(t_e, f_e)|^2$ is called the ambiguity function and is defined as [63]

$$|\chi(t_e, f_e)|^2 = \left|\int_{-\infty}^{\infty} x(t)x^*(t + t_e)\exp\left(j2\pi f_e t\right)\mathrm{d}t\right|^2, \tag{6.24}$$

where $x(t)$ is the transmitted waveform, the superscripted * denotes the complex conjugate, t_e is the temporal mismatch error, and f_e is the frequency (e.g., Doppler)
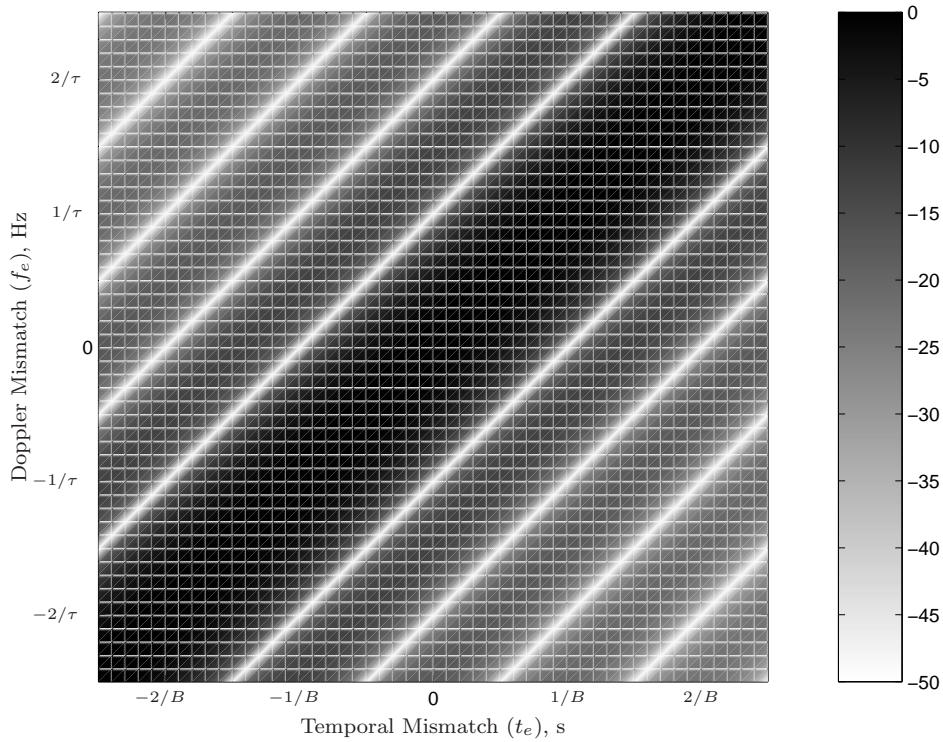
Figure 6.3:   Central region of the ambiguity diagram for an LFM waveform (50.0 dB dynamic range). Both Doppler tolerance and range-Doppler coupling result from the linear ridge in the ambiguity function's center.

mismatch error between the matched filter parameters (e.g, the scene center) and the scatterer. The ambiguity function is an important validation tool since it uses the actual waveform to calculate the impulse response, not an idealized approximation of the support region. This approach is used to verify the concepts presented in Section 6.2.

Figure 6.3 illustrates two LFM waveform properties critical to the aliasing artifact problem. First, the ambiguity function peak (0.0 dB) persists across a wide frequency range. This behavior is known as Doppler tolerance and indicates matched filter output amplitude is essentially constant as a function of filter/scatterer frequency mismatch [116]. While Doppler tolerance is an asset in MTI applications, where high speed targets exhibit a wide variety of Doppler shifts, it is a liability in

SAR systems, allowing Doppler shifted aliasing artifacts into the resulting imagery. The second LFM waveform effect is known as range-Doppler coupling.

The 45° slope in the waveform's ambiguity surface causes this effect. Range-Doppler coupling dictates while matched filter output amplitude is uniform, mismatches in frequency also lead to mismatches in observed delay (i.e., range) [116]. Targets with large Doppler shifts appear at incorrect range values. Range-Doppler coupling is relatively insignificant for MTI applications which only seek to determine approximate target location. However, range-Doppler coupling can lead to SAR image defocusing and is therefore unacceptable for WAM-SAR. Figures 9.8 and 9.9 illustrate range-Doppler coupling.

6.4 Stepped-Frequency Waveforms

The previous section demonstrated that by setting PRF $= 1/\tau$, it should be possible to virtually eliminate Doppler aliasing provided one can collect data filling the rectangular data support region defined by bandwidth B and duration τ. The measurement tool used to collect this data is a radar waveform. This section presents one class of waveforms that can be used to fill the data support region, resulting in a good approximation to the data requirements outlined in Section 6.2.

6.4.1 Background on Stepped-Frequency Waveforms.   A Stepped-Frequency (SF) waveform of bandwidth B and uncompressed duration τ, is built by dividing a waveform into N equal duration subpulses consisting of a single frequency, uniform amplitude sinusoid. There are N such frequencies equally spaced across the waveform bandwidth. The frequencies can be arranged in any desired order. An SF waveform can be analytically represented as

$$x(t) = \frac{1}{\sqrt{\tau}} \sum_{n=0}^{N-1} \text{rect}\left(\frac{t - n\tau_s}{\tau_s}\right) \exp\left(j2\pi f_n t\right), \qquad (6.25)$$

where $f_n \in \{f_0, f_1, ..., f_{N-1}\}$ is the frequency of the nth subpulse, and τ_s is the subpulse duration. The $1/\sqrt{\tau}$ constant ensures the SF waveform has unit energy.

A common way of representing SF waveform time-frequency characteristics is through a grid similar to the one shown in Fig. 6.4 [34, 52]. In this figure, each of $N = 8$ subpulses has been assigned a fixed frequency value which it maintains for $\tau_s = \tau/8$ seconds. These values are noted by the black blocks. Equivalently, the SF characteristics of Fig. 6.4 can be represented using an $N \times N$ time-frequency matrix $\mathbf{K}$ with ones corresponding to filled blocks and zeros elsewhere

$$\mathbf{K} = \begin{bmatrix} 1 & 0 & 0 & 0 & 0 & 0 & 0 & 0 \\ 0 & 0 & 0 & 0 & 0 & 0 & 0 & 1 \\ 0 & 0 & 0 & 0 & 0 & 1 & 0 & 0 \\ 0 & 0 & 1 & 0 & 0 & 0 & 0 & 0 \\ 0 & 1 & 0 & 0 & 0 & 0 & 0 & 0 \\ 0 & 0 & 0 & 0 & 0 & 0 & 1 & 0 \\ 0 & 0 & 0 & 0 & 1 & 0 & 0 & 0 \\ 0 & 0 & 0 & 1 & 0 & 0 & 0 & 0 \end{bmatrix}. \tag{6.26}$$

This construction of $\mathbf{K}$ is known as a *permutation matrix* and contains exactly one non-zero entry in each row and each column. There are $N!$ unique permutation matrices for a given value of N [145].

To ensure each SF subpulse samples the scene over its entire designated frequency band of width B/N, the waveform bandwidth B and duration τ are related by [116]

$$B\tau = N^2. \tag{6.27}$$

This requirement can be derived by noting B/N is the 4.0 dB width of the Fourier transform of a $\tau_s = \tau/N$ duration pulse. When $B\tau < N^2$, a significant portion of the energy in a given subpulse extends outside its allotted portion of the total bandwidth. When $B\tau > N^2$, gaps result in the waveform's frequency coverage and range aliasing

184
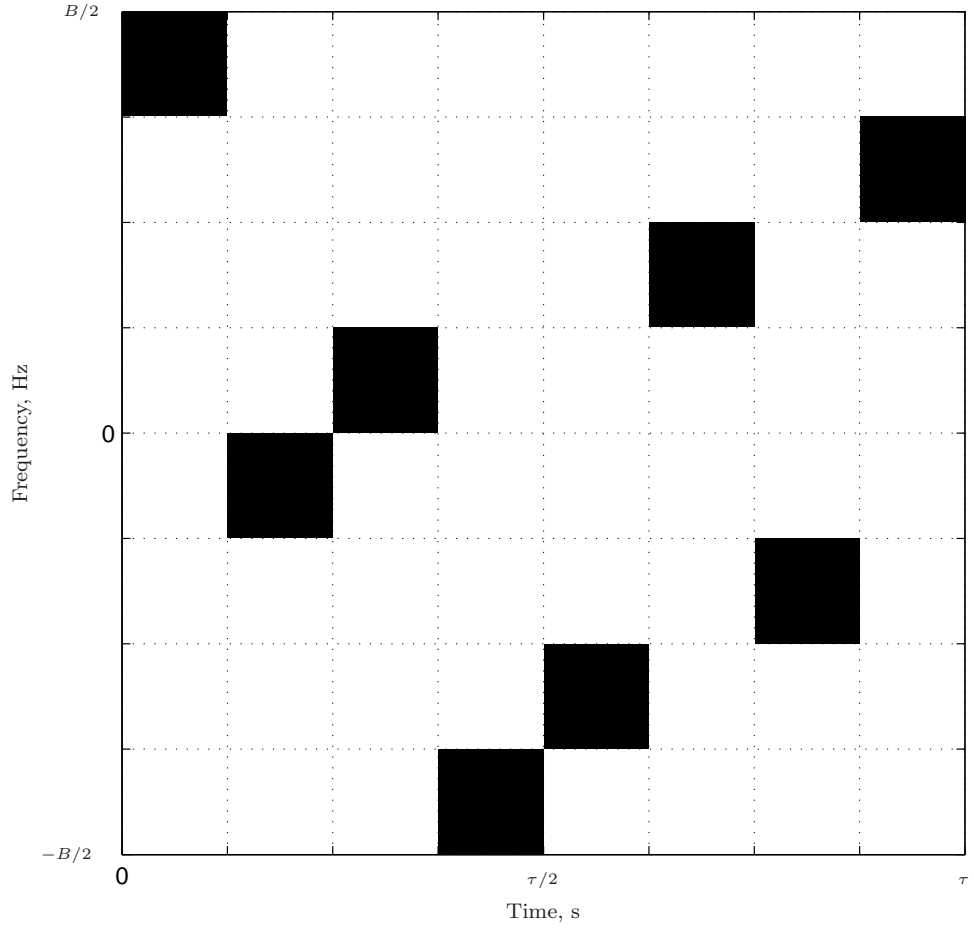
Figure 6.4: Specification for a randomly ordered SF waveform ($N = 8$, Frequency converted to baseband). Shaded regions indicate waveform's time-frequency coverage. Note, B and τ are not necessarily equal since they have different units, but are related via (6.27) [88].
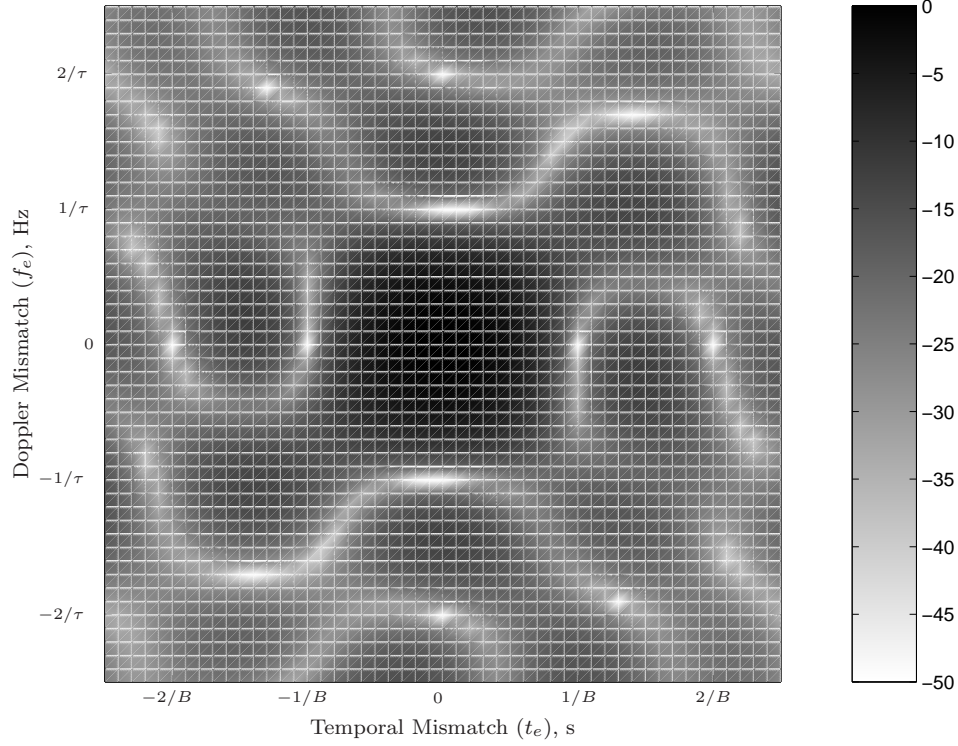
Figure 6.5: Central region of the ambiguity diagram for a single random SF waveform realization ($N = 100$, 50.0 dB dynamic range). Noise-like ambiguity surface determined by subpulse frequency order.

occurs. Due to the roughly uniform energy spreading across the subpulses in both frequency and time, a single SF waveform provides the required data in N of the N^2 blocks specified by the data support region. Also note that by dividing through by N^2, (6.27) can also be written as

$$\delta f \, \tau_s = 1, \tag{6.28}$$

where $\delta f \triangleq B/N$ is the uniform spacing between subpulse frequencies.

Figure 6.5 shows the central region of an SF waveform ambiguity function with $N = 100$ subpulses. Subpulse frequency order was chosen at random. Along both the $t_e = 0$ and $f_e = 0$ axes, nulls appear at integer multiples of $1/B$ and $1/\tau$, respectively. However, since only N of N^2 blocks in the permutation matrix have been filled, the overall ambiguity response differs from the desired 2-D $|\text{sinc}(\cdot)|^2$ response.

6.4.2 Combinations of Stepped-Frequency Waveforms.   Better approxima-
tion of the desired 2-D $|\text{sinc}(\cdot)|^2$ ambiguity function requires generating a waveform
which entirely fills the $B \times \tau$ support region. While one SF waveform is not suffi-
cient, combining the range profiles generated by multiple SF waveforms produces the
desired effect.

Figure 6.6 illustrates the process used to sample the scene and form the SAR
image. Each block in the CW SAR waveform is a subpulse consisting of a uniform
amplitude single frequency sinusoid. There are N subpulses in each SF waveform and
P SF waveforms in the overall SAR signal. Each of the N frequencies occurs once
within each SF waveform. The received echoes are match-filtered to produce P range
profiles. These range profiles are each treated as the response from a single SF wave-
form in the CPI and are coherently combined by the SAR imaging system to produce
the final image. The remainder of this section shows varying the subpulse frequency
order on a waveform-to-waveform basis achieves the desired impulse response leading
to a $|\text{sinc}(\cdot)|^2$ ambiguity function.

To illustrate how this ambiguity function is formed, (6.16) is rewritten as

$$\hat{p}_p(t, f_d) = h_p(t, f_d) * p(t, f_d), \tag{6.29}$$

where $\hat{p}_p(t, f_d)$ is the estimate acquired with the pth waveform and $h_p(t, f_d)$ represents
a generic impulse response associated with the pth waveform. Coherently combining
a set of P range profiles (inherent in the SAR imaging process) allows this equation
to be rewritten as

$$\hat{p}(t, f_d) = \sum_{p=1}^{P} \hat{p}_p(t, f_d) = \sum_{p=1}^{P} \left[h_p(t, f_d) * p(t, f_d) \right]. \tag{6.30}$$

Using the distributive property of convolution, $p(t, f_d)$ can be removed from the sum
giving,

$$\hat{p}(t, f_d) = \left[\sum_{p=1}^{P} h_p(t, f_d) \right] * p(t, f_d). \tag{6.31}$$
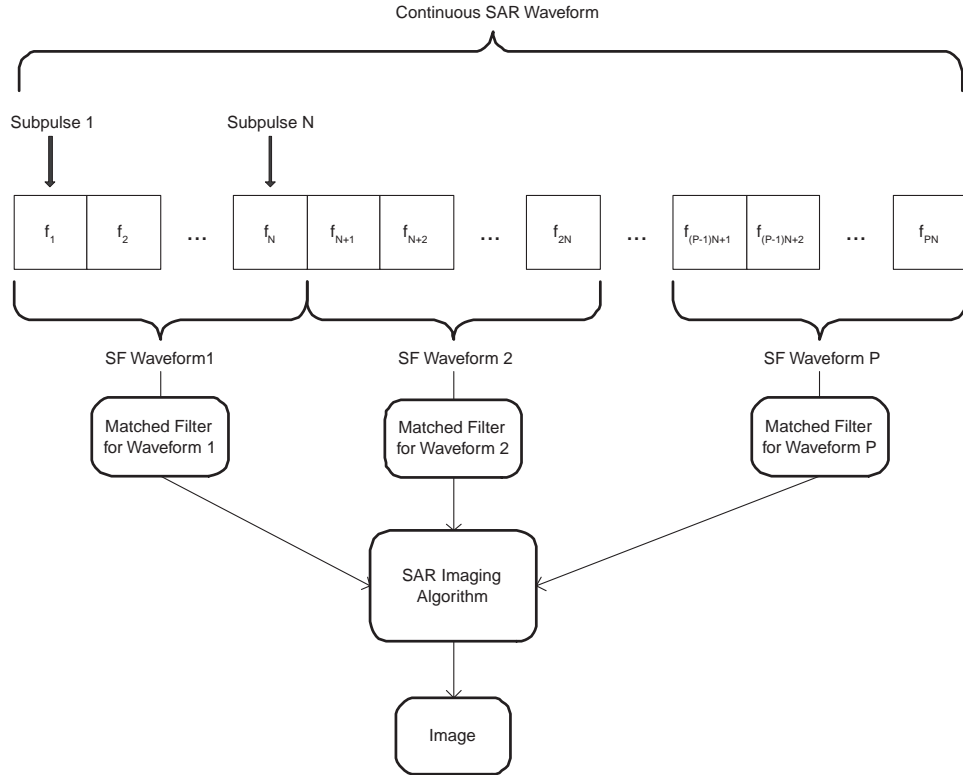
Figure 6.6: Continuous SAR waveform divided into SF waveforms and subpulses (adapted from [88]). Each matched filter produces a single range profile. These profiles are then combined by the SAR imaging algorithm.

The individual $h_p(t, f_d)$ impulse response functions are calculated as the 2-D Fourier transform of their associated data support regions $H_p(f, t_d)$. Using this fact and the linearity of the Fourier transform gives

$$\hat{p}(t, f_d) = \left\{ \mathcal{F}^{-1} \left[\sum_{p=1}^{P} H_p(f, t_d) \right] \right\} * p(t, f_d), \tag{6.32}$$

where $H_p(f, t_d)$ represents the data support region of the pth waveform. Equation (6.32) shows the effective impulse response when summing a series of range profiles (as done in (6.30)) is determined by the sum of their data support regions. By changing the frequency order on subsequent SF waveforms, different subsets of the desired $B \times \tau$ support region are sampled. Thus, summing range profiles from a series of different SF waveforms produces the same range profile as would be generated from a single waveform with a data support region equal to the sum of the data support regions of the individual SF waveforms. Note, (6.32) assumes the scene does not change throughout generation of P range profiles. Since the SAR platform is in motion, this assumption is not strictly correct. However, as shown in the simulated imagery that follows, platform motion is slow enough to achieve the desired effect.

6.5 *Subpulse Frequency Order Selection*

The previous section illustrated how the combination of range profiles from multiple SF waveforms effectively combines their data support regions. The only difference between these SF waveforms is their subpulse frequency order. This section outlines metrics and methods for guiding subpulse frequency order selection.

6.5.1 Selection Metrics.   The key to the proposed anti-aliasing technique is uniformly filling the data support region. Quantifying the degree of uniformity is most convenient using the permutation matrix viewpoint of SF waveforms introduced in (6.26). Since the matrix representation of each SF waveform is an $N \times N$ permutation matrix $\mathbf{K}$, the data support region coverage can be represented by summing

permutation matrices from P distinct SF waveforms. The result is termed a *composite permutation matrix*, denoted $\mathbf{A}$ with elements a_{kl} and defined as

$$\mathbf{A} = \sum_{p=0}^{P-1} \mathbf{K}_p. \tag{6.33}$$

The degree of uniformity in $\mathbf{A}$ can be calculated via a simple two step process. First, matrix $\mathbf{A}$ is normalized by the ratio P/N (which denotes the value of a_{kl} for uniformly filled $\mathbf{A}$). Second, the average variance of each element of the normalized version of $\mathbf{A}$ is computed via

$$\operatorname{var}\left(\frac{N}{P} a_{kl}\right) = \frac{1}{N^2} \sum_{k=0}^{N-1} \sum_{l=0}^{N-1} \left(\frac{N}{P} a_{kl} - 1\right)^2. \tag{6.34}$$

The data support region is uniformly filled when $\operatorname{var}(N/P \cdot a_{kl}) = 0$. This filling occurs when $a_{kl} = P/N \ \forall \, k, l$.

Uniformly filling the data support region is not the only important consideration when selecting subpulse frequency order. Another consideration involves the matched filter's response when multiple SF waveforms are present. This concern is critical since the CW transmission requirement dictates multiple SF waveform echoes are received at a given time. Ideally, applying the matched filter for one waveform to the echo from a different waveform should result in a complete energy cancelation. In this case, the waveforms are termed orthogonal.

Analytically, two waveforms $x(t)$ and $y(t)$ are temporally orthogonal when their inner product is zero. The inner product $\langle \cdot, \cdot \rangle$ is defined as

$$\langle x, y \rangle = \int_{-\infty}^{\infty} x(t) y^*(t) \mathrm{d}t. \tag{6.35}$$

Since SF waveforms are collections of non-overlapping single-frequency subpulses, the inner product of a full waveform is the sum of the inner products of the N subpulses.

Combining this fact with (6.25) gives the following

$$\langle x, y \rangle = \frac{1}{\tau} \sum_{n=0}^{N-1} \int_{-\infty}^{\infty} \text{rect}\left(\frac{t - n\tau_s}{\tau_s}\right) \exp\left[j2\pi \left(f_n^x - f_n^y\right) t\right] \mathrm{d}t. \tag{6.36}$$

The argument of the exponential function contains the expression $(f_n^x - f_n^y)$ denoting the difference in frequency between the nth subpulse of x and y. Furthermore, (6.36) assumes the two SF waveforms are perfectly aligned in time. Due to the uniform spacing of subpulse frequencies, the quantity $(f_n^x - f_n^y)$ is known to be an integer multiple of δf, thus

$$\langle x, y \rangle = \frac{1}{\tau} \sum_{n=0}^{N-1} \int_{-\infty}^{\infty} \text{rect}\left(\frac{t - n\tau_s}{\tau_s}\right) \exp\left(j2\pi m_n \delta f \, t\right) \mathrm{d}t, \tag{6.37}$$

where m_n is an integer denoting the number of frequency steps separating f_n^x and f_n^y. The integral in (6.37) is recognizable as the Fourier transform of a rect function. Evaluating this Fourier transform (and dropping the phase term) yields

$$\langle x, y \rangle = \frac{1}{\tau} \sum_{n=0}^{N-1} \tau_s \text{sinc}\left(m_n \delta f \tau_s\right). \tag{6.38}$$

Using (6.28), (6.38) reduces to

$$\langle x, y \rangle = \frac{\tau_s}{\tau} \sum_{n=0}^{N-1} \text{sinc}\left(m_n\right) = \frac{1}{N} \sum_{n=0}^{N-1} \text{sinc}\left(m_n\right). \tag{6.39}$$

Equation (6.39) indicates if the nth subpulse of both x and y are at the same frequency (implying $m_n = 0$), the contribution from that subpulse to the total inner product is $1/N$. Such an occurrence is called a coincidence [116]. However, if a given subpulse contains two different frequencies, m_n is a non-zero integer, $\text{sinc}(m_n) = 0$, and the subpulse contributes nothing to the total inner product. Thus, if the subpulses of two SF waveforms are arranged such that none of the frequencies occur at the same time within the waveform, the two waveforms are temporally orthogonal.

If the two SF waveforms are offset in time, the inner product no longer equals zero, even if there are no coincidences (although the inner product remains quite low, near $1/N$ [116]). However, since these cross correlation sidelobes are different for each subpulse frequency order (and hence different for each SF waveform), they do not add coherently over a waveform sequence, making their effect negligible.

6.5.2 Random Selection. Perhaps the most obvious approach to subpulse frequency order selection is to randomly re-order the subpulse frequencies on a waveform-to-waveform basis. This approach not only guarantees each waveform contains one and only one subpulse at each frequency, but also ensures each waveform is created independently from all other waveforms.

Figure 6.7 shows the central region of the ambiguity function which results from combining the time-frequency auto-correlation functions of a series of 100 different SF waveforms, each with $N = 100$ subpulses. Subpulse frequency order was determined randomly on a waveform-to-waveform basis. As expected, the structure is essentially a 2-D $|\text{sinc}(\cdot)|^2$ function with nulls near non-zero integer multiples of $f_e = 1/\tau$. However, the nulls are not infinitely deep due to the non-uniform filling of the data support region.

As indicated in Section 6.5.1, the deviation from uniform filling of **A** can be quantified by calculating a normalized variance per (6.34). When using random subpulse frequency order selection, each element a_{kl} becomes a binomial random variable with probability $p = 1/N$ over $n = P$ Bernoulli trials. Given this information, it becomes possible to calculate both the expected value $E\{\cdot\}$ and variance $\text{var}(\cdot)$ of a_{kl} to be [78],

$$E\{a_{kl}\} = np = \frac{P}{N}, \tag{6.40}$$

$$\text{var}(a_{kl}) = np(1 - p) = \frac{P}{N}\left(1 - \frac{1}{N}\right). \tag{6.41}$$
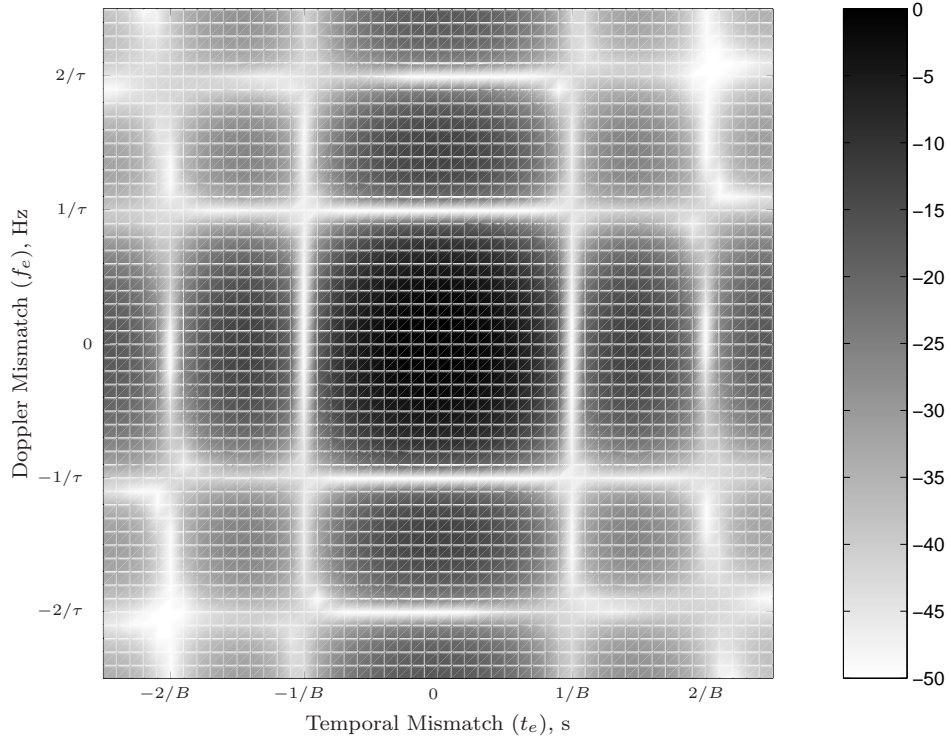
Figure 6.7:   Central region of the ambiguity diagram for the coherent combination of 100 random SF waveform realizations ($N = 100$, 50.0 dB dynamic range). The shape approximates a 2-D $|\text{sinc}(\cdot)|^2$ function with nulls of depths near -40.0 dB.

Recall the variance calculation in (6.34) used a normalized version of **A**. Thus, since [78]

$$\text{var}(kx) = k^2\text{var}(x), \tag{6.42}$$

where x is a random variable and k is a constant, the expected value for (6.34) under random subpulse frequency order selection is

$$E\left\{\text{var}\left(\frac{N}{P}a_{kl}\right)\right\} = \frac{N}{P}\left(1 - \frac{1}{N}\right) = \frac{N-1}{P}. \tag{6.43}$$

Since

$$\lim_{P\to\infty} \text{var}\left(\frac{N}{P}a_{kl}\right) = 0, \tag{6.44}$$

the data support region filling is approximately uniform for large P.

The second metric for characterizing SF waveforms is the inner product. The randomization process of subpulse frequencies ensures the odds of the same subpulse sharing the same frequency for any two independent waveform realizations is $1/N$, yet each of these waveforms has N different subpulses. Since the expectation operator is linear, the total expected value for the number of coincidences is simply $1/N \times N = 1$. Thus, from (6.39)

$$E\left\{\langle x, y \rangle\right\} = \frac{1}{N}, \tag{6.45}$$

and for large N, the expected value of the inner product becomes small.

6.5.3 Shuffled Circulant Matrix Selection.   Although random SF waveform selection provides good performance, it is possible to do significantly better with relatively little effort. The key to these improvements is the realization the $N \times N$ matrix defining the data support region can be treated as a puzzle where each SF waveform provides N of the N^2 pieces. Ideally, it should be possible to construct a series of N SF waveforms exactly filling the required space.

One method to precisely fill the data support region in only $P = N$ waveforms is to use a sequence consisting of N circularly shifted variants of the SF approximation to

an LFM down chirp. Equation (6.46) shows a matrix $\mathbf{Z}_c$ representing such a sequence for $N = 10$

$$
\mathbf{Z}_c = \begin{bmatrix}
1 & 2 & 3 & 4 & 5 & 6 & 7 & 8 & 9 & 10 \\
10 & 1 & 2 & 3 & 4 & 5 & 6 & 7 & 8 & 9 \\
9 & 10 & 1 & 2 & 3 & 4 & 5 & 6 & 7 & 8 \\
8 & 9 & 10 & 1 & 2 & 3 & 4 & 5 & 6 & 7 \\
7 & 8 & 9 & 10 & 1 & 2 & 3 & 4 & 5 & 6 \\
6 & 7 & 8 & 9 & 10 & 1 & 2 & 3 & 4 & 5 \\
5 & 6 & 7 & 8 & 9 & 10 & 1 & 2 & 3 & 4 \\
4 & 5 & 6 & 7 & 8 & 9 & 10 & 1 & 2 & 3 \\
3 & 4 & 5 & 6 & 7 & 8 & 9 & 10 & 1 & 2 \\
2 & 3 & 4 & 5 & 6 & 7 & 8 & 9 & 10 & 1
\end{bmatrix}. \tag{6.46}
$$

The structure of $\mathbf{Z}_c$ in (6.46) is known as a circulant matrix [145]. Elements labeled 1 comprise the permutation matrix defining subpulse frequency order for the first SF waveform. Elements labeled 2 represent the order for the second waveform, and so on. Each set of numbers represents a valid permutation matrix, and all the permutation matrices fit together perfectly without overlapping.

Unfortunately, there is a significant problem which arises using this approach. Time shifts of two SF waveforms generated by $\mathbf{Z}_c$ can result in up to $N-1$ subpulse frequency coincidences. The combined range profiles of all N SF waveforms should, theoretically, eliminate the effects of these coincidences. However, simulations have shown the subtle changes in range profiles due to platform motion prevent perfect cancelation. Stated another way, the cross-correlation sidelobes resulting from SF waveforms defined by $\mathbf{Z}_c$ are too high to be ignored.

To eliminate this problem, note exchanging either rows or columns of a permutation matrix results in a new permutation matrix with a different subpulse order. Thus, the permutation matrix defining subpulse frequency order for any possible SF waveform with N subpulses can be represented as a "shuffling" of either the rows or columns of any $N \times N$ permutation matrix.

Using the shuffling principle, the subpulse frequency order for a set of N SF waveforms with N subpulses can be defined by randomly shuffling first the rows, then the columns of a circulant matrix $\mathbf{Z}_c$. The result is called a shuffled circulant matrix $\mathbf{Z}_s$. An example of such a matrix is

$$\mathbf{Z}_s = \begin{bmatrix} 4 & 10 & 7 & 5 & 6 & 9 & 1 & 2 & 8 & 3 \\ 6 & 2 & 9 & 7 & 8 & 1 & 3 & 4 & 10 & 5 \\ 2 & 8 & 5 & 3 & 4 & 7 & 9 & 10 & 6 & 1 \\ 8 & 4 & 1 & 9 & 10 & 3 & 5 & 6 & 2 & 7 \\ 1 & 7 & 4 & 2 & 3 & 6 & 8 & 9 & 5 & 10 \\ 7 & 3 & 10 & 8 & 9 & 2 & 4 & 5 & 1 & 6 \\ 9 & 5 & 2 & 10 & 1 & 4 & 6 & 7 & 3 & 8 \\ 5 & 1 & 8 & 6 & 7 & 10 & 2 & 3 & 9 & 4 \\ 10 & 6 & 3 & 1 & 2 & 5 & 7 & 8 & 4 & 9 \\ 3 & 9 & 6 & 4 & 5 & 8 & 10 & 1 & 7 & 2 \end{bmatrix}. \tag{6.47}$$

All ten SF waveform codes fit perfectly together, covering all N^2 elements using only N SF waveforms, but each individual code appears essentially random, minimizing cross-correlation sidelobe concerns.

Figure 6.8 shows the central region of the ambiguity function created by coherently combining 100 members of a 100-length code defined by a shuffled circulant matrix. A comparison to Fig. 6.7 illustrates the shuffled circulant matrix approach provides deeper nulls at precisely the desired locations, which implies better Doppler filtering performance.

Comparing Fig. 6.7 to Fig. 6.3 illustrates another benefit of SF waveform SAR imaging. Unlike the LFM waveform ambiguity function (Fig. 6.3), the Combined SF waveform ambiguity function does not exhibit any range-Doppler coupling. This
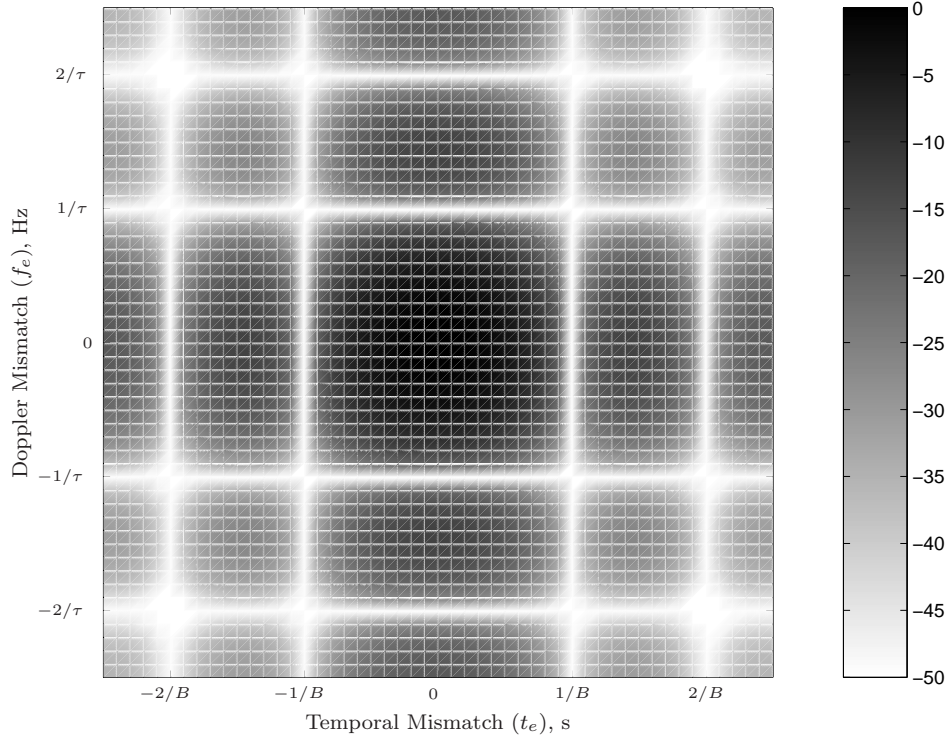
Figure 6.8:   Central region of ambiguity diagram for the coherent combination of all 100 SF waveforms specified by a 100×100 shuffled permutation matrix (50.0 dB dynamic range). The shape approximates a 2-D $|\mathrm{sinc}(\cdot)|^2$ function with nulls of depth greater than -50.0 dB.

feature ensures slight variations in Doppler frequency throughout the scene will not cause defocusing[2].

Since successive blocks of the data support region are filled in a rigidly defined fashion, the calculation of $\text{var}(N/P \cdot a_{kl})$ is now deterministic. The elements a_{kl} of $\mathbf{A}$ must contain either the value $\text{floor}(P/N)$ or $\text{ceil}(P/N)$, where the floor and ceil functions round their arguments down or up to the nearest integer, respectively. The full expression for the variance is

$$
\text{var}\left(\frac{N}{P}a_{kl}\right) = \frac{N - \text{mod}(P, N)}{N}\left[\frac{N}{P}\,\text{floor}\left(\frac{P}{N}\right) - 1\right]^2
$$
$$
+ \frac{\text{mod}(P, N)}{N}\left[\frac{N}{P}\,\text{ceil}\left(\frac{P}{N}\right) - 1\right]^2, \quad (6.48)
$$

where $\text{mod}(P, N)$ returns the remainder of P/N. Figure 6.9 illustrates a comparison of (6.43) and (6.48) for $N = 100$, $P = 1$ to 200. At $P = 1$, the two methods give the same result. Yet as P increases, the more structured SF waveform definition process achieves significantly better results. When P is an integer multiple of N, the shuffled circulant matrix approach guarantees a uniformly filled data support region, resulting in the ideal $\text{var}(N/P \cdot a_{kl}) = 0$ condition.

Using shuffled circulant matrices for SF waveform generation is also advantageous from the standpoint of the inner product. Since each waveform is explicitly designed to prevent the same frequency from occurring in the same subpulse on two different waveforms, the inner product is guaranteed to equal zero. Thus, the N SF waveforms generated by a shuffled circulant matrix form an orthonormal set.

6.6 Summary

This chapter introduced a new waveform diversity-based anti-aliasing technique for wide-angle SAR imagery. This technique solves the second of the two WAM-

---

[2]This statement is *not* claiming SF waveforms solve the problem of shifting locations for *moving* targets. Moving targets in SAR imagery are blurred and/or shifted depending on their velocity vector orientation. These effects are explored in [33, 40, 47, 66, 94].
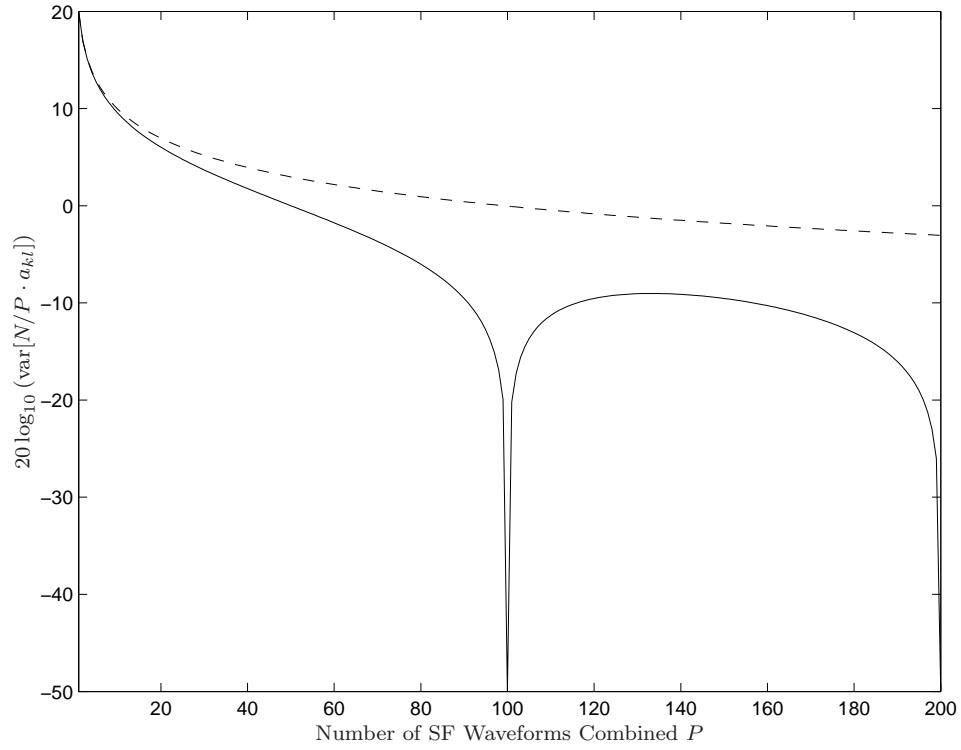
Figure 6.9: Comparison of expected variance calculations for sequences of SF waveforms ($N = 100$) defined via random (dotted line) and circulant matrix (solid line) approaches. Note, $\mathrm{var}[N/P \cdot a_{kl}] = 0$ when P is a non-zero integer multiple of N.

SAR implementation issues introduced in Chapter II. The chapter began by deriving the aliasing problem from an antenna array perspective, before introducing platform Doppler shifts, demonstrating the equivalence of Doppler and cross range aliasing artifacts. Having mathematically defined the problem, the chapter demonstrated a theoretical anti-aliasing method based on required scene information. After illustrating the limitations of traditional LFM waveforms, the chapter then showed how continuous sequences of randomized SF waveforms provide the required data. Finally, a new SF waveform definition method based on matrix "shuffling" was shown to produce orthonormal waveform sets, leading to improved technique performance. Chapters VII-IX provide both simulation and laboratory data results demonstrating technique effectiveness.

VII. 2-D Monostatic Point Scatterer Anti-Aliasing
Technique Simulation

C hapter VI proposed a new technique for eliminating cross range aliasing arti-
facts in Synthetic Aperture Radar (SAR) images using Stepped-Frequency (SF)
waveforms. This chapter demonstrates the technique using a Two-Dimensional (2-D)
monostatic point scatterer simulation. It begins by developing the simulator itself
and then demonstrates the desired technique in both one and two dimensions. The
point scatterer simulation code is included in Appendix D. All code was written in
`Matlab`®. This chapter's results are independently verified in [92].

7.1   In-Phase and Quadrature Sampling

While the actual transmitted waveforms are continuous, the computer simula-
tion must deal with discrete waveform samples. The same is true of modern radar
systems which perform signal processing using digitally sampled waveform echoes
verses older analog processing techniques. Due to the digital nature of both the sim-
ulated and true radar data, sampling becomes a critical issue. One common solution
is to use In-phase and Quadrature (I/Q) sampling.

The key to digital representation of continuous signals is the sampling theorem,
which states for a given continuous real signal $x_c(t)$ of finite bandwidth B, digital
samples taken at time intervals of $t_i \leq 1/2B$ can be used to unambiguously reproduce
the original continuous signal [91]. Recovery of the original continuous signal from
the digital data (denoted $x(t)$) is achieved using an appropriately designed filter.

The I/Q sampling process begins by breaking the continuous signal $x_c(t)$ into
two components. The first is an exact signal copy and the second is a copy delayed
by 90° in phase. These two signals are then sampled at intervals of t_i, resulting in the
digital I and Q signal components denoted $x_I(t)$ and $x_Q(t)$, respectively. Since two
samples are being taken at each sampling interval t_i, this interval only needs to be
half of the Nyquist sampling rate,

$$t_i \leq \frac{1}{B}. \tag{7.1}$$

The I/Q sampling approach provides several advantages. First, while the number of samples (and therefore the amount of digital data) is the same whether being sampled with one or two channels, the dual channel approach allows the sampling rate of each channel to be slower. This procedure simplifies the Analog-to-Digital (A/D) converter design. While this process has no impact on a simulation, the impact on hardware implementation can be significant. Second, the use of I/Q sampling prevents blind phases [116]. In single channel sampling, samples are not guaranteed to occur at signal positive/negative peak values and a loss of energy can occur in the sampled signal. In certain situations, successive samples can occur at zero crossings, resulting in samples of zero energy and therefore *blinding* the radar to those phases. Using I/Q sampling, the 90° phase delay eliminates blind phases ensuring the sampled signal energy $|x_I(t)|^2 + |x_Q(t)|^2$ is uniform, regardless of signal phase characteristics. Finally, the use of I/Q sampling simplifies mathematical representation by allowing the use of complex notation.

Delaying the incoming signal phase by 90° (i.e., adding $-\pi/2$ radians) is equivalent to application of a filter with transfer function $H(f)$ defined by [144]

$$H(f) = -j\,\mathrm{sgn}f, \tag{7.2}$$

where

$$\mathrm{sgn}f = \begin{cases} 1, & f > 0 \\ 0, & f = 0 \\ -1, & f < 0. \end{cases} \tag{7.3}$$

The ImPulse Response (IPR) $h(t)$ of $H(f)$ is

$$h(t) = \frac{j}{\pi t}. \tag{7.4}$$

The filtered version of the continuous signal $x_c(t)$ is therefore

$$\hat{x}_c(t) = h(t) * x_c(t), \tag{7.5}$$

202

where $\hat{x}_c(t)$ is known as the Hilbert transform of $x_c(t)$ [144].

Since the in-phase and quadrature components are samples of the same signal with a 90° phase difference, the two real-valued data samples can be easily represented using a single complex number, allowing the digitally sampled signal $x(t)$ to be written as

$$x(t) = x_\mathrm{I}(t) + j\, x_\mathrm{Q}(t), \tag{7.6}$$

where $x_\mathrm{I}(t)$ and $x_\mathrm{Q}(t)$ are the sampled versions of $x_c(t)$ and $\hat{x}_c(t)$ respectively. This representation also significantly impacts the signal's frequency spectrum. A standard, real-valued signal has an even spectrum. By using the complex I/Q representation of (7.6), the spectrum is folded over onto the positive frequency half of the spectrum function which doubles the spectrum's amplitude (see Fig. 7.1).

If the center frequency f_c is removed from the complex signal $x(t)$, the result is a complex baseband signal $x_b(t)$. This approach allows $x(t)$ to be rewritten as

$$x(t) = x_b(t) \exp(j2\pi f_c t). \tag{7.7}$$

The baseband complex signal $x_b(t)$ is often called the complex envelope of $x(t)$ [144]. Complex envelope notation dramatically simplifies mathematical signal manipulation. Consider for example a continuous sinusoidal signal $x_c(t) = \cos(t)$. Application of the Hilbert transform to $\cos(t)$ results in $\sin(t)$ giving

$$x(t) = \cos(t) + j\, \sin(t) = \exp(jt). \tag{7.8}$$

Since the exponential function is also the Fourier transform integral's kernel, Fourier analysis with the complex envelope signals is relatively easy. After the desired processing is complete, the true transmitted/received signal may be found simply by taking the real component of the complex result.

(a) Real signal spectrum

(b) Complex signal spectrum
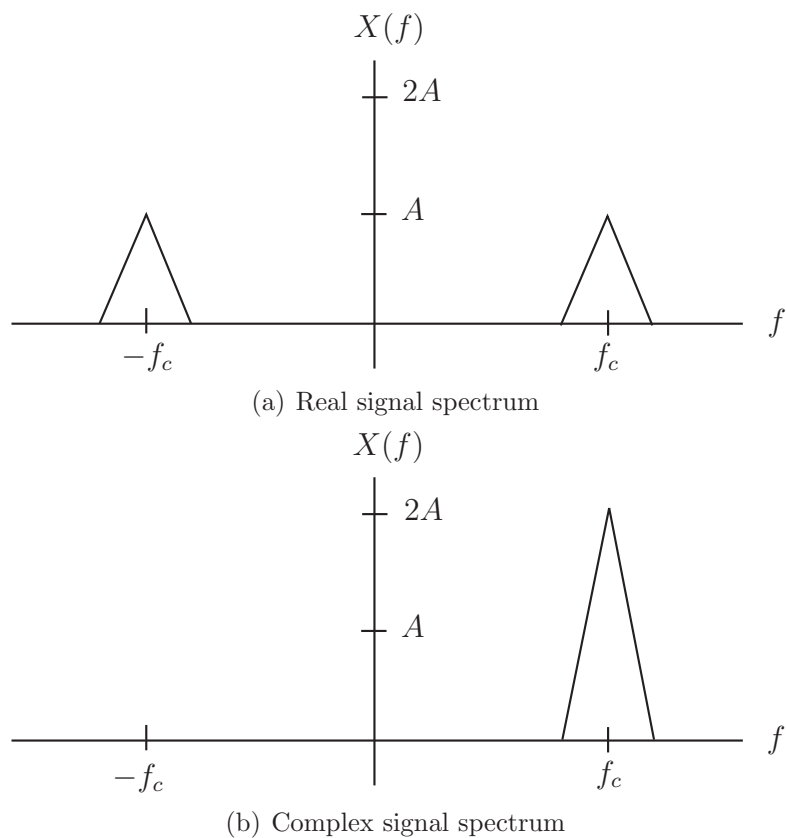
Figure 7.1: Real and complex-valued signal spectra. The use of complex values (from I/Q representation) causes a fold over of the spectrum.

7.2   Linear Frequency Modulation Waveform Simulation

Simulation of traditional SAR imaging systems requires Linear Frequency Modulation (LFM) waveforms. These waveforms are used for comparison purposes with the SF waveform-based anti-aliasing approach. Using complex envelope notation, LFM waveforms may be expressed as (6.23)

$$x(t) = \text{rect}\left(\frac{t}{\tau}\right) \exp[2\pi(f_c t + \alpha t^2)], \tag{7.9}$$

where

$$\text{rect}\left(\frac{t}{\tau}\right) = \begin{cases} 1, & -\frac{\tau}{2} \leq t < \frac{\tau}{2} \\ 0, & \text{otherwise}, \end{cases} \tag{7.10}$$

τ is the pulse width, f_c is the center frequency and α is the chirp rate. The waveform's instantaneous frequency $f_i(t)$ can be found by taking the phase term's time-derivative

$$f_i(t) = \frac{\mathrm{d}}{\mathrm{d}t}(f_c t + \alpha t^2) = f_c + 2\alpha t. \tag{7.11}$$

This equation allows estimation of the bandwidth B as[1]

$$B \approx |2\alpha\tau|. \tag{7.12}$$

The analog expression for an LFM waveform makes generating LFM waveform samples simple. The user defines a vector of sample times and evaluates (7.9) at those times. Figures 7.2-7.4 illustrate the simulated LFM waveform behavior in the time and frequency domains. For these figures, the following parameters were used: $f_c = 5$ MHz, $B = 10$ MHz, $\tau = 100$ μs, and $\alpha = B/2\tau = 5 \times 10^{10}$ s^{-2}. Note, $t_i = 3/B$ indicating sampling at three times the Nyquist rate since the complex envelope representation generates two samples at each time step. The ratio of the

---

[1]This bandwidth value is only an approximation. The true signal bandwidth is broadened by the transmit pulse's finite duration.
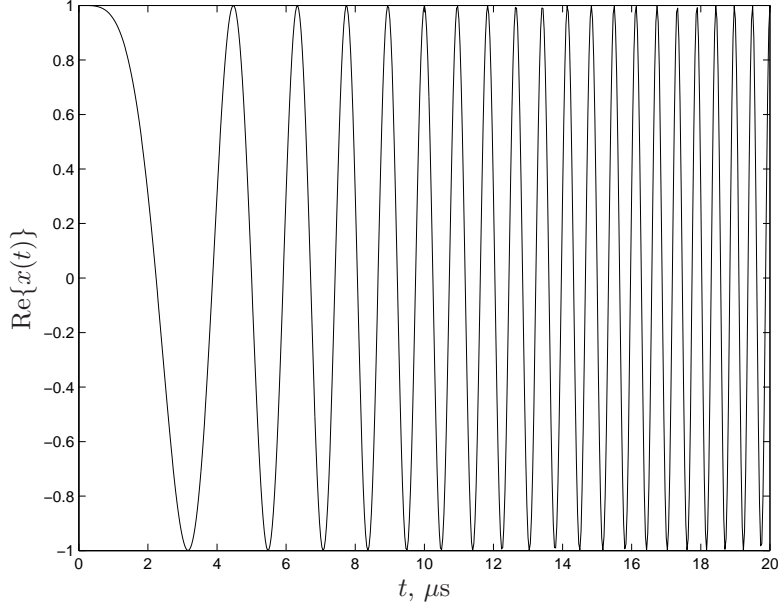
Figure 7.2:   LFM waveform Re$\{x(t)\}$. Frequency increases with time due to positive α.

true sampling rate to the Nyquist sampling rate is known as the oversampling ratio η.

Figure 7.2 shows the real component Re$\{x(t)\}$ (i.e., I channel only) of the first 20 μs of the time domain waveform $x(t)$ generated by (7.9). The real component is the actual transmitted wave. As expected, the waveform oscillates between -1 and 1. The oscillation frequency begins at $f_c - \alpha\tau = 0$ Hz and increases rapidly. The magnitude of the complex (i.e., I/Q sampled) wave is simply the magnitude of the exp$(\cdot)$ function and is therefore equal to one at all times.

Figure 7.3 illustrates the frequency spectrum magnitude $|\mathcal{F}[x(t)]|$ of the complex sampled waveform whose real component was plotted in Fig. 7.2. The notation $|\cdot|$ denotes the magnitude operation while $\mathcal{F}$ represents the Fourier Transform (FT). The frequency axis runs from $-3B/2$ to $3B/2$, the entire alias-free region. Outside these bounds, the frequency spectrum can be determined by replicating the current figure. The waveform's spectrum clearly exhibits roughly uniform energy for $0 \leq f \leq B$. The shape is consistent with that shown in [65]. Spectrum bandwidth covers one-third of the alias-free region as a consequence of the factor of three oversampling ratio $\eta = 3$.

206
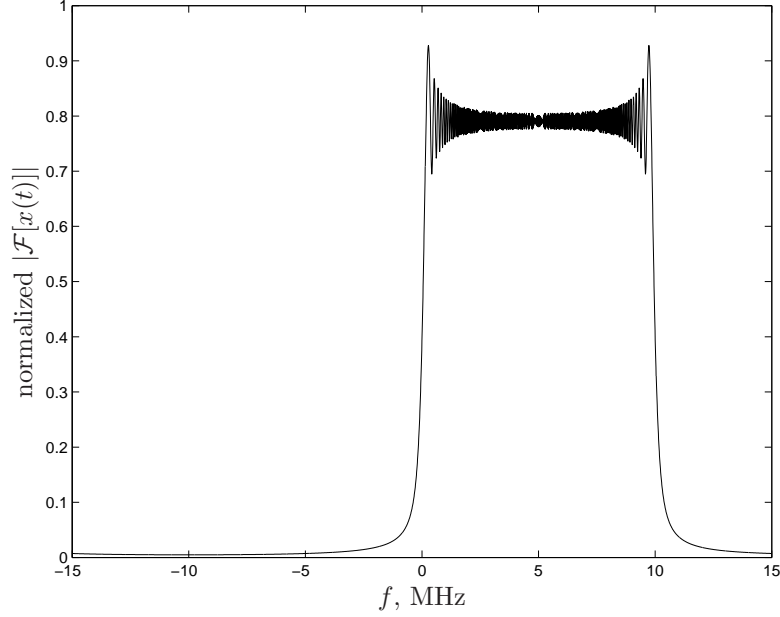
Figure 7.3: Frequency spectrum magnitude of I/Q sampled LFM waveform $x(t)$.

Figure 7.4 shows the frequency spectrum magnitude of the simulated waveform's real component. The loss of half the samples has caused a reflection about the $f = 0$ axis, cutting both the spectrum amplitude and oversampling ratio by a factor of two.

Figure 7.5 illustrates the result of applying a matched filter to the complex LFM signal. This operation produces the square root of the ambiguity function's zero Doppler cut $|\chi(t_e, 0)|$ (see (6.24)). The null-to-null width is $c/B = 30$ meters, as expected. Additional nulls appear every $c/2B = 15$ meters. The number of samples from one null to the next is three, again representative of the oversampling ratio.

7.3 Stepped-Frequency Waveform Simulation

SF waveforms are a contiguous series of single-frequency sinusoidal subpulses with carefully chosen subpulse frequencies. This section demonstrates SF waveform implementation, validating expected time domain and frequency domain behavior.
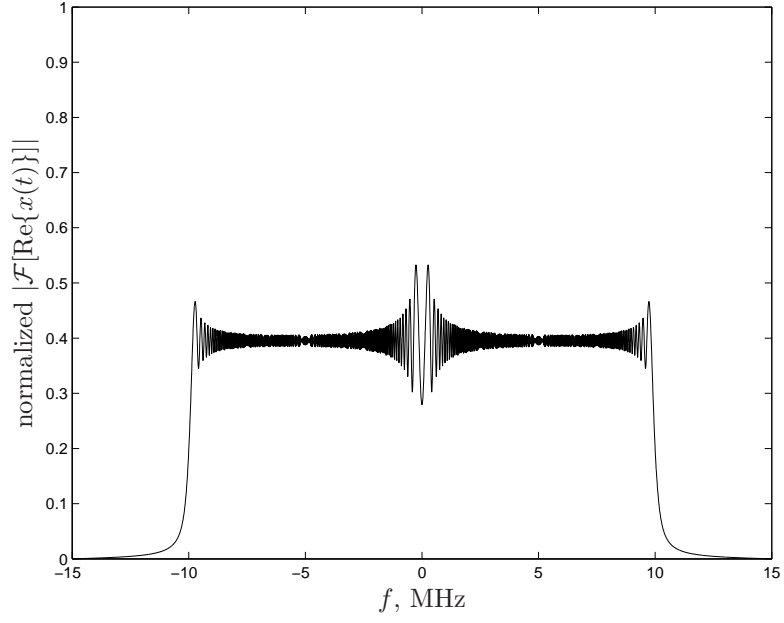
Figure 7.4: Frequency spectrum magnitude of real LFM waveform $\mathrm{Re}\{x(t)\}$.
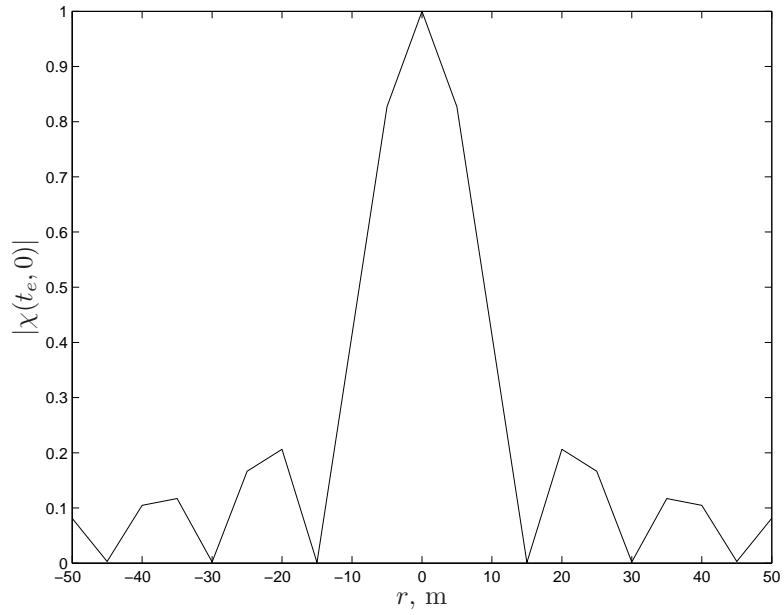
Figure 7.5: $|\chi(t_e, 0)|$ for an LFM waveform. Time mismatch error t_e converted to range r via $r = ct_e/2$.

Analytically, an SF subpulse with duration τ_s and frequency f is represented as

$$x(t) = \text{rect}\left(\frac{t}{\tau_s}\right)\exp(j2\pi f t). \qquad (7.13)$$

The waveform's N subpulses follow each other without any time gaps. This requirement allows mathematical representation of the entire waveform as

$$x(t) = \sum_{n=0}^{N-1}\text{rect}\left(\frac{t - n\tau_s}{\tau_s}\right)\exp(j2\pi f_n t). \qquad (7.14)$$

The subpulse frequencies $\{f_n\}$ are uniformly distributed across the bandwidth B and can be arranged in any order. The bandwidth B, waveform duration $\tau = N\tau_s$, and number of subpulses N are related via the equation [34, 116]

$$B\tau = N^2, \qquad (7.15)$$

which can also be represented as [79]

$$\delta f \tau_s = 1, \qquad (7.16)$$

where $\delta f = B/N$ is the minimum difference between subpulse frequency values. The importance of this relationship is demonstrated in the following paragraphs.

The easiest way to construct an SF waveform would be to build duration τ waveforms at each frequency, window them appropriately using the rect($\cdot$) function and then sum the N copies together. Unfortunately, this approach is very inefficient in terms of both memory usage and computation load. To simplify the process, each SF waveform is constructed by building a frequency vector to accompany the time vector. The sampling interval $t_i = 1/\eta B$ implies the total number of complex samples is $\tau/t_i = \eta N^2$. The time vector runs linearly from zero to τ, but the frequency vector is broken into N chips, each with ηN samples. Each of these chips corresponds to a single subpulse and the frequency value within each chip is held constant.
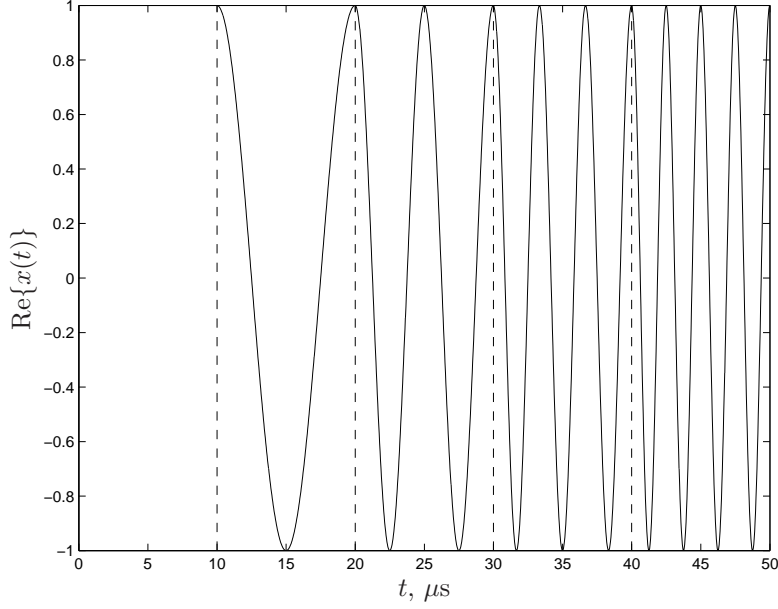
Figure 7.6: SF waveform $\mathrm{Re}\{x(t)\}$ with subpulse frequencies arranged to simulate an LFM waveform. Dotted lines show divisions between subpulses. Note that exactly one cycle is added per subpulse as predicted by (7.16).

Figure 7.6 shows the first 50 μs of a simulated SF waveform's real component $\mathrm{Re}\{x(t)\}$. The waveform parameters are $B = 10$ MHz and $N = 100$ implying $\tau = N^2/B = 1000\ \mu$s. The subpulse frequencies are arranged in a monotonically increasing fashion to simulate a standard LFM waveform. Dotted lines show divisions between successive subpulses. Each subpulse adds exactly one additional cycle (as predicted by (7.16)). This relationship also ensures that with a starting phase of $0°$ and a high enough sampling rate, the sampled SF waveform is virtually continuous. Transitions between subpulses exhibit only curvature discontinuity. This fact is true for any temporal subpulse order, although the greater the frequency gap between successive subpulses, the greater the curvature discontinuity and the more noise-like the resulting frequency spectrum.

Figure 7.7 shows the SF waveform's frequency spectrum magnitude when the subpulse frequencies are arranged in a monotonically increasing order. This figure is virtually identical to the true LFM spectrum depicted in Fig. 7.3.

210
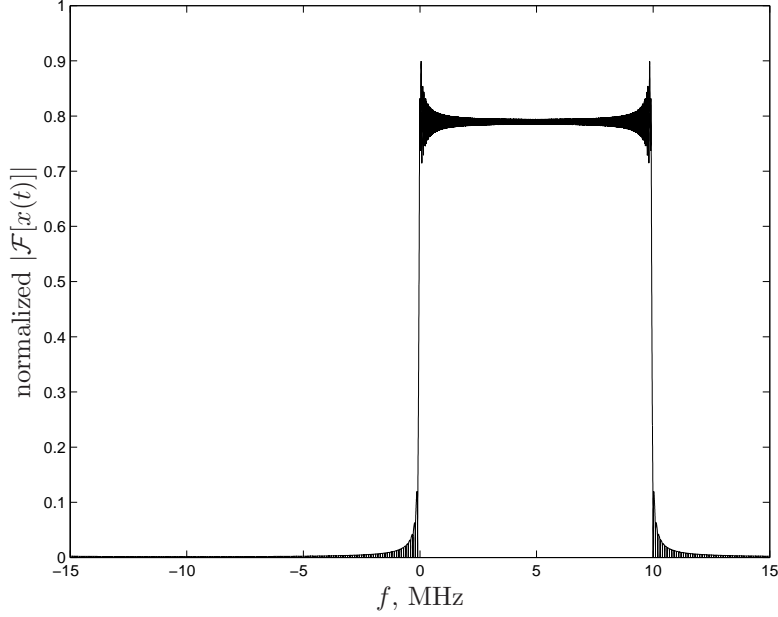
Figure 7.7: Frequency spectrum magnitude of SF approximation to an LFM waveform ($B = 10$ MHz, $N = 100$).

One way to verify SF waveform frequencies occur at the expected time is through the Short Time Fourier Transform (STFT). The STFT takes the FT of a fixed width SF waveform data window and then steps this window along each point in the time-domain SF waveform representation. Setting the STFT window width equal to the subpulse width $\tau_s = \tau/N$ allows the user to examine the SF waveform frequency's temporal behavior. Figure 7.8 shows the SF waveform's STFT. As expected, the frequency increases in a step-like fashion. Due to the finite subpulse duration, an individual frequency is spread to cover a band of approximately B/N MHz. From basic Fourier Transform (FT) properties (Appendix A) the uniform temporal width τ_s gives a null-to-null frequency width of $2/\tau_s$. Using (7.16) this width equates to $2\delta f$ implying a true bandwidth criterion of

$$20 \log_{10} \left[\text{sinc} \left(\frac{1}{2} \right) \right] \approx -4 \, \text{dB}. \tag{7.17}$$

211
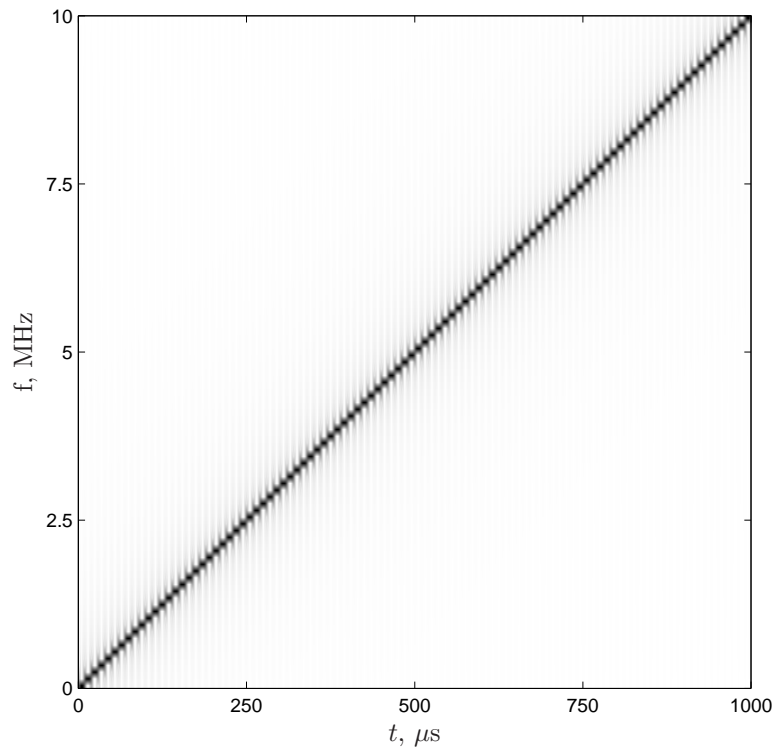
Figure 7.8: STFT of SF waveform ($B = 10$ MHz, $N = 100$, window width $= \tau_s$). Frequency is monotonically increasing in a discretized LFM fashion.
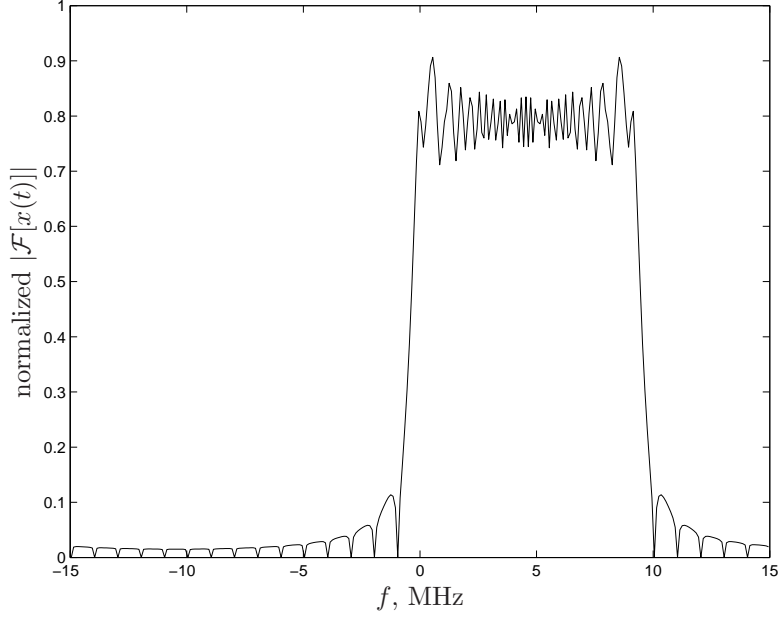
Figure 7.9: Frequency spectrum magnitude of SF approximation to an LFM waveform ($B = 10$ MHz, $N = 10$).

In Figures 7.9 and 7.10, the number of SF subpulses N was reduced from 100 to 10. The result is a much more coarse LFM waveform approximation. Figure 7.9 shows the frequency spectrum magnitude. It is more coarse than the $N = 100$ case (Fig. 7.7) although it does exhibit the same general shape. The same is true of the STFT shown in Fig. 7.10. These results show that for large N, appropriately designed SF waveforms provide excellent approximations to LFM, but as N becomes smaller the approximation begins to break down.

One key SF waveform feature is the ability to reorder the subpulse frequencies. This ability is what makes approximate filling of the $B \times \tau$ data support region possible. Figure 7.11 shows the frequency spectrum magnitude for an SF waveform ($B = 10$ MHz, $N = 100$) with randomized subpulse frequency order. Despite this randomization, the spectrum still covers the same 10 MHz bandwidth. The frequency coverage in this region appears much more noise-like. This effect is caused by placing subpulses with drastically different frequencies next to each other in the time-domain waveform. Figure 7.12 shows the result of applying the STFT to the SF waveform.
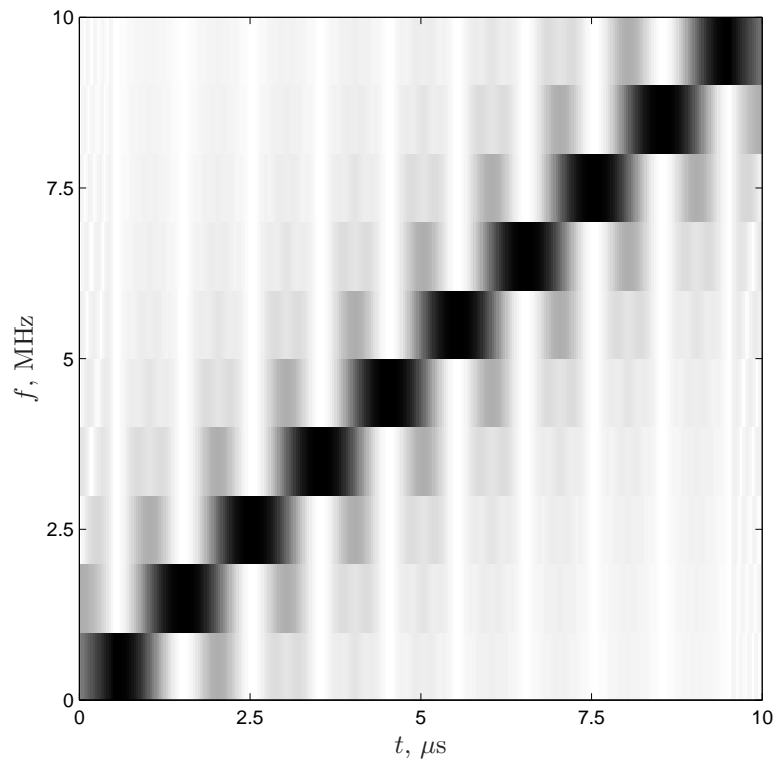
Figure 7.10:   STFT of SF waveform ($B = 10$ MHz, $N = 10$, window width $= \tau_s$). Frequency is monotonically increasing in a discretized LFM fashion.
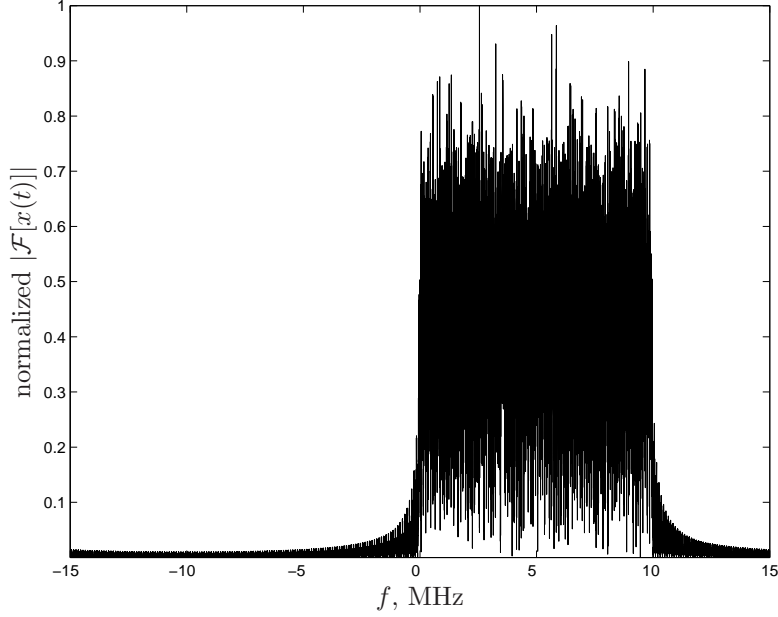
Figure 7.11: Frequency spectrum magnitude of a randomized SF waveform ($B = 10$ MHz, $N = 100$).

The randomized frequency order is clearly evident. Figure 7.13 shows a close-up of Fig. 7.11 around the 5 MHz region. Even though the spectrum is quite noisy, it does not contain any significant gaps. The spectrum nodes (e.g., at $f = 5$ MHz) occur at the true frequency values $\{f_n\}$ used to generate the subpulses.

Figure 7.14 demonstrates the SF waveform's noisy spectrum has not significantly degraded performance. It shows the square root of the zero Doppler cut of the randomized SF waveform's ambiguity function $|\chi(t_e, f_e)|$. As expected, the overall shape is sinc-like in nature, with its null-to-null resolution defined by c/B. The sidelobe structure has been slightly perturbed by the noisy spectrum, but the sidelobe magnitudes remain quite small.

Up to this point, all SF waveforms have been constructed with strict adherence to (7.15), which defines the relationship between the bandwidth B, pulsewidth τ, and number of subpulses N. If $B\tau < N^2$, the subpulse duration is too short, causing excessive energy spreading into neighboring data support region blocks. This effect negatively impacts auto and cross-correlation sidelobe structure. However, a much
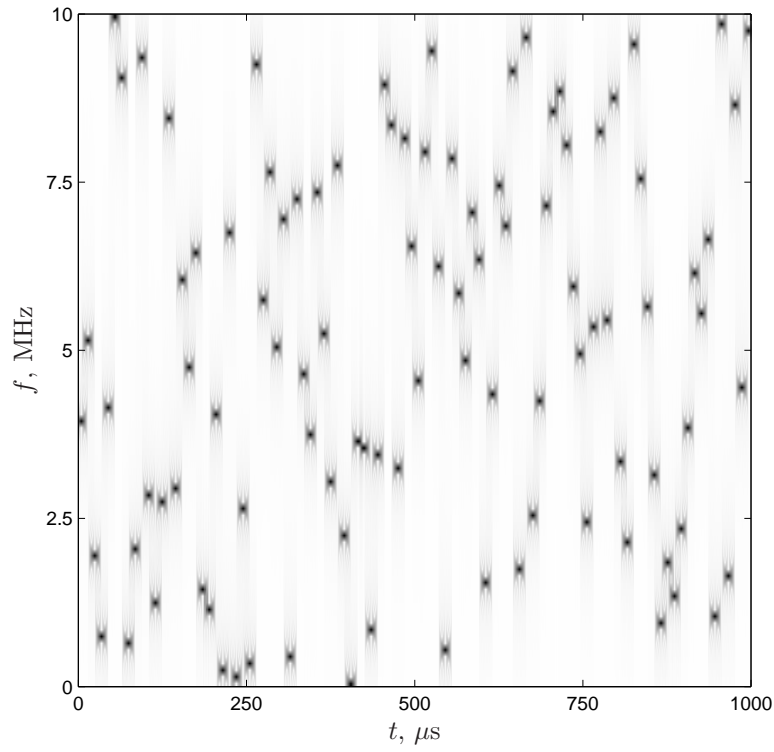
Figure 7.12: STFT of a randomized SF waveform ($B = 10$ MHz, $N = 10$, window width $= \tau_s$).
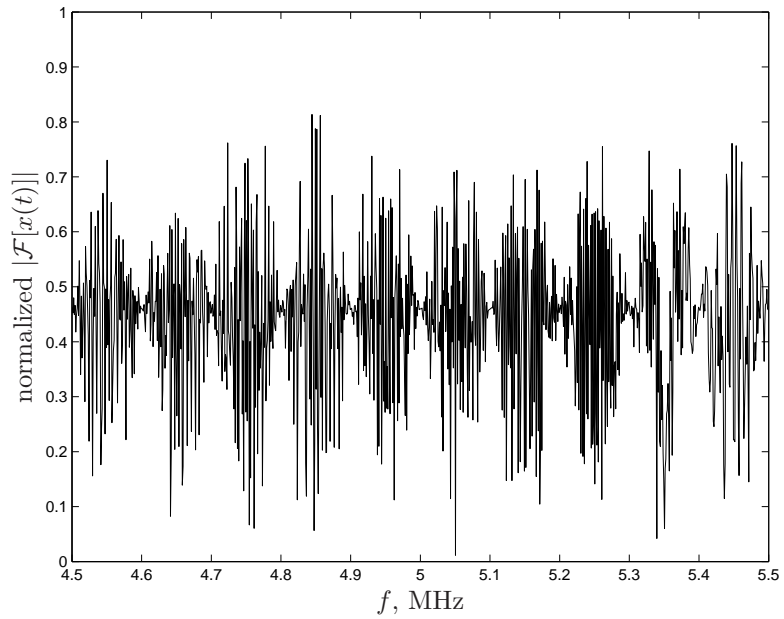
Figure 7.13: Close-up of a randomized SF waveform's frequency spectrum magnitude ($B = 10$ MHz, $N = 100$).
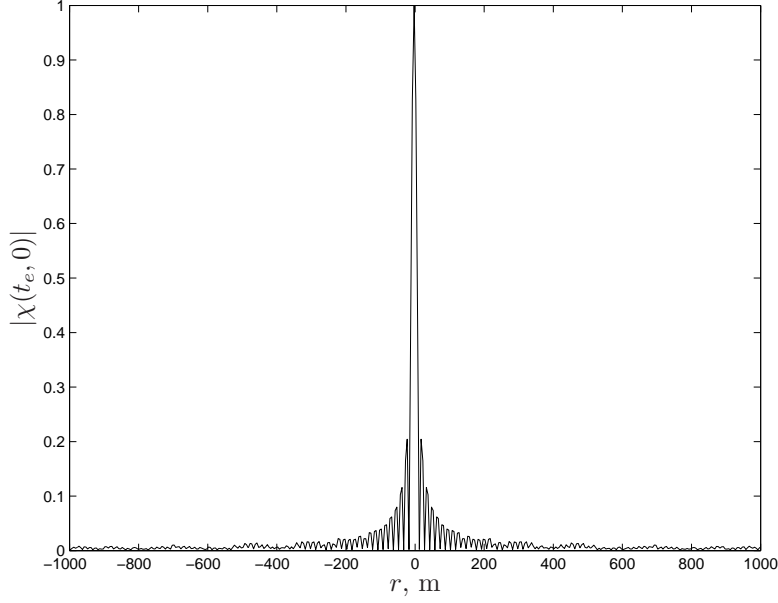
Figure 7.14: $|\chi(t_e, 0)|$ for a randomized SF waveform. Time mismatch error t_e converted to range r via $r = ct_e/2$.

more significant consequence occurs when $B\tau > N^2$, as illustrated by the following figures.

Figure 7.15 shows the frequency spectrum magnitude of a randomized SF waveform with $B = 20$ MHz, $N = 100$, and $\tau = 1000\,\mu\text{sec}$ (implying $B\tau = 2N^2$). Due to the increase in bandwidth, the oversampling ratio η is reduced from 3 to 1.5, but is still significantly above Nyquist. The frequency spectrum variation within the waveform bandwidth is even more pronounced than in Fig. 7.15. This effect is more clearly visible in Fig. 7.16, which shows a zoomed image of the frequency spectrum. In this case, the excessive frequency spacing has led to an approximately sinusoidal variation within the waveform's spectrum. The spectrum peaks correspond to the true frequencies used to form individual subpulses. These frequency spectrum gaps lead to serious repercussions in the waveform ambiguity function (Fig. 7.17). Recall from
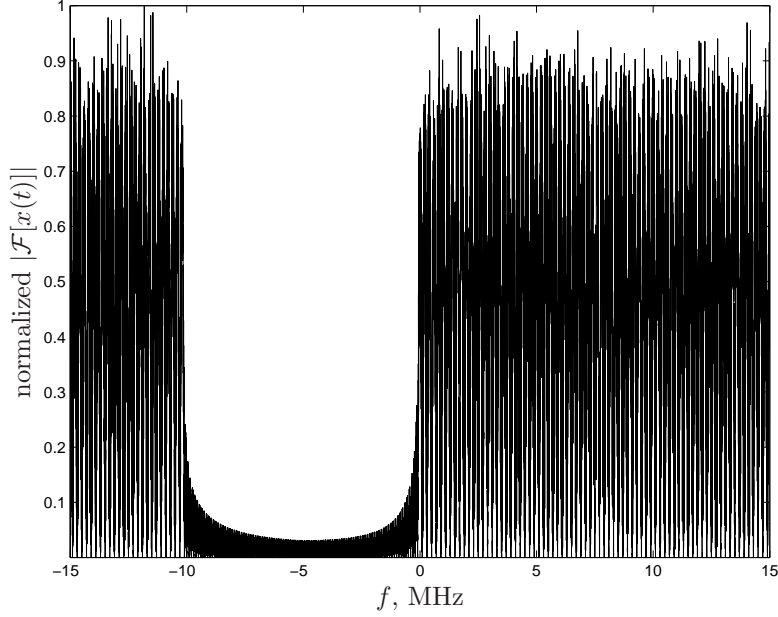
Figure 7.15: Frequency spectrum magnitude of a randomized SF waveform ($B = 20$ MHz, $N = 100$). Equation (7.15) violated.

Section 3.10, the unambiguous range extent Δr is determined by (3.27)[2]

$$\Delta r = N\frac{c}{2B},\tag{7.18}$$

where N is the number of frequency samples. When the spectrum was continuous, $N \to \infty$, implying no limit to range swath size (at least from a sampling perspective). However, with gaps in the frequency information, there is a maximum range swath

$$\Delta r = N\frac{c}{2B} = 100\frac{3e8}{2 \cdot 20e6} = 750 \text{ m}.\tag{7.19}$$

This limitation manifests itself in Fig. 7.17 where aliased copies of the ambiguity function peak appear at $\pm\Delta r$ from the reference radius.

Figures 7.15-7.17 illustrate the importance of obeying (7.15). There are proposed methods to circumvent this limitation by imposing some form of frequency di-

---

[2]Equation 3.27 defined range in x-direction due to the traditional narrow-angle convention. No such assumption is made here, thus Δr is substituted for Δx.
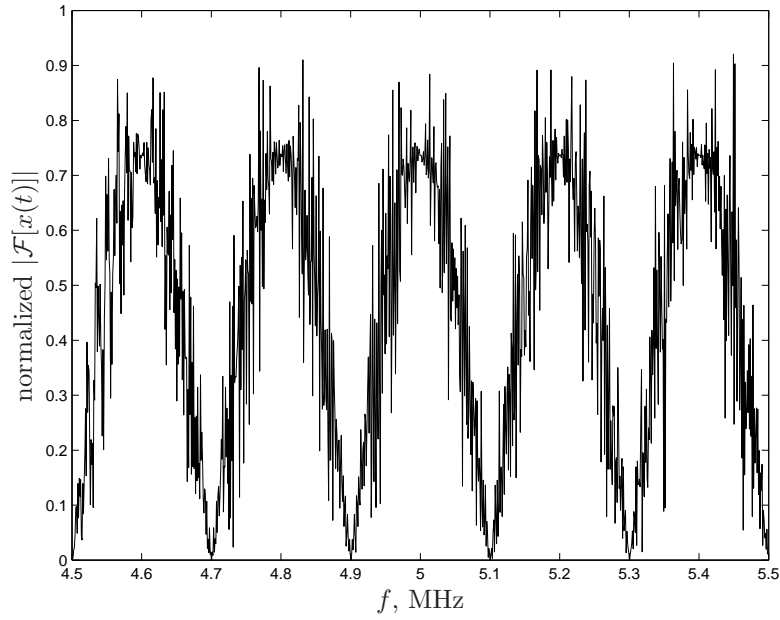
Figure 7.16: Close-up of a randomized SF waveform's frequency spectrum magnitude ($B = 20$ MHz, $N = 100$). Equation (7.15) violated.
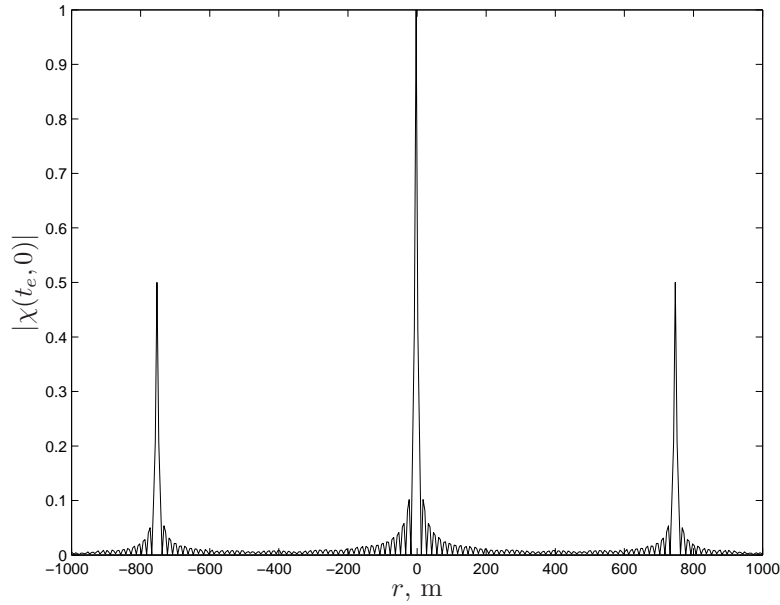
Figure 7.17: $|\chi(t_e, 0)|$ for a randomized SF waveform. Time mismatch error t_e converted to range r via $r = ct_e/2$. Equation (7.15) violated causing range aliasing artifacts.

versity on the subpulses themselves, allowing the user to increase system bandwidth (and thus improve range resolution) without decreasing subpulse width τ_s and/or increasing the number of subpulses. One promising approach involves superimposing LFM chirps on the individual SF subpulses [79]. This method was validated with the proposed anti-aliasing technique in [92].

7.4 Generation of Simulated Point Scatterer Data

With the demonstrated ability to produce SF waveforms with user defined parameters, it becomes possible to build a point scatterer simulation to test the anti-aliasing technique. This section outlines the basic structure and assumptions used to generate the simulation data.

First, it should be noted the simulation was limited to two dimensions. This is consistent with the principle that real SAR data processed in the 2-D slant range/cross range collection plane can easily be projected into the 2-D ground plane (e.g., by appropriate specification of image domain coordinates as illustrated in Sec. 5.6.2). Chapter VIII extends the simulator to the 3-D bistatic case. Most SAR systems traverse approximately linear flight paths as they image the ground. This linear flight path can be treated as the z-axis of a cylindrical coordinate system (ρ, z, ϕ) defining the collection geometry. As the data is collected, 2-D SAR processing determines the slant range ρ and cross range z-coordinates of each scatterer, but is unable to determine the angle ϕ [126]. In other words, each point scatterer is represented as a circular cut of the cylindrical collection geometry. This angular ambiguity can be broken in different ways, but the most common is a two step process accounting for the physical realities of SAR data collection. First, target echoes are assumed to come from ground-based objects. By intersecting the ground plane (or suitable warped contour map, see Chapter V) with the cylindrical collection geometry, the ambiguity is reduced from a circle, to two points, one on each side of the flight path. This situation is termed the left-right ambiguity [126]. Breaking this ambiguity is accomplished by assuming the SAR antenna's finite beamwidth contains only one of

220
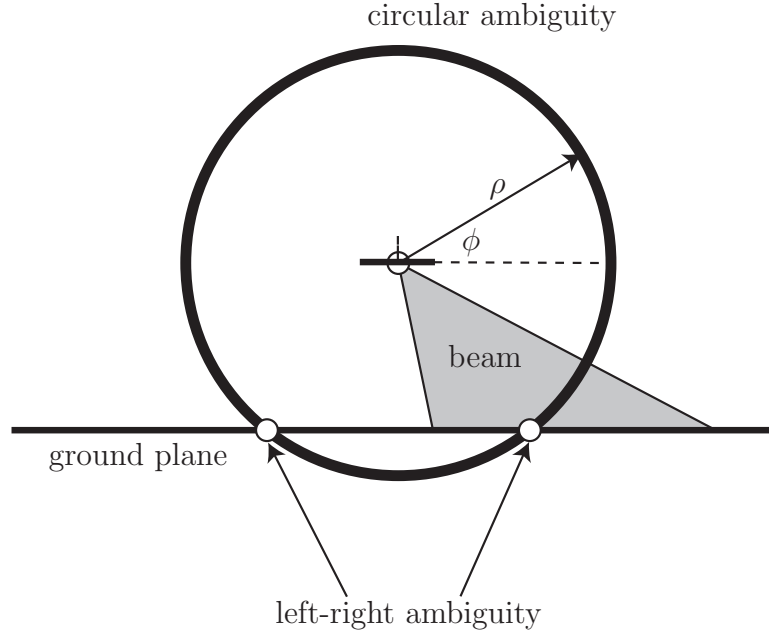
Figure 7.18:   2-D $\rho\phi$-plane of a 3-D SAR collection geometry. The SAR platform is at the figure's center. Assuming a roughly linear flight path, location of a single point scatterer at range ρ results in an ambiguous ϕ value. Assuming a flat ground plane reduces this circular ambiguity to the 2 point left-right ambiguity. The finite beam (gray shaded region) breaks the final ambiguity.

the two points. Figure 7.18 illustrates these ambiguities by showing the 2-D $\rho\phi$-plane for a 3-D SAR collection geometry.

The simulator begins by querying the user for a number of critical parameters. These parameters can be broken down into four categories: platform, waveform, image, and scatterer parameters and are listed in Table 7.1. The next several paragraphs describe how the simulator uses this information to generate the scene's simulated radar echoes.

Having received the parameter list, the simulator determines the platform's spatial location for each Coherent Processing Interval (CPI) pulse by dividing the synthetic aperture length L into uniformly spaced segments of length $\delta u = v_a/\text{PRF}$. The center of each segment denotes the SAR platform location for a single CPI pulse. This process makes use of the start-stop approximation, assuming the radar plat-

Table 7.1:   Key simulator parameters

Parameter	Type	Description	Units
v_a	platform	platform (aircraft) velocity	m/s
PRF	platform	pulse repetition frequency	Hz
L	platform	synthetic aperture length	m
$R_{\min}$	platform	minimum range	m
$R_{\max}$	platform	maximum range	m
$\Delta\theta$	platform	beamwidth	deg
f_c	waveform	center frequency	GHz
B	waveform	bandwidth	MHz
N	waveform	number of subpulses	unitless
I(x_c, y_c)	image	image center	(m, m)
D(x, y)	image	image dimensions	(m, m)
NUM(x, y)	image	pixel numbers in x & y axes	unitless
$s_n(x, y)$	scatterer	location	(m, m)

form is at a fixed location during transmission/reception of each waveform. If this assumption is too restrictive, the geometry can be treated in a bistatic fashion, where the transmission and reception locations are separated by a distance defined by the platform velocity and round-trip waveform propagation time[3].

After determining the platform location, a time vector t is created for recording the radar echoes. The time vector spans

$$\frac{cR_{\min}}{2} \le t < \frac{cR_{\max}}{2} + \tau, \tag{7.20}$$

and is sampled at twice the bandwidth (i.e., twice Nyquist). This time period covers uncompressed echo energy from all scatterers falling within the specified range swath $R_{\min}$ to $R_{\max}$. The time vector, along with the waveform parameters and desired subpulse frequency order, are then used to build a reference transmit waveform $w_{\text{TX}}(t)$ of duration τ

$$w_{\text{TX}}(t) = \sum_{n=0}^{N-1} \text{rect}\left(\frac{t - n\tau_s}{\tau_s}\right) \exp(j2\pi f_n t). \tag{7.21}$$

---

[3]While the start-stop approximation allows for the use of fixed range values for a given CPI pulse, it does not mean the Doppler shift associated with the platform velocity can be ignored. This Doppler shift is critical to the Doppler filter-based anti-aliasing technique.

Different waveforms may be generated by changing the subpulse frequency order.

Under the point scatterer assumption, the expected echo from each of the M scatterers is simply a delayed and Doppler shifted version of the transmitted waveform. Incorporating these effects into the transmitted waveform gives the expected waveform echo from the mth scatterer

$$w_{\text{RX}_\text{m}}(t) = A_m \sum_{n=0}^{N-1} \text{rect}\left(\frac{t - n\tau_s - 2r_m/c}{\tau_s}\right) \exp[j2\pi(f_n + f_{d_m}) \cdot (t - 2r_m/c)], \quad (7.22)$$

where A_m, r_m, and f_{d_m} are amplitude, range, and Doppler shift due to the mth scatterer, respectively. The scatterer amplitude is calculated on a binary basis. All scatterers falling within the main beam ($\Delta\theta$) have value $A_m = 1$. All others receive value $A_m = 0$. This approach does not model the fine structure of the azimuth beam or the dependence of amplitude on range. These effects are not important for demonstration of the anti-aliasing technique, but could be added without difficulty.

Since the point scatterer assumption treats each scatterer independently, the combined effect of all scatterers can be found via superposition. The received radar echo $w_{\text{RX}}(t)$ at a given location along the synthetic aperture is therefore given by

$$w_{\text{RX}}(t) = \sum_{m=0}^{M-1} w_{\text{RX}_\text{m}}(t), \quad (7.23)$$

which is then converted to baseband via

$$w_{\text{RX}_\text{b}}(t) = w_{\text{RX}}(t) \exp(j2\pi f_c t), \quad (7.24)$$

and saved along with the corresponding CPI pulse number and subpulse frequency order. The process is repeated for each location along the synthetic aperture. At each location, ranges and Doppler shifts are recalculated according to the instantaneous geometric relationship between the platform and scatterers. The subpulse frequency

order is also varied according to the user-defined method (Chapter VI described these methods).

Before closing this section, it should be noted that the simulator does not account for cross-correlation effects associated with matched filtering echoes of one SF waveform with another waveform composed of a different subpulse frequency order. In a real system this situation occurs since the continuous transmission requirement ensures returns from multiple pulses are present in the raw SF radar echoes. However, since use of shuffled circulant matrices results in orthonormal SF waveform sets, the effects of these additional waveform echoes are negligible.

7.5 Point Scatterer Data Processing

The raw baseband SF waveform echoes generated by the point scatterer simulator contain all the information necessary to form 2-D SAR images over any ground patch within the simulated beamwidth $\Delta\theta$ and range extent $\Delta R = R_{\max} - R_{\min}$.

To produce these images, the SAR image generation code begins by using the set of scenario parameters to calculate the platform/scatterer locations as well as the waveform sampling parameters. These calculations are identical to those performed during data generation. The code then uses the image center location to define a rectangular pixel grid used to build the SAR image. After these preliminary steps, the code moves through each waveform sequentially. For a given waveform (i.e., CPI pulse), the appropriate subpulse frequency order is used to build a digital matched filter waveform $w_{\mathrm{MF}}(t)$ given by

$$w_{\mathrm{MF}}(t) = \sum_{n=0}^{N-1} \mathrm{rect}\left(\frac{t - n\tau_s - 2r_c/c}{\tau_s}\right) \exp[j2\pi(f_n + f_{d_c}) \cdot (t - 2r_c/c)], \qquad (7.25)$$

where r_c and f_{d_c} are the instantaneous range and Doppler shift to the scene center. This digital waveform is then converted to baseband. Note, the use of a fixed image center $I(x_c, y_c)$ to calculate the matched filter parameters implies spotlight mode processing, despite the stripmap mode collection geometry.

224

Matched filter application is performed in the frequency domain to obtain the spatial frequency domain version of the One-Dimensional (1-D) range profile $P(k_r)$

$$P(k_r) = \mathcal{F}[w_{\text{RX}}(t)] \cdot \mathcal{F}^*[w_{\text{MF}}(t)]. \tag{7.26}$$

At this point generation of a 1-D complex range profile $f(r)$ could be accomplished with the Inverse Fourier Transform (IFT)

$$p(r) = \mathcal{F}^{-1}[P(k_r)]. \tag{7.27}$$

However, since the SAR imaging routine is built using back-projection techniques, the range profile must be filtered to account for the differential $k_r \mathrm{d}k_r \mathrm{d}\theta$ in the 2-D monostatic back-projection integral. The true equation for the filtered complex range profile to be used in 2-D SAR image formation is therefore

$$q(r) = \mathcal{F}^{-1}[k_r F(k_r)]. \tag{7.28}$$

Having obtained the complex filtered range profile $q(r)$ the final step is back-projecting this information over the pixel grid. The back-projection step completes the processing of a single CPI pulse. The process is then repeated for each CPI pulse. The resulting 2-D back-projections of the complex range profiles are coherently summed to yield a single complex image. Since only one waveform is processed at a time, the total computer memory requirements are much lower than with other SAR imaging approaches (e.g., Polar Format Algorithm (PFA) and Range Migration Algorithm (RMA)). Chapter V gives a more complete discussion of back-projection imaging.

7.6   Point Scatterer Simulation Results

Using the data generation code and SAR imaging code outlined in Sections 7.4 and 7.5, a SAR imaging scenario was defined to validate anti-aliasing technique performance. This section presents the simulation results in both one and two dimensions.

225

Table 7.2: 2-D monostatic simulation parameters.
*Determined by B, N and (6.27).

Parameter	Description	Value
v_a	Platform Velocity	100 & 200 m/s
PRF	Pulse Repetition Frequency	2,000 Hz
L	Synthetic Aperture Length	200 m
$R_{\min}$	Minimum Range	75,000 m
$R_{\max}$	Maximum Range	100,000 m
$\Delta\theta$	Beamwidth	90°
f_c	Center Frequency	10 GHz
B	Bandwidth	20 MHz
N	Number of Subpulses	100
τ	Waveform Duration*	500 μs

Table 7.3: Scatterer attributes: number, location, and Doppler shift (f_d). Origin $(0,0)$ at synthetic aperture center. Range from SAR platform to each scatterer is calculated relative to scatterer 5.

Scat.	Location				f_d (v_a = 100 m/s)		f_d (v_a = 200 m/s)	
Num.	x, m	y, m	range, m	θ, deg	Hz	PRF	Hz	PRF
1	69,681	52,659	-160	37.1	4,020	2.01	8,039	4.02
2	78,320	39,154	134	26.7	2,991	1.50	5,982	2.99
3	83,846	26,020	286	17.2	1,976	0.99	3,952	1.98
4	86,393	13,235	-99	8.7	1,010	0.51	2,019	1.01
5	87,500	0	0	0.0	0	0.0	0	0.0
6	86,793	-13,235	297	-8.7	-1,001	-0.50	-2,001	-1.00
7	83,192	-26,020	-334	-17.4	-1,990	-1.00	-3,980	-1.99
8	78,120	-39,315	-45	-26.7	-2,997	-1.50	-5,994	-3.00
9	70,031	-52,659	120	-37.0	-4,007	-2.01	-8,013	-4.01

Table 7.2 lists the simulation parameters. Table 7.3 lists the scatterer information. Two cases were simulated using platform velocities of $v_a = 100$ m/s and $v_a = 200$ m/s. The 2-D cartesian grid's origin is defined at the synthetic aperture center. Doppler shifts and ranges in Tab. 7.2 are calculated from the synthetic aperture center, but their actual values change slightly throughout the simulation as a function of instantaneous SAR platform location.

7.6.1 Case 1: $v_a = 100$ m/s. The first simulation case was run with a platform velocity of 100 m/s. Using this value, the scatterer Doppler shifts differ by
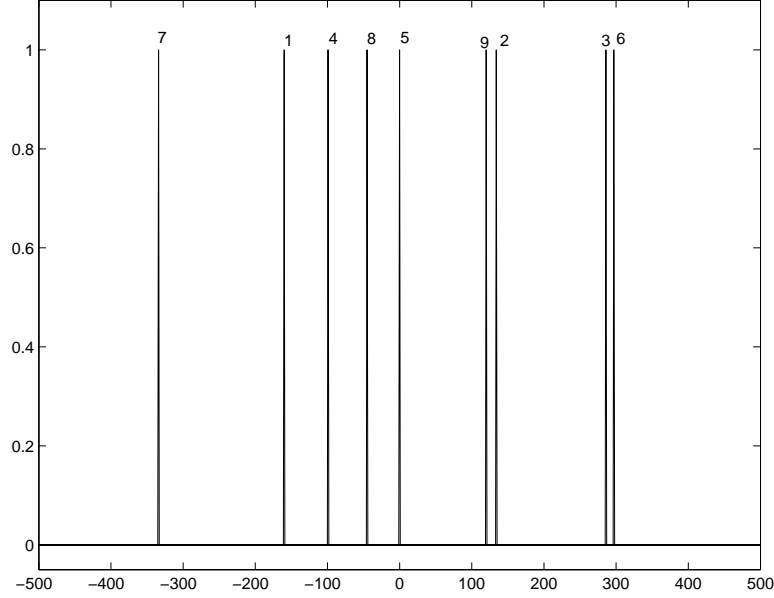
Figure 7.19: True range profile without Doppler filtering (Adapted from [88]).

approximately PRF/2. This case was examined to demonstrate how the anti-aliasing technique only eliminates scatterers at integer PRF multiples, but that these are the only scatterers which lead to cross range aliasing.

7.6.1.1 1-D Results: Range Profiles.

Before forming 2-D SAR images, a series of 1-D range profiles were generated to verify the desired SF waveform Doppler filtering properties [88]. Each range profile was formed with the platform fixed at the synthetic aperture center, but the Doppler shifts to each scatterer were still included as though the platform was moving at $v_a = 100$ m/s. Matched filtering was performed with respect to scatterer 5, giving all scatterers range values consistent with the "range" column of Tab. 7.3. The qualitative comparison of range profiles is a common analysis technique in the literature (e.g., [115, 125]).

Figure 7.19 shows the true range profile magnitude $|p(r)|$ formed by plotting a series of unit amplitude spikes corresponding to scatterer range. The Doppler shifts do not influence scatterer amplitude. There are no sidelobes since this plot is an idealization and not in indicative of any realizable waveform.

227
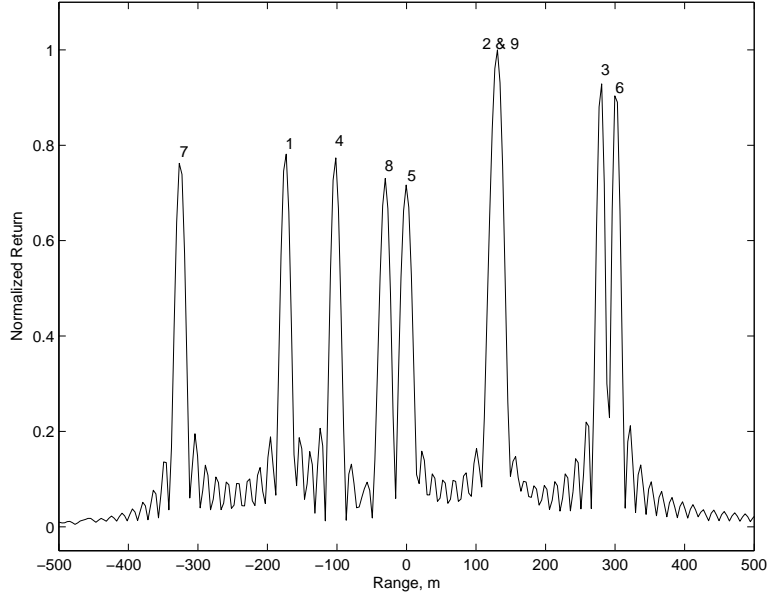
Figure 7.20: Range profile generated by LFM waveform (Adapted from [88]). Responses from scatterers 2 and 9 merged into a single response near 130 m.

Figure 7.20 illustrates the range profile magnitude obtained using a standard LFM waveform. This waveform was actually generated by ordering the $N = 100$ subpulse frequencies of an SF waveform in a monotonically increasing fashion. As discussed in Section 7.3, for large N the differences between the analytically generated LFM waveform and the SF approximation are negligible[4]. As expected, the finite LFM waveform bandwidth determines the range profile resolution. Significant sidelobe energy is also visible. Only eight distinct scatterers are visible in the LFM range profile. The range-Doppler coupling and limited waveform resolution has combined the responses from scatterers 2 and 9 at approximately 130 m, giving this peak a significantly larger response than the other scatterers. The responses from scatterers 3 and 6 are not combined because the range-Doppler coupling effect pushes their responses further apart instead of closer together.

---

[4]This fact was also verified by comparing to a "true" LFM waveform simulation. However, for the sake of keeping the simulation code as uniform as possible, SF LFM waveform approximations were used for all presented results.
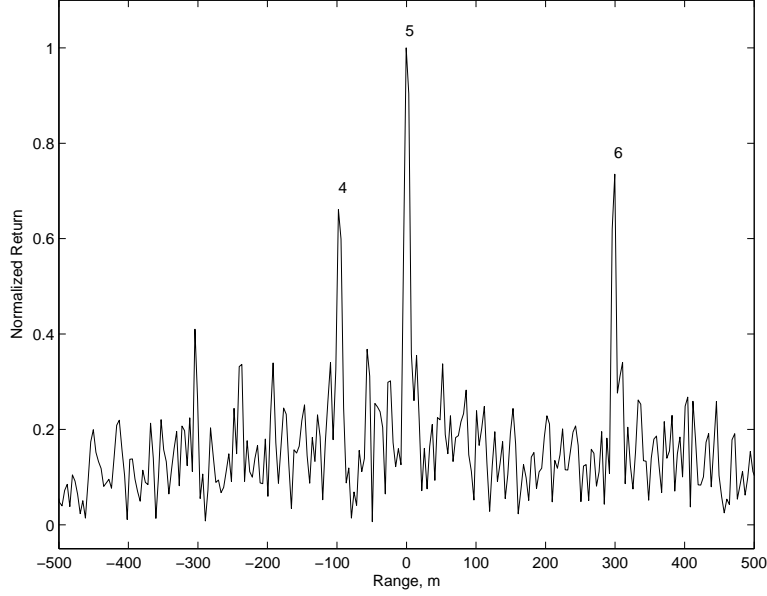
Figure 7.21:   Range profile generated from a single SF
pulse with random subpulse order (Adapted from [88]).

Figure 7.21 shows the range profile magnitude generated using a single SF wave-form with randomized subpulse frequency order. Scatterer 5 is essentially unaffected since the matched filter parameters are tuned to this scatterer's location. Scatterers 4 and 6 are also clearly visible, but somewhat reduced in amplitude. Other scatterers are obscured by a large noise floor which has appeared across the entire range swath. This noise floor is caused by the noise-like nature of the ambiguity function for a single randomized SF waveform.

Figure 7.22 contains the range profile magnitude formed by the coherent combi-nation of 100 random SF waveform realizations. Since the SF pulse contains $N = 100$ subpulses, the $B \times \tau$ data support region has $N^2 = 10,000$ blocks. By using 100 sep-arate subpulses, the entire data support region is filled in a *roughly* uniform fashion, creating the desired 2-D $|\text{sinc}(\cdot)|^2$ ambiguity response. The return amplitude from scatterer 5 is essentially equivalent to the LFM waveform case (Fig. 7.20), but the other scatterers have all been altered. Scatterers 4 and 6 appear at roughly 0.6 while scatterers 2 and 8 appear at roughly 0.2. Scatterers 1,3,7, and 9 have been essentially removed from the range profile. These results are consistent with a 2-D $|\text{sinc}(\cdot)|^2$
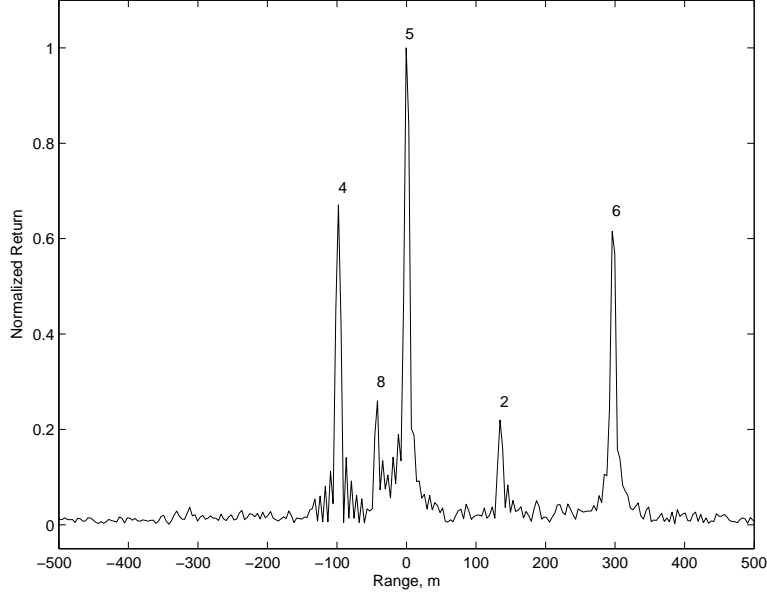
Figure 7.22:   Coherent combination of range profiles generated by 100 realizations of randomly ordered SF pulses (Adapted from [88]).

ambiguity function whose null-to-null width in along the Doppler axis is $2\mathrm{PRF} = 2\tau$. Note, scatterers 2 and 8 are expected to appear at the first sidelobe peak. This expectation is consistent with their amplitudes of $20\log_{10}(0.2) \approx -14.0$ dB. The more uniform data support region sampling has also dramatically reduced the noise-floor. Although not apparent in this figure, the 2-D $|\mathrm{sinc}(\cdot)|^2$ ambiguity function eliminates the range-Doppler coupling effect, ensuring range profile echoes appear at the correct range locations.

Figure 7.23 also shows the results from coherently combining range profiles from 100 SF waveform echoes. However, this time the subpulse frequency order was determined by a shuffled circulant matrix, guaranteeing uniform filling of the data support region. The result is a reduction in the range profile noise-floor, leading to even better performance in the final 2-D SAR images.

The Doppler filtering properties demonstrated in Figs. 7.22 and 7.23 are exactly what is required to perform anti-aliasing in 2-D SAR imagery. Even though only four of the eight aliased scatterers have been removed by the Doppler filter, the scatterers
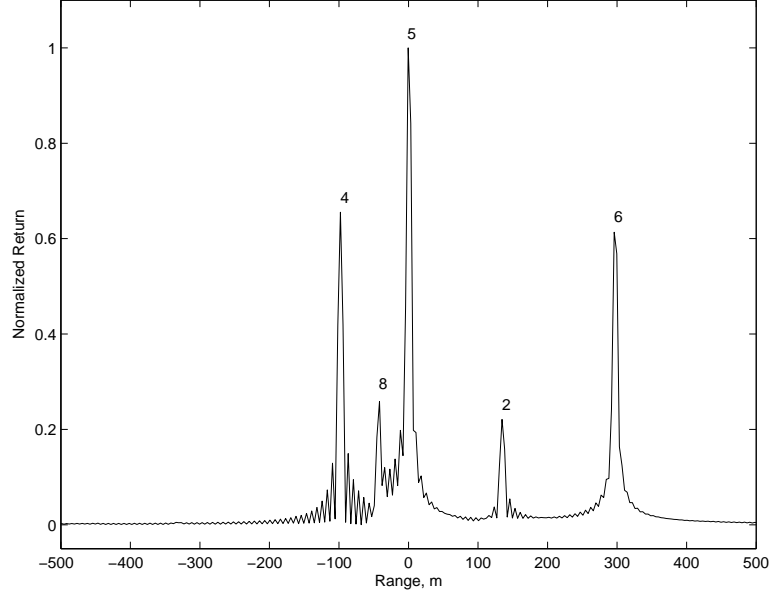
Figure 7.23: Coherent combination of range profiles generated by all 100 SF subpulse ordering schemes dictated by a composite permutation matrix.

which remain have Doppler shifts equal to non-integer Pulse Repetition Frequency (PRF) multiples, and will therefore be removed by the spatial cross range filter built via the SAR imaging process. This fact is demonstrated next.

7.6.1.2 2-D Results: SAR Images.   Using the 2-D SAR simulator described previously, a series of 2-D images were generated using both LFM and SF waveforms for the $v_a = 100$ m/s case. Each image has dimensions of one square kilometer and should contain only one scatterer. All images were normalized and given a $20 \log_{10}(N) = 40.0$ dB dynamic range. This value was selected because the sidelobe peaks of an SF waveform are usually less than or equal to $1/N$ [116]. These images illustrate the utility of the Doppler aliasing reduction technique introduced in Chapter VI.

Figure 7.24 shows the image of scatterer 5 produced with an LFM waveform. The true scatterer is visible at the image center as a well-focused cross-shaped IPR, consistent with the 2-D FT nature of the back-projection imaging process. Four aliased scatterers appear as defocused patches throughout the image. The defocusing

231
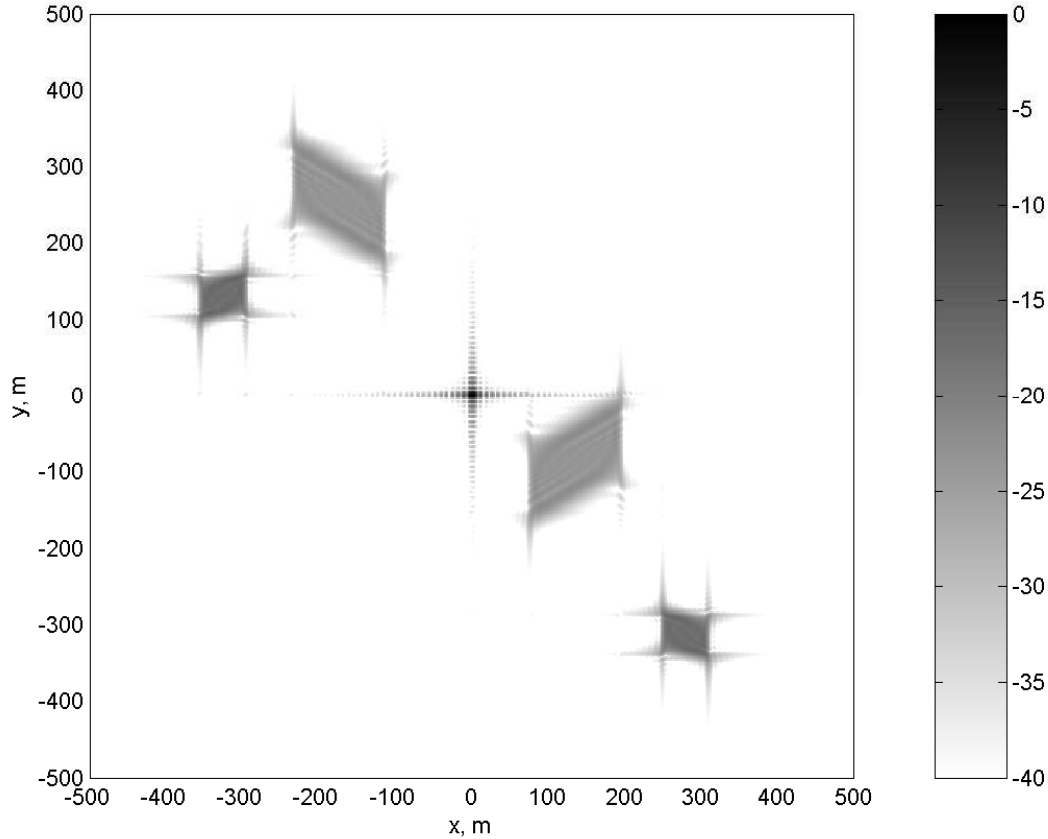
Figure 7.24:   LFM image of scatterer 5 for $v_a = 100$ m/s (40.0 dB dynamic range). Scatterer 5 is well focused at image center. Other scatterers alias into the image (adapted from [87]).

results from the SAR algorithm's attempts to focus these aliased scatterers as though they appeared within the image grid. The two smaller patches correspond to Doppler shifts of approximately $\pm$PRF (scatterers 3 and 7), while the larger patches correspond to Doppler shifts of approximately $\pm$2PRF (scatterers 1 and 9). Only five of the nine scatterers appear in the image. Scatterers with Doppler shifts equal to non-integer PRF multiples (i.e., scatterers 2, 4, 6, and 8) are not present. Note, the smaller patches have higher peak values, making them the greater filtering challenge.

Figure 7.25 shows the image of scatterer 5 produced with SF waveforms defined by a shuffled circulant matrix. The true scatterer appears in its correct location, but the aliasing artifacts have been mitigated.

232
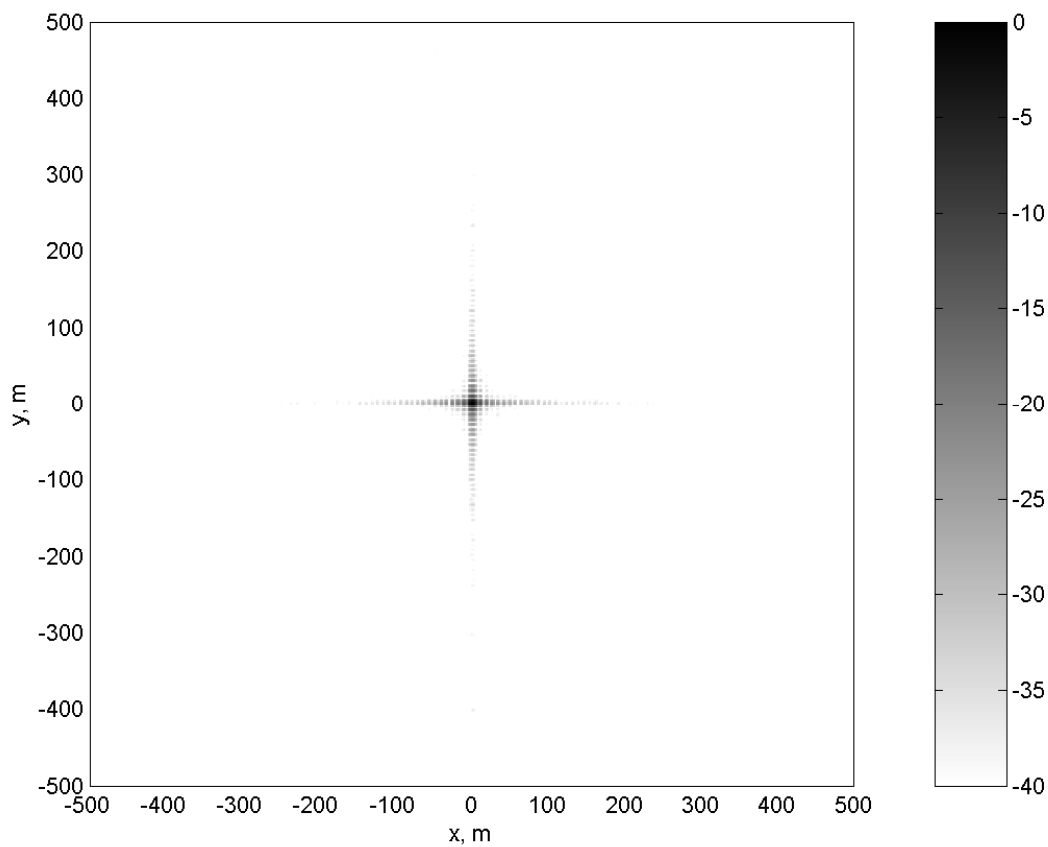
Figure 7.25: SF shuffled circulant image of scatterer 5 for $v_a = 100$ m/s (40.0 dB dynamic range). Aliasing artifacts have been completely mitigated (adapted from [87]).

7.6.2 Case 2: $v_a = 200$ m/s. Increasing the platform velocity from 100 m/s to 200 m/s has several important consequences for the SAR system. First, doubling the velocity doubles the required PRF. Since the simulation's PRF value is held constant at 2000 Hz, doubling the velocity doubles the number of cross range ambiguities. This fact is evident in Tab. 7.3 since for the $v_a = 200$ m/s case, the Doppler shifts of all nine scatterers differ by (approximately) integer PRF multiples. The addition of extra ambiguities makes the anti-aliasing problem more challenging for two reasons. First, more scatterers need to be mitigated. Second, the defocusing of the first ambiguous scatterer pair is less severe, increasing the maximum aliased energy amplitude.

7.6.2.1 2-D Results: SAR Images. As in the $v_a = 100$ m/s case, the SAR simulation code produced both LFM and shuffled circulant matrix SF images of scatterer 5. Figure 7.26 shows the LFM image. The returns from scatterers 1, 3, 5, 7, and 9 are virtually identical in both amplitude and location to those in Fig. 7.24 (the $v_a = 100$ m/s case). However, this time returns from scatterers 2, 4, 6, and 8 are also visible. The returns from scatterers 4 and 6 exhibit the least defocusing, giving their aliased signatures higher amplitudes and making them harder to eliminate. These two scatterers are also the closest to scatterer 5 in terms of distance in the xy-plane.

Figure 7.27 shows the image of scatterer 5 produced with SF waveforms defined by a shuffled circulant matrix. Despite the addition of the even numbered scatterers, the technique still mitigates the aliasing artifacts. However, a few noise-like, low-level pixels are visible around the image. This effect is a consequence of the noise-like ambiguity structure of individual SF waveforms. Since SAR platform motion prevents perfect combination of the individual SF waveform ambiguity surfaces (Sec. 6.4.2) minor noise-like effects creep into the imagery. These effects are quantified in the next section.

Figures 7.28 and 7.29 show similar results for images of scatterer 8. These images were formed by processing the *same* simulation data with different matched filter
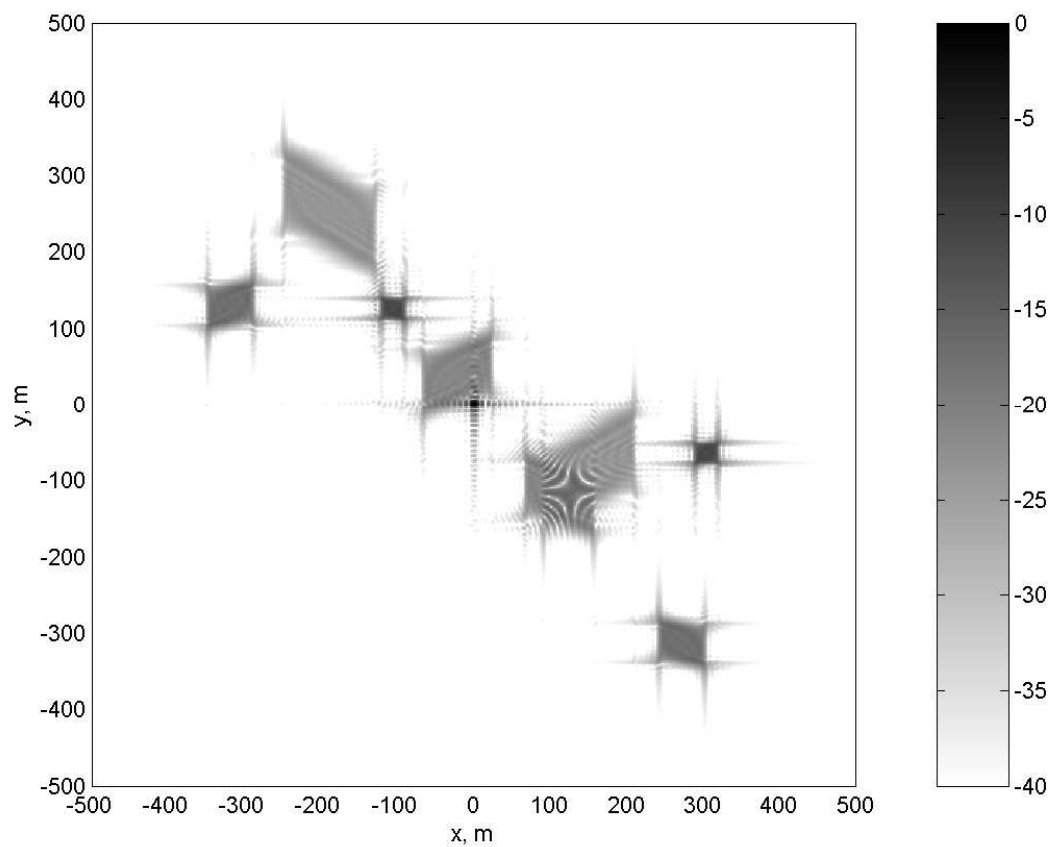
Figure 7.26:   LFM image of scatterer 5 for $v_a = 200$ m/s (40.0 dB dynamic range). Scatterer 5 is well focused at image center. Other scatterers alias into the image.
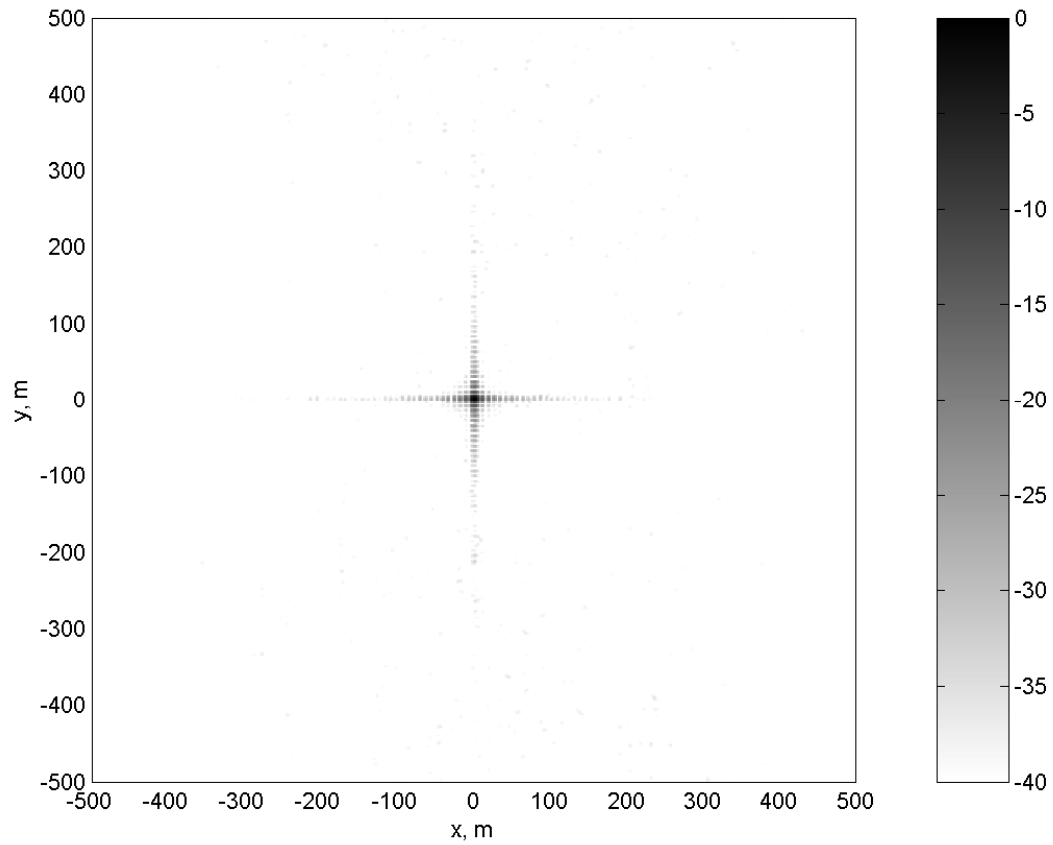
Figure 7.27: SF shuffled circulant image of scatterer 5 for $v_a = 200$ m/s (40.0 dB dynamic range). Aliasing artifacts have been mitigated.
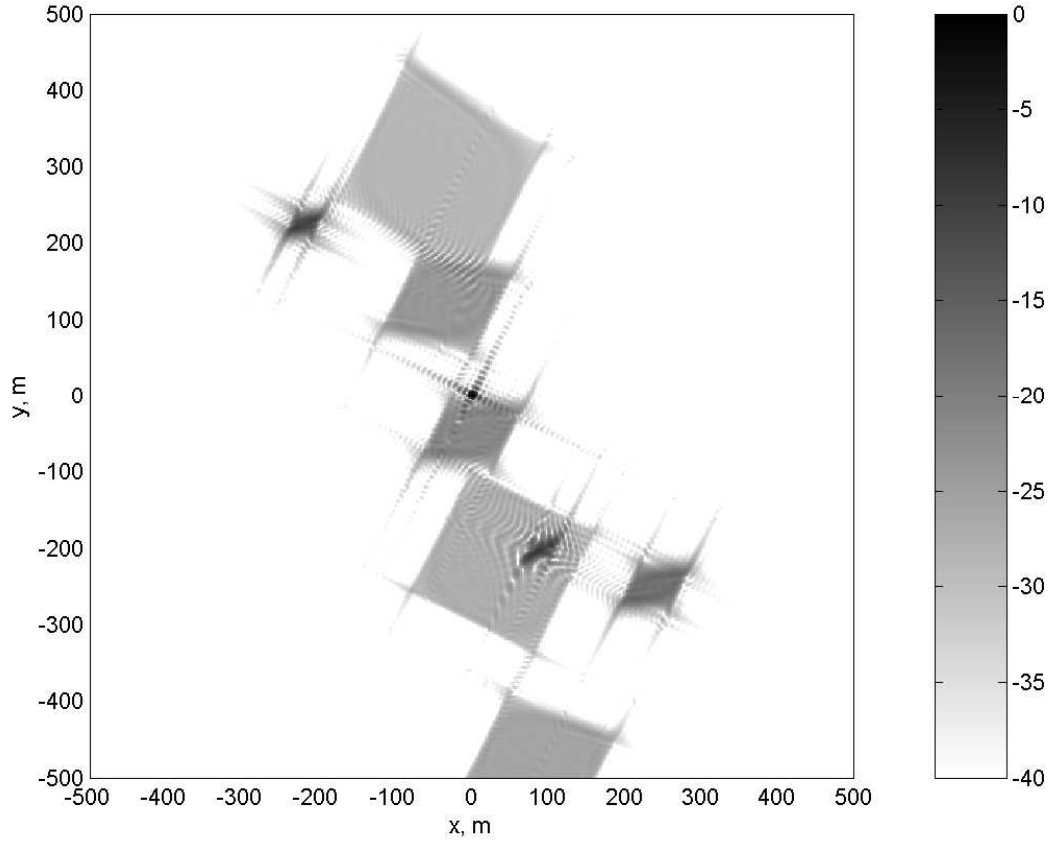
Figure 7.28:   LFM image of scatterer 8 for $v_a = 200$ m/s (40.0 dB dynamic range). Scatterer 8 is well focused at image center. Other scatterers alias into the image.

parameters (corresponding the range and Doppler of scatterer 8 instead of scatterer 5). The true scatterer response has been rotated due scatterer 8's non-zero θ angle.

7.6.2.2 *Performance Metrics.*   In addition to the qualitative comparison of simulated SAR imagery, it is also important to quantify anti-aliasing technique effectiveness. A normalized energy metric performs this quantification. The simulator was used to produce a series of "ideal" images containing only one scatterer at a time. The unnormalized ideal image energy was calculated by summing over pixel values in the final ideal image (i.e., the squared magnitude of the complex matrix generated by the back-projection algorithm). This value was then used to normalize the energies
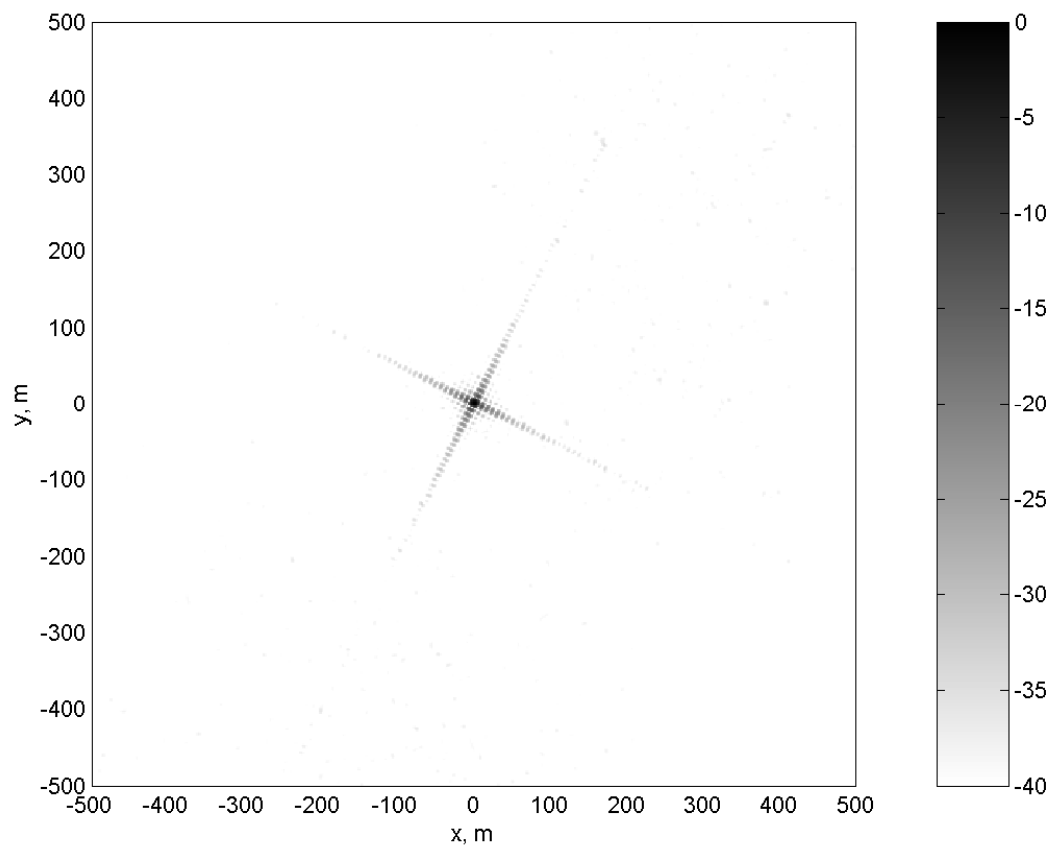
Figure 7.29:   SF shuffled circulant image of scatterer 8 for $v_a = 200$ m/s (40.0 dB dynamic range). Aliasing artifacts have been mitigated.

Table 7.4: Normalized 2-D monostatic SAR image energy.

Waveform	Scatterer	Figure	Energy	Reduction
Ideal	5	-	1.0000	-
LFM	5	7.26	3.7155	-
SF shuffled	5	7.27	1.0002	99.99%
Ideal	8	-	1.0000	-
LFM	8	7.28	3.6639	-
SF shuffled	8	7.29	1.0004	99.98%

of both the LFM and SF shuffled circulant images, giving the results presented in Table 7.4.

As depicted in Table 7.4, the LFM waveform results in a significant increase in normalized image energy over the ideal case. With eight aliased artifacts, one might expect a normalized energy of 9.0. However, the non-zero energy contributions of the -40.0 dB image floor reduce this value. In both the scatterer 5 and scatterer 8 images, the SF shuffled approach eliminates virtually all aliased artifact energy (defined as normalized energy minus one). Performance in the $v_a = 100$ m/s case, where low-level noise-like pixels are not observed, is even better.

7.7   Summary

This chapter developed and demonstrated a 2-D monostatic point scatterer simulation of the anti-aliasing technique. Using complex envelope notation, both LFM and SF waveform simulations in one and two dimensions were presented. The simulation parameters came from relevant the Global Hawk and WAM-SAR specifications outlined in Chapter II. The LFM simulation results clearly illustrate the aliasing artifact problem, clouding 1-D range profiles and 2-D SAR images with excess energy. SF simulation results remove these artifacts, restoring pristine range profiles and imagery. The chapter also quantifies anti-aliasing technique performance using an energy metric, demonstrating how more than 99% of the aliased energy is elimi-

nated. Appendix D contains the point scatterer simulation code used to obtain the 2-D simulation results. These simulation results are independently verified in [92].

VIII. 3-D Monostatic and Bistatic Anti-Aliasing

The anti-aliasing technique introduced in Chapter VI and simulated in Chapter VII assumed a Two-Dimensional (2-D) monostatic data collection geometry. However, successful Wide-Angle Multistatic Synthetic Aperture Radar (WAMSAR) implementation requires extension of the anti-aliasing technique to a Three-Dimensional (3-D) bistatic geometry.

Chapter VI showed how coherently combining a series of Stepped-Frequency (SF) waveform echoes with appropriately chosen subpulse frequency orders yields a 2-D $|\text{sinc}(\cdot)|^2$ ambiguity function $|\chi(t_e, f_e)|^2$. Figure 8.1 illustrates the central region of this ambiguity function for an SF waveform collection.

The technique's ability to remove aliased energy comes from the persistent nulls at key Doppler values. Buried within this approach is the implicit assumption that an aliasing artifact's Doppler shift f_d is not a function of g, the ground range[1]. Analytically, this assumption is expressed as

$$\frac{\partial f_d}{\partial g} = 0. \tag{8.1}$$

As the following development shows, this assumption is valid in the 2-D monostatic case but invalid in the general 3-D monostatic/bistatic case. None-the-less, the violation of (8.1) is not so severe as to preclude aliasing artifact mitigation in militarily significant 3-D monostatic/bistatic scenarios.

This chapter begins by deriving the Doppler shift f_d for an arbitrary 3-D bistatic scenario. It then evaluates anti-aliasing performance under 3-D monostatic and 3-D bistatic conditions. These evaluations are performed using a 3-D version of Chapter VII's point scatterer simulator. The simulation results, including both simulated SAR images and normalized energy calculations, demonstrate effective anti-aliasing performance despite violation of (8.1).

---

[1]Ground range measures the distance between the platform and scatterer projections into the xy-plane (see Fig. 3.2). This assumption could also be expressed using the true range (i.e., slant range) r, but the 2-D image plane figures in this chapter make use of g more convenient.
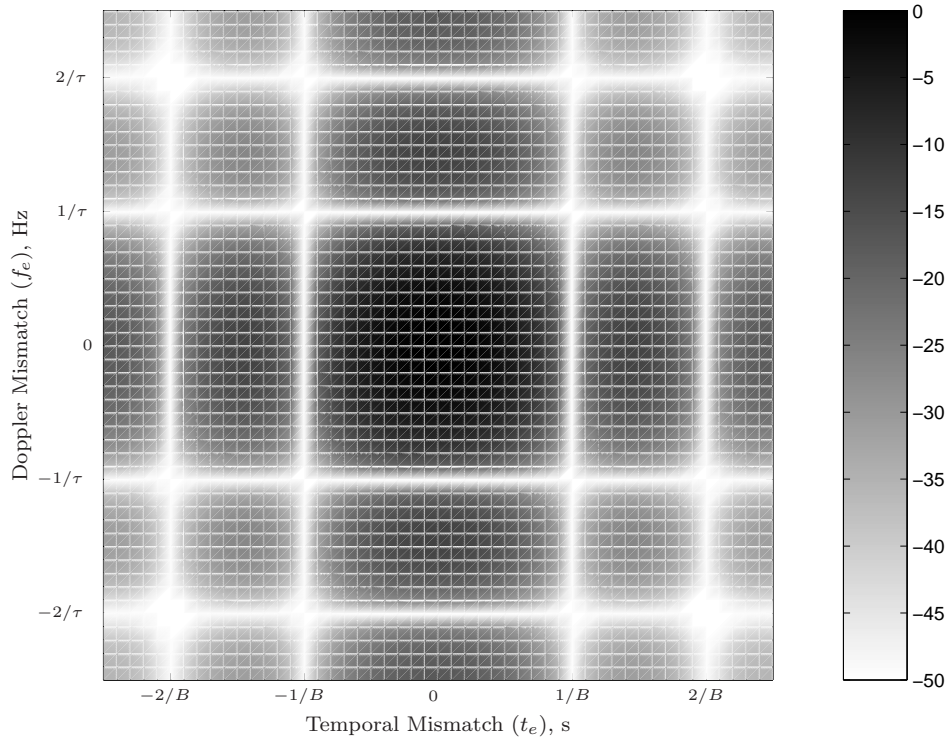
Figure 8.1: Central region of ambiguity diagram for the coherent combination of all 100 SF waveforms specified by a 100×100 shuffled permutation matrix (50.0 dB dynamic range). The shape approximates a 2-D $|\mathrm{sinc}(\cdot)|^2$ function with nulls of depth greater than -50.0 dB. Reprinted from Fig. 6.7.

8.1 Bistatic Doppler Shift

Examination of 3-D bistatic anti-aliasing requires an appropriate expression for Doppler shift. This section derives such an expression from first principles.

Basic kinematics states distance x equals rate v times time t

$$x = vt. \tag{8.2}$$

Algebraic manipulation of (8.2) gives

$$\frac{1}{t} = \frac{v}{x}. \tag{8.3}$$

For an ElectroMagnetic (EM) wave propagating in free space, the velocity v is simply c, the speed of light. Choosing the distance x equal to one wavelength λ, the term $1/t$ represents frequency f (i.e., the number of wavelengths per second). Equation (8.3) can therefore be rewritten as

$$f = \frac{c}{\lambda}. \tag{8.4}$$

If an EM wave propagates directly from a transmitter to a receiver, the frequency measured by the receiver f_m is determined not only by the wave's original frequency f, but also by the relative velocity v_r between the transmitter and receiver

$$f_m = \frac{c + v_r}{\lambda}. \tag{8.5}$$

Doppler shift is calculated as the difference between the measured and transmitted frequencies

$$f_d = f_m - f = \frac{v_r}{\lambda}. \tag{8.6}$$

In radar applications, EM waves propagate from the transmitter to a scatterer and then to the receiver[2]. The existence of two propagation legs means the Doppler shift is composed of two terms

$$f_d = \frac{v_{\text{TX}_r}}{\lambda} + \frac{v_{\text{RX}_r}}{\lambda},$$ (8.7)

where v_{TX_r} is the relative velocity between the transmitter and scatterer and v_{RX_r} is the relative velocity between the receiver and scatterer.

Assuming the scatterers are stationary, Chapter V's arbitrary 3-D bistatic geometry can be used to determine relative velocities v_{TX_r} and v_{RX_r}. Figure 8.2 illustrates this geometry. The unit vectors $\bar{u}_{\text{TX}}$ and $\bar{u}_{\text{RX}}$ point from scene center to the transmitter and receiver, respectively. Analytically they are defined as

$$\bar{u}_{\text{TX}} = \begin{bmatrix} \cos(\theta_{\text{TX}}) \cos(\phi_{\text{TX}}) \\ \sin(\theta_{\text{TX}}) \cos(\phi_{\text{TX}}) \\ \sin(\phi_{\text{TX}}) \end{bmatrix}$$ (8.8)

and

$$\bar{u}_{\text{RX}} = \begin{bmatrix} \cos(\theta_{\text{RX}}) \cos(\phi_{\text{RX}}) \\ \sin(\theta_{\text{RX}}) \cos(\phi_{\text{RX}}) \\ \sin(\phi_{\text{RX}}) \end{bmatrix},$$ (8.9)

where $(\theta_{\text{TX}}, \phi_{\text{TX}})$ and $(\theta_{\text{RX}}, \phi_{\text{RX}})$ are the azimuth/elevation angles from the scene center to the transmitter and receiver. Combining these unit vectors with $\bar{v}_{\text{TX}}$ and $\bar{v}_{\text{TX}}$, the 3-D cartesian velocity vectors for the transmitter and receiver, allows calculation of v_{TX_r} and v_{RX_r} via

$$v_{\text{TX}_r} = -\bar{v}_{\text{TX}} \cdot \bar{u}_{\text{TX}}$$ (8.10)

and

$$v_{\text{RX}_r} = -\bar{v}_{\text{RX}} \cdot \bar{u}_{\text{RX}},$$ (8.11)

---

[2]EM waves can also bounce between multiple scatterers before reaching the receiver. This situation is known as multipath. As long as the scatterers have similar velocities, the Doppler effects of multipath are minor and can be ignored.
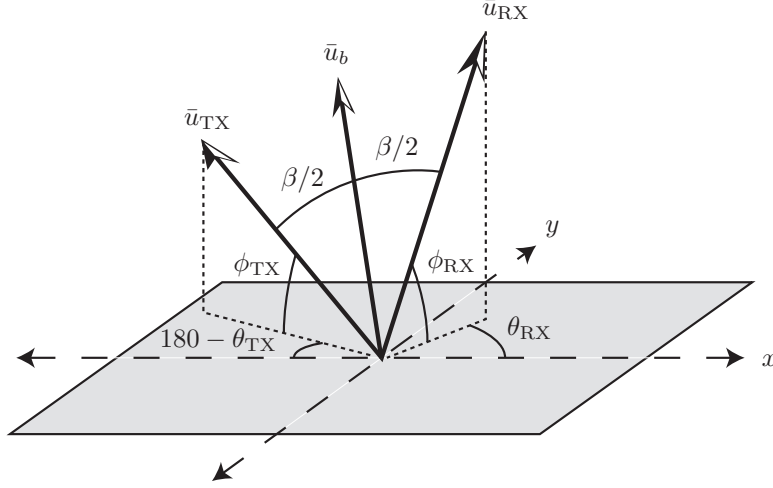
Figure 8.2: 3-D bistatic SAR/ISAR collection geometry. The unit vectors $\bar{u}_{\text{TX}}$ and $\bar{u}_{\text{RX}}$ point from the scene center towards the transmission and reception platforms, respectively. The bistatic angle β between these two vectors is bisected by the unit vector $\bar{u}_b$. Reprinted from Fig. 5.1.

where $\cdot$ denotes the dot product. The negative signs in (8.10) and (8.11) account for the fact that $\bar{u}_{\text{TX}}$ and $\bar{u}_{\text{RX}}$ are defined relative to scene center, while the Doppler shift f_d is defined relative to the transmitter/receiver locations. Using the preceding analysis, the final 3-D bistatic Doppler shift equation is

$$f_d = -\frac{1}{\lambda} \left(\bar{v}_{\text{TX}} \cdot \bar{u}_{\text{TX}} + \bar{v}_{\text{RX}} \cdot \bar{u}_{\text{RX}} \right). \tag{8.12}$$

The remainder of the Chapter demonstrates the anti-aliasing technique's abilities and limitations in 3-D monostatic and bistatic scenarios. Table 8.1 lists critical parameters for the four simulation cases: 2-D monostatic (Sec. 8.2.1), 3-D monostatic (Sec. 8.2.2), 3-D passive bistatic (Sec. 8.3.1), and 3-D circular-orbit multistatic (Sec. 8.3.2). Each row lists the transmit/receive locations and scene center in units of (km,km,kft). Platform velocity vectors $\bar{v}_{\text{TX}}$ and $\bar{v}_{\text{RX}}$ are in m/s. The ground range to scene center g_c is in km, while the Doppler shift to scene center is in Hz. In bistatic

Table 8.1:   3-D Simulation parameters. Each row denotes a different scenario: 2-D monostatic (from Sec. 7.6), 3-D monostatic, passive bistatic, and multistatic, respectively.

Section	TX loc. (km,km,kft)	RX loc. (km,km,kft)	$\bar{v}_{\text{TX}}$ m/s	$\bar{v}_{\text{RX}}$ m/s	Scene Center (km,km,kft)	g_c km	f_{d_c} Hz
8.2.1	(0,0,0)	(0,0,0)	$[0, 200, 0]^{\text{T}}$	$[0, 200, 0]^{\text{T}}$	(0,85.5,0)	50	0
8.2.2	(0,0,60)	(0,0,60)	$[0, 200, 0]^{\text{T}}$	$[0, 200, 0]^{\text{T}}$	(0,85.5,0)	50	0
8.3.1	(-50,30,60)	(0,0,20)	$[0, -50, 0]^{\text{T}}$	$[0, 200, 0]^{\text{T}}$	(0,30,0)	77.2	472
8.3.2	(50,50,60)	(0,0,60)	$[200, 0, 0]^{\text{T}}$	$[0, 200, 0]^{\text{T}}$	(0,50,0)	50	0

geometries

$$g_c = \frac{1}{2}\left(g_{\text{TX}} + g_{\text{RX}}\right), \tag{8.13}$$

where g_{TX} and g_{RX} are the ground ranges denoting distance between the scene center and the transmitter and receiver, respectively. Unless otherwise stated, the general simulation parameters such as frequency, Pulse Repetition Frequency (PRF), etc., are identical to the $v_a = 200$ m/s case from Table. 7.2. Scatterer location and number vary somewhat since the changing data collection geometries also change the spatial locations of points which alias into the SAR images.

8.2   Monostatic Scenarios

The scenario in Chapter VI assumed a 2-D monostatic Synthetic Aperture Radar (SAR) platform traversing a linear flight path in the $+y$-direction with velocity v_a. Allowing the platform a non-zero height z, the 3-D monostatic Doppler shift seen by the receiver is

$$f_d = -\frac{2}{\lambda}\begin{bmatrix} 0 \\ v_a \\ 0 \end{bmatrix} \cdot \begin{bmatrix} \cos(\theta_{\text{TX}})\cos(\phi_{\text{TX}}) \\ \sin(\theta_{\text{TX}})\cos(\phi_{\text{TX}}) \\ \sin(\phi_{\text{TX}}) \end{bmatrix} = -\frac{2v_a \sin\theta_{\text{TX}}\cos\phi_{\text{TX}}}{\lambda}. \tag{8.14}$$

The anti-aliasing technique assumes

$$\frac{\partial f_d}{\partial g} = 0, \tag{8.15}$$

246

Examining this assumption in the 3-D monostatic scenario requires evaluating

$$\frac{\partial f_d}{\partial g} = -\frac{\partial}{\partial g} \frac{2v_a \sin\theta_{\text{TX}} \cos\phi_{\text{TX}}}{\lambda}. \tag{8.16}$$

Assuming a planar scene, the elevation angle ϕ_{TX} may be calculated via

$$\phi_{\text{TX}} = \tan^{-1}\left(\frac{z}{g}\right), \tag{8.17}$$

where z is the platform height above the ground plane and g is the ground range. Substituting (8.17) into (8.16) gives

$$\frac{\partial f_d}{\partial g} = -\frac{\partial}{\partial g} \frac{2v_a \sin\theta_{\text{TX}}}{\lambda} \cos\left[\tan^{-1}(z/r)\right]. \tag{8.18}$$

Since azimuth angle θ_{TX} is not dependent on ground range g, the partial derivative can be pulled through the first term of (8.18),

$$\frac{\partial f_d}{\partial r} = -\frac{2v_a \sin\theta_{\text{TX}}}{\lambda} \frac{\partial}{\partial r} \cos\left[\tan^{-1}(z/r)\right]. \tag{8.19}$$

Substituting $a = \tan^{-1}(z/g)$ and applying the chain rule gives

$$\frac{\partial f_d}{\partial g} = \frac{2v_a \sin\theta_{\text{TX}}}{\lambda} \frac{\partial}{\partial a} \cos a \frac{\partial}{\partial g} \tan^{-1}(z/g). \tag{8.20}$$

Substituting $b = z/g$ and applying the chain rule again gives

$$\frac{\partial f_d}{\partial g} = \frac{2v_a \sin\theta_{\text{TX}}}{\lambda} \frac{\partial}{\partial a} \cos a \frac{\partial}{\partial b} \tan^{-1} b \frac{\partial}{\partial g}\left(\frac{z}{g}\right). \tag{8.21}$$

Evaluating the partial derivatives yields

$$\frac{\partial f_d}{\partial g} = \left(\frac{2v_a \sin\theta_{\text{TX}}}{\lambda}\right)(-\sin a)\left(\frac{1}{1+b^2}\right)\left(-\frac{z}{g^2}\right). \tag{8.22}$$

247

Replacing the substituted terms results in

$$\frac{\partial f_d}{\partial g} = -\frac{2v_a \sin\theta_{\text{TX}} \sin\left[\tan^{-1}(z/g)\right]}{\lambda}\left(\frac{z}{g^2 + z^2}\right).$$ (8.23)

Equation (8.23) represents the variation in Doppler as a function of ground range for a 3-D monostatic scenario. When $z = 0$ (i.e., the 2-D monostatic case), $\partial f_d/\partial g = 0$. Despite (8.23)'s non-zero value in the 3-D monostatic case, anti-aliasing performance is still quite good. Section 8.2.2 illustrates this fact.

8.2.1   2-D Monostatic Scenario.   Figure 8.3 illustrates the relationship between Doppler shift f_d and ground range g for the 2-D monostatic simulation scenario introduced in Sec. 7.6.2. Tables 7.2 and 7.3 contain the relevant simulation parameters. The remainder of this chapter contains many figures similar to Fig. 8.3, meriting an in-depth discussion of the information portrayed.

Figure 8.3 is a 2-D image domain plot covering an area of 400 km^2. The white star at $(0,0)$ denotes instantaneous SAR platform location. Using the monostatic platform velocity $\bar{v}_{\text{TX}} = \bar{v}_{\text{RX}} = [0,\ 200,\ 0]^{\text{T}}$, (8.12) is used to calculate the Doppler shift of each point (x, y). Each pixel's value v is then calculated according to

$$v = 20\log_{10}\left[\text{sinc}\left(\frac{f_d - f_{d_c}}{\text{PRF}}\right)\right],$$ (8.24)

where f_{d_c} is the Doppler shift at the scene center. Equation (8.24) uses the expected shuffled SF waveform ambiguity function to apply a One-Dimensional (1-D) $|\text{sinc}(\cdot)|^2$ function across the scene's normalized instantaneous Doppler shift. This operation maps the expected Doppler nulls onto the 2-D spatial domain ground plane allowing the user to view variations in null location as a function of ground range, thereby providing a visual representation of $\partial f_d/\partial g$.

The maximum v value (0.0 dB) occurs when the scene center's Doppler shift equals the pixel's Doppler shift (i.e., $f_{d_c} = f_d$). Points (x, y) meeting this criteria are denoted by the dotted white line running horizontally through the image. The white
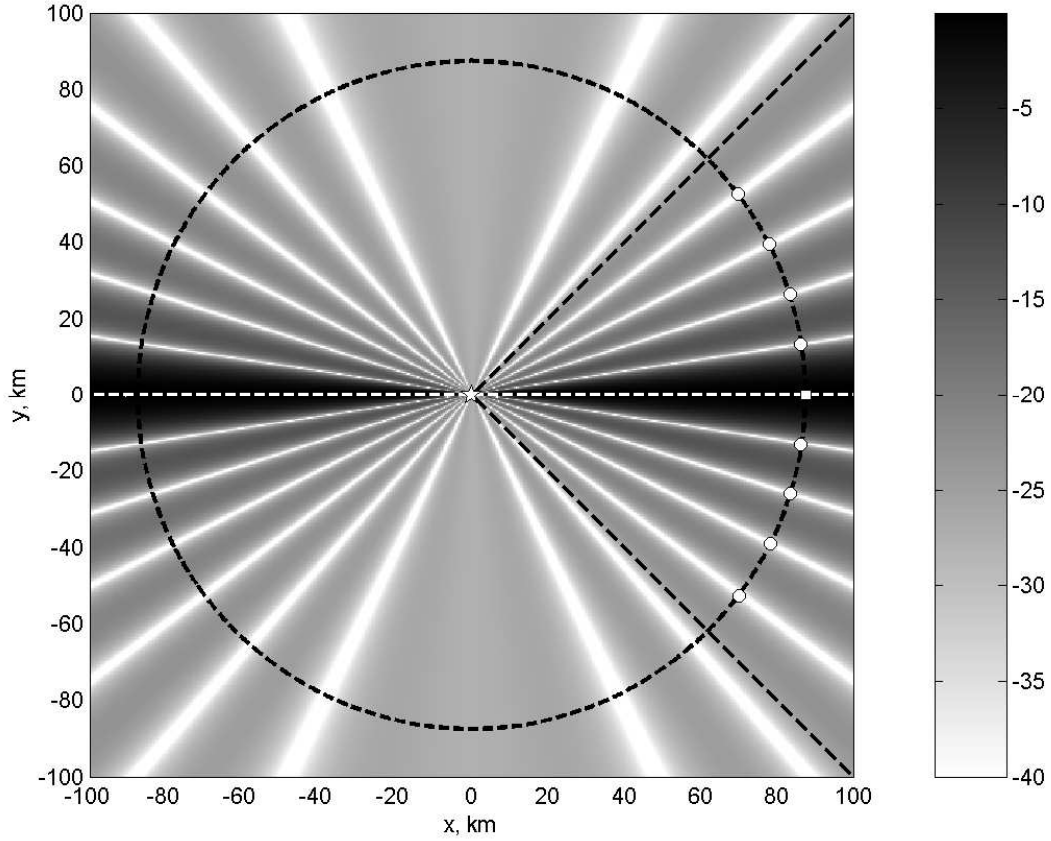
Figure 8.3: Plot of (8.24) for the 2-D monostatic scenario (40.0 dB dynamic range). The white star at $(0, 0)$ indicates platform location. The white box at $(87.5, 0)$ denotes the scene center. The white circles mark aliasing artifact locations. The dotted white line shows points where $f_d = f_{d_c}$. The dotted black circle shows points of equal ground range g_{g_c}. The dotted black lines denote $\Delta\theta = 90°$ beam edges. The radial null pattern indicates $\partial f_d / \partial g = 0$.

249

radial streaks are nulls resulting from $f_d - f_{d_c}$ values equal to non-zero integer PRF multiples.

The scene center (scatterer 5), indicated by the white square, is at $(87.5, 0)$. Scatterer 5's broadside location dictates a Doppler shift of $f_{d_c} = 0$. The other (aliased) scatterers are denoted by white circles. The dotted black circle defines the set of points where ground range g equals the range to the scene center g_c. The intersections of this circle and the dotted white line indicate the two points where $g = g_c$ and $f_d = f_{d_c}$. The right-hand point $(87.5, 0)$ is the scene center. The left-hand point $(-87.5, 0)$ aliases into the image regardless of the processing method used. This aliasing point results from the left-right ambiguity inherent in all SAR systems (Fig. 7.18). It is removed by assuming a finite (though still very wide) beam. The two dotted black lines extending from $(0, 0)$ to $(\pm 100, 100)$ denote the beamwidth $\Delta \theta = 90°$. Everything outside these lines is filtered out by the antenna's amplitude pattern. Alias-free images can be formed anywhere inside these lines, given appropriate range swath $\Delta R = R_{\max} - R_{\min}$ selection.

The messages conveyed by Fig. 8.3 are two fold. First, aliasing artifacts have been placed at all possible aliasing locations, as defined by the intersection of the $g = g_c$ circle, the $\Delta \theta = 90°$ beamwidth, and the nulls resulting from (8.24). As shown by the simulation results (see Figs. 7.26 and 7.27), none of these artifacts are present in the shuffled SF waveform image. Second, the nulls' radial orientation demonstrates $\partial f_d / \partial g = 0$, as predicted for the 2-D monostatic case by (8.23).

8.2.2 3-D Monostatic Scenario.   Having examined the 2-D monostatic case, the simulated SAR platform was raised to an altitude of $z = 60,000$ ft (near Global Hawk's maximum ceiling). As in the 2-D case, the velocity vector $\bar{v}_{\text{TX}} = \bar{v}_{\text{RX}} = [0, 200, 0]^{\text{T}}$ and scatterer 5 $(87.5, 0, 0)$ was again selected as scene center. Figure 8.4 illustrates how this 3-D scenario is mapped into the 2-D image domain. The instantaneous SAR platform location $(0, 0, 60)$ is directly above the coordinate system origin. The scatterers are confined to the xy plane, denoted by the grey plane. The small

white square represents the 1 km² image. It is centered on scatterer 5. The dotted sphere indicates the set of points at constant range, and intersects the plane in a circle of radius $g_c = 87.5$ km. Points within the gray plane are evaluated according to (8.24) for inclusion in Fig. 8.5.

Figure 8.5 provides a visual representation of $\partial f_d / \partial g$ in the 3-D monostatic case. Equation (8.24) determines individual pixel values. The white square at $(87.5, 0)$ denotes scene center. The 1 km² scene contains scatterer 5. The other eight scatterers are located at the eight white circles. These points' locations differ slightly from the 2-D monostatic case due to Doppler shifts caused by the non-zero platform altitude. As before, the dotted black circle indicates points with equal ground radius $g_c = 87.5$ km. The dotted black lines mark off the $\Delta \theta = 90°$ beamwidth. The white nulls indicate points whose Doppler shifts differ from the scene center by non-zero integer PRF multiples. The black "figure-eight" is explained in the following paragraphs.

The curvature in Fig. 8.5's nulls demonstrates $\partial f_d / \partial g \neq 0$. This effect is more severe for smaller ranges, begging the question of how big $\partial f_d / \partial g$ can become without significantly inhibiting anti-aliasing performance. In the 3-D monostatic case, this question can be answered quantitatively using (8.23).

Equation (8.23) calculates the instantaneous change in f_d as a function of g for an image domain point $(x, y, 0)$ observed by a SAR platform at $(0, 0, z)$ flying v_a m/s in the $+y$-direction. Note, $\theta = \tan^{-1}(y/x)$ and $r = \sqrt{x^2 + y^2}$. Given SAR image dimensions of 1 km², the maximum mismatch in ground range g_m between any image point and the scene center is approximately $g_m/2 = 500$ m. This observation allows estimation of the worst case Doppler mismatch f_{d_m} via

$$f_{d_m} = g_m \frac{2 v_a \sin \theta \sin \left[\tan^{-1}(z/r) \right]}{\lambda} \left(\frac{z}{r^2 + z^2} \right). \tag{8.25}$$

Being mismatched in Doppler by a frequency f_{d_m} implies certain aliasing artifacts do not sit precisely in ambiguity function nulls. This mismatch is not problematic unless the ambiguity function value at the mismatched point is greater then negative one

251
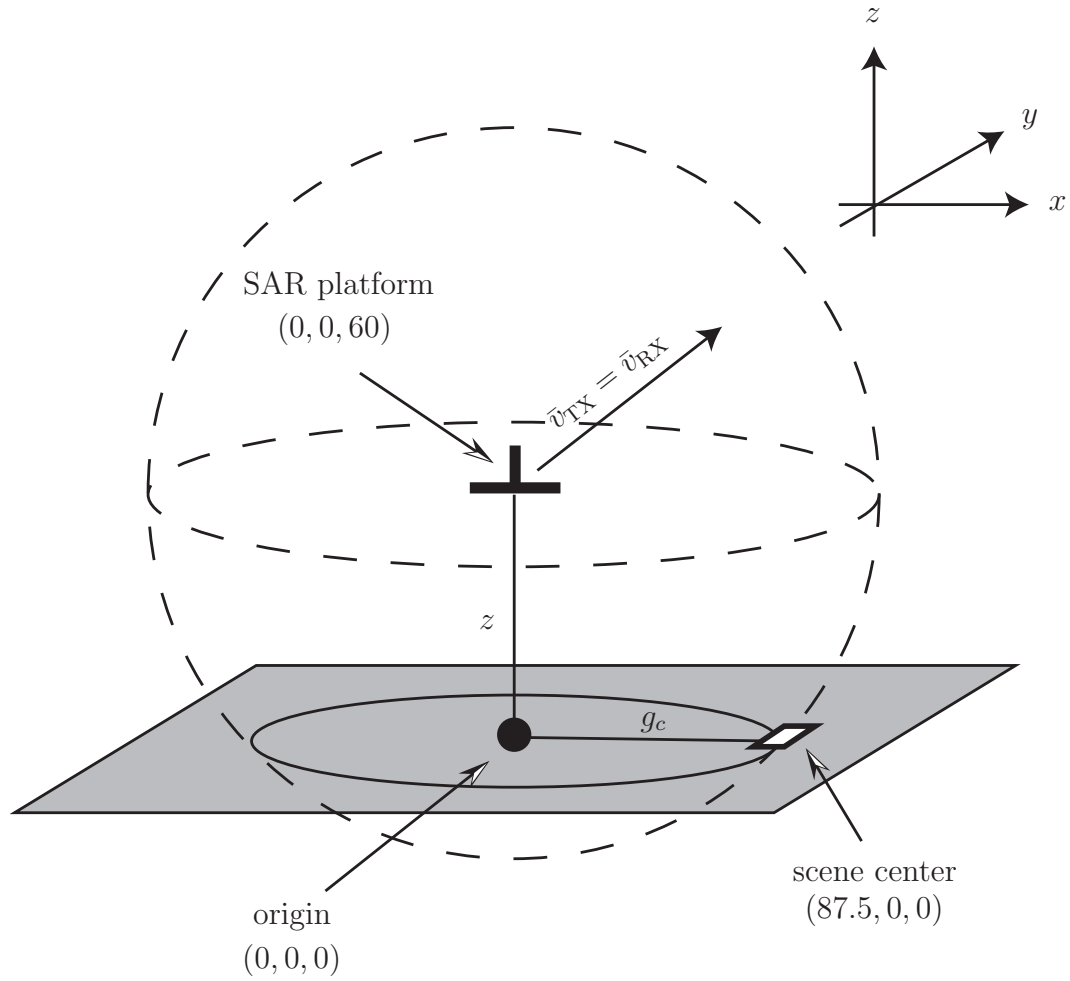
Figure 8.4: 3-D monostatic data collection scenario. The SAR platform is located at $(0, 0, 60)$. Platform velocity $\bar{v}_{\text{TX}} = \bar{v}_{\text{RX}} = 200\hat{y}$ m/s. The dashed sphere denotes points at the same radius as the scene center. The intersection of the sphere and gray ground plane forms a circle with radius $g = g_c$. The white square marks the 1 km^2 scene being imaged (figure is not drawn to scale).
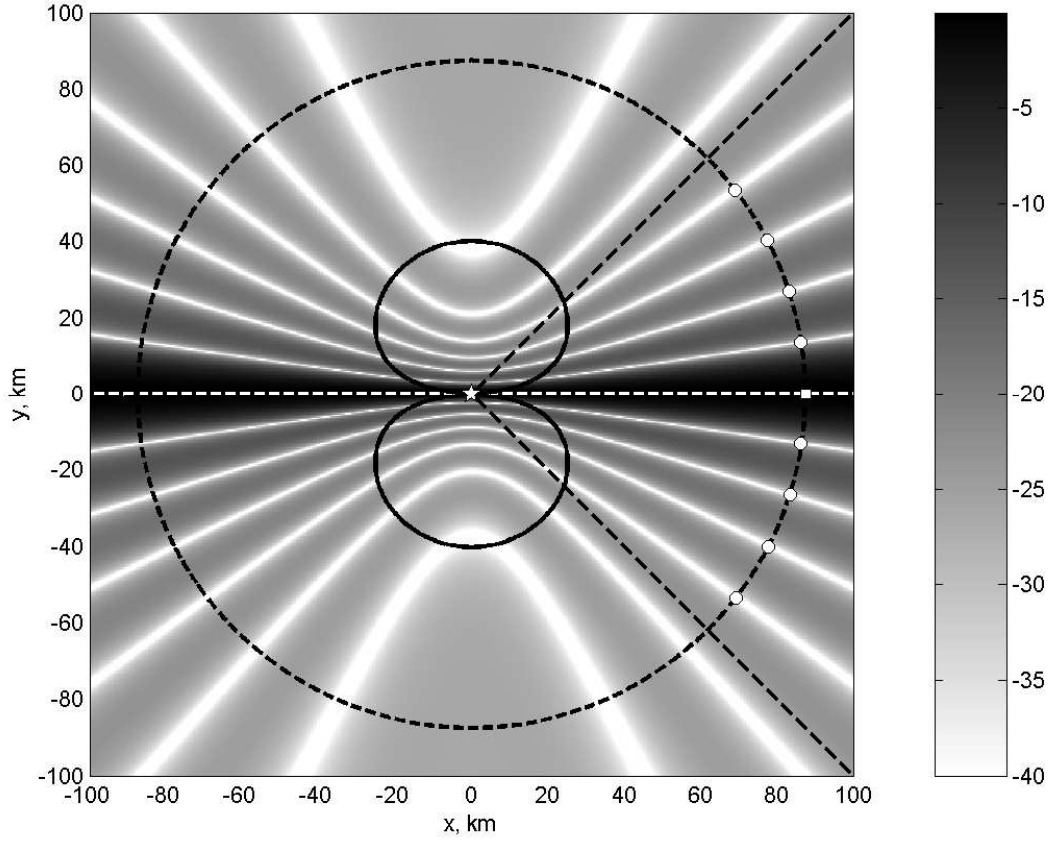
Figure 8.5: Plot of (8.24) for the 3-D monostatic scenario (40.0 dB dynamic range). The white star at $(0,0)$ indicates the platform projection into the ground plane. The white box at $(87.5, 0)$ denotes the scene center. The white circles mark aliasing artifact locations. The dashed white line $(y = 0)$ shows points where $f_d = f_{d_c}$. The dashed black circle shows points of equal ground range g_{g_c}. The dashed black lines indicate the $\Delta\theta = 90°$ beam edges. Points outside the black "figure-eight" denote the region where $\partial f_d/\partial g \approx 0$, yielding effective aliasing artifact mitigation (40.0 dB dynamic range).

times the image's dynamic range. Since this dynamic range is set according to the number of SF waveform subpulses N (Sec. 7.6), non-zero $\partial f_d/\partial r$ values are acceptable as long as

$$20 \log_{10} \left[\text{sinc} \left(1 - \frac{f_{d_m}}{\text{PRF}} \right) \right] < 20 \log_{10} \left(1/N \right). \tag{8.26}$$

Using (8.25) and (8.26) it is possible to calculate the minimum ground range g for adequate anti-aliasing performance at each angle θ. These values are indicated by the black "figure-eight" in Fig. 8.5 and span approximately 20-40 km for the given scenario. This span is very reasonable for the monostatic wide-angle SAR requirements outlined in Chapter II.

Despite the effort taken to generate Fig. 8.5, a better measure of technique effectiveness comes from the simulation results. These results are presented in Figs. 8.6 and 8.7. Key simulation parameters are listed in the second row of Table 8.1. Figure 8.6 shows the SAR image obtained of scatterer 5 using traditional Linear Frequency Modulation (LFM) waveforms. As in the 2-D case (Sec. 7.6.2), all nine scatterers are visible. However, the shuffled circulant matrix image in Fig. 8.7 only contains the desired scatterer.

8.3   Bistatic Scenarios

Section 8.2 derived an expression for $\partial f_d/\partial g$ in a 3-D monostatic scenario. Unfortunately, obtaining a similar expression in the bistatic case is not nearly so straightforward. None-the-less, it is still possible to demonstrate effective aliasing artifact mitigation in the 3-D bistatic scenario using the point scatterer simulator. This section presents simulation results for the two bistatic scenarios, demonstrating the technique's abilities and limitations in militarily significant bistatic data collection geometries.

8.3.1   Stand-off Transmitter/Passive Receiver Scenario.   One of the major motivations for bistatic radar systems is the ability to perform passive target de-
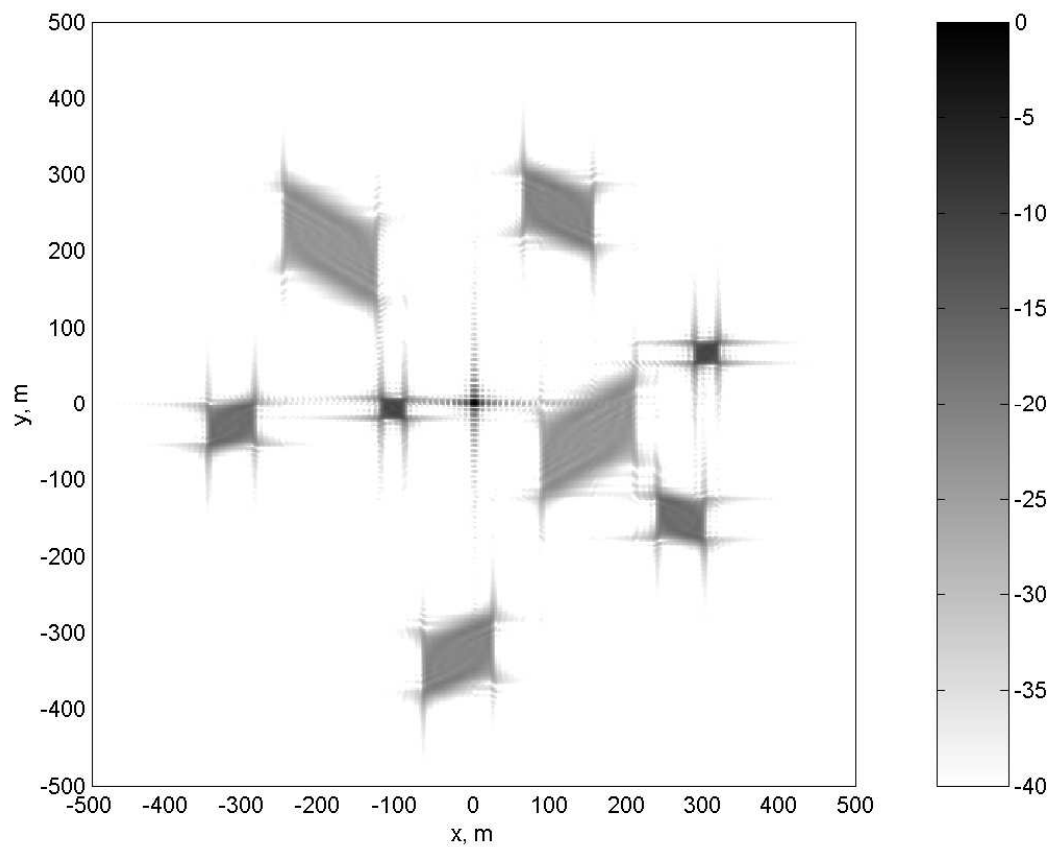
Figure 8.6:   LFM image of scatterer 5 for the 3-D monostatic scenario. Aliasing artifacts cloud the image (40.0 dB dynamic range).
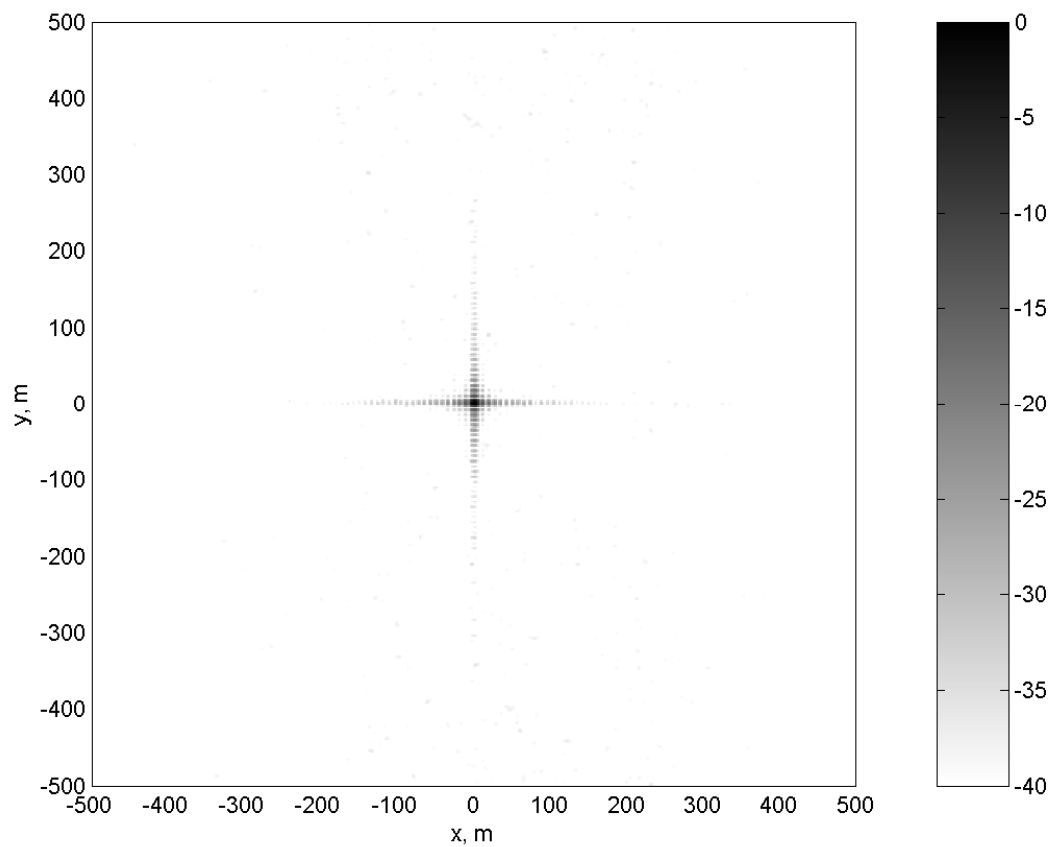
Figure 8.7: SF shuffled circulant matrix image of scatterer 5 for the 3-D monostatic scenario. Aliasing artifacts have been completely mitigated (40.0 dB dynamic range).
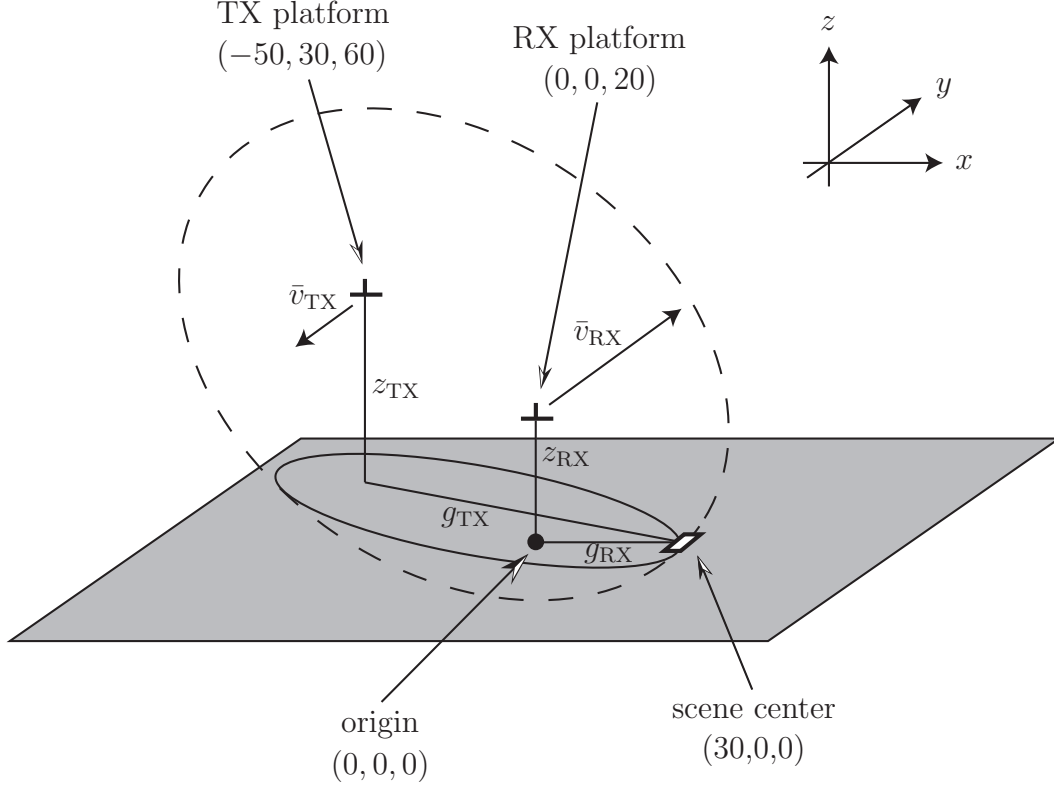
Figure 8.8: 3-D bistatic passive receiver data collection scenario. TX platform is located at $(-50, 30, 60)$ with a velocity of $\bar{v}_{\text{TX}} = -50\hat{y}$ m/s. RX platform is located at $(0, 0, 20)$ with a velocity of $\bar{v}_{\text{RX}} = 200\hat{y}$ m/s. The dashed ellipsoid denotes points at the same radius as the scene center. The intersection of the ellipsoid and the gray ground plane forms an ellipse passing through scene center. The white square indicates the 1 km^2 scene being imaged (figure is not drawn to scale).

tection and imaging using cooperative and/or non-cooperative signals from distant transmitters. Figure 8.8 illustrates such a scenario, using a slow (50 m/s), high altitude (60,000 ft), stand-off transmitter, and a fast (200 m/s), low altitude (20,000 ft), short range, passive receiver. The third row of Tab. 8.1 lists critical transmitter and receiver simulation parameters. The dotted ellipsoid denotes all points with the same range as scene center, indicated by the white square. The ellipsoid's foci are the transmit and receive platforms. The intersection of this ellipsoid and the gray xy-plane is an ellipse consisting of all points at ground range g_c from scene center.

Figure 8.9 shows the ground plane behavior of (8.24) for the 3-D bistatic scenario pictured in Fig. 8.8. The white stars at $(-50, 30)$ and $(0, 0)$ are the projections of the transmit (TX) and receive (RX) platforms into the ground plane. The scene contains five scatterers. The scene center is indicated by the white box at $(30, 0)$ while aliased scatterers are denoted by white circles. The dotted white line indicates $v = 0.0$ dB values. The dotted black ellipse denotes points at ground range $g_c = 0.5(g_{\mathrm{TX}} + g_{\mathrm{RX}})$. The dotted black lines mark edges of the intersection between transmit and receive platform $\Delta\theta = 90°$ beamwidths. The bistatic collection geometry has caused a nonuniform warping of ground plane Doppler shifts, indicating $\partial f_d / \partial g \neq 0$.

Figure 8.10 shows the LFM image obtained from this 3-D bistatic collection geometry. All five scatterers are visible, but only the true scatterer, is well focused. The aliased scatterers are somewhat defocused according to their distance from the scene center. Figure 8.11 illustrates the shuffled circulant matrix image. The aliasing artifacts have been mitigated.

The true scatterer response in both Fig. 8.10 and Fig. 8.11 exhibits non-orthogonal sidelobes. The scatterer's sidelobes lay in the constant g and constant f_d directions. In the monostatic scenario, these directions are orthogonal, but in the generic 3-D bistatic scenario they are not. This behavior is another consequence of $\partial f_d / \partial g \neq 0$.

8.3.2 Multistatic Circular-Orbit Scenario. The final case under examination is a multistatic circular-orbit scenario where two high altitude, fast moving platforms fly circular orbits over a scene. Each platform can process its own waveform echoes (3-D monostatic) as well as echoes from the other platform (3-D bistatic). This section examines the 3-D bistatic component of this multistatic scenario.

Figure 8.12 depicts the circular-orbit 3-D bistatic scenario. The scene center $(50, 50, 0)$ is broadside of both platforms at a ground range of 50 km. Six aliasing artifacts are also present. Figure 8.13 shows the behavior of the warped Doppler fields along the ground plane. The intersection of the $\Delta\theta = 90°$ transmit and receive beams forms a channel running toward the lower right-hand image corner. This channel
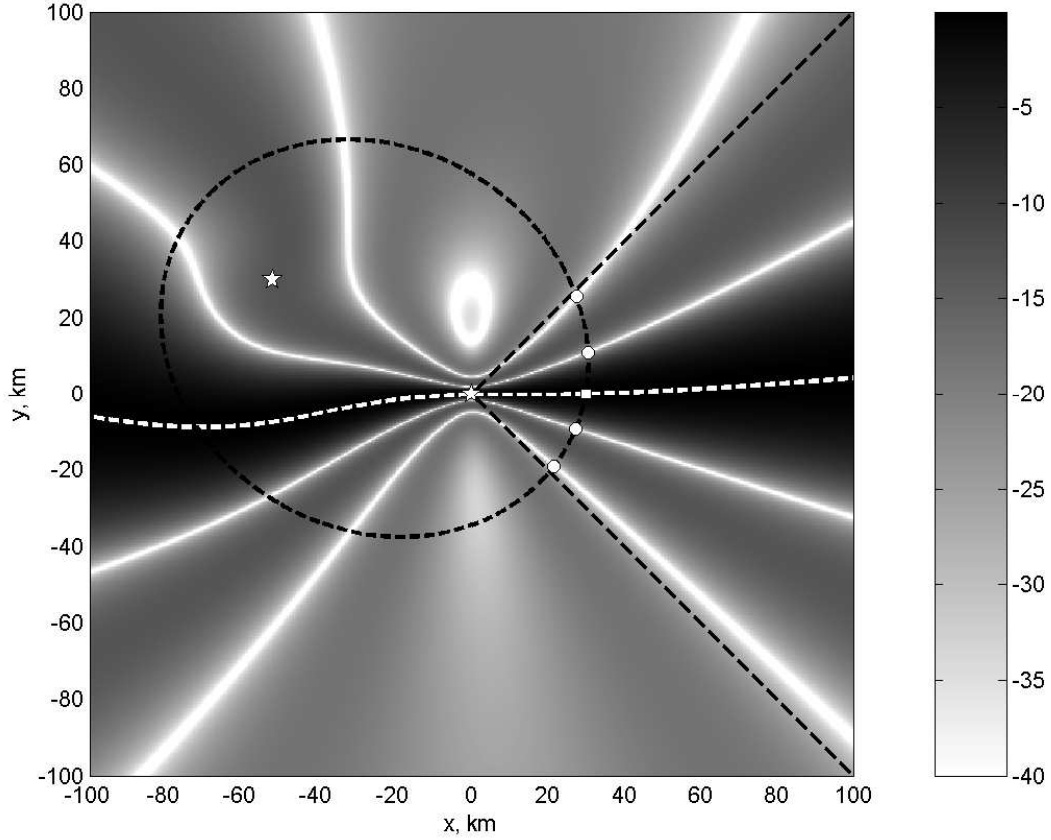
Figure 8.9:   Plot of (8.24) for the 3-D bistatic passive receiver scenario (40.0 dB dynamic range). The white star at $(-50, 30)$ indicates the TX platform projection into the ground plane. The white star at $(0, 0)$ indicates the RX platform projection into the ground plane. The white box at $(30, 0)$ denotes the scene center. The white circles mark aliasing artifact locations. The dashed white line shows points where $f_d = f_{d_c}$. The dashed black ellipse shows points of equal ground range g_{g_c}. The dashed black lines denote $\Delta\theta = 90°$ beam edges. The warped Doppler behavior results from the bistatic collection geometry (40.0 dB dynamic range).
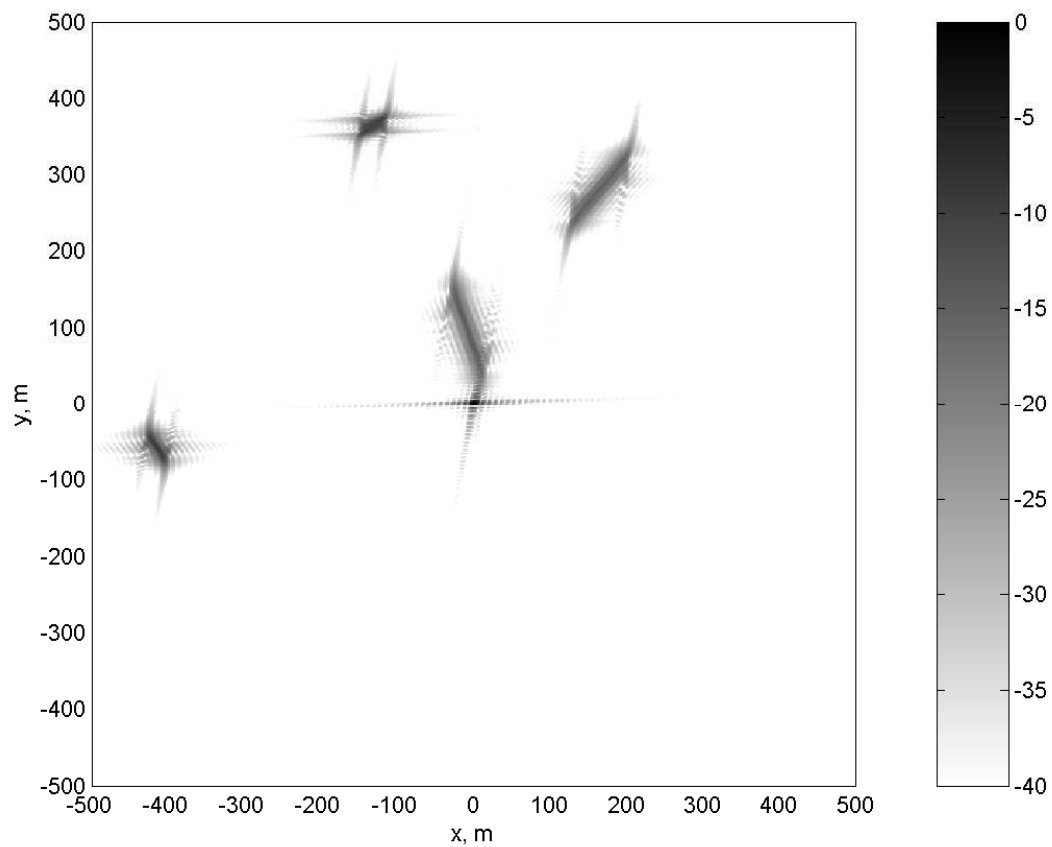
Figure 8.10:   LFM image for 3-D bistatic passive receiver scenario. Aliasing artifacts cloud the image (40.0 dB dynamic range).
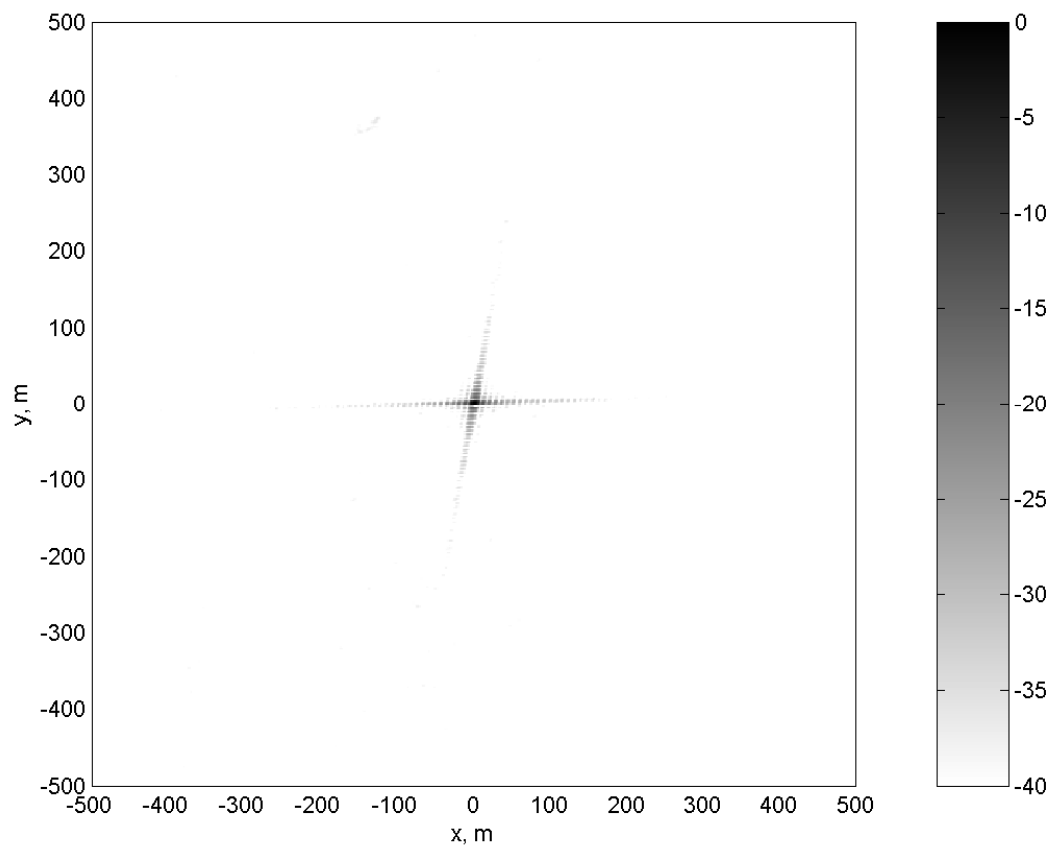
Figure 8.11: SF shuffled circulant matrix image for the 3-D bistatic passive receiver scenario. Aliasing artifacts have been completely mitigated (40.0 dB dynamic range).
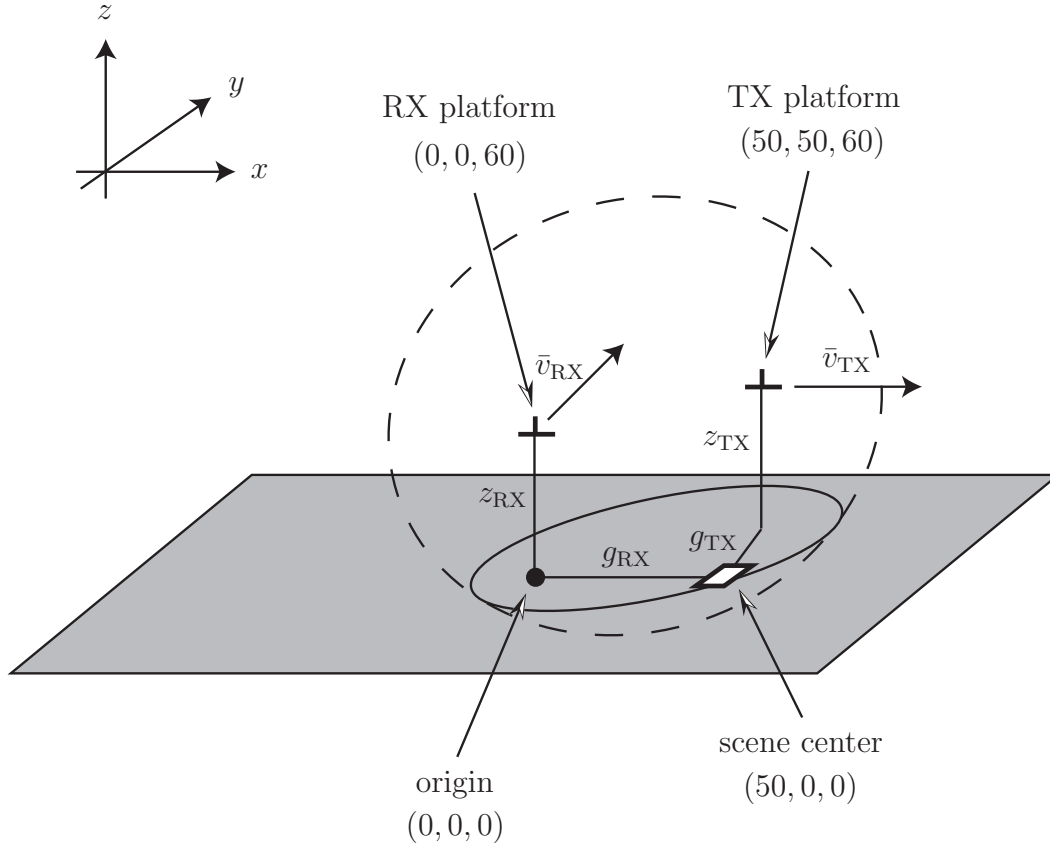
Figure 8.12:   3-D multistatic circular-orbit data collection scenario. TX plat-
form is located at $(50, 50, 60)$ with a velocity of 200 m/s in the $+x$-direction.
RX platform is located at $(0, 0, 60)$ with a velocity of 200 m/s in the $+y$-
direction. The dotted ellipsoid denotes points at the same radius as the scene
center. The intersection of the ellipsoid and the gray ground plane forms an
ellipse passing through scene center. The white square indicates the 1 km^2
scene being imaged (figure is not drawn to scale).

is indicated by the dashed black lines. At the scene center, the constant Doppler
direction (dashed white line) and constant range direction (dashed black ellipse) are
orthogonal. This fact is not true at the aliased scatterer locations, as indicated by
the curved white nulls running through the white circles.

Figure 8.14 shows the LFM image. The true scatterer is well focused. The
other six aliased scatterers are defocused. Figure 8.15 illustrates the shuffled circulant
matrix result. The majority of aliasing artifact energy has been eliminated, but for the
first time, one artifact is not completely removed. The low level pixels at $(-400, -250)$
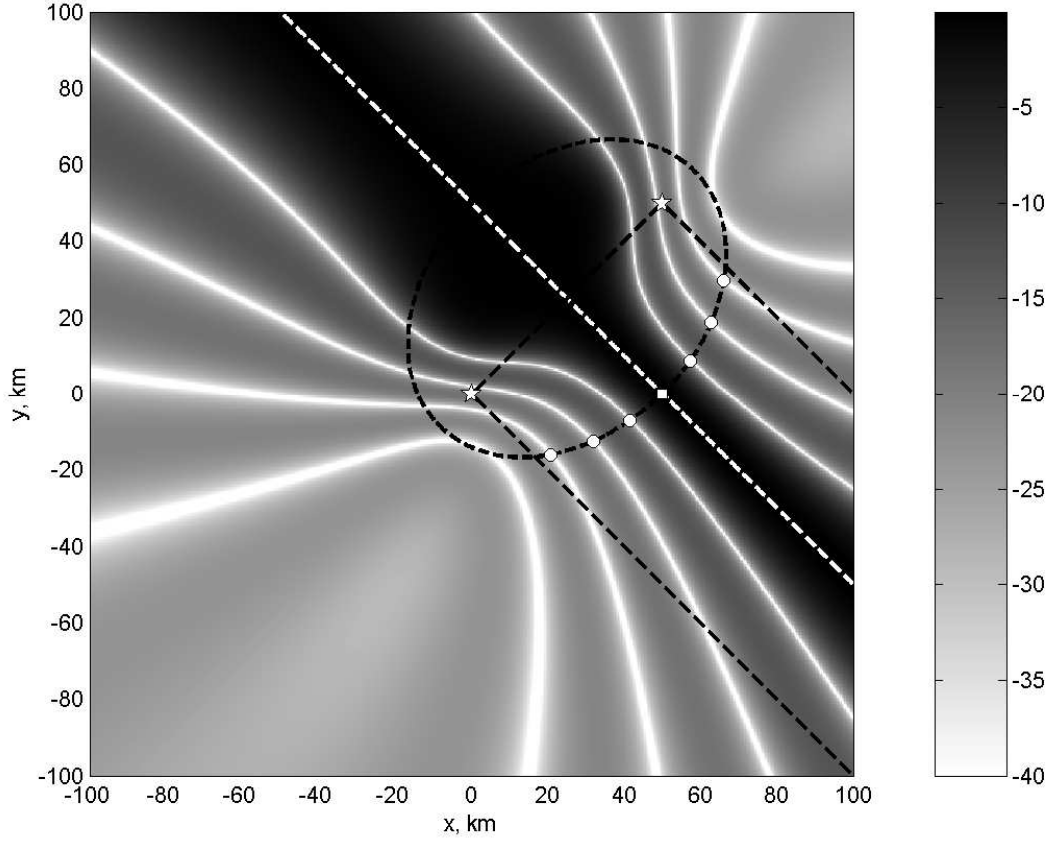
Figure 8.13:   Plot of (8.24) for the 3-D bistatic circular-orbit scenario (40.0 dB dynamic range). The white star at $(50, 50)$ indicates the TX platform projection into the ground plane. The white star at $(0, 0)$ indicated the RX platform projection into the ground plane. The white box at $(50, 0)$ denotes the scene center. The white circles mark aliasing artifact locations. The dashed white line shows points where $f_d = f_{d_c}$. The dashed black ellipse shows points of equal ground range g_{g_c}. The dashed black lines denote $\Delta\theta = 90°$ beam edges. The warped Doppler behavior results from the bistatic collection geometry (40.0 dB dynamic range).
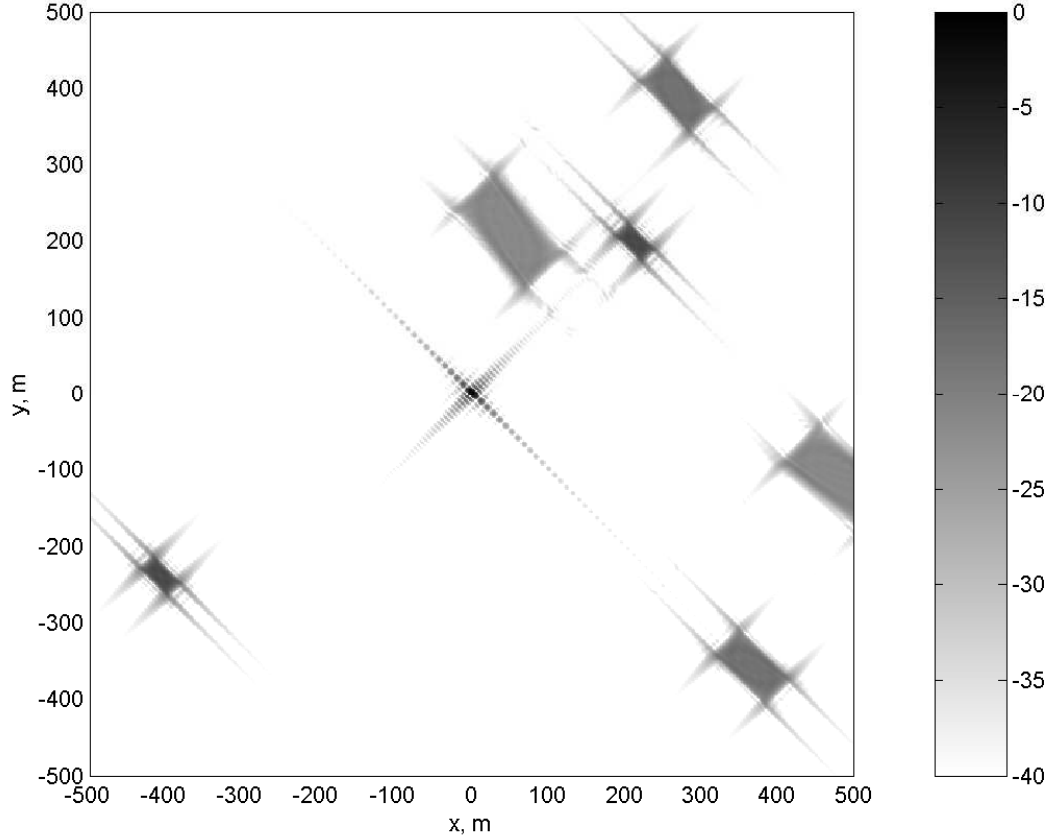
Figure 8.14:   LFM image for the 3-D bistatic circular-orbit scenario. Aliasing artifacts cloud the image (40.0 dB dynamic range).

demonstrate null depth is marginally less the 40.0 dB required by the image's dynamic range.

The presence of a small amount of aliasing artifact energy at $(-400, -250)$ is not a major cause for concern. According to the basic simulation parameters in Table 7.2, these SAR images were produced using only $L/v_a = 1$ s of simulated data. The true WAM-SAR approach will have integration times measured in minutes, not seconds (Sec. 2.2.2). During this additional integration time, the aliased artifact responses exhibit much more severe defocusing due to the larger variation in range between the true scatterer and aliased scatterers. This additional defocusing reduces the aliased response amplitude and should push the remaining artifact energy beneath the image's -40.0 dB floor.
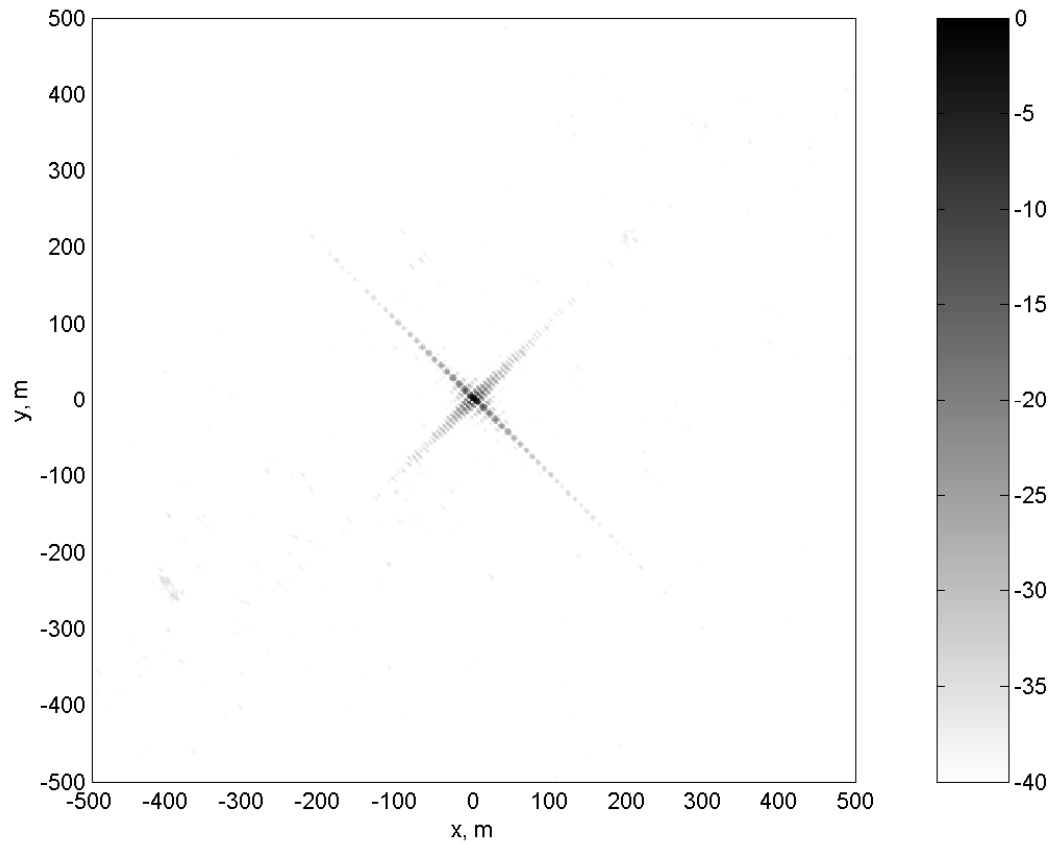
Figure 8.15: SF shuffled circulant matrix image for the 3-D bistatic circular-orbit scenario. Aliasing artifacts have been mitigated (40.0 dB dynamic range).

One additional feature of Figs. 8.14 and 8.15 merits mention. In all previous simulation images, the range and cross range resolutions were approximately equal. However, in Figs. 8.14 and 8.15, the range resolution, defined along a line from the upper left-hand to lower right-hand image corners, is noticeably degraded. This degradation is due to the large bistatic angle β used in the data collection scenario. The bistatic angle β can be calculated via the dot product definition

$$\bar{u}_{\mathrm{TX}} \cdot \bar{u}_{\mathrm{RX}} = |\bar{u}_{\mathrm{TX}}||\bar{u}_{\mathrm{RX}}| \cos \beta. \tag{8.27}$$

Using the relevant simulation parameters, solving (8.27) for the bistatic angle yields $\beta = 83.2°$. Recall from Chapter V, 4.0 dB range resolution δr can be calculated via (5.32)

$$\delta r = \frac{c}{2B \cos(\beta/2)}. \tag{8.28}$$

Using $\beta = 83.2°$, the range resolution increases by a factor of $\cos(\beta/2) = 1.34$. This result is consistent with the degraded range resolution observed in Figs. 8.14 and 8.15.

8.4 Aliasing Artifact Energy Reduction

As in Chapter VII, the 3-D anti-aliasing results can be quantified using a normalized energy metric. The "ideal" image contains only the true scatterer located at the scene center. The presence of aliasing artifacts increases the total image energy and provides a quantitative measure of anti-aliasing performance. The unnormalized ideal image energy was calculated by summing over pixel values in the final ideal image (i.e., the squared magnitude of the complex matrix generated by the back-projection code). This value was then used to normalize the energies of both the LFM and shuffled circulant matrix images, giving the results presented in Table 8.2.

The first three rows of Table 8.2 repeat the first three rows of Tab. 7.4 for convenience. These rows illustrate anti-aliasing performance in the 2-D monostatic scenario. Virtually all of the extraneous energy is filtered out of the "shuffled" image. The next three rows contain data from the 3-D monostatic scenario. Although the

266

Table 8.2:　　Normalized 3-D monostatic/bistatic SAR image energy.

Scenario	Waveform	Figure	Energy	Reduction
2-D Monostatic	Ideal	-	1.0000	-
2-D Monostatic	LFM	7.26	3.7155	-
2-D Monostatic	Shuffled	7.27	1.0002	99.99%
3-D Monostatic	Ideal	-	1.0000	-
3-D Monostatic	LFM	8.6	3.8508	-
3-D Monostatic	Shuffled	8.7	1.0012	99.96%
Passive Receiver Bistatic	Ideal	-	1.0000	-
Passive Receiver Bistatic	LFM	8.10	2.1960	-
Passive Receiver Bistatic	Shuffled	8.11	0.9988	100%
Circular-Orbit Bistatic	Ideal	-	1.0000	-
Circular-Orbit Bistatic	LFM	8.14	3.1874	-
Circular-Orbit Bistatic	Shuffled	8.15	1.0002	99.99%

reduction percentage is slightly smaller, technique performance is still excellent. The third set of rows appears somewhat strange, showing a "shuffled" image with less energy than its "ideal" counterpart. Since the shuffled SF waveform definition procedure relies on a random process, tiny variations creep into final image pixel values. These random variations may be the cause of this result. Also note, this image had substantially less aliased energy to eliminate since only four aliasing artifacts were present. Whatever the cause, aliasing artifact energy is clearly mitigated. The final three rows of Tab. 8.2 show artifact mitigation performance in the circular-orbit bistatic scenario. Again, energy reduction is virtually perfect. Note, Fig. 8.15 did contain a tiny amount of residual energy near $(-400, -250)$, but these pixels contribute a negligible amount of aliasing energy. Taken together with the simulated SAR images, Tab. 8.2 demonstrates excellent aliasing artifact mitigation in 3-D monostatic/bistatic scenarios, despite the fact $\partial f_d / \partial g \neq 0$.

8.5　Summary

The anti-aliasing technique introduced in Chapter VI and simulated in Chapter VII mandated a 2-D monostatic data collection geometry. However, WAM-SAR requires a more general treatment. This chapter extended the technique first to 3-D

monostatic and finally to 3-D bistatic geometry. It began by illustrating how aliasing artifact Doppler behavior in 3-D scenarios violates one of the basic anti-aliasing technique assumptions. Despite this violation, point scatterer simulation examples in both 3-D monostatic and 3-D bistatic geometries show excellent performance. Normalized image energy calculations support this claim. The chapter also included a quantitative tool to estimate performance limits in a 3-D monostatic scenario. In additional to anti-aliasing technique validation, the simulation results also demonstrated the bistatic range resolution losses predicted by Chapter V.

IX. Complex Target Validation: Methodology & Results

Theoretical derivation of the anti-aliasing technique (see Chapter VI) is built around the ambiguity function concept. The ambiguity function $|\chi(t_e, f_e)|^2$ is defined as (6.24)

$$|\chi(t_e, f_e)|^2 = \left| \int_{-\infty}^{\infty} x(t)x^*(t + t_e) \exp(j2\pi f_e t) \mathrm{d}t \right|^2, \qquad (9.1)$$

where $x(t)$ represents the transmitted waveform and the superscripted * denotes the complex conjugate. This equation calculates the matched filter's output magnitude for an ideal point target, mismatched in delay and frequency by time mismatch error t_e and frequency mismatch error f_e, respectively.

The ambiguity function definition inherently assumes the scene consists of ideal point scatterer targets. This assumption was used to build the simulator in Chapter VII. Unfortunately, real targets do not typically respond as ideal point scatterers. They are often both complex (i.e., composed of more than one dominant scatterer within a resolution cell) and distributed (i.e., total target extent exceeds a resolution cell), especially for high resolution radar imaging applications. Under these circumstances, a waveform's ambiguity function or auto/cross-correlation properties might not accurately reflect the true target response. This fact necessitates examination of diverse waveform effects on complex/distributed targets.

Radar Cross Section (RCS) chambers are one popular way of characterizing real target scattering characteristics. Calibrated RCS chamber data provides the target response to far-field illumination in a free-space environment at a fraction of the cost/complexity associated with data collected by operational radar systems. As discussed in Chapter IV, many modern RCS chambers operate by transmitting a series of relatively long, single-frequency pulses and measuring the target response at a predetermined range delay corresponding to the target center. The pulsewidth τ is made sufficiently long for the transmitted pulse to cover the entire target simultaneously. This requirement ensures the target response characteristics are identical to those

of a Continuous Wave (CW) radar [73]. This CW illumination means only a single complex sample is necessary to represent the target response to a given frequency at a given orientation angle. Generation of One-Dimensional (1-D) range profiles and Two-Dimensional (2-D) Inverse Synthetic Aperture Radar (ISAR) images is then accomplished using Fourier Transforms (FTs) and/or other related techniques [28].

Most RCS chambers have limited waveform generation capability. Furthermore, the filtered output data represents the target's spatial frequency response and is essentially waveform independent. This independence means that while RCS chambers can characterize the complicated scattering mechanisms of real targets, they have very limited capability for studying diverse waveform effects on these targets.

This chapter proposes a technique for using RCS chamber spatial frequency data to generate high quality approximations of raw (unmatched filtered) time-domain waveform echoes. With such data it becomes possible to study Stepped-Frequency (SF) waveform response to complex and/or distributed targets without the added difficulty and expense of generating actual SF waveforms. After validating the data conversion technique, this chapter demonstrates the desired SF waveform Doppler filtering properties using high-fidelity Xpatch simulation data generated by the Air Force Research Laboratory (AFRL) and ISAR data from the Air Force Institute of Technology's (AFIT's) RCS chamber. These results validate the anti-aliasing technique for complex/destributed targets.

9.1 *Stepped-Frequency Waveform Review*

Recall from Chapter VI, SF waveforms are formed by concatenating a series of N single-frequency sinusoidal subpulses. Each subpulse has a duration τ_s giving the complete SF waveform a duration of $\tau = N\tau_s$. Each of the N subpulses has a unique frequency f_n. These frequencies are uniformly spaced by a frequency difference δf and span a total 4.0 dB bandwidth of $B = N\delta f$. Analytically, the complete SF

transmitted waveform $w_{\text{TX}}(t)$ can be written as (see (6.25))

$$w_{\text{TX}}(t) = \sum_{n=0}^{N-1} \text{rect}\left(\frac{t - n\tau_s}{\tau_s}\right) \exp(j2\pi f_n t), \tag{9.2}$$

where $\text{rect}(\cdot)$ is defined as

$$\text{rect}(t) = \begin{cases} 1 & : & -\frac{\tau_s}{2} \leq t < \frac{\tau_s}{2} \\ 0 & : & \text{otherwise.} \end{cases} \tag{9.3}$$

From FT theory, it is well known that finite subpulse duration effectively spreads individual subpulse bandwidth. This effect determines the required relationship between B, τ, and N given by (6.27)

$$B\tau = N^2. \tag{9.4}$$

While frequency spacing is tightly controlled by (9.4), any subpulse frequency order is valid. By arranging the subpulse frequencies in a monotonically increasing or decreasing order, the SF waveform provides a good approximation to a Linear Frequency Modulation (LFM) chirp. By randomizing the frequencies, a more noise-like frequency-hopped waveform is produced.

9.2   Waveform Generation Technique

The expected radar echo for a CW single-frequency waveform is simply an appropriately delayed copy of the transmitted waveform scaled by the complex In-phase and Quadrature (I/Q) sample measured in the RCS chamber. This observation is key to the waveform generation technique since an SF waveform (which cannot be produced by the RCS chamber radar) is simply a concatenated collection of finite duration single-frequency subpulses. Provided the temporal extent of the target τ_t is much less than duration of a subpulse τ_s, the SF waveform echo's instantaneous complex-valued amplitude is essentially determined by the CW I/Q value measured in the standard data collection process.
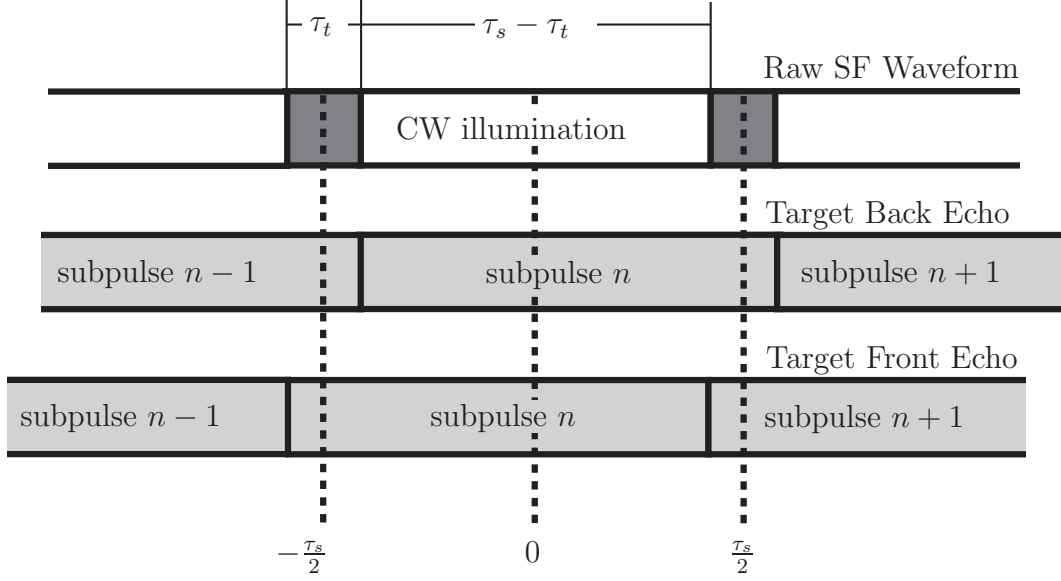
Figure 9.1:   SF waveform generation principle. Horizontal axis is time. Bottom row denotes echo timing off target front (subpulse width τ_s). Middle row denotes echo timing off target back (target extent τ_t). Top row denotes raw SF waveform generated by the technique. White regions indicate where the single-frequency CW illumination assumption is valid.

Figure 9.1 illustrates this principle. The majority of the desired raw SF waveform echo (top line) contains energy from the entire target and only one subpulse frequency, indicating complex echo amplitude is determined by the CW I/Q sample measured during standard data collection. Regions near subpulse edges only contain energy from part of the target as well as echoes from adjacent subpulse frequencies, indicating the CW I/Q sample is not completely accurate in these regions. Note, the subpulse width τ_s is not determined by the true pulse width used in RCS data collection, but by (9.4).

The proposed technique's goal is to produce an accurate raw SF waveform echo using only CW I/Q data. Therefore, CW assumption validity relates directly to SF waveform accuracy. The variable γ quantifies waveform accuracy. It represents the percent of the raw SF wave for which the single-frequency CW illumination assump-

tion is valid. It is determined by

$$\gamma = \begin{cases} 0 & : \quad \tau_s \leq \tau_t \\ 1 - \frac{\tau_t}{\tau_s} & : \quad \tau_s > \tau_t \end{cases}, \tag{9.5}$$

where

$$\lim_{\tau_s \to \infty} \gamma = \lim_{\tau_t \to 0} \gamma = 1, \tag{9.6}$$

implying the CW illumination assumption is valid at all times for infinitely long subpulses or infinitesimally narrow targets.

Assuming uniform subpulse frequency spacing and constant subpulse width, (9.4) can be manipulated to obtain (see (6.28))

$$\delta f = \frac{1}{\tau_s}. \tag{9.7}$$

Converting (9.7) into units of range with $r = ct/2$ gives

$$\Delta r_s = \frac{c\tau_s}{2} = \frac{c}{2\,\delta f} = N\frac{c}{2B}, \tag{9.8}$$

where Δr_s is the range extent of a subpulse and c is the propagation velocity. Frequency spacing also determines the alias-free target range extent Δr ((3.27)), thus

$$\Delta r = N\frac{c}{2B} = \Delta r_s, \tag{9.9}$$

indicating the ratio of subpulse width to target width is equal to the frequency over-sampling ratio[1], thereby determining γ.

Waveform generation technique implementation begins by building a digital copy of the raw SF waveform $w_{\mathrm{TX}}(t)$. The subpulses are ordered to form the user-specified frequency hopping pattern. The RCS chamber data is incorporated into

---

[1]The frequency oversampling ratio is the ratio of minimum subpulse frequency spacing δf to Nyquist frequency spacing.

this transmitted waveform by superimposing the appropriate I/Q sample on each subpulse. This procedure allows the received target echo $w_{\mathrm{RX}}(t)$ to be written as

$$w_{\mathrm{RX}}(t) = \sum_{n=0}^{N-1} A_n \mathrm{rect}\left(\frac{t - n\tau_s}{\tau_s}\right) \exp(j2\pi f_n t), \tag{9.10}$$

where A_n represents the complex-valued I/Q sample at the frequency f_n. Equation (9.10) assumes the CW spatial frequency value measured by the RCS chamber radar is valid over the entire subpulse width τ_s. In reality, it is only valid over a duration of $\tau_s - \tau_t$ in each subpulse. Note, a range (time) offset isn't necessary since the chamber processing references the I/Q samples to the target mount center.

9.3 Technique Validation

This section validates the raw SF waveform generation technique in both one and two dimensions. Comparisons between standard I/Q data processing results and matched filtered raw SF waveforms are presented.

9.3.1 1-D Validation: Complex Range Profiles. Due to the CW nature of the complex-valued I/Q samples, standard range profile generation $p_{\mathrm{std}}(r)$ is performed using an Inverse Fourier Transform (IFT) (see Chapter V)

$$p_{\mathrm{std}}(r) = \mathcal{F}^{-1}\left[A(k_r)\right], \tag{9.11}$$

where $\mathcal{F}^{-1}$ is the IFT and $A(k_r)$ is the set of all I/Q samples at the given orientation angle as a function of spatial frequency $k_r = 4\pi/\lambda$.

Calculation of the matched filtered range profile $p_{\mathrm{MF}}(r)$ using the raw SF waveform is accomplished in a few simple steps. First, both the transmitted $w_{\mathrm{TX}}(t)$ and received $w_{\mathrm{RX}}(t)$ signals are multiplied by a phase correction term

$$w'_{\mathrm{TX}}(t) = w_{\mathrm{TX}}(t) \exp\left[-j2\pi \min\{f_n\} t\right], \tag{9.12}$$

274

$$w'_{\text{RX}}(t) = w_{\text{RX}}(t) \exp\left[-j2\pi \min\{f_n\} t\right], \qquad (9.13)$$

where $\min\{f_n\}$ is the minimum frequency collected in the RCS chamber over $n \in \{0, ..., N-1\}$. This phase correction shifts the frequency band covered by the data to the range $0 \leq f_n \leq B$ and is necessary because of the inherent low-pass nature of digital IFT methods. Matched filtering of (9.12) is performed in the frequency domain, generating a range profile $p_{\text{MF}}(r)$

$$p_{\text{MF}}(r) = \mathcal{F}^{-1}\left\{\mathcal{F}\left[w'_{\text{RX}}(r)\right] \mathcal{F}^*\left[w'_{\text{TX}}(r)\right]\right\}, \qquad (9.14)$$

where $\mathcal{F}$ denotes the FT and the time t has been converted to range r using $r = ct/2$. Qualitatively, the raw SF waveform echo in (9.10) is considered valid when

$$p_{\text{std}}(r) \approx p_{\text{MF}}(r). \qquad (9.15)$$

The following paragraphs introduce a quantitative metric.

To test waveform validity, data was collected on a distributed target consisting of four vertical wires, 9.5 cm tall, embedded in a styrofoam block at the corners of a square with 15.2 cm sides. The radar used Vertical transmit / Vertical receive (VV) polarization and sampled the target response over frequencies $12 \leq f \leq 18$ GHz using $\delta f = 30$ MHz and over azimuth angles $-45° \leq \theta \leq 45°$, spaced by $\delta\theta = 0.45°$. This produced a square data matrix with 201 complex-valued frequency samples at each of the 201 azimuth locations [90].

Figure 9.2 shows a comparison of normalized $|p_{\text{std}}(r)|$ (solid line) and $|p_{\text{MF}}(r)|$ (dotted line) results at an arbitrary azimuth angle. The subpulse frequency order was randomized to generate a noise-like frequency hopped SF waveform. The results are virtually identical across the entire target range.

Figure 9.3 illustrates a comparison of the phase for the two range profiles depicted in Fig. 9.2. The phases are essentially equal at $r = 0$ and begin to degrade away target center as $|r|$ increases. This degradation is consistent with the understanding
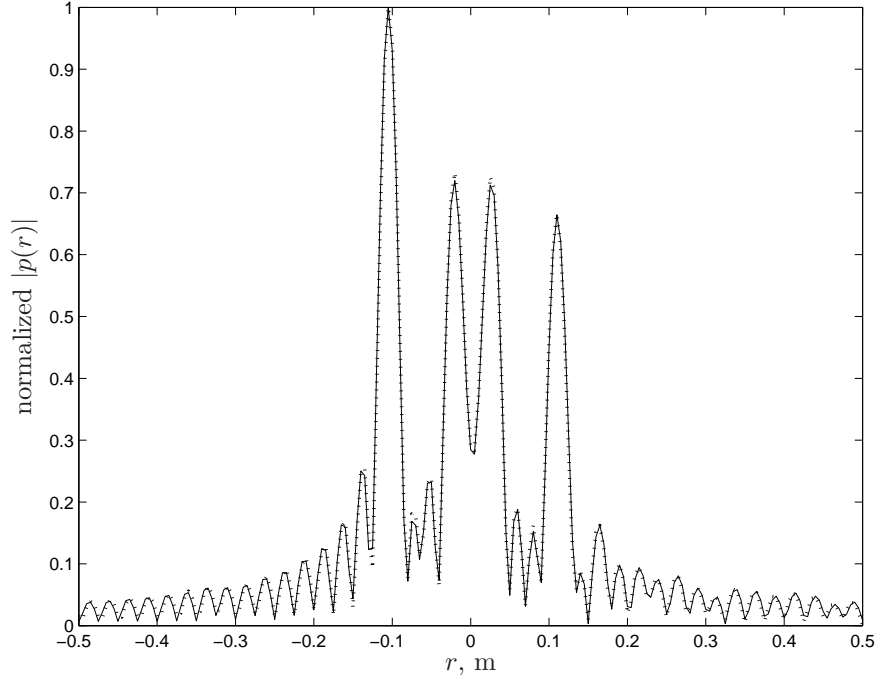
Figure 9.2: Comparison of $|p_{\mathrm{std}}(r)|$ (solid line) and $|p_{\mathrm{MF}}(r)|$ (dotted line) for a single range profile. Results are virtually identical.

that CW assumption validity is inversely proportional to target width. The actual target width is roughly 22 cm centered about $r = 0$. The sharp jump at $r \approx -11$ cm occurs at the target's front edge.

To get a more statistical sense of the technique's validity, the magnitude and phase errors of $p_{\mathrm{MF}}(r)$ were calculated for each of the 201 azimuth samples. The mean values of these errors are shown in Figs. 9.4 and 9.5. To test the effect of δf on technique accuracy, the range profiles were calculated using three different δf values. The solid lines show results from using all 201 frequency samples ($\delta f = 30$ MHz, $N = 201$). The dashed lines show results after decimating the frequency samples by a factor of two ($\delta f = 60$ MHz, $N = 101$). The dotted lines show results after decimating the frequency samples by a factor of four ($\delta f = 120$ MHz, $N = 51$). The target width (22 cm) and the three δf values, give γ values of 0.96, 0.91, and 0.84, respectively.

Figure 9.4 shows the mean error of $|p_{\mathrm{MF}}(r)|$. As expected, the minimum errors, within the target extent, occur at $r = 0$ and rise as $|r|$ increases. The peak errors

276
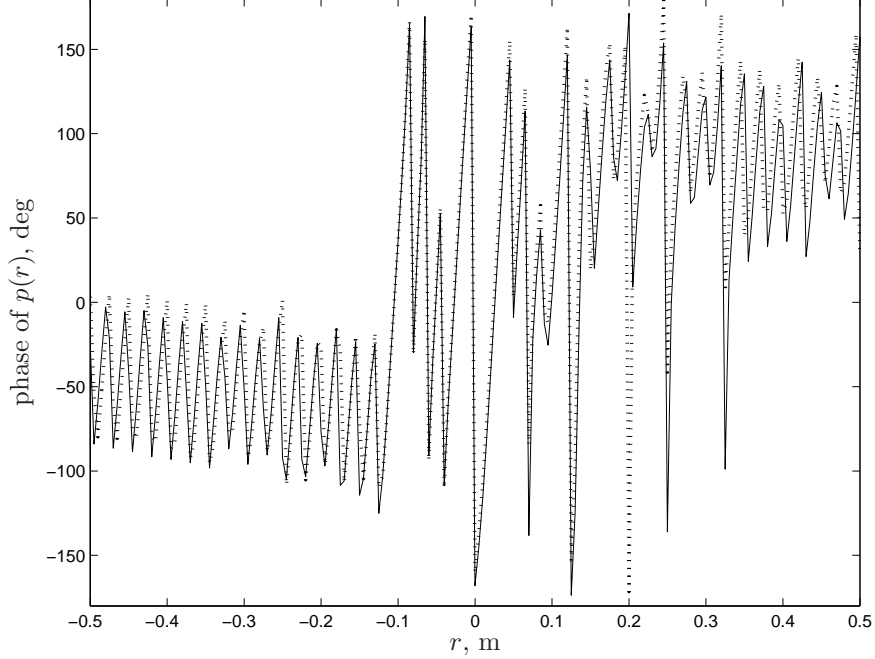
Figure 9.3: Comparison of $p_{\text{std}}(r)$ (solid line) and $p_{\text{MF}}(r)$ (dotted line) phases for a single range profile. Results are virtually identical near $r = 0$ and degrade as $|r|$ increases.

occur at roughly the maximum target extent and then fall rapidly. This decrease results from the lack of echo energy at large $|r|$. As expected, the errors get worse as δf increases, causing γ to decrease. In all cases, the worst case magnitude error is still quite small.

Figure 9.5 illustrates the mean phase error of $p_{\text{MF}}(r)$. The phase errors are at a minimum near $r = 0$. The increase for $|r| > 0$ is relatively smooth within the target extent, but becomes more oscillatory when the range falls outside the target region. As δf increases, both the minimum error and error growth rate increase significantly.

The results presented in Figs. 9.4 and 9.5 clearly demonstrate the links between γ and SF waveform accuracy. Based on these results, a $\gamma \geq 0.9$ should be adequate for the given target. The basis for this selection is the same as the far-field assumption used to derive the quite zone's cross range extent (Sec. 4.2). Phase errors are not deemed significant until they reach 22.5° ($\pi/8$ rad) [73]. By ensuring $\gamma \geq 0.9$, this requirement is met with reasonably high confidence.
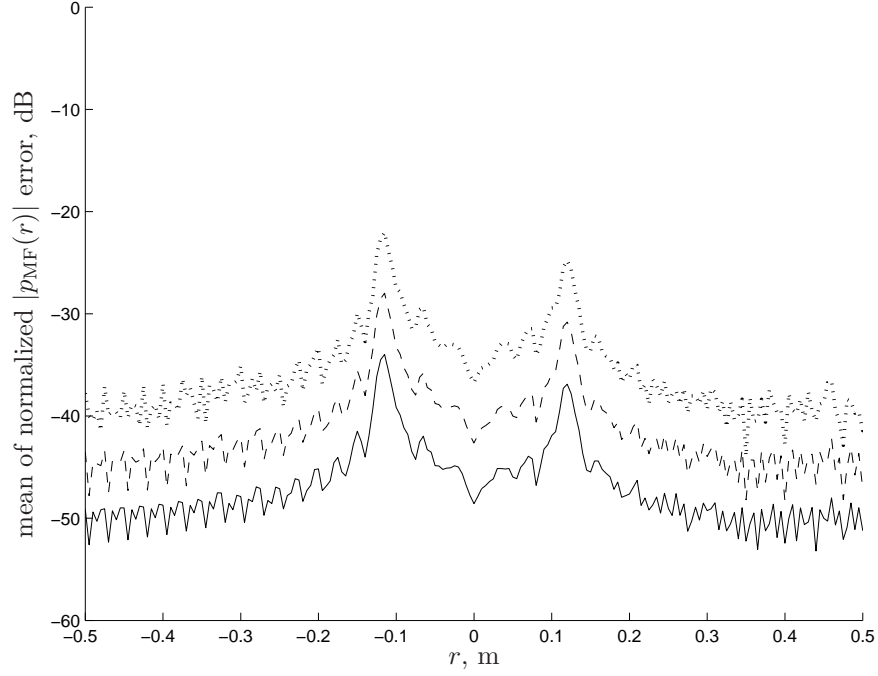
Figure 9.4:   Mean of normalized $|p_{\mathrm{MF}}(r)|$ error over all 201 range profiles. Solid, dashed, and dotted lines denote $\delta f = 30$, $\delta f = 60$, and $\delta f = 120$ MHz, respectively.
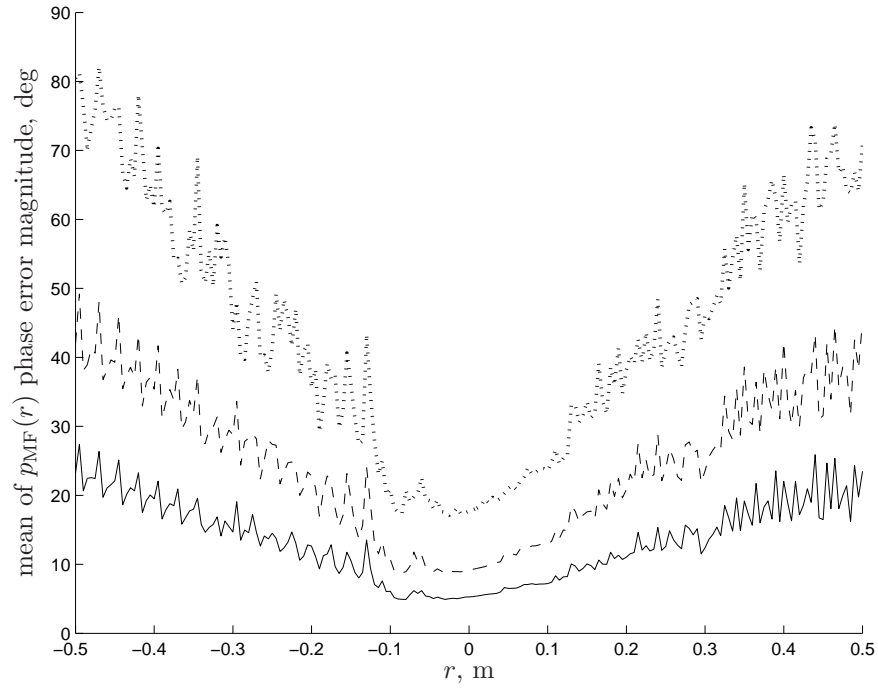
Figure 9.5:   Mean of $p_{\mathrm{MF}}(r)$ phase error magnitude over all 201 range profiles. Solid, dashed, and dotted lines denote $\delta f = 30$, $\delta f = 60$, $\delta f = 120$ MHz, respectively.
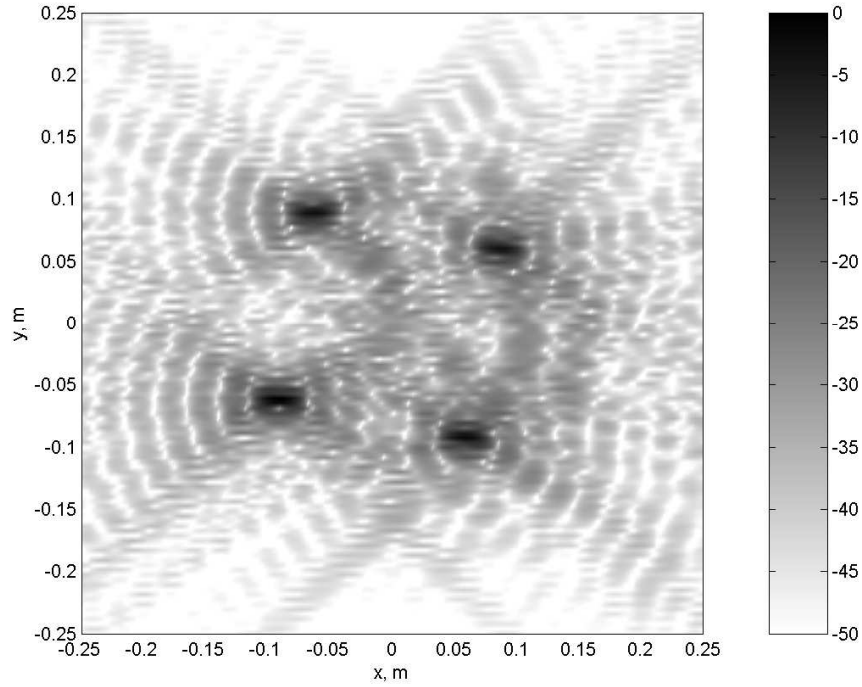
Figure 9.6:   ISAR image generated using traditional range pro-
files.

9.3.2   2-D Validation: ISAR Imagery.   While 1-D range profiles may be
sufficient for 1-D High Range Resolution (HRR) or Moving Target Indication (MTI)
applications, validation of the anti-aliasing technique mandates the production of 2-D
ISAR images.

Figure 9.6 illustrates the unwindowed ISAR image (50.0 dB dynamic range)
obtained using standard range profiles $p_{std}(r)$. The four vertical wires are clearly
visible. Sparse data in the 2-D spatial frequency domain causes the bow-tie shaped
sidelobes emanating from each wire [90].

Figure 9.7 is the image which results from processing raw SF waveforms gener-
ated from the I/Q data samples, decimated by a factor of two ($\gamma = 0.91$). As desired,
the resulting image is virtually indistinguishable from Fig. 9.6. Together, Figs. 9.6
and 9.7 illustrate SF waveform generation technique accuracy for 2-D ISAR imagery.

279
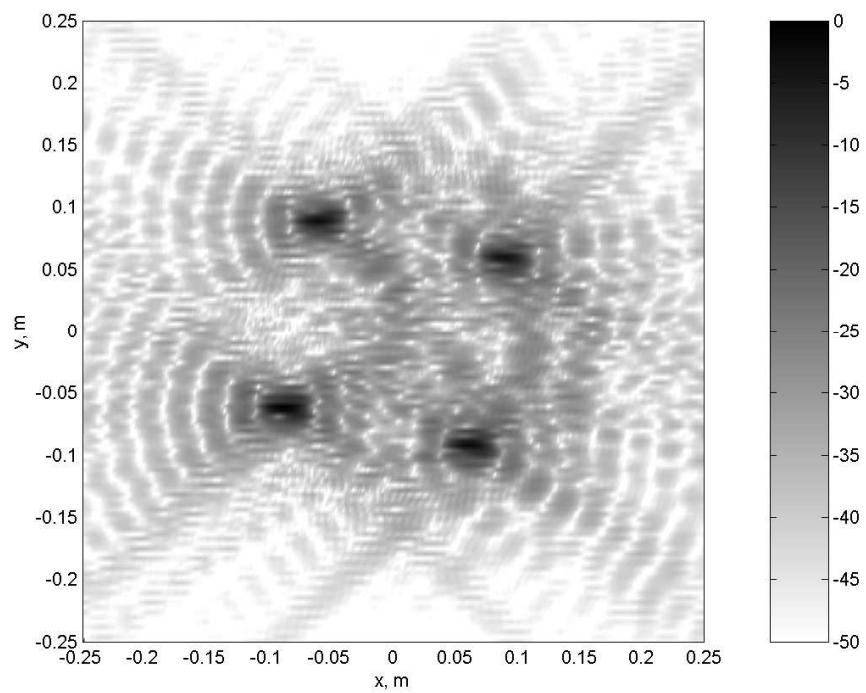
Figure 9.7: ISAR image generated using SF waveforms with random subpulse frequency order. As desired, this image matches Fig. 9.6.

9.4   LFM Waveform Effects

With a raw SF waveform generation technique, validated for both 1-D and 2-D data processing, it is now possible to examine waveform dependent effects using RCS chamber data. However, before examining the case of randomized SF waveform sets, some well known LFM waveform effects are illustrated using data from the distributed target introduced in Sections 9.3.1 and 9.3.2. This approach builds further confidence in the raw SF waveform generation process, since these results conform to well known LFM waveform effects. All data in this section has been decimated by a factor of two, implying $\delta f = 60$ MHz, $N = 101$, and $\gamma = 0.91$.

9.4.1   Range-Doppler Coupling.   One reason for the prevalence of LFM waveforms is the fact they exhibit roughly uniform gain over a wide Doppler frequency range, allowing HRR and MTI systems to detect targets with widely varying Doppler shifts. Unfortunately, LFM waveforms also suffer from an effect known as range-Doppler coupling, where large target Doppler shifts cause an apparent offset range [116]. Using the proposed SF waveform generation technique, this effect can be seen in the range profiles of complex and/or distributed targets.

Figure 9.8 shows the result of applying a Doppler shift of $f_d = 600$ kHz to the range profile of Fig. 9.2 by adding an additional exponential phase term to (9.13). The range profile is then calculated using (9.14). The dotted line shows the true range profile (Fig. 9.2), while the solid line indicates the range profile calculated using the Doppler shifted target echo. The central region of the profile is shifted by an amount ϵ_r where

$$\epsilon_r = \frac{\tau c}{2B} f_d = 2.55 \, \text{cm},\tag{9.16}$$

in accordance with the linear range-Doppler coupling relationship.

Using this Doppler offset on each range profile, it becomes possible to generate an ISAR image of the Doppler shifted target. This result is shown in Fig. 9.9. Comparing this to the image of the zero Doppler target (Fig. 9.7) shows the range-Doppler
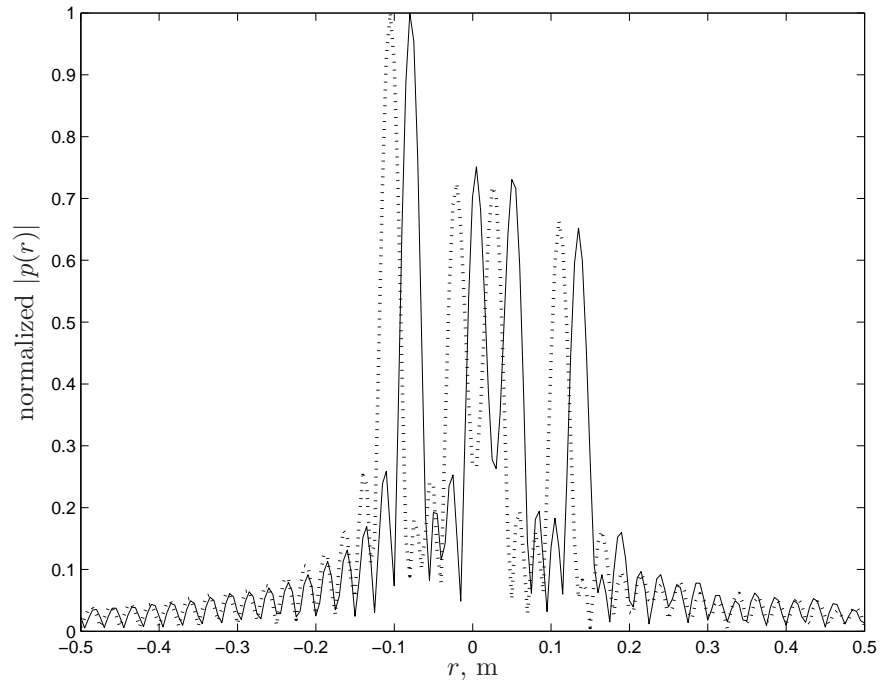
Figure 9.8: Range-Doppler coupling effect of an LFM upchirp on a 1-D range profile. Dotted line shows the true range profile calculated with a matched filter. Solid line shows range profile generated by a mismatch of $f_d = 600$ kHz.
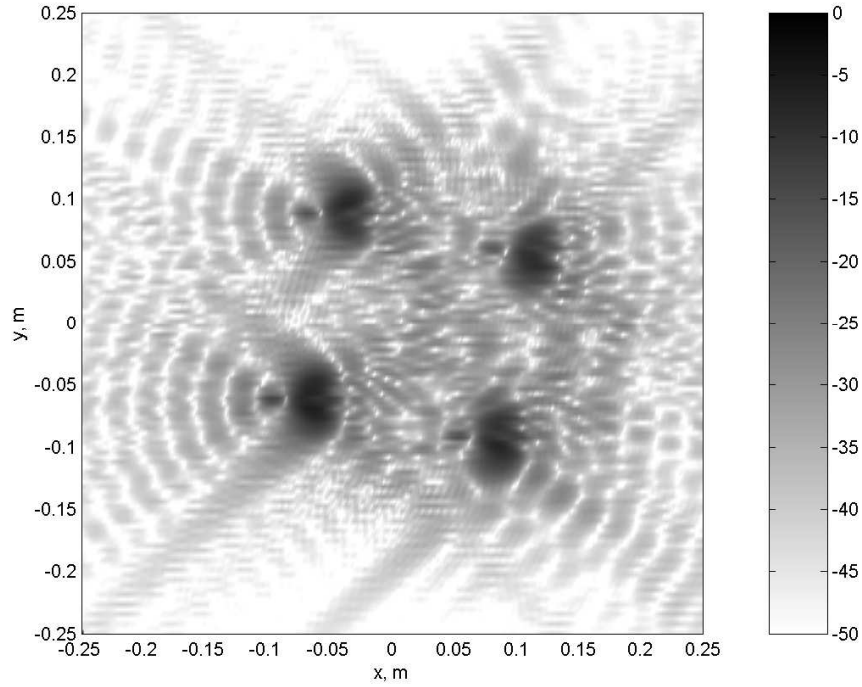
Figure 9.9:   Range-Doppler coupling effect of an LFM up-
chirp on a 2-D ISAR image. Defocusing is evident compared to
Fig. 9.7.

coupling caused ISAR target defocusing. This effect results from the variable target
azimuth angle θ which causes variation in the range-Doppler coupling direction.

9.4.2 Variable Chirp Direction.   A second interesting waveform genera-
tion technique application is for testing waveform cross-correlation properties. One
common limitation with HRR and MTI systems is their inability to provide a large
unambiguous range swath ΔR. One technique for increasing ΔR is to transmit an
alternating sequence of LFM upchirped and downchirped waveforms [116]. If these
two waveforms were orthogonal, this technique would essentially double the maximum
allowable ΔR. However, these two waveforms are not truly orthogonal, meaning some
residual target energy remains after matched filtering target echoes with the incorrect
waveform. Using the SF waveform generation technique, it is possible to observe the
non-orthogonality of the upchirped/downchirped LFM waveform pair.
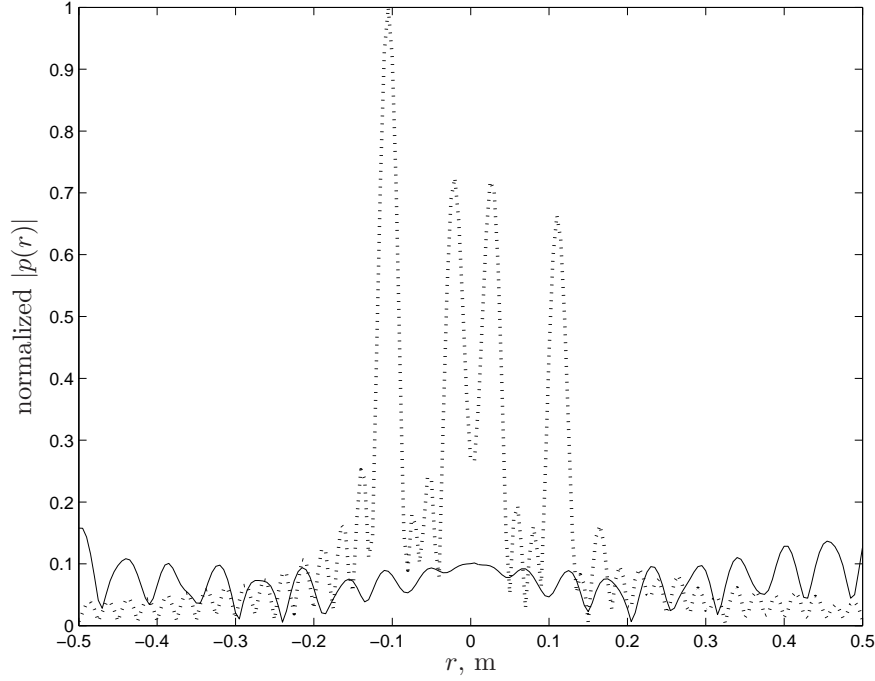
Figure 9.10:   Cross-correlation effects on a 1-D range profile.
Dotted line shows range profile generated by matched filtering
an LFM upchirp. Solid line shows range profile generated by
mismatched filtering with an LFM downchirp.

Figure 9.10 illustrates the result of applying an LFM downchirp filter to an LFM
upchirp target echo. The true matched filtered range profile (Fig. 9.2) is shown as
the dotted line, while the mismatched result is indicated by the solid line. The peak
target response has been reduced by about a factor of 10 (-20.0 dB).

Figure 9.11 shows the ISAR image generated from the coherent combination of
all 201 range profiles. While the four wires do appear at the right image coordinates,
the peak pixel value has fallen dramatically. The peak value results from the non-
coherent combination of the individual mismatch filtered range profiles. Assuming the
non-coherent target energy adds as the square root of the range profiles, the expected
peak image value, $\max[f(x,y)]$, can be estimated as

$$\max[f(x,y)] = 20\log_{10}\left(\frac{0.1}{\sqrt{201}}\right) \approx -43.0, \tag{9.17}$$

284
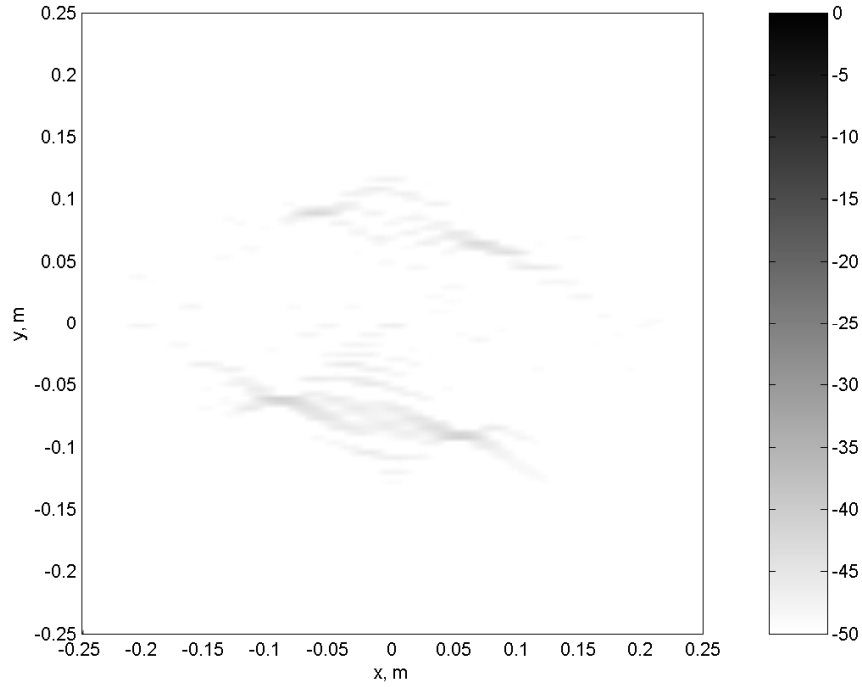
Figure 9.11:   Cross-correlation effects on a 2-D ISAR image. Mismatched filtering performed on LFM upchirp data using LFM downchirp reference.

where the expected peak value of a single mismatch filtered range profile is about 0.1 (taken from Fig. 9.10). The prediction in (9.17) is very close to the true image peak of -41.0 dB.

9.5   Xpatch Data Example

Having examined well-known LFM waveform dependent effects, it is now time to examine the Doppler filtering properties of randomized/shuffled SF waveforms sets on complex target data. The first data examined is high-fidelity Xpatch simulation data. Unlike AFIT's relatively small RCS chamber, Xpatch provides the ability to study life-sized complex/distributed targets at X-band frequencies.

9.5.1   Data Generation and Interpolation.   Xpatch is a well established tool for modeling electromagnetic scattering from complex targets [5]. It makes use of the

Table 9.1:   Xpatch data parameters.

Parameter	Value
Bandwidth, B	500 MHz
Azimuth, θ	$0° - 110°$
Elevation, ϕ	$0°$
Number of Azimuth Samples	1541
Number of Frequency Samples, N (original)	46
Number of Frequency Samples, N (interpolated)	250
Frequency Spacing, δf (original)	10.87 MHz
Frequency Spacing, δf (interpolated)	2.00 MHz

Shooting and Bouncing Ray (SBR) technique to model the scattering properties of complex objects in multiple dimensions. It can use either time domain or frequency domain methods. To spur development in electromagnetic imaging applications, the VISUAL-D Defense Advanced Research Projects Agency (DARPA) seedling team recently released a frequency domain Xpatch dataset providing scattering information for a backhoe [3]. As with RCS chamber data, each complex Xpatch sample in the backhoe dataset provides the target response to CW illumination at a given frequency f and azimuth angle θ. For this reason, Xpatch data can be converted to raw SF waveform echoes using the same technique developed for RCS chamber data.

In order to keep the Xpatch dataset of manageable size, the frequency domain sample spacing δf of the original data was set very close to Nyquist. Unfortunately, for sampling near Nyquist, $\tau_s \approx \tau_t$ implying the CW illumination assumption is *invalid* for the majority of the SF echo. This problem can be corrected in a few simple steps:

1. Take the 1-D FT of the Xpatch data at a given azimuth angle.

2. Zero pad the resulting range profile by the desired amount.

3. Take the Inverse 1-D FT to obtain Xpatch data resampled at a smaller δf value.

4. Repeat for data at each azimuth angle.

This procedure takes advantage of the fact the target is strictly space-limited, using a $\text{sinc}(\cdot)$ interpolator to increase the frequency domain data resolution. The key collection parameters of the original and interpolated data are given in Table 9.1.
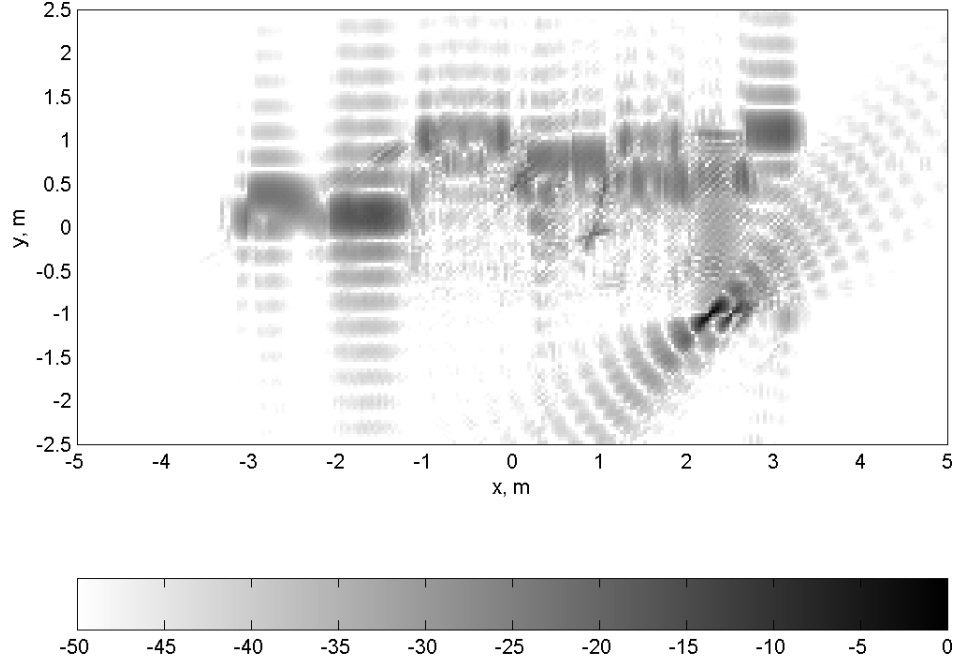
Figure 9.12:   Standard SAR image formed by taking the Fourier Transform of uninterpolated Xpatch data to form range profiles and then combining the profiles using back-projection.

9.5.2   SAR Image Results.   The images in this section illustrate the Doppler filtering properties of SF waveforms using the VISUAL-D Xpatch dataset. All images have a dynamic range of 50.0 dB [99].

Figure 9.12 shows the Synthetic Aperture Radar (SAR) image obtained using the original (uninterpolated) frequency domain Xpatch data. It does not use any SF waveforms or matched filtering and is shown as a baseline for comparison. No temporal windows were used for sidelobe control. The image contains two prominent point scatterers at about $(2, -1)$ as indicated by their bow-tie shaped sidelobe structure. The radar began at the right side of the image and was swept in a counterclockwise direction. This collection geometry explains why the top, but not the bottom, of the backhoe is visible.

Figure 9.13 shows the SAR image obtained after mapping the interpolated Xpatch data onto a set of SF waveforms. The subpulse frequency order was randomized for each waveform. The matched filter's Doppler value was set to zero, coinciding
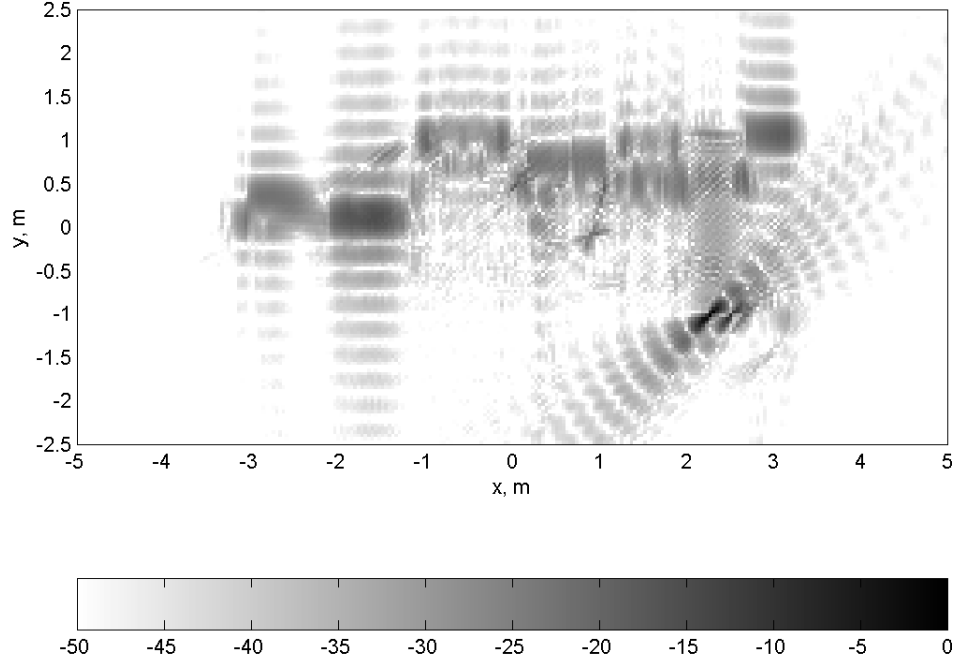
Figure 9.13:   SF/LFM waveform SAR image. Image is virtually identical to Fig. 9.12 demonstrating the validity of the Xpatch interpolation/conversion process.

with the SF waveform echoes. As expected, the result is virtually indistinguishable from the standard SAR image (Fig. 9.12) validating the data interpolation/conversion process. Figure 9.13 corresponds to the target image obtained from a spotlight SAR system using either SF or LFM waveforms. Waveform type is not important because for a Doppler mismatch of zero, subpulse frequency order does not noticeably effect the resulting image.

Figure 9.14 illustrates the SAR image obtained using an LFM waveform with a Doppler mismatch equal to the Pulse Repetition Frequency (PRF). The LFM waveform was simulated with an SF waveform whose subpulse frequencies were ordered in a monotonically increasing fashion, providing a discrete approximation to an LFM upchirp. Due to the inherent Doppler tolerance of the LFM waveform, the image appears largely unchanged despite the Doppler mismatch. Upon closer inspection, the image shows two important effects. First, the image appears shifted slightly in the $(+x, +y)$-direction. This effect is due to the inherent range-Doppler coupling ef-
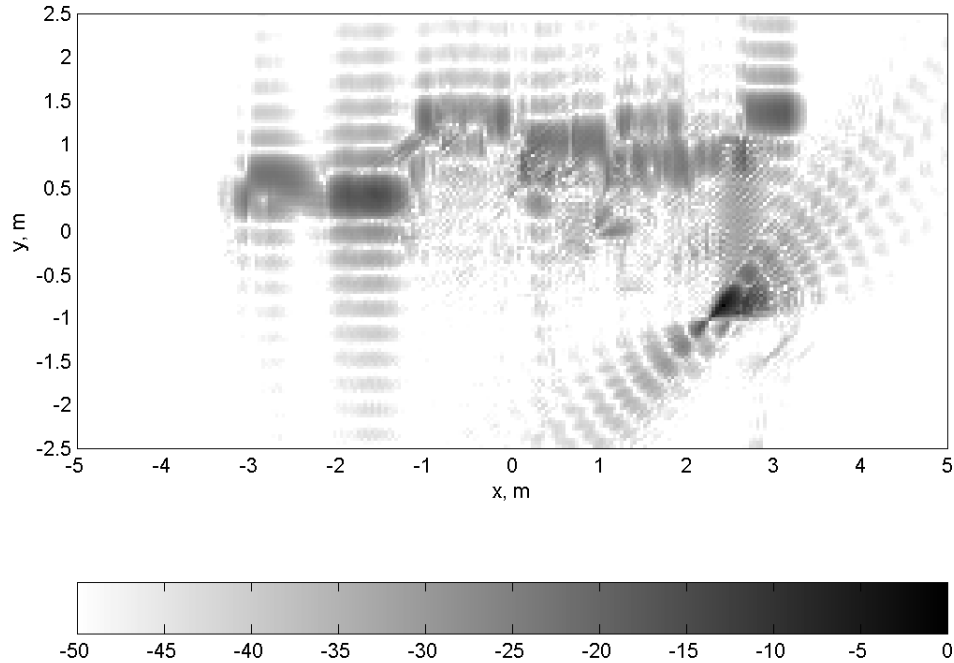
Figure 9.14: LFM waveform SAR image with Doppler mismatch equal to the PRF. Ideally, this image should be empty. This target aliases into the SAR image.

fects of LFM waveforms. Second, the changing azimuth angle (and thus the changing direction of the range-Doppler coupling) causes a defocusing effect. These effects are easiest to see by looking at the target's point scatterers.

The true message of Fig. 9.14 is not the mild degradation in image quality, but the fact there is an image at all. Since the Doppler mismatch is equal to the PRF, this Doppler shifted target would alias into the true SAR image, clouding the final result. In traditional SAR, aliasing is prevented by spatially filtering such targets using a narrow transmit beam. However, in wide-angle SAR no such spatial filter exists.

Figure 9.15 shows the SAR image obtained using randomized SF waveforms with a Doppler mismatch equal to the PRF. The subpulse frequency order was randomized for each waveform (i.e., azimuth angle). The SAR image formation routine has effectively combined the ambiguity responses of the individual waveforms, creating a null at the target Doppler value and filtering the aliased target out of the resulting image. The noise-like SF waveforms also produce a low-level noise floor with peaks

289
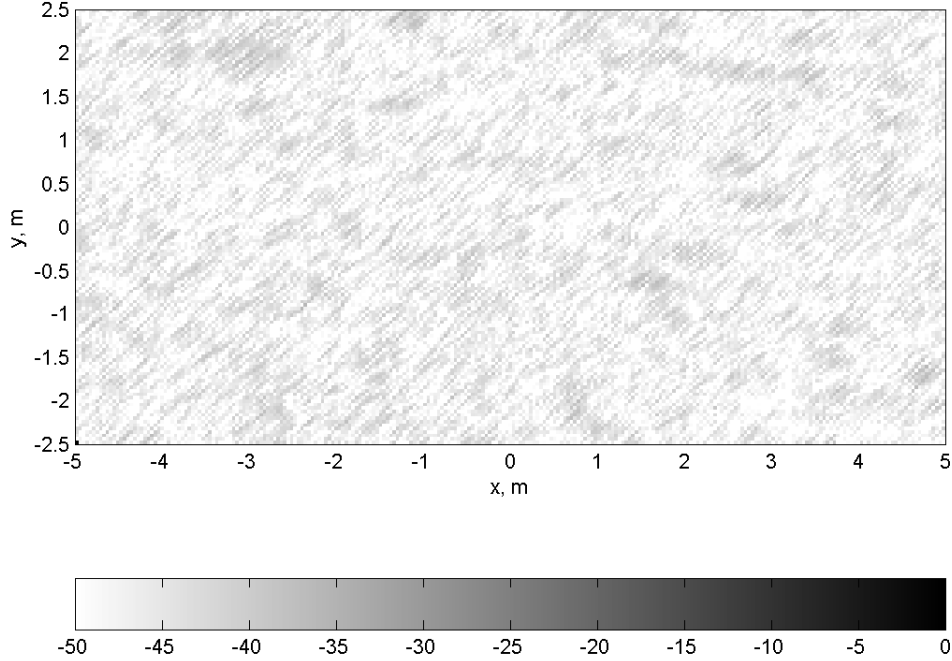
Figure 9.15: Randomized SF waveform SAR image with Doppler mismatch equal to the PRF. Anti-aliasing technique has mitigated the target, filtering the aliased energy out of the final image, and providing a result approximately equal to the ideal empty image.

of approximately $20 \log_{10}(1/N) \approx -48.0$ dB [116]. The ability of the individual SF waveform ambiguity surfaces to combine into a composite function assumes the range profiles do not change throughout the SAR collection. Since this assumption is not strictly correct, the composite ambiguity response is not a perfect 2-D $|\text{sinc}(\cdot)|^2$ function leading to the noise floor. If the Xpatch data was more finely sampled in azimuth (as it would be for any realistic SAR collection), this effect would be reduced.

Figure 9.16 illustrates the effect of SAR image formation using a Doppler mismatch of 1.5 times the PRF. Assuming the composite waveform's ambiguity properties represent a 2-D $|\text{sinc}(\cdot)|^2$ function, the target energy should be sitting at the peak of a $\text{sinc}(\cdot)$ function's first sidelobe, reducing its overall amplitude, but otherwise not effecting the image (e.g., no range-Doppler coupling causing shifting and defocusing). Since the target's Doppler shift is *not* equal to an integer PRF multiple, the SAR
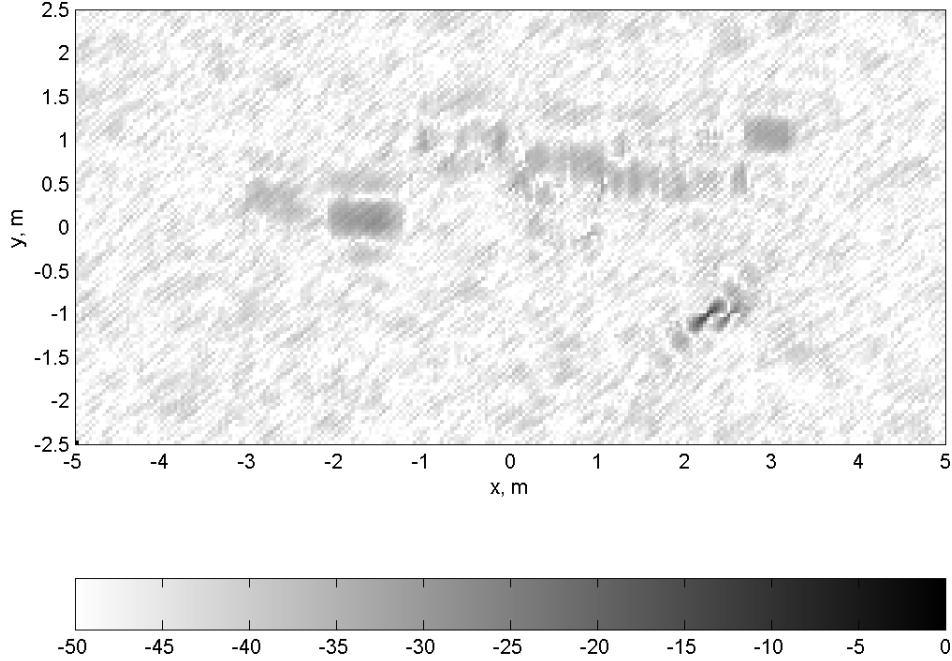
Figure 9.16: Randomized SF waveform SAR image with Doppler mismatch equal to 1.5 times the PRF. Anti-aliasing technique has reduced, but not eliminated, the target. However, since the Doppler shift is a non-integer PRF multiple, the target does not alias into the final SAR image.

image formation process automatically filters this energy out of the resulting image. No anti-aliasing is needed.

Table 9.2 lists the mean and peak pixel values associated with the LFM and SF waveform images in Figs. 9.13-9.16. The peak value of the SF/LFM SAR image with no Doppler offset (Fig. 9.13) is normalized to 0.0 dB. Using 50.0 dB dynamic range, the normalized image's mean pixel value is -43.1 dB. Using an LFM waveform and a Doppler offset equal to the PRF (Fig. 9.14) gives essentially the same mean value due to the LFM waveform's Doppler tolerance. All the target energy is still present in the image. However, the defocusing caused by range-Doppler coupling drops the peak image value by nearly 8.0 dB.

For the randomized SF waveform with Doppler mismatch equal to the PRF (see Fig. 9.15), the peak image value is reduced nearly 40.0 dB. Furthermore, these peak

Table 9.2:   Xpatch SAR image metrics.

Waveform	Doppler, PRF	Figure	Mean Value, dB	Peak Value, dB
LFM or SF	0	9.13	-43.0	0
LFM	1.0	9.14	-42.9	-7.6
SF	1.0	9.15	-48.1	-38.0
SF	1.5	9.16	-47.2	-13.5

locations do not coincide with the true target location. They are simply outliers in the random noise floor. The mean pixel value for this image is approximately equal to $20 \log_{10}(1/N)$.

Finally, the SF waveform image with a Doppler mismatch of 1.5 times the PRF (see Fig. 9.16) has a peak value of about -13.0 dB. This result is expected since the target's Doppler value puts it at the first sidelobe peak of a $\mathrm{sinc}(\cdot)$ function. The average pixel value is marginally higher than the -48.0 dB noise floor due to the contribution from this sidelobe peak.

9.6   RCS Chamber Data Example

The final dataset used to validate SF waveform Doppler filtering properties is an ISAR collection from AFIT's RCS chamber. Unlike the Xpatch data from Section 9.5, the results presented here are from measured data, and therefore include all scattering mechanisms as well as thermal noise. As in the Xpatch data case, the anti-aliasing technique performs well despite a non-ideal collection geometry.

9.6.1   Imaging Target.   The ISAR imaging target is a 1:18 scale Honda Civic model. A target photograph is shown in Fig. 9.17. The model is coated in metallic paint to ensure all surfaces appeared opaque to the radar illumination frequencies. Table 9.3 lists the collection parameters. Given the linear relationship between target size and frequency scaling, the resulting ISAR images are equivalent to full sized Civic images covering $667 \leq f \leq 1000$ MHz [35].

Figure 9.17:   Photograph of scale Honda Civic model ISAR target.

Table 9.3:   Civic data collection parameters.

Parameter	Value
Frequency, f	12-18 GHz
Frequency Spacing, δf	60 MHz
Number of Frequency Samples, N	101
Azimuth, θ	0°-359.6°
Azimuth Spacing, $\delta\theta$	0.4°
Number of Azimuth Samples	900
Elevation, ϕ	0°
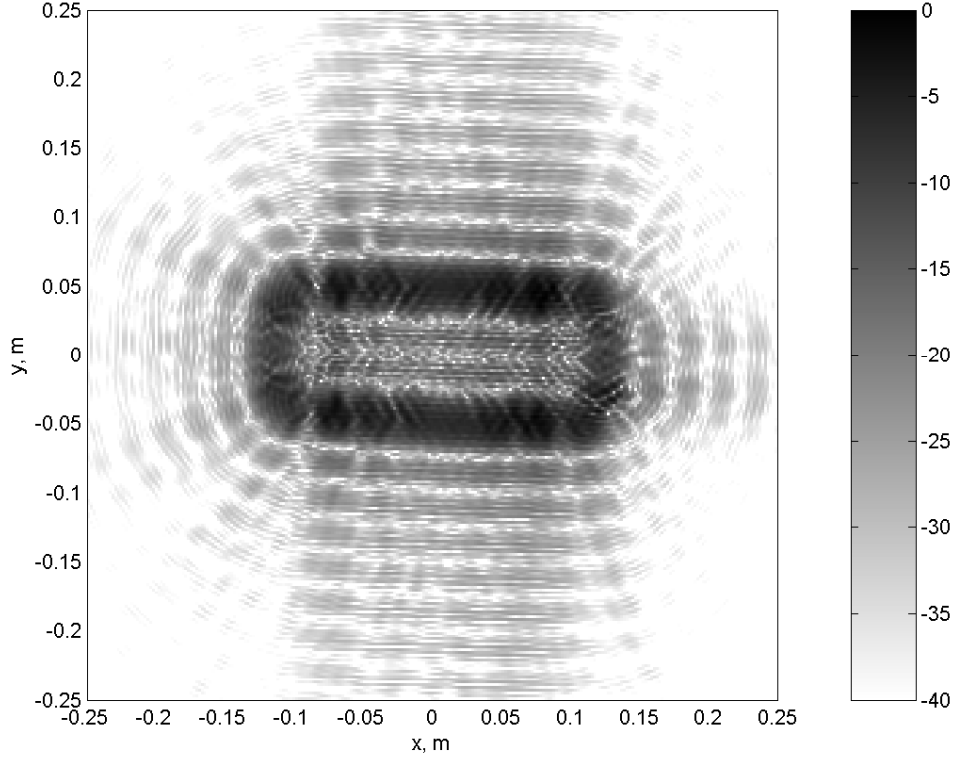
Figure 9.18:   Standard back-projection ISAR image of scale Honda Civic model. The hood is facing right, away from the monostatic antenna.

9.6.2 ISAR Image Results.   Figure 9.18 shows the Civic ISAR image obtained through standard back-projection processing. No sidelobe control windows were used. The target's front (hood) is facing right, away from the monostatic radar antenna. The image is dominated by a hollow rectangular box outlining the target. This behavior results from the target's symmetry and its relatively smooth surface at the X-band illumination frequencies. The box outline's width is determined by the collection's 4.0 dB range resolution $\delta r = c/2B = 2.5$ cm.

Using the RCS chamber data, it is possible to approximate the combined response of a scene consisting of one true Civic target, and a second Civic appearing as an aliasing artifact. This combined response is created using two versions of the I/Q data files. The first used the true collection parameters, and the second used a new azimuth angle θ', where $\theta' = \theta + 90°$. The combined received target echo $w_{\mathrm{RX}}^c(t)$ is

294

then calculated via

$$w_{\mathrm{RX}}^{c}(t) = w_{\mathrm{RX}}^{\theta}(t) + w_{\mathrm{RX}}^{\theta'}(t) \exp\left[j2\pi f_d(t)\right], \tag{9.18}$$

where $w_{\mathrm{RX}}^{\theta}(t)$ is the received signal from the true Civic and $w_{\mathrm{RX}}^{\theta'}(t) \exp\left[j2\pi f_d(t)\right]$ is the received signal from the aliased Civic, Doppler shifted by f_d Hz. Since the targets are separated by a large distance, their echoes are essentially independent. This independence allows the composite received signal $w_{\mathrm{RX}}^{c}(t)$ to be calculated via superposition.

Figure 9.19 shows the ISAR image obtained using an LFM waveform to form the combined received target echo $w_{\mathrm{RX}}^{c}(t)$. The Doppler shift f_d was set equal to the PRF. The image contains both the true Civic image (oriented horizontally) and the aliased Civic image (oriented vertically). The aliased Civic image is somewhat larger. This size increase results from range-Doppler coupling. Clearly the aliasing artifact presence inhibits proper image interpretation.

Figure 9.20 contains the ISAR image obtained using randomized SF waveforms with $w_{\mathrm{RX}}^{c}(t)$. The true Civic is reproduced accurately (as compared with Fig. 9.18), while the aliasing artifact has been eliminated. As expected, a noise floor has crept into the final image.

The mean noise floor level is higher than the expected $20\log_{10}(1/N) \approx -40.0$ dB value. This increase is due to the large $\delta\theta$ value inherent in ISAR data collection. During collection of the 101 SF waveform echoes needed to fill the $B \times \tau$ data support region, the target rotates by more than $40°$. Throughout this rotation, the range profile changes significantly, invalidating one of the assumptions used to derive the anti-aliasing technique in Chapter VI. This rotation is much more severe than the Xpatch example from Section 9.5 where less than $3.3°$ were swept out during data support region filling. However, in a real airborne scenario, the support region would be filled in a fraction of a degree, similar to the point scatterer simulations

295
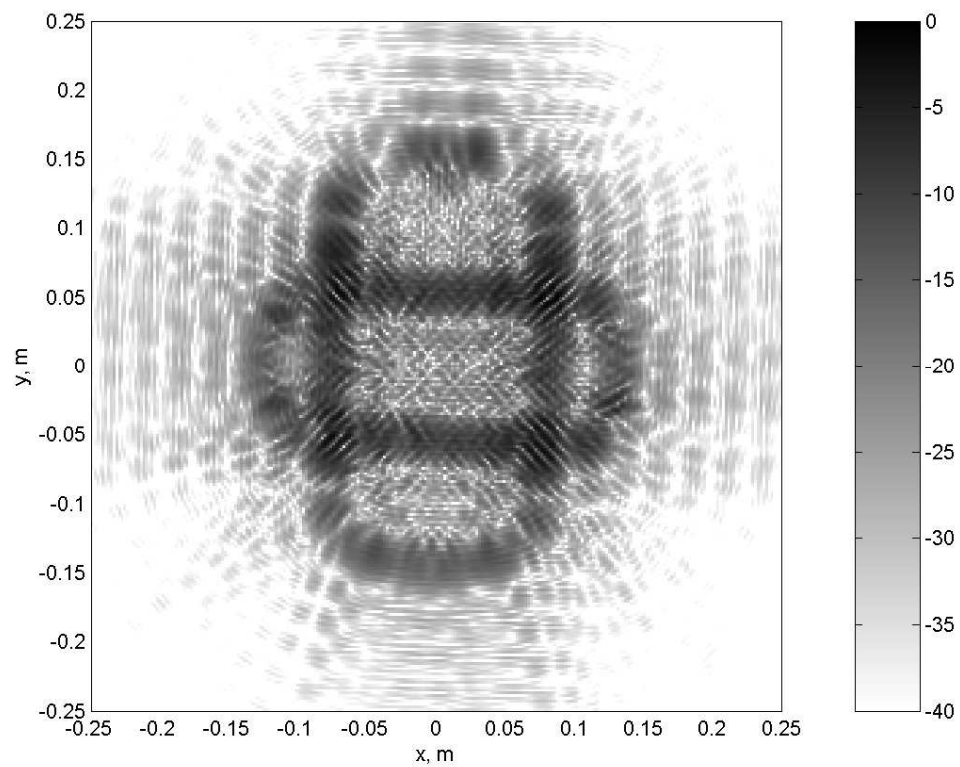
Figure 9.19:   Fused LFM waveform images of true and aliased Civic targets. The aliased Civic was rotated 90° and mismatched in Doppler by f_d = PRF. Range-Doppler coupling causes apparent expansion of the aliased target.
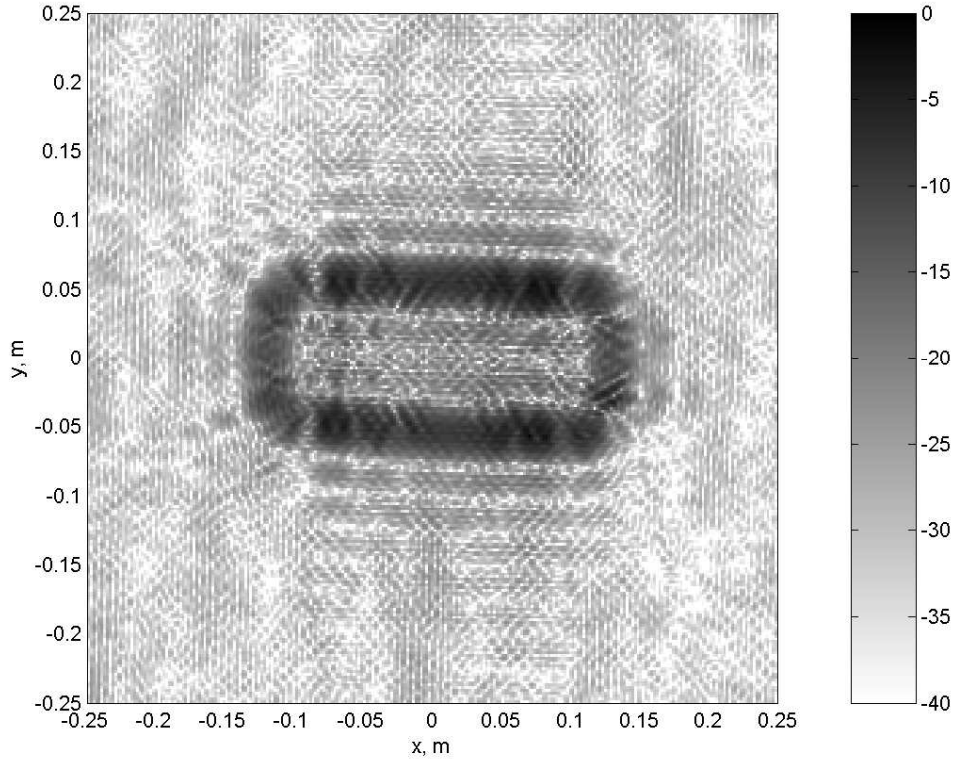
Figure 9.20: Fused SF waveform images of true and aliased Civic targets. Aliased artifact has been removed and a low-level noise floor has appeared.

in Chapter VII. This observation mitigates noise-floor concerns for the Wide-Angle Multistatic Synthetic Aperture Radar (WAM-SAR) scenario.

9.7 Summary

This chapter validated Doppler filtering properties of SF waveform sets using high fidelity Xpatch simulation data and measured RCS chamber data. Unfortunately, this data was collected in the waveform independent spatial frequency domain and therefore appears inappropriate for validated diverse waveform Doppler filtering performance. To eliminate this problem, the chapter begins by developing a new technique for converting waveform independent Xpatch/RCS chamber data into pre-matched filter SF radar echoes. The resulting technique was validated in one and two dimensions and used to demonstrate well-known LFM waveform effects including

297

range-Doppler coupling. The chapter continued by using the validated data conversion technique to demonstrate aliasing artifact mitigation using X-band Xpatch data from AFRL. The peak aliasing artifact amplitude was reduced by nearly 40.0 dB. The chapter concluded by testing anti-aliasing performance on RCS chamber data containing both aliased and true targets. The technique removed the aliased artifact without significantly perturbing the true target response. These results validate anti-aliasing performance for complex targets and thus solve the second of the two major WAM-SAR implementation problems presented in Chapter II.

X. Conclusions

Traditional Synthetic Aperture Radar (SAR) systems operate in one of two modes: stripmap or spotlight. stripmap mode systems produce moderate-to-low resolution imagery of large ground patches (Sec. 3.4). They are most useful for strategic-level reconnaissance efforts, locating buildings, terrain features, etc. spotlight mode SAR systems produce high resolution imagery over very small regions, providing a "soda-straw" view of specific high-interest areas (Sec. 3.5). While these high resolution images provide very useful tactical-level intelligence, their small coverage area limits their impact. Users must know *a priori* where they want to look.

One feature common to both stripmap mode and spotlight mode SAR is the use of narrow radar beams, typically only a few degrees wide. Using narrow beams, traditional SAR systems dramatically simplify the data collection and image formation processes. Narrow beams allow the user to make a host of assumptions including plane wave (e.g., far-field) illumination, linear SAR flight paths, and planar scenes. Narrow beams also limit the radar echo's Doppler spread, reducing Pulse Repetition Frequency (PRF) requirements and allowing the use of conventional antennas and simple waveforms.

10.1 WAM-SAR

One approach for simultaneously achieving high resolution and large area coverage involves using extremely wide radar beams [143]. Wide transmit beams continually illuminate large ground patches providing substantial angular data diversity and resulting in extremely high resolution imagery over the entire ground swath. Narrow band waveforms (Sec. 2.2.4), simultaneous SAR and Moving Target Indication (MTI) missions (Sec. 2.2.5), and high resolution change detection (Sec. 2.2.6) may also be possible using a wide angle SAR platform. These capabilities result in a radar platform capable of fulfilling most major radar missions in a tactical battlefield environment.

Most modern radars operate in a monostatic mode, using the same antenna for transmission and reception. Recent technology advances have made bistatic radar systems feasible, where one radar platform transmits radar waveforms while another, geographically separated platform, receives waveform echoes. When multiple transmit and/or receive platforms are used, the collection is termed multistatic. Bistatic/multistatic systems have a number of advantages. They provide diverse radar data, observing targets from a number of different orientations simultaneously. This angular diversity reduces the chance of severe target shadowing effects. Bistatic/multistatic systems also are much less prone to Electronic Warfare (EW) attack. Jammers must target radar receivers. If those receivers are not co-located with radar transmitters, they are much harder to detect and engage.

In an effort to combine the benefits of wide-angle radar beams and multistatic geometries, this research effort centered around a concept termed Wide-Angle Multistatic Synthetic Aperture Radar (WAM-SAR). While WAM-SAR advantages are significant, substantial issues complicate implementation. Although significant work remains to be done in the simultaneous SAR/MTI and change detection areas, demonstrating the ability to form focused, high resolution, alias-free images is the first priority in demonstrating WAM-SAR feasibility. For this reason, this research effort focused on these fundamental image formation issues.

10.2 Research Contribution Summary

Two major issues preclude formation of high resolution WAM-SAR imagery using traditional SAR methods. This research effort solved both issues. Each issue relates directly to wide-angle radar beam effects.

The first issue prohibiting WAM-SAR image formation involves the focusing of wide-angle monostatic/bistatic data. Use of wide beams means wavefront curvature is a measurable effect and must therefore be accounted for in the image formation process. Also, the long synthetic apertures used to collect radar data invalidate the traditional linear flight path/planar scene assumptions. Chapter III provides an

300

overview of SAR imaging, including an introduction to the relatively new and increasingly popular spatial frequency SAR imaging paradigm. Some of the imagery/concepts in Chapter III were published in [90]. Chapter IV develops data collection and calibration procedures used to validate subsequent SAR/ISAR imaging techniques. Data collected and calibrated using these procedures is contained in [43, 76, 86, 90]. Chapter V presents the WAM-SAR data focusing methodology. This chapter contains new derivations of arbitrary Three-Dimensional (3-D) bistatic geometry effects on SAR/ISAR data as well as derivations of wide-angle resolution and resolution-like metrics. Measured ISAR data validates these results. More importantly, the chapter contains an image processing approach that corrects for all three far-field assumption components, an assumption invalidated by the wide-angle beam. Being tomographic in nature, this approach does not rely on uniform spacing of synthetic aperture samples, allowing arbitrary SAR flight paths. Additionally, the method's inherently parallel nature permits seamless incorporation of warped ground plane information.

The second major issue precluding WAM-SAR image formation results from undersampling along the synthetic aperture. The large Doppler spread in the wide-angle radar echoes causes this undersampling, imposing an unrealistic PRF requirement. By failing to meet this requirement, cross range (i.e., Doppler) aliasing artifacts appear in the resulting images. Most previous SAR anti-aliasing work focused on the use of phased array antennas to place spatial filters at aliasing artifact locations [37, 143]. While theoretically feasible, this approach mandates massive data collection, transmission, and storage requirements. Additionally, the required element-level digitization of radar echoes necessitates an exceedingly expensive and complex antenna. Chapter VI introduces the theory for a new anti-aliasing technique based on waveform diversity methods. By using randomized Stepped-Frequency (SF) waveforms verses traditional Linear Frequency Modulation (LFM) waveforms, a WAM-SAR platform can produce a series of Doppler filter nulls at aliased artifact locations, mitigating their effects in the final image [89]. This chapter also defines an SF waveform subpulse

frequency order selection method leading to temporally orthonormal waveform sets. Chapter VII tests the anti-aliasing technique using a custom-built point scatterer simulator. Both One-Dimensional (1-D) and Two-Dimensional (2-D) results illustrate the desired effect, eliminating more than 99% of aliasing artifact energy [87–89]. These simulation results were independently verified in [92]. Chapter VIII extends the anti-aliasing technique and simulation results to the 3-D monostatic/bistatic case. Although these geometries violate one of the technique's assumptions, both derivation and simulation results illustrate excellent mitigation performance for various militarily-significant data collection geometries. As in the 2-D case, more than 99% of the aliasing artifact energy is mitigated. Finally, Chapter IX validates SF waveform Doppler filtering properties using third party complex target simulation data and measured Radar Cross Section (RCS) chamber data. It contains a new technique for converting these data products into SF waveform echoes without needing to transmit actual SF waveforms [84]. Using this approach, the anti-aliasing technique was shown to reduce peak energy from complex aliasing targets by nearly 40.0 dB [86].

Figure 10.1 provides a graphical overview of the major research results. The user desires a wide-angle data collection enabling simultaneous high resolution image formation over large ground swaths. Using conventional SAR processing methods, the wide-angle data is essentially useless. The two images under the "conventional processing" heading illustrate this fact. The top image shows a high resolution point scatterer image obtained from RCS chamber data (upper left-hand scattering response in Fig. 5.16(a)). Total image area is 20 cm^2. The point scatterer is defocused and translated due to the wide-angle data collection. Application of near-field corrections using the tomographic WAM-SAR approach results in the right-hand image (upper left-hand scattering response in Fig. 5.16(b)). In this case, the scatterer is both better focused and correctly located.

The lower images in Fig. 10.1 have an area of 1 km^2. The left-hand "conventional" image shows a well focused scatterer at the scene center and eight aliased or varying extent artifacts (Fig. 7.26). Using WAM-SAR's randomized SF waveform

302

approach, these artifacts are mitigated in the lower right-hand image (Fig. 7.26). Taken together, the images in Fig. 10.1 illustrate WAM-SAR's ability to produce focused alias-free high resolution imagery over large ground swaths, encapsulating the contributions of this research effort.

10.3   *Future Research*

This research demonstrates solutions to both the focused image generation and aliasing artifact mitigation problems faced by WAM-SAR. None-the-less, these efforts simply represent the beginning, not the end of WAM-SAR research possibilities. The following paragraphs suggest a number of additional high interest research areas.

While the anti-aliasing technique performs very well using SF waveforms, other waveform types are also possible. One variant involves superimposing LFM chirps on individual SF subpulses, allowing a smaller number of subpulses covering a given bandwidth and reducing data processing requirements [79]. At the author's suggestion, this technique was successfully demonstrated in [92]. In addition to illustrating the desired anti-aliasing effect, the resulting waveform also lowered the imagery noise floor, increasing the available dynamic range.

Another WAM-SAR waveform possibility is bandlimited white noise. Since white noise uniformly covers a given frequency band, it should not be difficult to build the required rectangular data support region, leading to alias-free images. Since the anti-aliasing technique mandates Continuous Wave (CW) transmission, use of noise waveforms means the WAM-SAR transmitter would act as a barrage noise jammer, flooding the battlefield with white noise. While friendly systems could recover the radar echoes, enemy systems would have to deal with a strong noise source. This scenario makes the noise waveform approach beneficial from both offensive and defensive EW perspectives.

Recall from Sec. 2.2.4 that while wide-angle collections allow high resolution imaging with narrowband waveforms, ImPulse Response (IPR) function sidelobe levels

Wide-angle data collection

Conventional
processing

WAM-SAR
processing

Focused imagery via
near-field tomography

Chapters III-V

Anti-aliasing via
waveform diversity

Chapters VI-IX
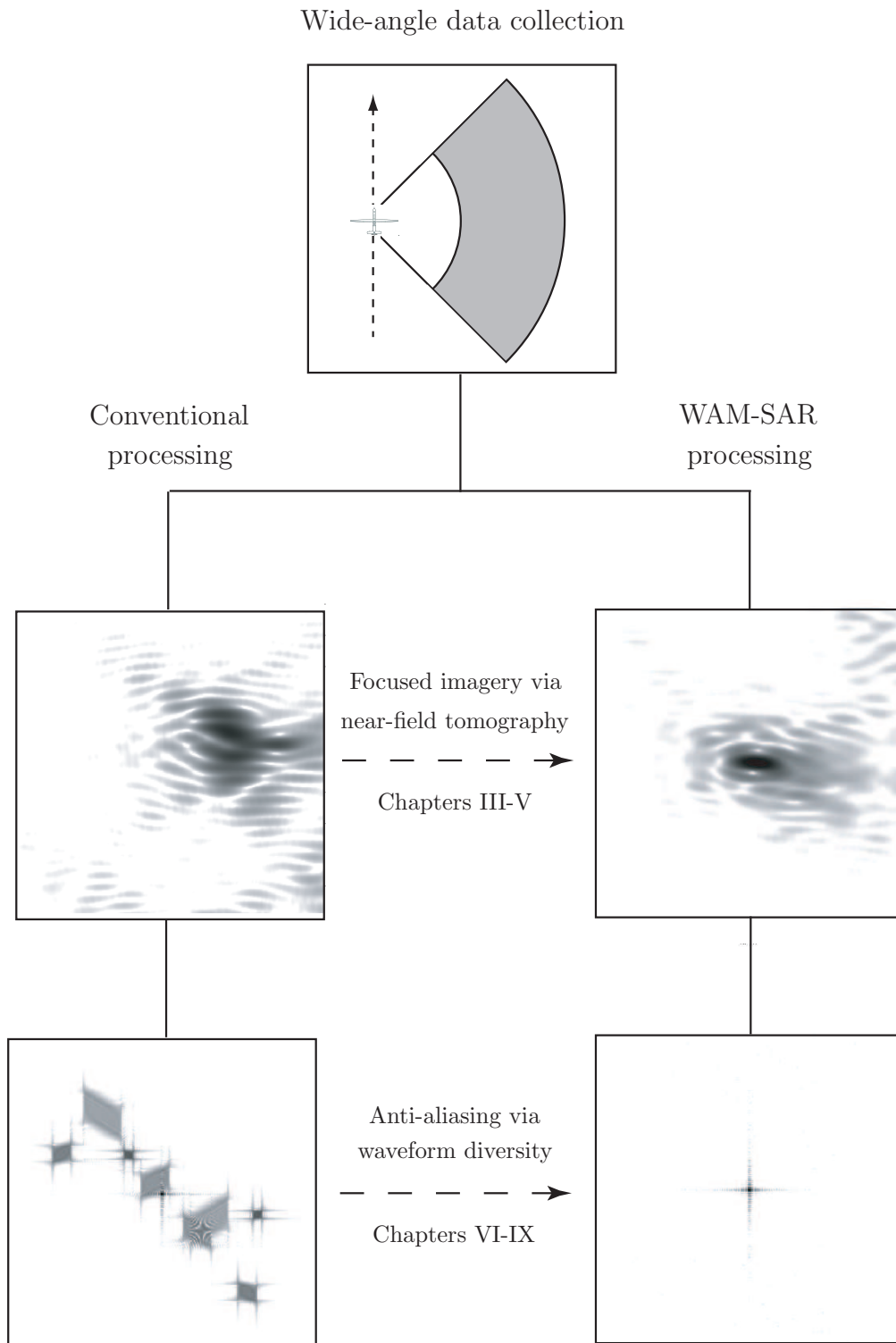
Figure 10.1:   WAM-SAR improvements over conventional processing for wide-angle data. Conventional processing of wide-angle results in defocusing (upper left-hand image) and aliasing (lower left hand image). WAM-SAR processing solves both the focusing (upper right-hand image) and aliasing (lower right-hand image) problems.

can become quite high. These large, bowtie-shaped sidelobes are caused by the sparse, non-uniform filling of the rectangular spatial frequency domain data support regions (e.g., Fig. 3.8) [90]. While sidelobe control is an issue long studied in radar, it has usually employed the narrow-angle assumption. Sidelobe control methods ranging from amplitude windows (i.e., tapers) to spectral estimation inherently assume 1-D or separable 2-D radar data (e.g., [38, 51, 80–82, 90]). Removing the narrow-angle assumption is likely to generate a host of new problems and opportunities and could substantially benefit WAM-SAR. Some preliminary work in this area is contained in [104].

While WAM-SAR makes available both monostatic and bistatic imagery from a number of simultaneous geometries, little research has been done on how to fuse these separate images into a single, high quality result. A good starting place for efforts in this area may be the polarimetric whitening filter originally developed to fuse SAR images containing multiple polarizations [102, 103].

Related to the multistatic data fusion problem is simply determining what flight paths result in the most valuable data. Do circular orbits perform the best? What elevation angles and bistatic angles provide the best combination of data diversity and image resolution? Some of these ideas are addressed in [108], but much room exists for additional research.

Finally, the variable bistatic image formation routine presented in Chapter V may also be useful for detecting flaws in RCS coatings. This is an important application for maintenance of stealth aircraft. Although the specular returns for a complex target are difficult to predict, by using a fixed transmit orientation and a variable bistatic receiver (i.e., a setup similar to AFIT's RCS chamber), the the majority of reflected energy could be collected. This collection and subsequent imaging might simplify the detection and localization of changes in target RCS characteristics. A further extension might entail placing probes directly on target surfaces, although

this requires modification of the imaging routines to account for the non free-space nature of the resulting data.

10.4   Final Thoughts

The data focusing and anti-aliasing methods presented in this research demonstrate the feasibility of high resolution SAR image formation over large ground patches using 3-D monostaic/bistatic/multistatic data collection geometries. It is the author's hope these results will motivate WAM-SAR concept expansion. With additional research in the areas mentioned above, as well as Sections. 2.2.5 and 2.2.6, WAM-SAR may well find its place on a future battlefield, proving a wealth of persistent real-time high resolution SAR/MTI data spanning vast terrain swaths. The availability of such data would enable commanders and operators alike to plan and conduct operations in shorter time spans, with greater efficiency, and with less risk to personnel and equipment.

Appendix A. Fourier Transform Definitions, Properties, and Pairs

This appendix defines the 1-D and 2-D Fourier Transform (FT) operations. It also reviews common FT properties. Information in this appendix is adapted from [64] and is frequently referred to throughout the dissertation document.

The 1-D FT of a function $f(t)$ is defined as

$$F(f) \triangleq \mathcal{F}[f(t)] \triangleq \int_{-\infty}^{\infty} f(t) \exp(-j2\pi f t) \mathrm{d}t, \tag{A.1}$$

where the units of f and t are reciprocals of each other. For many signal processing applications, t represents time in units of seconds implying f represents temporal frequency in units of inverse seconds. For radar applications the linear transform

$$r = \frac{ct}{2}, \tag{A.2}$$

is used to convert delay into range (c represents the wave's propagation velocity). This conversion allow the temporal radian frequency $k_r = 2\pi f$ to be rewritten as $4\pi/\lambda$ resulting in a radial spatial frequency k_r in units of rad/unit length. In range/spatial frequency variables, the 1-D Fourier transform can be rewritten as

$$F(k_r) \triangleq \mathcal{F}[f(r)] \triangleq \int_{-\infty}^{\infty} f(r) \exp(-jk_r r) \mathrm{d}r. \tag{A.3}$$

The resulting Fourier transform $F(k_r)$ in (A.3) differs from the $F(f)$ in (A.1) by the scaling constant $|2/c|$ as indicated by the scaling property in Table A.2. This constant is normalized out to simplify the definition.

The 1-D Inverse Fourier Transform (IFT) of a function $F(k_r)$ is defined as

$$f(r) \triangleq \mathcal{F}^{-1}[F(k_r)] \triangleq \int_{-\infty}^{\infty} F(k_r) \exp(jk_r r) \mathrm{d}k_r. \tag{A.4}$$

Since the FT is invertible, no information is lost as the functions are transformed between the range and spatial frequency domains.

SAR imaging forms estimates of scene reflectivity in two (or occasionally three) dimensions, making it necessary to extend the FT definition to multiple dimensions. The 2-D FT of $f(x, y)$ is defined as

$$F(k_x, k_y) \triangleq \mathcal{F}[f(x, y)] \triangleq \int_{-\infty}^{\infty} \int_{-\infty}^{\infty} f(x, y) \exp[-j(kx_x + ky_y)]\mathrm{d}x\mathrm{d}y. \qquad \text{(A.5)}$$

The 2-D IFT of $F(k_x, k_y)$ is defined as

$$f(x, y) \triangleq \mathcal{F}^{-1}[F(k_x, k_y)] \triangleq \int_{-\infty}^{\infty} \int_{-\infty}^{\infty} F(k_x, k_y) \exp[j(k_x x + k_y y)]\mathrm{d}k_x\mathrm{d}k_y \qquad \text{(A.6)}$$

The exponential kernel of the 2-D FT/IFT is separable. This property implies that the 2-D FT/IFT can be computed as successive 1-D transforms along each of the variables. This separability results from the orthogonal relationship between the x and y axes. Extension of the FT/IFT pair to n dimensions is straightforward.

The remainder of this appendix contains a series of tables describing useful properties and relationships which arise from the FT/IFT pair in one and two dimensions. Table A.1 defines a collection of special functions and operators used within the remaining tables. Table A.2 lists some of the important properties of 1-D FT/IFT operations. Table A.3 extends each of these properties to two dimensions and adds two new properties that have no meaning in 1-D FT theory. Each of these additional properties plays an important role in SAR imaging. The rotational property states that rotation of a function $f(x, y)$ by an angle θ, also rotates the FT $F(k_x, k_y)$ by the same angle θ. The importance of the separability property was addressed earlier in this appendix.

Table A.1:   Special functions and operators

Function	Definition
Dirac delta	$\delta(r) \triangleq 0,\ r \neq 0$
	$\lim_{\epsilon \to 0} \int_{-\epsilon}^{\epsilon} \delta(r)\mathrm{d}r \triangleq 1$
Sifting Property	$\int_{-\infty}^{\infty} f(r')\delta(r - r')\mathrm{d}r' = f(r)$
Rectangle	$\text{rect}\left(\frac{r}{R}\right) \triangleq \begin{cases} 1, & -\frac{R}{2} \leq r < \frac{R}{2} \\ 0, & \text{else} \end{cases}$
Triangle	$\text{tri}\left(\frac{r}{R}\right) \triangleq \begin{cases} 1 - |r/R|, & |r| \leq R \\ 0, & \text{else} \end{cases}$
Sinc	$\text{sinc}(r) \triangleq \frac{\sin(\pi r)}{r}$
Convolution	$f(r) * g(r) \triangleq \int_{-\infty}^{\infty} f(r - r')g(r)\mathrm{d}r'$
2-D Convolution	$f(x, y) * g(x, y) \triangleq \int_{-\infty}^{\infty} \int_{-\infty}^{\infty} f(x - x', y - y')g(x, y)\mathrm{d}x'\mathrm{d}y'$

Table A.2:   1-D Fourier transform properties

Property	$f(r)$	$F(k_r)$
Linearity	$a_1 f_1(r) + a_2 f_2(r)$	$a_1 F_1(k_r) + a_2 F_2(k_r)$
Conjugation	$f^*(r)$	$F^*(-k_r)$
Scaling	$f(ar)$	$\frac{F(k_r/a)}{|a|}$
Shifting	$f(r \pm r_0)$	$\exp(\pm j k_r r_0)F(k_r)$
Modulation	$\exp(\pm j k_{r0} r)f(r)$	$F(k_r \mp k_{r0})$
Convolution	$g(r) = h(r) * f(r)$	$G(k_r) = H(k_r)F(k_r)$
Multiplication	$g(r) = h(r)f(r)$	$G(k_r) = H(k_r) * F(k_r)$

Table A.3:   2-D Fourier transform properties

Property	$f(x, y)$	$F(k_x, k_y)$
Rotation	$f(\pm x, \pm y)$	$F(\pm k_x, \pm k_y)$
Linearity	$a_1 f_1(x, y) + a_2 f_2(x, y)$	$a_1 F_1(k_x, k_y) + a_2 F_2(k_x, k_y)$
Conjugation	$f^*(x, y)$	$F^*(-k_x, -k_y)$
Separability	$f_1(x)f_2(y)$	$F_1(k_x)F_2(k_y)$
Scaling	$f(ax, by)$	$\frac{F(k_x/a, k_y/b)}{|ab|}$
Shifting	$f(x \pm x_0, y \pm y_0)$	$\exp[\pm j(k_x x_0 + k_y y_0)]F(k_x, k_y)$
Modulation	$\exp[\pm j(k_{x0} x + k_{y0} y)]f(x, y)$	$F(k_x \mp k_{x0}, k_y \mp k_{y0})$
Convolution	$g(x, y) = h(x, y) * f(x, y)$	$G(k_x, k_y) = H(k_x, k_y)F(k_x, k_y)$
Multiplication	$g(x, y) = h(x, y)f(x, y)$	$G(k_x, k_y) = H(k_x, k_y) * F(k_x, k_y)$

Appendix B.   Bistatic ISAR Data Calibration Code

T his appendix contains `Matlab`® code used for bistatic ISAR data calibration. The background subtraction calibration procedure is derived in Chapter IV. Calibration is performed by calling the function `calibrate()` with the appropriate input arguments. The code then queries the user to locate the required Lintek 4000 data files.

Listing B.1:   Master file governing the calibration routine.(appendix2/calibrate.m)

```
   % function [data] = calibrate(theta,dia,pol);
   %
   % This routine calibrates bistatic RCS chamber data.  It assumes
   % data collection is performed using a fixed bistatic angle.   The
 5 % receiver angle measurement is relative to the unit vector
   % pointing in the propagation direction of the incident wave,
   % counter-clockwise rotation is positive.
   %
   % Inputs
10 %    theta       :    theta angle to receiver, degrees
   %    dia         :    diameter of calibration sphere, inches
   %    pol         :    polarization, (1=HH, 2=VV, 3=HV, 4=VH)
   %
   % Outputs
15 %    data.iq     :    complex IQ calibrated data
   %    data.freq   :    frequency vector, GHz
   %    data.az     :    azimuth vector, degrees
   %    data.pol    :    polarization, (1=HH, 2=VV, 3=HV, 4=VH)
   %    data.theta  :    theta angle to receiver, degrees
20 %
   % data.iq is scaled such that 20*log10(abs(data.iq)) = RCS in dB
   %
   % Written by Jonathan E. Luminati, 2005

25 function [data] = calibrate(theta,dia,pol);

   root = 'Some_Screwy_String';

   % read in the binary data for target, background, calibration, and
30 % cal background measurements
   for ext = {'tar' 'bkg' 'cal' 'cbk'},
       [f,az,iq,header] = readlintekfile([root '.' char(ext)]);
       az = unwrap((round(100*az)/100)*pi/180)*180/pi;
       root = header.FILENAME(1:end-4);
35     for data = {'f' 'az' 'iq'}
           eval([char(ext) '.' char(data) '=' char(data) ';'])
       end
   end

40 % replicate calibration data
```

310

```
   cal.iq = repmat(cal.iq(:,1),1,length(tar.az));
   cbk.iq = repmat(cbk.iq(:,1),1,length(tar.az));

   % determine exact.iq data using bistatic RCS calculation
45 if (pol==1) || (pol==2)
      exact = bistatic(dia,pol,tar.f*1e9,theta).';
      exact = repmat(exact,1,length(tar.az));
   else
      disp('WARNING: Cross-Polarization calibration not possible.');
50    exact = 0;
   end

   % calibrate and save data
   data.iq = exact .* ( tar.iq - bkg.iq ) ./ ( cal.iq - cbk.iq);
55 data.freq = tar.f';
   data.az = tar.az;
   data.pol = pol;
   data.theta = theta;

60 return
```

Listing B.2:   File for extracting required data from Lintek output files.
(appendix2/ReadLintekFile.m)

```
   % function [Freqs,Angles,IQ,Header] = readlintekfile(filename,...
   %    IEEE_type);
   %
   % Reads Lintek 4000 binary file.  Optional arguments specify the
 5 % file to read and the IEEE binary data format (big-endian or
   % little-endian).

   % Input:
   %    filename   :   file name
10 %    IEEE_type  :   file type
   %
   % Output:
   %    Freqs      :   Frequency data, GHz
   %    Angles     :   Angular oridentation data, degrees
15 %    IQ         :   Raw complex radar data
   %    Header     :   Header data
   %
   % Written by William D. Wood, 2002
   % Modified by Jonathan E. Luminati, 2005
20
   function [Freqs,Angles,IQ,Header] = readlintekfile(filename,...
      IEEE_type);

   if nargin<2 || ~strmatch(IEEE_type,strvcat('ieee-le','ieee-be','l'...
      ,'b'),'exact')
      IEEE_type = 'ieee-le';  % Default to AFIT range's format
25 end
```

```
   % Check to see if the file could be opened.
   % If not, prompt for filename.
   if nargin <1 || exist(filename)~=2
30     ext = filename(end-2:end);
       [File,Path]=uigetfile(['*.' ext], ['Radar ' upper(ext) ' file'...
           ]);
       filename = [Path File];    % alb added 10.09.02
       cd(Path);
   end
35
   fid = fopen(filename,'rb',IEEE_type);

   token = 'BEGIN';
   while ~strcmp(token,'END'),
40     tline = fgetl(fid);
       [token,value] = strtok(tline);
       if findstr(token,'WAVEFORM'), continue, end
       value=deblank(fliplr(deblank(fliplr(value))));
       if sum(double(value)-47==0 | double(value)-58==0 | isletter(...
           value))
45         eval(['Header.' token '=value;'])  % VALUE is numeric
       else
           eval(['Header.' token '=str2num(value);'])  % VALUE is a ...
               string
       end
   end
50
   fseek(fid,4096,'bof');  % position after 4096 byte header
   data=fread(fid,inf,'real*4');  % Read the binary data
   % Put data into martrix form, each column being a freq sweep.
   % Last 6 rows are the encoder packet
55 nFreq = Header.NUMFRQS0;
   data  = data(4*nFreq+1:end);  % Strip off bkg and cal types
   nAng  = length(data)/(2*nFreq+6);
   data=reshape(data,2*nFreq+6,nAng);

60 Angles = data(2*nFreq+1,:);
   Freqs = linspace(Header.STFRQ0,Header.SPFRQ0,nFreq)*1e-6;
   IQ = data(1:2:2*nFreq,:)+j*data(2:2:2*nFreq,:);

   return
```

Listing B.3:   Calculates the bistatic scattered field from the calibration sphere. (appendix2/bistatic.m)

```
   % function [iq] = bistatic_exact(dia,pol,freq,theta);
   %
   % Calculates the scaled ratio of scattered-to-incident E-fields
   % (Es/Ei) for a sphere.  It assumes the TX horn, sphere, and
 5 % RX horn define the "scattering plane."  The unit vector
```

```matlab
    % corresponding to the direction of TX propagation is defined
    % along the +z direction.   The unit vector corresponding to
    % the linearly polarized E-field of the TX wave is defined
    % along the +x direction.
10  %
    % Input:
    %    dia      : sphere diameter, inches
    %    pol      : polariazation, 1=HH, 2 = VV, 3 = HV, 4 = VH
    %    freq     : frequencies required, Hz
15  %    theta    : angle between the TX propagation vector and the RX
    %                propagation vector, deg.
    %                  theta = 0 implies forward scattering
    %                  theta = 180 implies backscatting (monostatic)
    %
20  % Output:
    %    iq       : 2*sqrt(pi)*r*Es/Ei
    %
    % Coordinate systems and scattered field equations are taken from
    % Harrington, "Time-Harmonic Electromagnetic Fields"
25  %
    % Written by Jonathan E. Luminati, 2005

    function [iq] = bistatic(dia,pol,freq,theta);

30  % define speed of light, m/s
    C = 3e8;

    % ensure theta between 0 and 180 and then convert to radians
    theta = mod(theta,360);
35  if theta>180
        theta = 360-theta;
    end
    theta = theta*pi/180;

40  % ensure freq vector oriented horizontally
    if size(freq,2)==1
        freq = freq';
    end

45  % convert sphere diameter to meters
    a = dia/2*0.0254;

    % set number of terms in sum
    n_max = 100;
50  n = [1:n_max]';
    n_ext = [0:n_max]';

    % calculate a_n
    a_n = repmat(j.^-n.*(2*n+1)./n./(n+1),1,length(freq));
55
    % calculate k_a
    k_a = 2*pi*freq/C*a;
```

```matlab
   % get required sherical Bessel/Hankle functions
60 J_sphere = zeros(n_max+1,length(freq));
   H_sphere = zeros(n_max+1,length(freq));
   for i = 1:n_max+1
       J_sphere(i,:) = besselj(i+0.5,k_a);
       H_sphere(i,:) = besselh(i+0.5,2,k_a);
65 end
   J_sphere = sqrt(pi*repmat(k_a,n_max+1,1)/2).*J_sphere;
   H_sphere = sqrt(pi*repmat(k_a,n_max+1,1)/2).*H_sphere;
   J_sphere_prime = -J_sphere(2:end,:) + repmat(n+0.5,1,length(freq))...
       ./repmat(k_a,n_max,1).*J_sphere(1:end-1,:);
   H_sphere_prime = -H_sphere(2:end,:) + repmat(n+0.5,1,length(freq))...
       ./repmat(k_a,n_max,1).*H_sphere(1:end-1,:);
70
   % calculate b_n
   b_n = -a_n.*J_sphere_prime./H_sphere_prime;

   % calculate c_n
75 c_n = -a_n.*J_sphere(1:end-1,:)./H_sphere(1:end-1,:);

   % get required associated Legendre fucntions and derivatives
   if theta==pi
       P_term = repmat((-1).^n.*n.*(n+1)/2,1,length(freq));
80     P_prime_term = P_term;
   else
       if theta==0
           theta=0.0001;
       end
85     P = zeros(n_max+1,1);
       for i = 1:n_max+1
           temp = legendre(i,cos(theta));
           P(i)=temp(2);
       end
90     P_prime_term = repmat(1/(cos(theta)^2-1)*(n.*P(2:end)-(n+1)*...
           cos(theta).*P(1:end-1)),1,length(freq))*sin(theta);
       P_term = repmat(P(1:end-1),1,length(freq))/sin(theta);
   end

   % calculate iq data
95 if pol == 1               % HH polarization
       iq = j*C/sqrt(pi)./freq.*sum(repmat(j.^n,1,length(freq)).*(b_n...
           .*P_prime_term-c_n.*P_term),1);
   elseif pol == 2           % VV polarization
       iq = j*C/sqrt(pi)./freq.*sum(repmat(j.^n,1,length(freq)).*(b_n...
           .*P_term-c_n.*P_prime_term),1);
   else                      % cross-polarization
100    iq = 0;
   end
```

Appendix C. ISAR Data Processing Code

This appendix contains `Matlab`® code used to produce orthographically correct 2-D near-field monostatic/bistatic ISAR images of targets on warped (3-D) image planes, eliminating defocusing/layover effects. This code was used to produce Figs. 5.21-5.22.

Listing C.1:   Master file governing the image generation routine. (appendix3/master.m)

```
% master.m
%
% Master file for creating 2-D orthographically
% correct images over warped (3-D) image planes
5 %
% Corrects for defocusing/layover effects.

% prepare workspace
clear all
10 close all

% load constants
constants

15 % load file
load(FILENAME)

% reduce samples to desired collection parameters
az_index = find(data.az>=min_az&data.az<=max_az);
20 freq_index = find(data.freq>=min_freq&data.freq<=max_freq);
data = struct('iq',data.iq(freq_index,az_index).','az',data.az(...
    az_index)','freq',data.freq(freq_index));

% load contour map data
load points
25
% bistatic countour image with near-feild wavefront
% curvature and ampltidue corrections
contour_image = bis_contour_NF_amp(data,points);
```

Listing C.2:   Constants file defining relevant parameters.(appendix3/constants.m)

```
% physical constants
C = 3e8;                              % speed of light, m/s
in2m = 0.0254;                        % conversion from in to m

5 % data boundries
min_az = 0;                           % degrees
max_az = 360;                         % degrees
min_freq = 12;                        % GHz
```

315

```
      max_freq = 18;                              % GHz
10
      % number of FFT points
      numFFTpts = 1024;

      % view movies during image formation (0 = no, 1 = yes)
15    mov = 1;

      % normalize by fixed value (0 = no, 1 = yes)
      norm_on = 0;
      norm_value = 69.6783;                       % dB
20
      % TX/RX locations in polar coordinates
      RX_pol = [8*12*in2m,73*pi/180,0];
      TX_pol = [27*12*in2m,180*pi/180,0];

25 % image dimesnions
      num_pixels = [128,128];                     % number of pixels
      dim_image = [-0.3 0.3 -0.3 0.3];     % image dimensions, meters
      dyn_range = 20;                             % dynamic range, dB

30 % filename
      FILENAME = 'bis00';

      % maximum half-beamwidth for amplitude correction
      % impliments pseudo-inverse instead of inverse filter
35 % to prevent excessive gain
      MAX_BEAM = 20;                              % degrees
```

Listing C.3:   ISAR image formation code.(appendix3/contour.m)

```
      % function image_data = contour(data,points);
      %
      % ISAR image generation code for creating 2-D
      % orthographically correct images over warped
 5 % (3-D) image planes.
      %
      % Corrects for defocusing/layover effects.

      function image_data = contour(data,points);
10
      % load constants
      constants;

      % define k_r;
15 k_r =   4*pi/C*data.freq*1e9;
      min_k_r = min(k_r);

      % establish cooridnates of final image (meters)
      x_image = linspace(dim_image(1),dim_image(2),num_pixels(1));
20 y_image = linspace(dim_image(3),dim_image(4),num_pixels(2));
      [X,Y] = meshgrid(x_image,y_image);
      X = X(:);
```

```matlab
    Y = Y(:);
    Z = griddata(points(:,1),points(:,2),points(:,3),X,Y,'cubic');
25
    % define the BP filter, only k_r needed since bistatic
    % angle is assumed constant
    H = k_r;

30  % load polynomial to correct for non-uniform antenna pattern
    load P

    % calculate delay values for each projection
    dr = C/2/((max(data.freq)-min(data.freq))*1e9)*(length(data.freq)/...
        numFFTpts);
35  r_exact = dr*[0:numFFTpts-1];
    r_exact = r_exact-mean(r_exact);

    % preallocate final image variables and intialize figure window
    image_data = zeros(num_pixels(2),num_pixels(1));
40  figure

    % intialize waitbar
    wait = waitbar(0,'Forming ISAR Image');

45  % loop over all theta angles
    for i = 1:length(data.az)

        % genrate low-pass versions of projections
        q = fftshift(ifft((data.iq(i,:).').*H,numFFTpts));
50
        % calculate the radii to image center
        [TX_x TX_y] = pol2cart(TX_pol(2)-data.az(i)*pi/180,TX_pol(1));
        TX_z = TX_pol(3);
        TX_r = sqrt(sum([TX_x TX_y TX_z].^2));
55
        [RX_x RX_y] = pol2cart(RX_pol(2)-data.az(i)*pi/180,RX_pol(1));
        RX_z = RX_pol(3);
        RX_r = sqrt(sum([RX_x RX_y RX_z].^2));

60      % calculate the required radii for the image
        r_required_TX = sqrt((X-TX_x).^2+(Y-TX_y).^2+(Z-TX_z).^2);
        r_required_RX = sqrt((X-RX_x).^2+(Y-RX_y).^2+(Z-RX_z).^2);
        r_required = 0.5*(r_required_TX+r_required_RX-TX_r-RX_r);

65      % interpolate q to radii required by the output image
        q_interp = interp1(r_exact,q,r_required).*exp(j*min_k_r*...
            r_required);

        % calculate antenna pattern corrections;
        % assumes pattern is separable in the el/az directions
70      A = -[TX_x;TX_y];
        B = [X'-TX_x;Y'-TX_y];
        angle = acos((A'*B)./sqrt(sum(A.^2))./sqrt(sum(B.^2)))*180/pi;
```

```matlab
        big_angle = find(angle>MAX_BEAM);
        angle(big_angle) = MAX_BEAM;
75      az_angle_weight_TX = P(1)*angle.^8+P(3)*angle.^6+P(5)*angle...
            .^4+P(7)*angle.^2+P(9);


        A = -[RX_x;RX_y];
        B = [X'-RX_x;Y'-RX_y];
        angle = acos((A'*B)./sqrt(sum(A.^2))./sqrt(sum(B.^2)))*180/pi;
80      big_angle = find(angle>MAX_BEAM);
        angle(big_angle) = MAX_BEAM;
        az_angle_weight_RX = P(1)*angle.^8+P(3)*angle.^6+P(5)*angle...
            .^4+P(7)*angle.^2+P(9);


        angle = asin(Z./r_required_TX)*180/pi'';
85      big_angle = find(angle>MAX_BEAM);
        angle(big_angle) = MAX_BEAM;
        el_angle_weight_TX = P(1)*angle.^8+P(3)*angle.^6+P(5)*angle...
            .^4+P(7)*angle.^2+P(9);


        angle = asin(Z./r_required_RX)*180/pi;
90      big_angle = find(angle>MAX_BEAM);
        angle(big_angle) = MAX_BEAM;
        el_angle_weight_RX = P(1)*angle.^8+P(3)*angle.^6+P(5)*angle...
            .^4+P(7)*angle.^2+P(9);


        % apply amplitude corrections
95      correction = r_required_TX.*r_required_RX./az_angle_weight_TX'...
            ./az_angle_weight_RX'./el_angle_weight_TX./...
            el_angle_weight_RX;
        correction = correction/max(max(correction));
        q_interp = correction.*q_interp;


        % form final image through back projection
100     image_data = image_data + reshape(q_interp,num_pixels(2),...
            num_pixels(1));


        % plot current image if "movie" is desired
        if mov
            temp_image = 20*log10(abs(image_data));
105         temp_image = temp_image-max(max(temp_image));
            index = find(temp_image<-dyn_range);
            temp_image(index) = -dyn_range;
            pcolor(x_image,y_image,temp_image)
            axis equal
110         axis tight
            shading flat
            pause(0.01)
        end


115     % update waitbar
        waitbar(i/length(data.az),wait);
```

```matlab
        end

120 % close waitbar
    close(wait)

    % plot final image
    clear temp_image;
125 image = 20*log10(abs(image_data));
    if norm_on
        image = image-norm_value;
    else
        image = image-max(max(image));
130 end
    index = find(image<-dyn_range);
    image(index) = -dyn_range;
    pcolor(x_image,y_image,image)
    axis equal
135 axis tight
    shading flat
    xlabel('x, m')
    ylabel('y, m')
    colorbar
```

Appendix D. *2-D Monostatic Point Scatterer Simulator*

T his appendix contains the 2-D monostatic point scatterer simulation code used
to produce the results in Chapter VII. All code is written in `Matlab`® .

Listing D.1:   Simulation constants and parameters.(appendix4/constants.m)

```matlab
% constants.m
%
% Sets basic constants and parameters for simulation

% physical constants
C = 3e8;            % speed of light

% file name root
DATANAME = 'data';
CODENAME = 'code';
IMAGENAME = 'image';

% collection parameters
VEL = 100;                      % platform velocity, m/s
PRF = 2000;                     % pulse repetition frequency, m/s
L = 200;                        % synthetic aperture length, m

% antenna parameters, simple antenna beam
MIN_RANGE_ANT = 75000;             % minimum range for antenna ...
    pattern, m
MAX_RANGE_ANT = 100000;        % maxium range for antenna pattern, m
BEAM = 90*pi/180;              % beamwidth, rad

% waveform parameters
B = 20e6;                      % bandwidth (Hz)
M = 100;                       % number of subpulses
Fc = 10e9;                     % center frequency (Hz)
Tp = M^2/B;                    % pulse time (s)
OVER = 2;                      % oversampling ratio
SAMP_PER_FREQ = 2*M;           % samples per frequency subpulse
METHOD = 1;                    % code selection method (1 = LFM, 2 = ...
    RND, 3 = SHF);

% set scatterer parameters
POINTS = [
    87500*cos(37.0*pi/180)-200 87500*sin(37.0*pi/180) 1;
    87500*cos(26.7*pi/180)+150 87500*sin(26.7*pi/180) 1;
    87500*cos(17.3*pi/180)+300 87500*sin(17.3*pi/180) 1;
    87500*cos(8.7*pi/180)-100 87500*sin(8.7*pi/180) 1;
    87500*cos(0) 87500*sin(0) 1;
    87500*cos(-8.7*pi/180)+300 87500*sin(-8.7*pi/180) 1;
    87500*cos(-17.3*pi/180)-350 87500*sin(-17.3*pi/180) 1;
    87500*cos(-26.7*pi/180)-50 87500*sin(-26.7*pi/180) 1;
    87500*cos(-37.0*pi/180)+150 87500*sin(-37.0*pi/180) 1;
];
NUM_SCAT = size(POINTS,1);
```

320

```
% scene (image) parameters
DIM = 1000;                    % size of square image, m
NUM_PTS = [512,512];           % number of point in final scene
DYN_RANGE = 50;                % dynamic range, dB
```

Listing D.2:   Generates raw (e.g., unmatched filtered) echoes.
(appendix4/datagen.m)

```
% datagen.m
%
% Generates SAR data using specified parameters.  Saves each
% pulse in the CPI as a separate file.  Echos are saved in
5 % uncompressed form to facilitate image formation through
% various methods.

% prepare workspace
clear all
10 close all

% load constants file
constants

15 % determine cross-range samples for SAR platform
dy = VEL/PRF;                    % sample spacing
y = [dy:dy:L];
if mod(length(y),2)              % ensure even number of samples
    y = [y y(end)+dy];
20 end
location =  y-mean(y);           % place origin at aperture center
NUM_PULS = length(y);            % number of pulses in CPI

% determine sample times
25 dt = Tp/M/SAMP_PER_FREQ;       % sampling rate, s
t_min = 2*MIN_RANGE_ANT/C;       % time of first sample, s
t_max = 2*MAX_RANGE_ANT/C+Tp;    % time of last sample, s
T = [t_min:dt:t_max];
NUM_SAMP = length(T);            % number of samples in each pulse
30 if mod(NUM_SAMP,2)             % ensure even number of samples
    T = [T T(end)+dt];
    NUM_SAMP = NUM_SAMP+1;
end

35 % set subpulse frequencies
FREQ = linspace(-B/2,B/2,M+1);
delta = diff(FREQ)/2;
FREQ = FREQ(1:end-1)+delta;
FREQ = FREQ+Fc;                  % shift to center frequency
40
% intialize waitbar
wait = waitbar(0,'Generating SAR Data');
```

```matlab
      % prepare to enter loop
45 data = zeros(1,NUM_SAMP);
   width = length(num2str(NUM_PULS));

   % loop over each pulse in the CPI
   for pulse = 1:NUM_PULS
50
       % determine subpulse frequency code using correct method
       switch METHOD
           case 1 % LFM
               code = 1:M;
55         case 2 % Randomized
               temp = rand(1,M);
               [temp code] = sort(temp);
           case 3 % Shuffled Circulant Matrix
               row = mod(pulse-1,M);
60             if row==0
                   code_matrix = shfmatrix(M);
               end
               code = code_matrix(row+1,:);
       end
65
       % build frequency vector
       freq_vec = repmat(FREQ(code),SAMP_PER_FREQ,1);
       freq_vec = freq_vec(:)';

70     % calculate range to each scatterer
       range = sqrt((POINTS(:,2)-location(pulse)).^2+(POINTS(:,1))...
           .^2)';

       % calculate the angle (from broadside) to each scatterer
       angle = atan2((POINTS(:,2)-location(pulse)),POINTS(:,1))';
75
       % calculate Dopper frequencies to each scatterer
       doppler = 2*VEL*sin(angle)*Fc/C;

       % intialize storage variable for composite echo
80     comp_echo = 0;

       % loop over each scatterer
       for s = 1:NUM_SCAT

85         % find delay to scatterer
           delay = 2*range(s)/C;

           % find first sample to see an echo
           front = T>=delay;
90         front = find(front);
           front = front(1);

           % extend frequency vector to cover all samples
```

```matlab
            ext_freq_vec = [zeros(1,front-1) freq_vec];
95          ext_freq_vec = [ext_freq_vec zeros(1,NUM_SAMP-length(...
                ext_freq_vec))];
            mask = ext_freq_vec>0;

            % generate waveform
            echo = exp(j*2*pi*ext_freq_vec.*(T-delay));
100         echo = mask.*echo;

            % scale scatterers by amplitude
            echo = echo.*POINTS(s,3);

105         % apply antenna pattern
            angle_mask = abs(angle(s))<=BEAM/2 & range(s)>...
                MIN_RANGE_ANT & range(s)<MAX_RANGE_ANT;
            echo = echo.*angle_mask;

            % apply doppler shift
110         echo = echo.*exp(j*2*pi*doppler(s)*(T-delay));

            % add to other scatterers
            comp_echo = comp_echo+echo;

115     end

        % convert to baseband
        data = comp_echo.*exp(-j*2*pi*(Fc-B/2)*T);

120     % create file name
        name = num2str(pulse);
        while length(name)<width
            name = strcat('0',name);
        end
125     dataname = strcat(DATANAME,name);
        codename = strcat(CODENAME,name);

        % save data
        save(dataname,'data');
130     save(codename,'code');

        % update waitbar
        waitbar(pulse/NUM_PULS,wait);

135 end

    % close waitbar
    close(wait);
```

```matlab
% [matrix,col,row] = shfmatrix(N)
%
% Generates shuffled circulant matrix of size NxN.
% Returns the matrix of N, N-length codes and the 2 keys
% needed to generate them.  Codes can be read from consecutive
% rows of the output matrix. The 3-D variable matrix stack
% breaks out the individual codes into permutation matricies.

function [matrix,col,row] = shfmatrix(N)

% storage matricies
ordered_matrix = [];
col_matrix = zeros(N);
row_matrix = zeros(N);

% generate the two keys for reordering the matrix
[temp col] = sort(rand(1,N));
[temp row] = sort(rand(1,N));
temp = [1:N];

% generate the ordered matrix and swapping matricies
for i = 1:N
    ordered_matrix = [ordered_matrix; temp];
    col_matrix(col(i),i)=1;
    row_matrix(row(i),i)=1;
    temp = circshift(temp,[0,1]);
end

% apply the swapping matricies
matrix = ordered_matrix;
matrix = (matrix*col_matrix);
matrix = (matrix'*row_matrix)';

% % generate individual permutation matricies
% matrix_stack = [];
% for i = 1:N
%     % form permutation matrix of intial code
%     for j = 1:N
%         matrix_stack(matrix(i,j),j,i)=1;
%     end
% end
% picture = 0;
% for i = 1:N
%     picture = picture + i*squeeze(matrix_stack(:,:,i));
% end

% end function
return
```

Listing D.4:   Master file for generating SAR images of all available scatterers. (appendix4/imagegen.m)

```matlab
% imagegen.m
%
% Forms and saves complex images of all scatterers in a
% given scene.  Assumes relevant data files already generated
% with datagen.m

% prepare workspace
clear all
close all

% load constants
constants

% prepare to enter loop
width = length(num2str(NUM_SCAT));

% loop over all scatterers
for scat = 1:NUM_SCAT

    % form image of current scatterer
    raw_image = BPimage(scat);

    % form name of image file
    name = num2str(scat);
    while length(name)<width
        name = strcat('0',name);
    end
    imagename = strcat(IMAGENAME,name);

    % save image
    save(imagename,'raw_image');

end
```

Listing D.5:   Back-projection SAR image formation code.(appendix4/BPimage.m)

```matlab
% function [raw_image] = BPimage(scat);
%
% Form back-projection image of desired scatterer.  Uses
% traditional (e.g., far-field) techinques, since low range
% resolution and short syntehtic aperture ensure minimal range
% mirgation effects.  Requires raw radar echo data and
% appropriate subpulse frequency order codes.

function [raw_image] = BPimage(scat);

% load constants file
constants
```

```matlab
   % extract image center
15 CENTER = [POINTS(scat,1:2)];

   % determine cross-range samples for SAR platform
   dy = VEL/PRF;                         % sample spacing
   y = [dy:dy:L];
20 if mod(length(y),2)                   % ensure an even number of samples
       y = [y y(end)+dy];
   end
   location =  y-mean(y);                % place origin at aperture center
   NUM_PULS = length(y);                 % number of pulses in CPI
25
   % determine sample times
   dt = Tp/M/SAMP_PER_FREQ;              % sampling rate, s
   t_min = 2*MIN_RANGE_ANT/C;            % time of first sample, s
   t_max = 2*MAX_RANGE_ANT/C+Tp;         % time of last sample, s
30 T = [t_min:dt:t_max];
   NUM_SAMP = length(T);                 % number of samples in each pulse
   if mod(NUM_SAMP,2)                    % ensure number of samples
       T = [T T(end)+dt];
       NUM_SAMP = NUM_SAMP+1;
35 end

   % set subpulse frequencies
   FREQ = linspace(-B/2,B/2,M+1);
   delta = diff(FREQ)/2;
40 FREQ = FREQ(1:end-1)+delta;
   FREQ = FREQ+Fc;                       % shift to center frequency

   % determine pixel locations in final image
   x_image = linspace(-DIM/2, DIM/2, NUM_PTS(1));
45 y_image = linspace(-DIM/2, DIM/2, NUM_PTS(2));
   [X,Y] = meshgrid(x_image,y_image);
   X = X(:);
   Y = Y(:);

50 % define the back projection filter
   H = linspace(-B/2,B/2,NUM_SAMP+1);
   delta = diff(H)/2;
   H = H(1:end-1)+delta;
   H = H+Fc;
55 H = 4*pi*H/C;

   % set number of FFT points
   num = 2^(nextpow2(NUM_SAMP)+3);

60 % determine radius values for each projection
   dr = C/B/2/OVER*NUM_SAMP/num;
   r_exact = dr*[0:num-1];
   r_exact = r_exact-mean(r_exact);
   r_exact = r_exact'-dr/2;
65
```

326

```matlab
    % prepare to enter the loop
    width = length(num2str(NUM_PULS));
    raw_image = zeros(NUM_PTS(1),NUM_PTS(2));
    text = strcat(['Forming BP Image: Scatterer ',num2str(scat), ' of ...
        ',num2str(NUM_SCAT)]);
70  wait = waitbar(0,text);

    % loop over each pulse
    for pulse = 1:NUM_PULS

75      % create file name
        name = num2str(pulse);
        while length(name)<width
            name = strcat('0',name);
        end
80      dataname = strcat(DATANAME,name);
        codename = strcat(CODENAME,name);

        % load data
        load(dataname);
85      load(codename);

        % define frequency vector
        freq_vec = repmat(FREQ(code),SAMP_PER_FREQ,1);
        freq_vec = freq_vec(:)';
90
        % define delay to scene center (after t_min)
        ref_delay = 2*(sqrt((CENTER(2)-location(pulse)).^2+CENTER(1)...
            .^2))/C;

        % define angle to scene center
95      angle = atan2((CENTER(2)-location(pulse)),CENTER(1));

        % define doppler to scene center
        doppler = 2*VEL*sin(angle)*Fc/C;

100     % find first sample to see an echo
        front = T>=ref_delay;
        front = find(front);
        front = front(1);

105     % extend frequency vector to cover all samples
        ext_freq_vec = [zeros(1,front-1) freq_vec];
        ext_freq_vec = [ext_freq_vec zeros(1,NUM_SAMP-length(...
            ext_freq_vec))];
        mask = ext_freq_vec>0;

110     % generate reference waveform
        ref = exp(j*2*pi*ext_freq_vec.*(T-ref_delay)).*exp(j*2*pi*...
            doppler*(T-ref_delay));
        ref = mask.*ref;
```

```
        % convert to baseband
115     ref = ref.*exp(-j*2*pi*(Fc-B/2)*T);

        % prep for matched filter application
        fft_ref = conj(fftshift(fft(ref)));

120     % apply matched filter
        data = (fftshift(fft(data)).*fft_ref);

        % generate low-pass versions of the projections
        q = ifftshift(ifft((data.*H),num)).';
125
        % calculate the required radii for the image
        r_required = X.*cos(angle)+Y.*sin(angle);

        % interpolate Q to radii required by the output image
130     q_interp = interp1q(r_exact,q,r_required).*exp(j*2*pi*(Fc-B/2)...
            /C*2*r_required);

        % form the image through coherent addition
        raw_image = raw_image+reshape(q_interp,NUM_PTS(1),NUM_PTS(2));

135     % update waitbar
        waitbar(pulse/NUM_PULS,wait);

    end

140 % close waitbar
    close(wait);
```

Listing D.6:   Calculates the unnormalized image energy.(appendix4/energy.m)

```
    % function [total_energy] = energy(scat);
    %
    % Calculates the unnormalized image energy for use in
    % quantifying anti-aliasing performance.  Normalization
  5 % value determined by cacluating the energy in an
    % ''ideal'' image formed from simulation data
    % containing only one point scatterer.

    function [total_energy] = energy(scat);
 10
    % load constants
    constants

    % load raw image
 15 width = length(num2str(NUM_SCAT));
    name = num2str(scat);
    while length(name)<width
        name = strcat('0',name);
    end
 20 imagename = strcat(IMAGENAME,name);
    load(imagename);
```

```matlab
% calculate image energy
det_image = abs(raw_image)/max(max(abs(raw_image)));
det_image = 20*log10(det_image);
small = find(det_image<-DYN_RANGE);
det_image(small) = -DYN_RANGE;
det_image = 10.^(det_image/20);
det_image = det_image.^2;
total_energy = sum(sum(det_image));
```

Bibliography

1. Abramowitz, Milton and Irene A. Stegun (editors). *Abramowitz and Stegun: Handbook of Mathematical Functions*. U.S. Department of Commerce, 10 edition, 1972.

2. Aeroflex Lintek Corporation. "4000 Series Radar Datasheet". http://www.aeroflex.com/systems/radar/datasheets/4000.pdf, 2004.

3. AFRL/SNA. "Backhoe Data Sample & VISUAL-D Challenge Problem". https://www.sdms.afr.af.mil/ main.htm, 2004.

4. AFRL/SNS. "AFRL/SNS Compact RCS/Antenna Measurement Range". http://www.wrs.afrl.af.mil/other/mmf/comprcs.htm, 2005.

5. Andersh, D., J. Moore, S. Kosanovich, D. Kapp, R. Bhalla, R. Kipp, T. Courtney, A. Nolan, F. German, J. Cook, and J. Hughes. "Xpatch 4: The Next Generation in High Fidelity Electromagnetic Modelling and Simulation Software". *The Record of the IEEE 2000 International Radar Conference*, 844–849. 2005.

6. Anderson, J. M., M. A. Temple, and M. E. Oxley. "Nonlinear Suppression of Range Ambiguities in Pulse-Diverse Radar". *Electonics Letters*, 37(20):1252–1253, September 2001.

7. Aubry, W. M., R. J. Bonneau, R. D. Brown, E. D. Lynch, M. C. Wicks, R. A. Schneible, A. D. George, and M. A. Krumme. "Airborne Sensor Concept to Image Shallow-Buried Targets". *Proceedings of the IEEE Radar Conference*, 233–236. IEEE, 2002.

8. Ausherman, Dale A., Adam Kozuma, Jack L. Walker, Harrison M. Jones, and Enrico C. Poggio. "Developments in Radar Imaging". *IEEE Transactions on Aerospace and Electronic Systems*, AES-20(4):363–400, July 1984.

9. Baker, C. J. and A. L. Hume. "Netted Radar Sensing". *IEEE AESS Systems Magazine*, 3–6, February 2003.

10. Balanis, Constantine A. *Advanced Engineering Electromagnetics*. John Wiley & Sons, Inc., New York, NY, 1989.

11. Balanis, Constantine A. *Antenna Theory*. John Wiley & Sons, Inc., New York, NY, 2 edition, 1997.

12. Bamler, Richard. "A Comparison of Range-Doppler and Wavenumber Domain SAR Focusing Algorithms". *IEEE Transactions on Geoscience and Remote Sensing*, 30(4):706–713, July 1992.

13. Barbarossa, Sergio and Alfonso Farina. "Space-Time-Frequency Processing of Sythetic Aperture Radar Signals". *IEEE Transactions on Aerospace and Electronic Systems*, 30(2):341–358, April 1994.

14. Basu, S. and Y. Bresler. "$O(N^3 \log N)$ Backprojection Algorithm for the 3-D Radon Transform". *IEEE Transactions on Medical Imaging*, 21(2):76–88, February 2002.

15. Bauck, J. L and W. K. Jenkins. "Tomographic Processing of spotlight mode Synthetic Aperture Radar Signals with Compenstation for Wavefront Curvature". *International Conference on Acoustics, Speech, and Signal Processing, ICASSP-88*, volume 2, 1192–1195. 1988.

16. Bauck, J. L. and W. K. Jenkins. "Convolution-Backprojection Image Reconstruction for Bistatic Synthetic Aperture Radar". *IEEE International Symposium on Circuits and Systems*, volume 3, 1512–1515. 1989.

17. Belhadj, Z., A. Saad, S. El Assad, J. Saillard, and D. Barba. "Comparative Study of Some Algorithms for Terrain Classification using SAR Images". *IEEE International Conference on Acousitcs Speech and Signal Processing, ICASSP-94*, volume 5, V/165–V/168. IEEE, 1994.

18. Bennett, A. J. and D. Blacknell. "The Extraction of Building Dimensions from High Resolution SAR Imagery". *Proceedings of the 2001 IEEE Radar Conference*, 182–187. IEEE, 2003.

19. Bi, Zhaoqiang, Jian Li, and Zheng-She Liu. "Super Resolution and SAR Imaging via Parametric Spectral Estimation Methods". *IEEE Transactions in Aerospace and Electronic Systems*, 35(1):267–281, January 1999.

20. Boshra, Michael and Bir Bhanu. "Predicting and Upper Bound on SAR ATR Performance". *IEEE Transactions on Aerospace and Electronics Systems*, 37(3):876–888, July 2001.

21. Bradley, Christopher J. *The Calibration of Bistatic Radar Cross Section Measurements.* Master's thesis, Graduate School of Engineering and Management, Air Force Institute of Technology, Wright-Patterson Air Force Base, OH, 2001.

22. Broquetas, A., J. Palau, L. Jofre, and A. Cardama. "Spherical Wave Near-Field Imaging and Radar Cross-Section Measurement". *IEEE Transactions on Antennas and Propagation*, 46(5):730–735, May 1998.

23. Brown, William M. "Synthetic Aperture Radar". *IEEE Transactions on Aerospace and Electronic Systems*, AES-3(2):217–229, March 1967.

24. Brown, William M. "SAR Resloution in the Presence of Phase Errors". *IEEE Transactions on Aerospace and Electronic Systems*, 24(6):808–814, November 1988.

25. Cabrera, Sergio D. and Thomas W. Parks. "Extrapolation and Spectral Estimation with Iterative Weighted Norm Modification". *IEEE Transactions on Signal Processing*, 39(4):842–850, April 1991.

26. Cafforio, C., C. Prati, and F. Rocca. "SAR Data Focusing Using Seismic Migration Techniques". *IEEE Transactions on Aerospace and Electronic Systems*, 27(2):194–207, March 1991.

27. Callaghan, G. D. and I. D. Longstaff. "Wide-Swath Space-Borne SAR and Range Ambiguity". *Radar 97*, 248–252. 1997.

28. Carrara, Walter G., Ron S. Goodman, and Ronald M. Majewski. *Spotlight Synthetic Aperture Radar: Signal Processing Algorithms.* Artech House, Norwood, MA, 1995.

29. Carrara, Walter G., Ron S. Goodman, and Mark A. Ricoy. "New Algorithms for Widefield SAR Image Formation". *Proceedings of the IEEE 2004 Radar Conference*, 38–43. IEEE, Philadelphia, PA, 2004.

30. Chernaikov, M., T. Zeng, and E. Plakidis. "Ambiguity Function for Bistatic SAR and its Application in SS-BSAR Performance Analysis". *Proceedings of the IEEE 2003 Radar Conference*, 343–348. IEEE, 2003.

31. Chiang, Hung-Chih, Randolph L. Moses, and Lee C. Potter. "Model-Based Classification of Radar Images". *IEEE Transactions on Information Theory*, 46(5):1842–1854, August 2000.

32. Chiota, Robert J. "Global Hawk Integrated Sensor Suite". www.raytheon.com, 2000.

33. Coe, D. J. and R. G. White. "Moving Target Detection in SAR Imagery: Experimental Results". *IEEE International Radar Conference*, 644–649. 1995.

34. Costas, John P. "A Study of a Class of Detection Waveforms Having Nearly Ideal Range-Doppler Ambiguity Properties". *Proceedings of the IEEE*, 72(8):996–1009, August 1984.

35. Crispin Jr., J. W. and A. L. Maffett. "Radar Cross-Section Estimation for Simple Shapes". *Proceedings of the IEEE*, 833–848, August 1965.

36. Curlander, John C. and Robert N. McDonough. *Synthetic Aperture Radar: Systems and Signal Processing.* John Wiley & Sons, Inc., New York, NY, 1991.

37. Currie, A. and M. A. Brown. "Wide-Swath SAR". *IEE Proceedings-F*, 139(2):122–135, April 1992.

38. DeGraaf, Stuart E. "SAR Imaging via Modern 2-D Spectral Estimation Methods". *IEEE Transactions on Image Processing*, 7(5):729–761, May 1998.

39. Desai, Mita D. and W. Kenneth Jenkins. "Convolution Backprojection Image Reconstruction for Spotlight Mode Synthetic Aperture Radar". *IEEE Transactions on Image Processing*, 1(4):505–517, October 1992.

40. Dias, Jose M. B. and Paulo A. C. Marques. "Miltiple Moving Target Detection and Trajectory Estimation Using a Single SAR Sensor". *IEEE Transactions on Aerospace and Electronic Systems*, 39(2):604–624, April 2003.

41. Dicke, R. H. "Object Detection System". U.S. patent no. 2,624,876, Jan 6, 1953.

42. Domik, G., F. Leberl, and J. Cimino. "Multiple Incidence Angle SIR-B Experiment Over Argentina: Generation of Secondary Image Products". *IEEE Transactions on Geoscience and Remote Sensing*, GE-24:492–498, 1986.

43. Dwyer, D., J. Luminati, M. Havrilla, and E. Rothwell. "Bistatic Scattering from a Resistive Sheet Using a Modified PO Current". *URSI National Radio Science Meeting Abstracts*, 85. URSI, URSI, Boulder, CO, 2005.

44. Ender, Joachim H. G. "Space-Time Adaptive Processing for Sythetic Aperture Radar". *IEE Colloquium on Space-Time Adaptive Processing*, 6/1–6/18. 1998.

45. Ender, Joachim H. G. "Space-Time Processing for Multichannel Synthetic Aperture Radar". *Electronics and Communication Engineering Journal*, 29–38, February 1999.

46. Fennell, M. T. and R. P. Wishner. "Battlefield Awareness via Synergistic SAR and MTI Exploitation". *IEEE AES Systems Magazine*, 39–45, February 1998.

47. Fienup, J. R. "Detecting Moving Targets in SAR Imagery by Focusing". *IEEE Transactions on Aerospace and Electronic Systems*, 37(3):794–809, July 2001.

48. Fortuny, J. "An Efficient 3-D Near-Field ISAR Algorithm". *IEEE Transactions on Aerospace and Electronic Systemts*, 34(4):1261–1269, October 1998.

49. Franceschetti, Giorgio, Riccardo Lanari, Vito Pascazio, and Gilda Schirinzi. "Wide Angle SAR Processors and Thier Quality Assessment". *Geoscience and Remote Sensing Symposium, 1991*, volume 1, 287–290. IEEE, 1991.

50. Franceschetti, Giorgio, Riccardo Lanari, Vito Pascazio, and Gilda Schirinzi. "WASAR: a Wide-Angle SAR Processor". *IEE Proceedings-F*, 139(2):107–114, April 1992.

51. Gerchberg, R. W. "Super-Resolution through Error Engergy Reduction". *Optica Acta*, 21(9):709–720, 1974.

52. Golomb, Solomon W. and Herbert Taylor. "Constructions and Properties of Costas Arrays". *Proceedings of the IEEE*, 72(9):1143–1163, September 1984.

53. Goodman, Nathan A., Sih Chung Lin, Devindran Rajakrishna, and James M. Stiles. "Processing of Multiple-Receiver Spaceborne Arrays for Wide-Area SAR". *IEEE Transactions on Geoscience and Remote Sensing*, 40(4):841–852, April 2002.

54. Goodman, Ron, Sreenidhi Tummala, and Walter Carrara. "Issues in Ulta-Wideband, Widebeam SAR Image Formation". *IEEE International Radar Conference*, 479–485. 1995.

55. Graham, Lee C. "Synthetic Interferometric Radar for Topographic Mapping". *Proceedings of the IEEE*, 62(6):763–768, June 1974.

56. Griffiths, H. D. and P. Mancini. "Ambiguity Suppression in SARs Using Adaptive Array Techniques". *IGARSS '91*, 1015–1018. 1991.

57. Griffiths, Hugh. "Synthetic Aperture Radar (SAR)". IEE 2002 Radar Conference, October 2002.

58. Hansen, R. C. "The Segmented Aperture Synthetic Aperture Radar (SASAR)". *IEEE Transactions on Aerospace and Electronic Systems*, AES-10(6):800–804, November 1974.

59. Harrington, Roger F. *Time-Harmonic Electromagnetic Fields*. IEEE Press Series on Electromagnetic Wave Theory. IEEE Press, Piscataway, NJ, 1002.

60. Herman, Gabor T. *Image Reconstruction from Projections*. Academic Press, Inc., New York, NY, 1980.

61. Hilland, Jefferey E., Frederick V. Stuhr, Anthony Freeman, David Imel, Yuhsyen Shen, Rolando L. Jordan, and Edward R. Caro. "Future NASA Spaceborne SAR Missions". *IEEE AES Systems Magazine*, 9–16, November 1998.

62. Horne, A. M. and G. Yates. "Bistatic Synthetic Aperture Radar". *RADAR 2002*, 6–10. 2002.

63. IEEE. *IEEE Standard Radar Definitions*. Technical Report 686-1990, 1990.

64. Jain, Anil K. *Fundamentals of Digitial Image Processing*. Prentice Hall, Englewood Cliffs, New Jersy, 1989.

65. Jakowatz Jr., Charles V., Daniel E. Wahl, Paul H. Eichel, Dennis C. Ghilia, and Paul A. Thompson. *spotlight mode Synthetic Aperture Radar: A Signal Processing Approach*. Kluwer Academic Publishers, Boston, MA, 1996.

66. Jao, Jen King. "Theory of Sythetic Aperture Radar Imaging of a Moving Target". *IEEE Transactions on Geoscience and Remote Sensing*, 39(9):1984–1992, 2001.

67. John Edwin Ross, III. *Application of Transient Electromagnetic Fields to Transient Target Discrimination*. Ph.D. thesis, Michigan State University, East Lansing, MI, 1992.

68. Johnson, Richard C. (editor). *Antenna Engineering Handbook*. McGraw-Hill, Inc., New York, NY, 3 edition, 1993.

69. Kak, Avinash C. and Malcolm Slaney. *Principles of Computerized Tomographic Imaging*. IEEE, New York, NY, 1988.

70. Kinsey, Richard. "Phased Array Beam Spoiling Technique". *Antennas and Propagation Society International Symposium*, volume 2, 698–701. 1997.

71. Kirk Jr., John C. "A Discussion of Digital Processing in Synthetic Aperture Radar". *IEEE Transactions on Aerospace and Electronic Systems*, AES-11(3):326–337, May 1975.

72. Knott, E. F. and T. B. A. Senior. "How far is far?" *IEEE Transactions on Antennas and Propagation*, 22(5):732–734, September 1974.

73. Knott, Eugene F., John F. Shaeffer, and Michael T. Tuley. *Radar Cross Section*. Artech House, 2 edition, 1993.

74. Kovaly, J.J. *High Resolution Radar Fundamentals*. Artech House, Boston, MA, 1977.

75. LaHaie, Ivan J. "Overview of an Image-Based Technique for Predicting Far-Field Radar Cross Section from Near-Field Measurements". *IEEE Antennas and Propagation Magazine*, 45(6):159–169, December 2003.

76. Lee, J., M. Havrilla, E. Rothwell, and J. Luminati. "Bistatic Scattering from a Curved Resistive Sheet Using a Modified PO Current". *URSI National Radio Science Abstracts*. 2005.

77. Lee, W. K., H. D. Griffiths, and R. Benjamin. "Integrated Sidelobe Energy Reduction Technique Using Optimal Polyphase Codes". *Eletronics Letters*, 35(24):2090–2091, November 1999.

78. Leon-Garcia, Alberto. *Probability and Random Processes for Electrical Engineering*. Addison-Wesley Publishing Company, Inc., Reading, MA, 2 edition, 1994.

79. Levanon, Nadav and Eli Mozeson. "Othogonal Train of Modified Costas Pulses". *Proceedings of the IEEE 2004 Radar Conference*, 255–259. 2004.

80. Li, Jian and Petre Stocia. "An Adaptive Filtering Approach to Spectral Estimation and SAR Imaging". *IEEE Transactionson Signal Processing*, 44(6):1469–1484, June 1996.

81. Li, Jian and Peter Stoica. "Efficient Mixed-Spectrum Estimation with Applications to Target Feature Extraction". *IEEE Transactions on Signal Processing*, 44(2):281–295, February 1996.

82. Li, Jian, Peter Stoica, and Zhisong Wang. "On Robust Capon Beamforming and Diagonal Loading". *IEEE Transactions on Acoustics, Speech, and Signal Processing,*, 51(7):1702– 1715, July 2003.

83. Lombardo, P., M. Sciotti, and L. M. Kaplan. "SAR prescreening using both target and shadow information". *Proceedings of the 2001 IEEE Radar Conference*, 147–152. IEEE, 2001.

84. Luminati, J. E., T. B. Hale, M. A. Temple, M. J. Havrilla, and M. E. Oxley. "Generation of Raw Stepped-Frequency Waveform Echoes Using RCS Chamber Measurements". *Proceedings of the IEEE 2005 International Radar Conference*,

927–932. Institute of Electrical and Electronics Engineers (IEEE), Arlington, VA, May 2005.

85. Luminati, Jonathan E. and Todd B. Hale. "Doppler Aliasing Artifact Reduction Using Stepped-Frequency Waveforms". *Measurement and Signal Intelligence (MASINT) Workshop.* Air Force Institute of Technology, Wright-Patterson AFB, OH, September 2004.

86. Luminati, Jonathan E., Todd B. Hale, and Michael J. Havrilla. "Mitigation Of Complex Target Doppler Aliasing Artifacts in SAR Imagery Using Stepped-Frequency Waveforms". *Proceedings of SPIE Symposium on Defense and Security: Algorithms for Synthetic Aperture Radar Imagery XII*, 54–63. The International Society for Optical Engineering (SPIE), Orlando, FL, March 2005.

87. Luminati, Jonathan E., Todd B. Hale, Michael A. Temple, Michael J. Havrilla, and Mark E. Oxley. "Doppler Aliasing Artifact Filtering in SAR Imagery Using Randomised Stepped-Frequency Waveforms". *IEE Electronics Letters*, 40(22):1447–1448, October 2004.

88. Luminati, Jonathan E., Todd B. Hale, Michael A. Temple, Michael J. Havrilla, and Mark E. Oxley. "Doppler Aliasing Artifact Reduction in SAR Imagery Using Stepped-Frequency Waveforms". *1st International Waveform Diversity & Design Conference.* Institution of Electrical Engineers (IEE), Edinburgh, Scotland, November 2004. CD Proceedings.

89. Luminati, Jonathan E., Todd B. Hale, Michael A. Temple, Michael J. Havrilla, and Mark E. Oxley. "Cross-Range Aliasing Artifact Reduction in SAR Imagergy Using Stepped-Frequency Waveforms". *IEEE Transactions on Aerospace and Electronic Systems*, 2005. Submitted for Publication January 2005.

90. Luminati, Jonathan E. and William Wood. "Fourier Transform and Back-Projection Methods of SAR/ISAR Imaging Using Circumscribed Processing Regions". *20th Annual Review of Progress in Applied Computational Electromagnetics.* ACES, Syracuse, NY, 2004.

91. Mahafza, Bassem R. *Radar Systems Analysis and Design Using MATLAB.* Chapman & Hall/CRC, Boca Raton, FL, 2000.

92. McMahon, Jason. *Doppler Aliasing Reduction In Wide-Angle Synthetic Aperture Radar Using A Linear Frequency Modulated Random Stepped-Frequency Waveform.* Master's thesis, Graduate School of Engineering and Management, Air Force Instutute of Technology, Wright-Patterson Air Force Base, OH, 2005.

93. Mensa, Dean L. *High Resolution Radar Cross Section Imaging.* Artech House, Norwood, MA, 1991.

94. Minardi, M. J., L. A. Gorham, and E. G. Zelnio. "Ground Moving Target Detection and Tracking Based on Generalized SAR and Change Detection". *Proceedings of SPIE Symposium on Defense and Security: Algorithms for Synthetic*

Aperture Radar Imagery XII, 156–165. The International Society for Optical Engineering (SPIE), Orlando, FL, March 2005.

95. Monzon, Cesar. "A Cross-Polarization Bistatic Calibration Device for RCS Measurements". *IEEE Transactions on Antennas and Propagation*, 51(4):833–839, April 2003.

96. Moreira, Alberto. "Suppressing the Azimuth Ambiguities in Synthetic Aperture Radar Images". *IEEE Transactions on Geoscience and Remote Sensing*, 31(4):885–895, July 1993.

97. Moreira, Joao R. and Wolfgang Keydel. "A New MTI-SAR Approach Using the Refelctivity Dispalcement Method". *IEEE Transactions on Geoscience and Remote Sensing*, 33(5):1238–1244, September 1995.

98. Moses, Randy. 2005. Ohio State University Professor, Personal Interview.

99. Munson Jr., David C., James Dennis O'Brian, and W. Kenneth Jenkins. "A Tomographic Formulation of Spotlight-Mode Synthetic Aperture Radar". *Proceedings of the IEEE*, 71(8):917–925, August 1983.

100. Munson Jr., David C. and Robert L. Visentin. "A Signal Processing View of Strip-Mapping Synthetic Aperture Radar". *IEEE Trans. Acoust. Speech Signal Processing*, 37(12):2131–2147, Dec 1989.

101. Naraghi, M., W. Stromberg, and M. Daily. "Geometric Rectification of Radar Imagery Using Digital Terrain Models". *Photogrammetric Engineering and Remote Sensing*, 49:195–199, 1983.

102. Novak, L. M. and M. C. Burl. "Optimal Speckle Reduction in Polarimetric SAR Imagery". *IEEE Transactions on Aerospace and Electronic Systems*, 26(2):293–305, March 1990.

103. Novak, L. M., M. C. Burl, and W. W. Irving. "Optimal Polarimetric Processing for Enhanced Target Detection". *IEEE Transactions on Aerospace and Electronic Systems*, 29(1):234–244, January 1993.

104. Potter, Lee C. *DARPA Gotcha Seedling*. Technical report, Ohio State University, 2003.

105. Potter, Lee C. and Randolph L. Moses. "Attributed Scatttering Centers for SAR ATR". *IEEE Transactions on Image Processing*, 6(1):79–91, January 1997.

106. Prati, C., F. Rocca, D. Giancola, and A. Monti Guarnieri. "Passive Geosynchronous SAR System Reusing Backscattered Digital Audio Broadcasting Signals". *IEEE Transactions on Geoscience and Remote Sensing*, 36(6):1973–1976, November 1998.

107. Raney, R. Keith, H. Runge, Richard Bamler Ian G. Cumming, and Frank H. Wong. "Precision SAR Processing Using Chirp Scaling". *IEEE Transactions on Geoscience and Remote Sensing*, 32(4):786–799, July 1994.

108. Rigling, Brian and Randy Moses. "Flight Path Strategies for 3-D scene reconstruction from bistatic SAR". *IEE Proceedings-F*, 151(3):149–157, June 2004.

109. Rigling, Brian and Randy Moses. "Polar Format Algorithm for bistatic SAR". *IEEE Transactions of Aerospace and Electronic Systems*, 40(4):1147–1159, October 2004.

110. Rignot, Eric J. and Jakob J. van Zyl. "Change Detection Techniques for ERS-1 SAR Data". *IEEE Transactions on Geoscience and Remote Sensing*, 31(4):896–906, July 1993.

111. Rihaczek, August W. and Stephen J. Hershkowitz. *Theory and Practice of Radar Target Identification*. Artech House, Boston, MA, 2000.

112. SAIC. "Xpatch® Overview". http://www.saic.com/products/software/xpatch/, 2003.

113. Schurmann, Stuart R. "Radar Characterization of Ship Wake Signatures and Ambient Ocean Clutter Features". *IEEE AES Magazine*, 3–10, August 1989.

114. Sherwin, C.W., J.P. Ruina, and R. D. Rawcliff. "Some Early Developments in Synthetic Aperture Radar Systems". *IRE Transactions on Military Electronics*, MIL-6, Apr 1962.

115. Sitler, K. L., M. A. Temple, R. C. Novack, and J. A. Hughes. "High Range Resolution Profiling Using Phase Coded Stepped-Frequency Waveforms". *IEE Electronics Letters*, 38(1):46–48, January 2002.

116. Skolnik, Merril I. *Introduction to Radar Systems*. McGraw Hill, Boston, MA, 3 edition, 2001.

117. Soumekh, Mehrdad. *Synthetic Aperture Radar Signal Processing*. John Wiley & Sons, Inc., New York, NY, 1999.

118. Soumekh, Mehrdad, David A. Nobles, Michael C. Wicks, and Gerard J. Genello. "Signal Processing of Wide Bandwidth Wide Beamwidth P-3 SAR Data". *IEEE Transactions on Aerospace and Electronic Systems*, 37(4):1122–1141, October 2001.

119. Soumekh, Merhad. "Reconnaissance with Ultra Wideband UHF Synthetic Aperture Radar". *IEEE Signal Processing Magazine*, 21–40, July 1995.

120. Steyskal, Hans, John K. Schindler, Peter Franchi, and Robert J. Mailoux. "Pattern Synthesis for TechSat21 - a Distributed Space-Based Radar System". *IEEE Antennas and Propagation Magazine*, 45(4):19–25, August 2003.

121. Stimson, George. *Introduction to Airborne Radar*. SciTech Publishing, Inc., Raleigh, NC, 2 edition, 1998.

122. Stolt, R. "Migration by Fourier Transform". *Geophysics*, 43:23–48, 1978.

123. Stratton, J. A. *Electromagnetic Theory*. McGraw-Hill, New York, NY, 1941.

124. Strozzi, Tazio, Urs Wegmuller, Charles L. Werner, Andreas Wiesmann, and Volker Spreckls. "JERS SAR Interferometry for Land Subsidence Monitoring". *IEEE Transactions on Geoscience and Remote Sensing*, 41(7):1702–1708, July 2003.

125. Temple, M. A., K. L. Sitler, R. A. Raines, and J. A. Hughes. "High Range Resolution (HRR) Improvment Using Synthetic HRR Processing and Stepped-Frequency Polyphase Coding". *IEE Proceedings on Sonar, Radar, and Navigation*, 151(1):41–47, February 2004.

126. Ulander, Lars M. H., Hans Hellsten, and Gunnar Stenström. "Synthetic-Aperture Radar Processing Using Fast Factorized Back-Projection". *IEEE Transactions on Aerospace and Electronic Systems*, 39(3):760–775, July 2003.

127. Villasenor, John D. "Change Detection on Alaska's North Slope Using Repeat-Pass ERS-1 SAR Images". *IEEE Transactions on Geoscience and Remote Sensing*, 31(1):227–236, January 1993.

128. Walker, Jack L. "Range-Doppler Imaging of Rotating Objects". *IEEE Transactions on Aerospace and Electronic Systems*, AES-16(1):23–52, January 1980.

129. Walterscheid, I., A. R. Brenner, and J. H. G. Ender. "Results on Bistatic Synthetic Aperture Radar". *IEE Electronic Letters*, 40(19):1224–1225, September 2004.

130. Wehner, D. R. *High Resolution Radar*. Artech House, Norwood, MA, 1987.

131. Weib, Matthias. "Synchronization of Bistatic Radar Systems". *Proceedings International Geoscience and Remote Sensing Symposium 04*, volume 3, 1750–1753. IGARSS, 2004.

132. White, R. G. and M. L. Williams. "Processing of ISAR and Spotlight SAR Data to Very High Resolution". *International Geoscience and Remote Sensing Symposium, IGARSS '99*, volume 1, 32–34. 1999.

133. Wiley, C. A. "Pulsed Doppler Radar Methods and Apparatus". U.S. patent no. 3,196,436, July 20, 1953.

134. Wiley, Carl A. "Synthetic Aperture Radars". *IEEE Transactions on Aerospace and Electronic Systems*, AES-21(3):440–443, May 1985.

135. Wong, F. H and I. G. Cumming. "Error Sensitivites of a Secondary Range Compression Algorithm for Processing Squinted Satellite SAR Data". *International Geoscience and Remote Sensing Symposium, IGARSS '89*, 2584–2587. 1989.

136. Wood, William D. *EENG 627 Course Notes*. Graduate School of Engineering and Management, Air Force Institute of Technology, Wright-Patterson AFB, OH, 2003.

137. Xiao, Shu, David C. Munson, Samit Basu, and Yoram Bresler. "An $N^2\log N$ Back-Projection Algorithm for SAR Image Formation". *Conference Record of*

the Thirty-Fourth Asilomar Conference on Signals, Systems and Computers, volume 1, 3–7. 2000.

138. Xu, Xiaojian and Ram M. Narayanan. "FOPEN SAR Imaging Using UWB Step-Frequency and Random Noise Waveforms". *IEEE Transactions on Aerospace and Electronic Systems*, 37(4):1287–1299, October 2001.

139. Yakim-Simen, F., E. Nezry, and J. Ewing. "A Legendary Lost City Found in the Honduran Tropical Forest Using ERS-2 and JERS-1 SAR Imagery". *Geoscience and Remote Sensing Symposium, IGARSS '99 Proceedings*, volume 5, 2578–2580. IEEE, 1999.

140. Yegulalp, Ali F. "Fast Backprojection Algorithm for Synthetic Aperture Radar". *The Record of the 1999 IEEE Radar Conference*, 60–65. 1999.

141. Younis, Marway, Christian Fischer, and Werner Wiesbeck. "Digital Beamforming in SAR Systems". *IEEE Transactions on Geoscience and Remote Systems*, 41(71):1735–1739, July 2003.

142. Younis, Marway and Werner Wiesbeck. "SAR with Digital Beamforming on Receive Only". *Geoscience and Remote Sensing Symposium, IGARSS '99 Proceedings*, volume 3, 1773–1775. 1999.

143. Zelnio, Edmund. 2003. AFRL/SNA Division Cheif, Personal Interview.

144. Ziemer, R. E. and W. H. Tranter. *Principles and Communications: Systems, Modulaton, and Noise*. John Wiley & Sons, Inc., New York, NY, 4 edition, 1995.

145. Zwillinger, Daniel (editor). *CRC Standard Mathematical Tables and Formulae*. Chapman & Hall/CRC, Boca Raton, FL, 31 edition, 2003.

Vita

Captain Jonathan E. Luminati graduated as valedictorian of Radford High School's class of 1994 in Honolulu, HI. He completed his undergraduate degree in electrical engineering at Cornell University, graduating Magna Cum Laude with Honors in May 1998. He earned his commission through AFROTC Detachment 520 at Cornell University where he was recognized as a Distinguished Graduate and recipient of the Lovelace Award, recognizing the outstanding graduating ROTC cadet in each of four regions nationwide. After graduation, he remained at Cornell University for an additional year, obtaining his Master of Engineering degree in May 1999.

Captain Luminati's first assignment was to the Space Vehicles directorate of the Air Force Research Laboratory at Kirtland AFB, NM. During this time he worked at the Countermeasures-Hands-On-Program (CHOP), developing countermeasures for various missile defense related applications. The following year he worked at the Optical Surveillance System Program Office (SPO). In August 2002, Captain Luminati entered the Graduate School of Engineering and Management, Air Force Institute of Technology. Upon graduation, he will be assigned to the Washington DC area.

REPORT DOCUMENTATION PAGE

Form Approved
OMB No. 0704–0188

1. REPORT DATE *(DD–MM–YYYY)*	2. REPORT TYPE	3. DATES COVERED *(From — To)*
08–07–2005	Doctoral Dissertation	Sept 2002 — July 2005

4. TITLE AND SUBTITLE

Wide-Angle Multistatic
Synthetic Aperture Radar:
Focused Image Formation and
Aliasing Artifact Mitigation

5a. CONTRACT NUMBER

5b. GRANT NUMBER

5c. PROGRAM ELEMENT NUMBER

6. AUTHOR(S)

Jonathan E. Luminati, Capt, USAF

5d. PROJECT NUMBER

5e. TASK NUMBER

5f. WORK UNIT NUMBER

7. PERFORMING ORGANIZATION NAME(S) AND ADDRESS(ES)

Air Force Institute of Technology
Graduate School of Engineering and Management
2950 Hobson Way
WPAFB OH 45433-7765

8. PERFORMING ORGANIZATION REPORT NUMBER

AFIT/DS/ENG/05-04

9. SPONSORING / MONITORING AGENCY NAME(S) AND ADDRESS(ES)

Mr. Edmund Zelnio, DR-IV, Senior Engineer, AFRL/SNA
2241 Avionics Circle, WPAFB, OH 45433,(937) 255-4949 x4280

Mr. William Baldygo, AFRL/SNRT
26 Electronic Parkway, Rome, NY 13441, (315) 330-4149

10. SPONSOR/MONITOR'S ACRONYM(S)

11. SPONSOR/MONITOR'S REPORT NUMBER(S)

12. DISTRIBUTION / AVAILABILITY STATEMENT

Approved for Public Release; Distribution is Unlimited

13. SUPPLEMENTARY NOTES

14. ABSTRACT   Traditional monostatic Synthetic Aperture Radar (SAR) platforms force the user to choose between two image types: larger, low resolution images or smaller, high resolution images. Switching to a Wide-Angle Multistatic Synthetic Aperture Radar (WAM-SAR) approach allows formation of large high-resolution images. Unfortunately, WAM-SAR suffers from two significant implementation problems. First, wavefront curvature effects, non-linear flight paths, and warped ground planes lead to image defocusing with traditional SAR processing methods. A new 3-D monostatic/bistatic image formation routine solves the defocusing problem, correcting for all relevant wide-angle effects. Inverse SAR (ISAR) imagery from a Radar Cross Section (RCS) chamber validates this approach. The second implementation problem stems from the large Doppler spread in the wide-angle scene, leading to severe aliasing problems. This research effort develops a new anti-aliasing technique using randomized Stepped-Frequency (SF) waveforms to form Doppler filter nulls coinciding with aliasing artifact locations. Both simulation and laboratory results demonstrate effective performance, eliminating more than 99% of the aliased energy.

15. SUBJECT TERMS

synthetic aperture radar, back-projection, Doppler aliasing, stepped-frequency

16. SECURITY CLASSIFICATION OF:

a. REPORT	b. ABSTRACT	c. THIS PAGE	17. LIMITATION OF ABSTRACT	18. NUMBER OF PAGES	19a. NAME OF RESPONSIBLE PERSON
U	U	U	UU	371	Todd B. Hale, Maj, USAF

19b. TELEPHONE NUMBER *(include area code)*
(937) 255–3636, ext 4639

Standard Form 298 (Rev. 8–98)
Prescribed by ANSI Std. Z39.18